TEAM tAO

8 October 2004

Science

Vol. 306 No. 5694
Pages 181–356 $10

AAAS Annual Meeting

The Nexus: Where Science Meets Society

17-21 February 2005
Washington, DC

AAAS

Science

COVER The AAAS Annual Meeting is widely recognized as the world's premier showcase of advances in science, technology, and engineering. The upcoming meeting in Washington, D.C., 17 to 21 February 2005, will attract more than 9000 participants, including 1000 press registrants from around the world. [Illustration: Jeffrey Pelo]

Volume 306
8 October 2004
Number 5694

DEPARTMENTS

NEWS OF THE WEEK

NEWS FOCUS

214

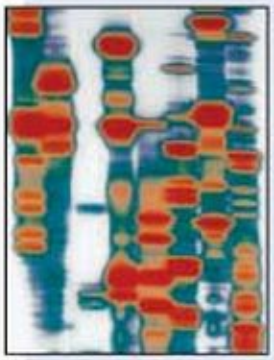

231

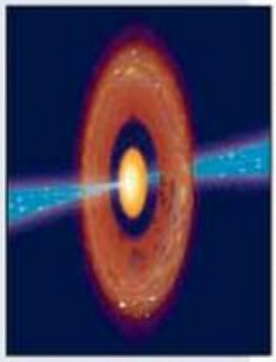

235

LETTERS

BOOKS *ET AL.*

POLICY FORUM

PERSPECTIVES

Contents continued

SCIENCE EXPRESS www.sciencexpress.org

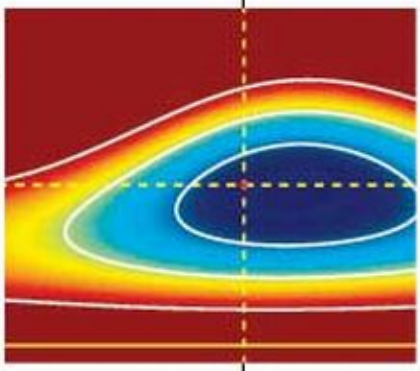

TECHNICAL COMMENT ABSTRACTS

242

BREVIA

RESEARCH ARTICLES

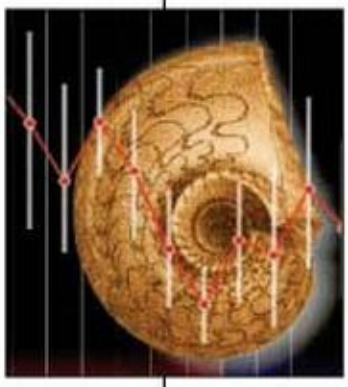

264

REPORTS

Contents continued

Science

Reports Continued

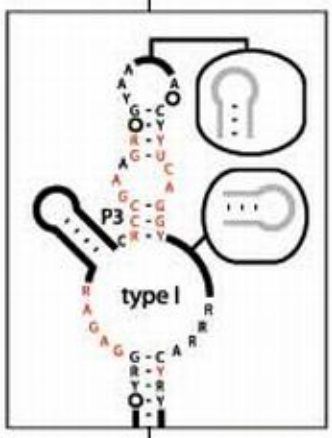

233 & 275

286

AAAS
ADVANCING SCIENCE, SERVING SOCIETY

SCIENCE (ISSN 0036-8075) is published weekly on Friday, except the last week in December, by the American Association for the Advancement of Science, 1200 New York Avenue, NW, Washington, DC 20005. Periodicals Mail postage (publication No. 484660) paid at Washington, DC, and additional mailing offices. Copyright © 2004 by the American Association for the Advancement of Science. The title SCIENCE is a registered trademark of the AAAS. Domestic individual membership and subscription (51 issues): $130 ($74 allocated to subscription). Domestic institutional subscription (51 issues): $500. Foreign postage extra: Mexico, Caribbean (surface mail) $55; other countries (air assist delivery) $85. First class, airmail, student, and emeritus rates on request. Canadian rates with GST available upon request, GST #1254 88122. Publications Mail Agreement Number 1069624. Printed in the U.S.A.

Change of address: allow 4 weeks, giving old and new addresses and 8-digit account number. Postmaster: Send change of address to Science, P.O. Box 1811, Danbury, CT 06813–1811. Single copy sales: $10.00 per issue prepaid includes surface postage; bulk rates on request. Authorization to photocopy material for internal or personal use under circumstances not falling within the fair use provisions of the Copyright Act is granted by AAAS to libraries and other users registered with the Copyright Clearance Center (CCC) Transactional Reporting Service, provided that $13.00 per article is paid directly to CCC, 222 Rosewood Drive, Danvers, MA 01923. The identification code for Science is 0036-8075/03 $15.00. Science is indexed in the *Reader's Guide to Periodical Literature* and in several specialized indexes.

Contents continued

Science
www.scienceonline.org

sciencenow www.sciencenow.org Daily News Coverage

The Brain Goes Bilingual
Picking up a new language may depend on neural word processing.

Smelling Like Sperm
Receptor sperm use to locate egg also functions in nose.

2004 Ig Nobel Prizes Announced
This year's awards honor work on country music, farting fish, and comb-over hairdos.

Quarterly Author Index
www.sciencemag.org/feature/data/aindex.shl

Computer science faculty achieve diversity.

science's next wave www.nextwave.org Career Resources for Young Scientists

MiSciNet: A Model of Departmental Diversity *C. Parks*
Three African-American professors in Auburn University's computer science department discuss diversity.

MiSciNet: MentorDoctor—The Making of a Mentor *Next Wave Staff*
A newly hired faculty member gets tips on how to be a successful mentor.

Career Development Center: Mentorship and Collaboration *GrantDoctor*
A young scientist can and should have more than one mentor/advisor.

Career Development Center: The Red Herring *J. Boss and S. Eckert*
How do you know when the time is right to give up on your old project and find a new one?

Global/US: Developing International Networks in Science and Technology *K. Mo*
The Chinese Association of Science and Technology helped his professional career in international research.

Netherlands: NWO/*Science*'s Next Wave Talents Days 2004—A Report *H. Obbink*
Young Dutch researchers gathered at Slot Zeist to participate in a scientific careers workshop. [in Dutch]

science's sage ke www.sageke.org Science of Aging Knowledge Environment

Perspective: Genes, Longevity, and Technology—Meeting Report from the 2nd Conference on Functional Genomics of Aging in Crete *R. Baumeister and M. Hertweck*
Scientists discuss aging from a systems viewpoint.

News Focus: Fanning the Flames *R. J. Davenport*
Telomerase aggravates oxidative damage in mitochondria.

Aging meeting in Crete.

Regulation of gene expression by IκB.

science's stke www.stke.org Signal Transduction Knowledge Environment

Perspective: Expanded Nuclear Roles for IκBs *P. W. Bates and S. Miyamoto*
Proteins of the IκB family are ascribed new roles as nuclear regulators including direct transcriptional activators.

Perspective: Migrate, Differentiate, Proliferate, or Die—Pleiotropic Functions of an Apical 'Apoptotic Caspase' *S. Kumar*
Flies reveal roles for caspases in processes beyond programmed cell death.

Separate individual or institutional subscriptions to these products may be required for full-text access.

U.S. Science Dominance Is the Wrong Issue

The quality, breadth, and depth of the presentations at the recent multidisciplinary Euroscience Open Forum 2004 in Stockholm, Sweden, made two things clear. First, superb science is being carried out in many countries; second, the scientific enterprise has become truly global in character. Most sessions included participants from a variety of countries, as did many papers. From the perspective of the world's largest general scientific society and one that has itself become more and more international over the years (20,000 AAAS members come from outside the United States), this globalization of science is cause for celebration. Better still, more countries are making productive investments in their science infrastructures, and this portends well for the future of all humankind.

At the same time, recent weeks have seen strident laments from many American quarters, to the effect that the United States may be losing its longstanding global preeminence in science. Some of that concern was triggered when the U.S. National Science Board issued its Science and Engineering Indicators, 2004 report last May. It showed that the United States is no longer the largest producer of scientific information. The European Union is outpacing the United States in the total number of papers published. Moreover, the U.S. share of major science prizes has decreased significantly over the past decade.

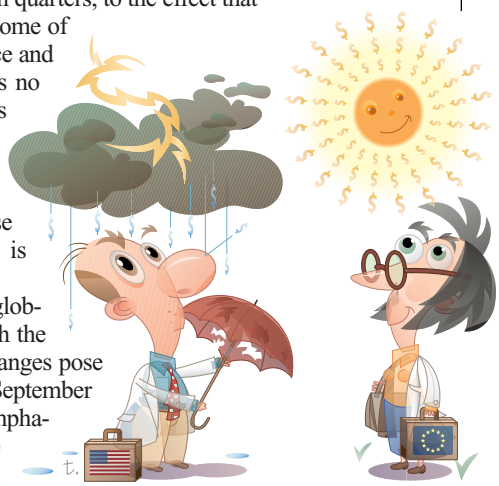

For those Americans who take an overly nationalistic view of the scientific enterprise, this might be bad news. From a more global viewpoint, however, these facts signal a long-awaited and very positive trend: Better and better science is being done all over the world.

The United States should not be wasting energy right now on the question of its global scientific dominance. A far more fundamental issue is clouding the future. Both the U.S. policy climate and funding trends for science are deteriorating, and those changes pose significant risk to the future of U.S. science. On the funding front, the events of September 11, 2001, led to a major shift in the priorities for support of science, a shift that emphasized areas closely related to defense and homeland security at the apparent expense of many other scientific domains. The most recent fiscal year 2005 congressional budget markups would provide notable increases only for defense and homeland security R&D. The rest would be funded at flat levels on average, with some important agencies experiencing decreases. The projections for the next few years are equally dismal (see http://www.aaas.org/spp/rd/). How can we recruit the best young people to science careers if they foresee a grim funding picture for their future work?

The relationship between science and large segments of the U.S. public and policy communities is also eroding. Much recent public discussion has focused on whether there is now more political and ideological interference in the conduct of science and the use of its products than in the past. But the historical question does not really matter. What matters is that we are now experiencing a counterproductive overlay of politics, ideology, and religious conviction on the U.S. climate for science.

The list is alarming. Debates about intelligent design and about stem cell research often pit religious beliefs against scientific data and therapeutic promise, respectively. A recent ruling by the Department of the Treasury held that U.S. scientific journals could not edit and publish papers with authors from trade-embargoed countries. Last year, a motion to force the National Institutes of Health (NIH) to cancel funding for an array of grants on sexual behavior, drug abuse, and HIV/AIDS failed by only two votes in the U.S. Congress. Then, a month ago, Congress actually did second-guess peer review and voted to prohibit funding for two NIH grants whose subject matter made them uncomfortable. They also voted to restrict international scientific travel. Other examples can be found in the claimed distortions of data reporting on health disparities, climate change, costs of Medicare drug coverage, etc.

Worry about whether the United States is better in science than everyone else in the whole world is misplaced anxiety. We need to focus our full energy on the U.S. home front, because the serious erosion of the climate that originally led to America's preeminence in science is now threatening its very eminence—and thus, its future.

Alan I. Leshner
Chief Executive Officer, American Association for the Advancement of Science
Executive Publisher, Science

CREDIT: TERRY E. SMITH

Published by AAAS

This Week

PAGE 209
Clear sailing for Kyoto?

210
Of lice and men

SEISMOLOGY

Parkfield Keeps Secrets After A Long-Awaited Quake

Last week's moderate-to-strong earthquake in central California has justified seismologists' belief that Parkfield (population 37) was the place to wait for a sizable quake they could study. "It's right in the very middle of our network," says geophysicist Malcolm Johnston of the U.S. Geological Survey (USGS) in Menlo Park, California, about the densest fault-monitoring system in the world. It cost more than $10 million over 20 years. "We got great stuff," says Johnston.

But they didn't get it entirely right. When seismologists began the Parkfield Earthquake Prediction Experiment in the 1980s, they expected to capture the next magnitude 6 in unprecedented detail within a few years. Instead, they had to wait 2 decades, a delay that casts additional doubt on models of predictable seismic behavior. And far from providing practical experience in the nascent science of short-term earthquake prediction, Parkfield 2004 seems to have given no warning that would lend hope to the field of short-term quake forecasting. All in all, Parkfield has driven home the point that even one of the world's best behaved fault segments can be pretty cantankerous.

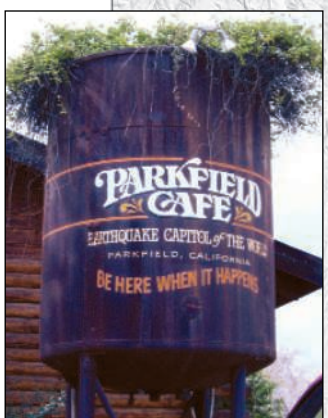

Twenty years ago, the 25-kilometer section of the San Andreas fault that runs under the town of Parkfield seemed like a model seismic citizen. Earthquakes of about magnitude 6, noted two USGS seismologists, had ruptured the same Parkfield segment of the San Andreas in 1857, 1881, 1901, 1922, 1934, and 1966. The average of 22 years between recurrences seemed reliable enough (after rationalizing 1934's "early" arrival), so the next quake in the series should arrive in 1988, give or take 5 years. The National Earthquake Prediction Evaluation Council, a federal committee advising the USGS director, had concurred with that long-term forecast.

But the accuracy of that "give-or-take" forecast had long ago come into question. Now, 16 years after the forecast's most probable date, official quake forecasts say the likelihood of the next Parkfield quake occurring in 2004 was just 5% to 10%. The delay only reinforces the idea that "earthquake recurrence is less regular than had been hoped," says seismologist William Ellsworth of the USGS in Menlo Park. "There are real practical limits to the type of forecast we made at Parkfield."

The limits of quake forecasting became clearer still when seismologists looked at the magnitude-6.0 event on 28 September, which caused little damage to the sparsely populated region 75 kilometers inland from the coast. Seismologist Ross Stein of USGS Menlo Park recalls a number of 1980s ideas about quakes that would have favored predictability. They included the idea that quakes could recur with some regularity; that the more time a fault had to build up strain, the larger the eventual quake would be; and that the same fault segment would rupture in the same "characteristic" quake—the same magnitude and same section of fault—each time.

Of these and other optimistic quake ideas, "the only one still alive at Parkfield is the characteristic earthquake," says Stein. The quake's timing certainly wasn't regular. And to judge by the amount of fault strain accumulated in the intervening 38 years, Parkfield 2004 should have released 20 times the energy that it did and have been a magnitude 6.7.

Even the characteristic aspect does not hold up in detail, Stein notes. The same 25 kilometers of fault broke as in 1966 and 1934, producing a similar-magnitude quake. But in 2004 the rupture started at the southeast end of the segment and ran northwestward, the opposite direction from those that struck in '34 and '66. Parkfield earthquakes—once considered among the most regular of quakes—"are certainly not peas in a pod," observes Menlo Park's Johnston.

Unfortunately for the prediction experiment at Parkfield, the individuality of quakes there extended to geophysical activity before the main shock, activity that seismologists once hoped could be used to predict the main event. The 1966 Parkfield main shock was preceded by a number of possible and even certain precursors. They included a flurry of microearthquakes 2 to 3 months before, cracks in the ground along the fault at least 11 days prior, and a magnitude-5.1 foreshock 17 minutes ahead of the main shock. A magnitude-5 foreshock preceded the 1934 Parkfield quake by 17 minutes as well.

Nothing obvious heralded the 2004 Parkfield quake. "At the moment, nothing has jumped off the screen," ▶

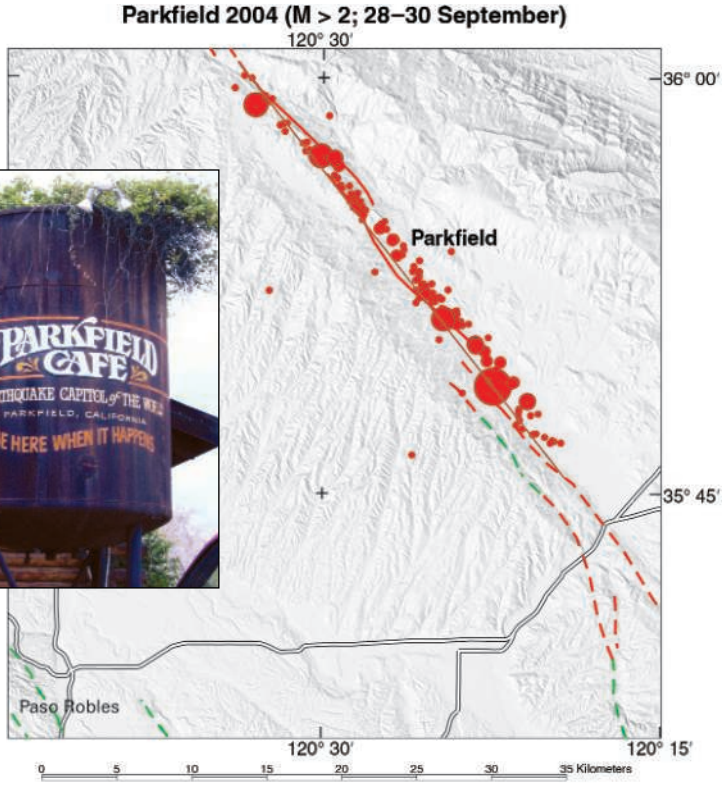

Back at last. The Parkfield earthquake (largest red circle marking its starting point among aftershocks) took far longer than average to recur on the San Andreas fault (red line) and gave no obvious warning of its return.

CREDITS: USGS

Published by AAAS

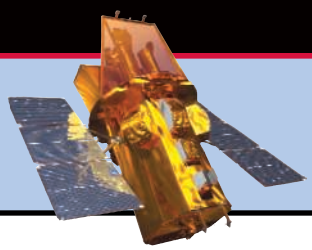

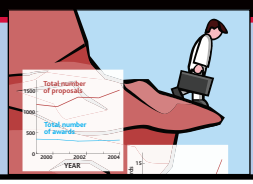

says Ellsworth. A vastly improved seismometer network at Parkfield detected no foreshocks down to magnitude 0, says Robert Nadeau of the University of California, Berkeley. (Magnitudes can be even smaller and negative.) Johnston reports nothing obvious from the dense networks of creepmeters, magnetometers, and strainmeters scattered along the fault. The only possible precursor being discussed is a slow, subtle straining around the fault that began on 27 September. Johnston thinks it may be the long-sought signature of a main shock's very beginnings, so-called nucleation. Colleagues are reserving judgment.

Despite all the disappointments, seismologists haven't lost faith in their quest to understand how earthquakes behave. "The [Geological] Survey bet the farm, lost, was humbled, but stuck it out," says Stein. "In the end, it was the right choice." Earthquake prediction aside, the recording of strong ground shaking in unprecedented detail creates a great opportunity to learn how to build safer, more quake-resistant buildings, says engineering seismologist Anthony Shakal of the California Geological Survey in Sacramento. "Our science advances on the basis of great data," adds Stein, and that is what they got. **–RICHARD A. KERR**

2004 NOBEL PRIZES

Axel, Buck Share Award for Deciphering How the Nose Knows

The sweet smell of success greeted Richard Axel and Linda Buck this week as the two U.S. neuroscientists were awarded the 2004 Nobel Prize in physiology or medicine for their pioneering work on the sense of smell.

The pair first worked together as professor and postdoc in Axel's lab at Columbia University in New York City and have since worked independently to answer fundamental questions about how the brain notices odors wafting through the air. Both are now investigators of the Howard Hughes Medical Institute. Their work has enticed researchers from other fields to study olfaction. "They're magnificent scientists who made a key discovery that opened a big area of research," says Solomon Snyder, a neuroscientist at Johns Hopkins University in Baltimore.

That discovery, reported in a landmark 1991 paper in *Cell*, was the first description of olfactory receptors, the proteins responsible for turning a smell into something the brain can understand. The receptors are embedded on the surfaces of neurons at the back of the nasal cavity. When the receptors bind to odorant molecules sucked into the nose, they trigger a biochemical cascade that ultimately generates a nerve impulse that transmits information to the brain. The paper described a family of about 1000 genes that encode olfactory receptors in rats. The receptor proteins belong to a large class of proteins already familiar to researchers for the variety of roles they play in cell signaling.

Some previous work had suggested that olfactory receptors belonged to this class—G protein–coupled receptors—but the sheer number of olfactory receptors was far greater than anyone had expected, says Columbia's Stuart Firestein, who was not involved in the research. The human visual system, he points out, is able to distinguish myriad colors using only three types of receptors—ones tuned to blue, green, and red. (Subsequent research has revealed that humans have fewer working olfactory receptor genes than rodents—only about 350.) "The work was clearly a breakthrough," says Peter Mombaerts of Rockefeller University in New York City, who joined Axel's lab as a postdoc after reading the 1991 paper and went on to start his own olfactory research laboratory.

PHYSIOLOGY OR MEDICINE

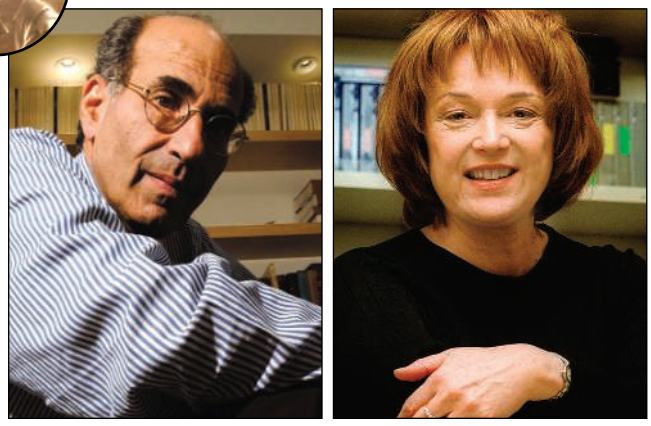

Smells like Stockholm. Richard Axel (*left*) and Linda Buck share the 2004 Nobel Prize in physiology or medicine for their research on olfaction.

Identifying the receptors paved the way to understanding how information about smell is organized in the brain. Independently, Axel and Buck, who is now at the Fred Hutchinson Cancer Research Center in Seattle, Washington, determined that each olfactory receptor neuron expresses one—and only one—olfactory receptor protein. This provided an essential clue to understanding how the brain distinguishes smells. Each odor activates a unique combination of olfactory neurons, allowing the brain to distinguish, say, a good apple from a rotten one.

Axel, 58, and Buck, 57, are both known among colleagues as extremely thorough scientists. "Richard will never publish anything unless it's a really important step forward," says Snyder. The same goes for Buck, who becomes only the sixth woman to win the physiology or medicine Nobel in its 103-year history.

Although the duo's work has answered important questions about the sense of smell, it has also posed additional puzzles. Researchers have just begun to make inroads, for example, toward understanding how an olfactory neuron chooses which receptor gene to express (*Science*, 19 December 2003, p. 2088).

The layered mysteries of the olfactory system are part of the draw for Buck. "It's a wonderful, never-ending puzzle," she says. "I can't think of anything else I'd rather be working on." **–GREG MILLER**

NOBEL AWARDS

David Gross, David Politzer, and Frank Wilczek have received the 2004 Nobel Prize in physics. Look for full coverage of that award and the other science prizes in next week's issue.

CREDITS: (LEFT TO RIGHT) JENNIFER ALTMAN/POLARIS IMAGES; DAN LAMONT; (INSET) THE NOBEL FOUNDATION

Published by AAAS

CREDIT: PHOTOS.COM

CLIMATE CHANGE

Russia, Reluctantly, Backs Kyoto

MOSCOW—After a heated debate last week, the Russian cabinet approved the Kyoto Protocol and sent it to the State Duma, the lower house of the Russian parliament. Observers expect the Duma to ratify it, and if it does, the treaty clears a critical threshold on its way to being accepted as international law. But this will likely do little to quell the fierce debate among Russian researchers and some officials over the merits of the treaty and its ability to reduce greenhouse gas emissions. Also unclear is how firmly Russia and other signatories would enforce the agreement.

Kyoto supporters have been lobbying Russia for years to support the treaty because the country is responsible for 17% of 1990 greenhouse gas emissions, the levels on which the protocol is based. The treaty only comes into force when enough countries have signed up to account for 55% of 1990 emissions. With the United States, the world's biggest emitter, opting out, the protocol would collapse without Russia's participation.

Geographer and biologist Mikhail Zalikhanov, a member of the Duma committee on environment, says that he thinks the Duma will ratify the treaty, but with some provisos. "At the moment I cannot say exactly what these reservations will be, but in the current situation Russia will not benefit from the ratification and may lose much in the future," he says. The treaty requires Russia to stay below its 1990 emissions level until 2012.

But European nations have been pressuring Russia to sign up. Prior to last week's cabinet meeting, Russian President Vladimir Putin met with European Commission President Romano Prodi, while Russian Prime Minister Mikhail Fradkov met with the acting prime minister of the Netherlands, Gerrit Zalm, currently president of the European Union. Fradkov told reporters that the protocol would have trouble in the Duma and might have to be amended. Putin's economic adviser Andrey Illarionov was even more pessimistic, saying forced reductions in industrial output would cost Russia $1 trillion by 2012. "This is a very bad day for the economy and the environment—and civilization," he told a meeting in Washington, D.C., last week.

Opposition in the scientific establishment surfaced earlier this year when Putin asked the Russian Academy of Sciences (RAS) to examine the treaty. A panel of 25 prominent researchers and experts, including RAS President Yuri Osipov and Illarionov, concluded in May that the protocol does not have any scientific basis and would be ineffective in stabilizing greenhouse gas emissions.

In the short term, however, Russia may be able to cash in on the treaty. Russia's greenhouse gas emissions, which fell dramatically after the collapse of the Soviet Union in 1991, have yet to come back up to 1990 levels. According to Yuri Israel, director of the RAS Global Climate Institute, "we can even count on profiting from selling the greenhouse gas quotas to other countries." Experts disagree, however, on how long it will take Russian emissions to rise again to 1990 levels. Illarionov predicts it will happen as early as 2007, perhaps forcing Russia to buy emissions credits from other nations. "Those expecting Russia to be a net seller of CO_2 emission credits will be greatly disappointed," says Illarionov. Israel thinks the country will make at most $100 million.

–ANDREY ALLAKHVERDOV AND VLADIMIR POKROVSKY

Allakhverdov and Pokrovsky are writers in Moscow. With reporting by David Malakoff.

ScienceScope

Spain's Mixed Science Budget

BARCELONA—Spanish scientists heard good and bad news last week: R&D will get a hefty 35% increase in the 2005 budget, but the plan has left many wondering how much basic science will benefit.

Spain's investment in R&D—about 1% of its gross domestic product—is one of the lowest in Europe. So scientists were elated when Socialist Prime Minister José Luis Rodríguez Zapatero followed through on a campaign promise to boost R&D funding. But the budget details disclosed on 30 September left many confused. For example, more than 90% of the planned growth in the R&D National Fund, which supports most science programs, is to be paid in no-interest government loans. The largest share appears slated for technology parks, innovation centers, and large facilities such as a synchrotron in Barcelona and a 10-meter optical telescope in the Canary Islands. The government also will create a new merit-based funding agency modeled on the U.S. National Science Foundation.

Government officials said the loans were necessary to "keep budgetary stability." But public sector scientists "are very worried; loans work best in the private sector," says Jordi Camí, director of the Barcelona-based Municipal Institute of Biomedical Research. Researchers may have to get used to the idea: The Socialist-controlled parliament is expected to approve the budget as it stands.

–XAVIER BOSCH

Montana BSL Lab Advances

Groups opposing a federal biodefense laboratory in Montana have agreed to a plan that may let the project proceed.

The National Institutes of Health's (NIH's) Rocky Mountain Laboratories in Hamilton, Montana, plans to build a biosafety level 4 facility for studying the most dangerous pathogens, such as Ebola virus. Three citizen groups sued NIH in August, charging that its environmental impact statement was inadequate (*Science*, 20 August, p. 1088). After a federal judge ordered mediation, the two sides signed a settlement last week agreeing to added safeguards. The lab will distribute a list of pathogens being studied to local doctors, for example, and has agreed not to weaponize pathogens. NIH also agreed to get public comment on a draft emergency plan before the lab opens in 2007. With the judge's approval, the August suit will be dismissed.

"They put a lot of mechanisms in place that we thought were important," says Alexandra Gorman of Women's Voices for the Earth in Missoula, one of the groups that sued. Construction should begin soon, a lab spokesperson says. **–JOCELYN KAISER**

Published by AAAS

HUMAN ORIGINS

Louse DNA Suggests Close Contact Between Early Humans

Lice may be the bane of teachers trying to stop the parasites from leaping from head to head, but their persistent association with people is proving a boon to researchers probing modern human origins. Because lice are species-specific parasites, their history is thought to parallel our own. Now a genetic analysis of head lice suggests that two distinct species of early humans had close physical contact after a long period of isolation. "The work [gives] us an indirect but informative new window on modern human origins," says paleontologist Chris Stringer of the Natural History Museum in London.

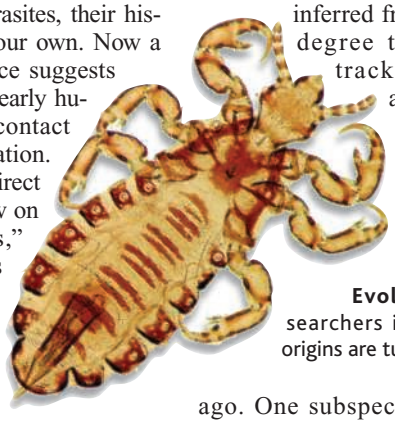

Evolutionary partner. Researchers itching to track human origins are turning to lice for answers.

Stringer and others have argued that our species, *Homo sapiens*, migrated out of Africa and quickly replaced other human species, such as *H. erectus* in Asia, without interbreeding. A competing theory, multiregional evolution, contends that modern humans appeared when *Homo sapiens* from different geographical regions mated with each other as well as with archaic *Homo* populations, blurring regional and species boundaries. A middle-ground proposal suggests that as modern humans from Africa spread across the globe, they interbred with archaic humans, but that only African genes persisted. After analyzing lice data, Dale Clayton, an evolutionary biologist at the University of Utah, Salt Lake City, says that the history of these pests best fits the third hypothesis.

For the work, Clayton and postdoc David Reed, now an evolutionary biologist at the University of Florida, Gainesville, compared mitochondrial DNA from lice, primarily *Pediculus humanus*, to existing data on human evolution. They analyzed six louse species, including two from humans, three from other primates, and one from a rodent. They used the sequences of two mitochondrial genes plus morphological traits to draw the louse family tree, which they then compared to the *Homo* tree.

Because lice never leave their human hosts, the lice data are "a completely independent line of evidence" that helps confirm human prehistory, says Clayton. For example, according to the parasite's DNA, lice specific to humans and lice specific to chimpanzees appeared 5.6 million years ago, confirming previous work suggesting that the ancestors of chimps and humans diverged at about this time, Reed, Clayton, and their colleagues report in the 5 October online *Public Library of Science*. The lice also suffered a dramatic population decline and then recovery about 100,000 years ago, a bottleneck that parallels the story inferred from human genes. "The degree to which [the louse] tracks human history [is] amazing," says Reed.

The data also revealed that two genetically distinct lineages of *P. humanus* appeared about 1.18 million years ago. One subspecies is now distributed worldwide and infects either the head or the body, whereas the other only inhabits the New World and only lives on scalps. Clayton argues that the two lice subspecies must have diverged at about the same time that two human lines—perhaps Asian *H. erectus* and the African ancestors of *H. sapiens*—became established. The fact that the lice grew so far apart genetically suggests that they had little or no contact with each other—which implies that their human hosts were also separated. Consequently, "long-term gene flow such as is envisaged in the multiregional model is ruled out from these data," says Stringer.

But the data do suggest that there must have been some contact among different kinds of early humans. Today, there is only one species of human—but two subgroups of lice. So the lice thought to have been living on *H. erectus* must have jumped to *H. sapiens* at some point before *H. erectus* went extinct, perhaps as late as 30,000 years ago. The researchers think the shift occurred through skin-to-skin contact, as might occur during fighting or sex.

Some researchers are convinced by this scenario. "The pattern they found is as clear as a bell," says anthropologist Henry Harpending of the University of Utah, who was not involved with the work. But Milford Wolpoff of the University of Michigan, Ann Arbor, author of the multiregional hypothesis, calls the new study a "fringe explanation." He notes that the divergence of the louse subspecies does not necessarily imply a million-year separation, because populations can diverge without isolation. He adds that the story "doesn't work at all with our studies," which he says indicate frequent contact between different archaic humans.

Clayton and Reed hope to pin down the question of contact among human species by studying the genetic history of lice transmitted almost exclusively through sexual intercourse. "If we get pubic lice, which are a different genus, and get the same results, then we would know that there is something very interesting going on," says Clayton.

–ELIZABETH PENNISI

RESEARCH COMMUNITY

Janelia Farm to Recruit First Class

Neuronal circuitry and imaging technologies will be the focus of the new Janelia Farm Research Campus of the Howard Hughes Medical Institute (HHMI). This week HHMI begins recruiting staff in these fields for its $500 million, 280-scientist institute in Ashburn, Virginia, scheduled to open in late 2006.

Janelia Farm director Gerald Rubin says he wants to recreate the close-knit feeling of legendary labs such as the Laboratory of Molecular Biology in Cambridge, U.K., where well-funded investigators free of grant-seeking pressures work in small groups (*Science*, 9 May 2003, p. 879). There will be at least one difference: Janelia will emphasize technology. Last week, a hardhat-clad Rubin showed off the vast concrete bays and corridors of Janelia's main building at a bucolic site along the Potomac River, about 64 kilometers from Washington, D.C. It could accommodate the largest nuclear magnetic resonance machine or microscope, but at this point, he says, "we have no idea what we're going to put in it."

To decide on Janelia's research focus, HHMI held five workshops earlier this year and asked scientific leaders to think about problems tough enough to require 100 people working for 10 years. The advisers ruled out areas such as membrane proteins, figuring that they could be studied at existing labs. But the "challenging" and "highly interdisciplinary" problem of how a fruit fly assesses motion and distance to land softly on a wall made the cut, Rubin says. So did building new optical and other microscopes for imaging subcellular structures and living systems.

One workshop participant, molecular biologist Eva Nogales of HHMI, the University of California, Berkeley, and Lawrence Berkeley National Laboratory, hopes Janelia's teams will devise new detectors ▶

CREDIT: VINCENT S. SMITH/UNIVERSITY OF GLASGOW

and computational methods for imaging nonhomogenous macromolecules. "It could be a quantum leap in what is being done right now," Nogales says.

Applications for the first batch of Janelia's 24 group leaders—biologists, chemists, engineers, computer scientists, and physicists are all invited—are due 15 December. But be warned: Appointments, although renewable beyond the initial 6 years, will be untenured. "We want people who say, 'Give me some resources and get out of my way,' " says Rubin. "That will appeal to some people [but] scare the daylights out of others."

–JOCELYN KAISER

PALEONTOLOGY

T. rex Clan Evolved Head First

Like reclusive celebrities, tyrannosaurs have risen to evolutionary stardom while keeping their origins shrouded in mystery. Now, the most primitive tyrannosauroid yet discovered has revealed the basic blueprint from which *Tyrannosaurus rex* and its kin evolved. The fossils, so well preserved that one even shows a "protofeather" fuzz covering the body, are described this week in *Nature*. Among other details, they show that tyrannosaurs began evolving the deadly design of their heads before their bodies morphed into powerhouses. "I think people are going to be tremendously excited about this," says Matthew Carrano of the Smithsonian Institution. "It's certainly going to clarify a huge amount about the evolution of tyrannosaurs."

Paleontologists have found about a dozen species of tyrannosaurs. Most lived late in the Cretaceous Period, which ended 65 million years ago. Isolated bones have been found from older and more primitive tyrannosaurs, but not all have been accepted as ancestors. The new specimens—one fairly complete skeleton, plus parts of two others—come from western Liaoning Province in China. "It's the best primitive tyrannosauroid that we have," says Thomas Holtz of the University of Maryland, College Park.

After farmers unearthed them, the specimens were studied by Xing Xu and colleagues from the Institute of Vertebrate Paleontology and Paleoanthropology in Beijing, along with Mark Norell of the American Museum of Natural History in New York City. Teeth and other features pegged the roughly 135-million-year-old creature as a tyrannosauroid. The skull has many familiar attributes, including bones shaped like those that apparently helped later tyrannosaurs launch swift, bone-jarring ambushes. The team dubbed the new creature *Dilong paradoxus* for "surprising emperor dragon."

Those surprises include features that distinguish *D. paradoxus* from its descendents. Its small body, 1.6 meters long, gives researchers a chance to study which aspects of *T. rex*'s anatomy are truly tyrannosaurian rather than due to gargantuan size. And compared with *T. rex*, *D. paradoxus* had relatively long arms. Maybe developing the head for attacking—a safer approach than hands-on grappling with prey—enabled *D. paradoxus*'s descendants to grow larger and handle bigger prey, speculates Oliver Rauhut of the Bavarian State Collection of Paleontology and Geology in Munich, Germany.

Another previously unknown feature of tyrannosauroids is the soft pelt of 2-centimeter-long fibers, called protofeathers. These have been found in more primitive ancestors outside the tyrannosaur group, but large tyrannosaurs appear to have sported reptile-like scales instead. Norell proposes that smaller tyrannosaurs needed fuzz to stay warm but that their larger descendants, like modern elephants, shed their insulation to keep from overheating.

–ERIK STOKSTAD

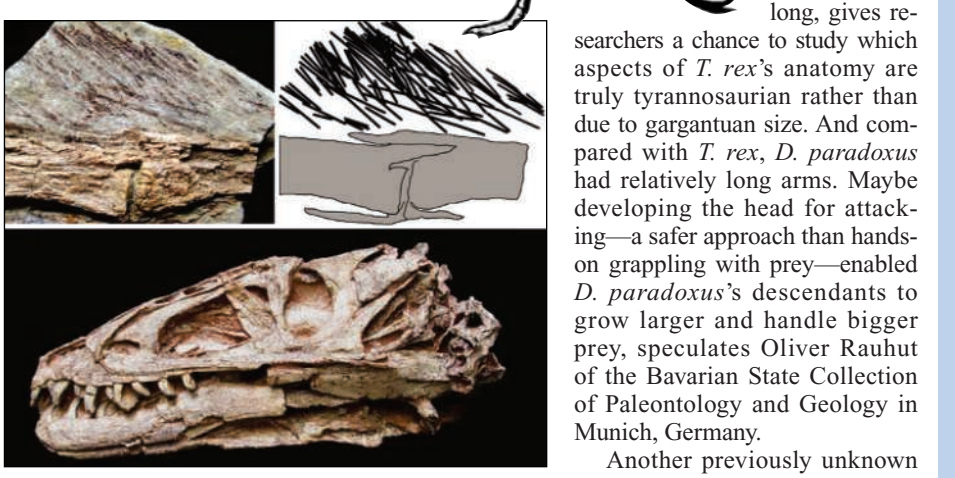

Forging a head. *Dilong paradoxus* sported downy "protofeathers" and an advanced *T. rex*–like skull.

CREDITS: X. XU *ET AL.*, *NATURE* **431**, 680 (2004)

ScienceScope

Senator Moves on Kennewick

American Indians aren't giving up on the battle to keep Kennewick Man, the 9400-year-old bones found in Washington state in 1996, out of scientists' hands. Last July, a federal court barred several tribes from claiming the bones because they couldn't prove that the remains came from a person related to a current tribe (*Science*, 30 July, p. 591). Last week, Senator Ben Nighthorse Campbell (R–CO) tacked a two-word amendment onto a bill (S. 2843) that would make such claims easier to prove.

Currently, the Native American Graves Protection and Repatriation Act defines "Native American" as "relating to a tribe, people, or culture that is indigenous to the United States." Campbell's amendment changes the wording to "is *or was* indigenous," removing the need to show a link to living Indians.

It was a "sneaky" move, says Alan Schneider, the scientists' Portland, Oregon, lawyer. But it may not have any immediate impact: Congress watchers say the legislation is unlikely to pass the Senate this year, and it might not apply retroactively if it passed.

Meanwhile, on 8 September four tribes moved to reintervene in the Kennewick case, petitioning to veto studies they oppose.

–CONSTANCE HOLDEN

Report Faults Biosafety Panels

A watchdog group says that many institutional biosafety committees (IBCs) that oversee potentially risky experiments at U.S. research institutes fail to comply with rules on public access.

The U.S. government wants to give the committees, set up in the 1970s to oversee genetic engineering experiments, a new role in weighing "dual use" research: studies whose data could be exploited by future bioterrorists. But a survey of 355 IBCs by the Sunshine Project, an Austin, Texas, group (*Science*, 6 August, p. 768), found that 44% of the panels were unable or unwilling to provide minutes of their most recent meetings, as required by guidelines from the National Institutes of Health (NIH). Another 36% produced minutes that lacked key information, according to the report. Dozens of IBCs appear not to meet regularly at all.

The survey "shows some weaknesses in the system," admits Stefan Wagener, president of the American Biological Safety Association, but he adds that doesn't mean safety is compromised. The scrutiny already has prompted NIH's Office of Biotechnology Activities, which oversees the IBCs, to order the panels to convene regular meetings and release reasonably detailed minutes.

–MARTIN ENSERINK

AIDS TREATMENT

Drugmakers Test Restrictions on Generics in U.S. Programs

Last spring, the Bush Administration triggered howls of outrage from AIDS researchers and activists around the world when it insisted that U.S. government programs could only use drugs approved by the U.S. Food and Drug Administration (FDA) to treat HIV-infected people in poor countries. Many saw the policy as a thinly veiled effort to favor big pharmaceutical companies over the manufacturers of cheaper generic drugs. The issue came to a full boil in July at the international AIDS conference in Bangkok, where several leading AIDS researchers lambasted the policy and AIDS activists disrupted a talk by Randall Tobias, the Administration's global AIDS coordinator (*Science*, 23 July, p. 470).

In the next few weeks, some—but not all—of the heat could be taken out of this dispute. In an effort to defuse the issue, the Administration announced a plan in May for FDA to put applications from manufacturers of generics on a fast track, with a decision in 2 to 6 weeks. That commitment is about to be put to the test: *Science* has learned that South Africa's Aspen Pharmacare submitted an application to FDA in early September for six generic anti-HIV drugs it manufactures, and two Indian companies, Cipla and Ranbaxy, plan to file applications soon. If approved, these companies' drugs could eventually be used in the President's Emergency Plan for HIV/AIDS Relief (PEPFAR), a $15 billion program that aims to treat 2 million people in 15 developing countries over the next 5 years.

Critics, however, are unlikely to be assuaged. For one, it may already be too late for any generics to qualify for the next round of treatment under PEPFAR: Companies that want to supply FDA-registered drugs to the program must submit their proposals by 15 October, and "it's going to come down to the wire whether we're registered by then," says Stavros Nicolaou, a senior executive at Aspen. Moreover, generic drugs that have not been submitted for FDA approval would still be ruled out.

Many AIDS researchers also question the rationale underlying the Administration's position: that generics might not contain "bioequivalent" doses of the branded drugs, allowing the virus to develop resistance more easily. "There's no biologic basis in the fear that slight differences in bioequivalence will make the slightest difference in effect," says Bernard Hirschel, head of the HIV/AIDS unit at the University of Geneva in Switzerland. Herschel points out that the World Health Organization has already approved many generic drugs, and "it's hard to see that there's any substantial difference between the WHO and the FDA processes."

CREDIT: J. COHEN

Demand for access. Demonstrators in Bangkok protest policies that block the use of certain generic drugs in HIV/AIDS programs.

Insisting on brand-name drugs, he says, limits the availability of the most effective treatment strategies, sows confusion, and stymies cutting-edge treatment research in developing countries because U.S.-funded research projects must also use FDA-approved drugs.

Daniel Berman, who coordinates a drug-access campaign for Médecins Sans Frontières, argues that the FDA requirement could inadvertently increase drug-resistance problems. Berman notes that fixed-dose combinations—ideally, one pill that combines three AIDS drugs—are easier for people to take and thus lead to better adherence to regimens, a critical strategy to avoid resistance. No big pharmaceutical companies make this fixed-dose combination, nor does Aspen. "The politics of the Bush Administration have prevented the easier treatment of patients," charges Berman.

Mark Dybul, chief medical officer for Tobias's office, says, however, that several African clinicians, citing adverse experiences in the past with poorly made generic drugs, have thanked him for insisting on FDA approval. "In the long run I think everyone will recognize this is the right decision," says Dybul. "Our policy is safe and effective drugs at the lowest possible cost for everyone in the world." He adds that the cost of branded drugs is only about three times that of generics and is dwarfed by the costs of building infrastructure and training clinicians how to use the treatments. "People are making this huge noise about a relatively small amount of money," he says.

—JON COHEN

COSMOLOGY

A Slanted View of the Early Universe

In the Atacama Desert of northern Chile, a microwave telescope has taken the best snapshot of an exquisitely faint echo of the big bang. In a paper published online by *Science* this week (www.sciencemag.org/cgi/content/abstract/1105598), astronomers present detailed pictures of the polarization of the cosmic microwave background (CMB)—the faint and ubiquitous image of the fiery universe when it was less than 400,000 years old.

"A photon is left with the imprint of the last few times it scatters" off the cloud of glowing gas in the infant universe, says telescope team member Carlos Contaldi, an astrophysicist at the Canadian Institute for Theoretical Astrophysics in Toronto. "[Polarization] is a very clean picture" of the structure of the cosmos when it was extremely young.

The telescope, known as the Cosmic Background Imager (CBI), has been observing the CMB for years in hopes of testing theories about how the universe was born. Two years ago, CBI presented what was then the best picture of the CMB (*Science*, 31 May 2002, p. 1588). Even after the CMB-observing Wilkinson Microwave Anisotropy Probe (WMAP) blew most of its competition out of the water (*Science*, 19 December 2003, p. 2038), CBI still held an edge in observing very small features in the CMB.

Now, the CBI team has released the results of nearly 2 years of observing polarization in the CMB: the extremely hard-to-spot directionality of incoming light. First detected by another instrument in 2002 (*Science*, 27 September 2002, p. 2184), the polarization paints a sharp picture of the early universe, as it remains relatively unchanged during a photon's multibillion-year journey to Earth. "It shows that [the primordial gas] was behaving exactly as we expected it to behave," says team member Anthony Readhead, an astronomer at the California Institute of Technology in Pasadena.

Even stronger confirmation is expected when WMAP releases its own polarization results, probably within weeks, and other ground-based experiments follow suit. But CBI will still provide data about features in the CMB that are too small for the other experiments to resolve.

—CHARLES SEIFE

A long-awaited satellite should find scores of gamma ray bursts, sparking a rapid response from telescopes that span the globe

Astronomers Eager for a Swift New Vision of the Universe

"Swifts fly expertly on their first try," a writer for *National Geographic* once observed about the graceful, darting birds. Astronomers trust that those words will hold true for a satellite called Swift, which hopes to start flitting around space next month in search of gamma ray bursts—the biggest explosions in the universe.

"This is the first astronomical satellite that can rapidly change direction with its own onboard brains," says principal investigator Neil Gehrels of NASA's Goddard Space Flight Center (GSFC) in Greenbelt, Maryland. That agility will allow Swift to swivel its "eyes" onto a new burst within minutes. What it "sees" should yield insights about the earliest incandescent moments of each explosion, thought to arise from especially violent supernovas that form black holes at their cores.

The satellite also will send notice of every burst to a fleet of telescopes on the ground, from robotic instruments that respond in seconds to the planet's most powerful telescopes. The unprecedented reach of this network promises to lift the veils on what drives the tightly beamed blast waves.

"Swift will take us from burst-by-burst science to very deep studies using hundreds of bursts," says astrophysicist Joshua Bloom of the Harvard-Smithsonian Center for Astrophysics (CfA) in Cambridge, Massachusetts. Bloom hopes that Swift's most distant bursts will let scientists peer back to the first few hundred million years of cosmic history: "The early universe may have been a ripe petri dish for making what we think were the first gamma ray bursts. They are our best hopes for probing this very hot era in cosmology."

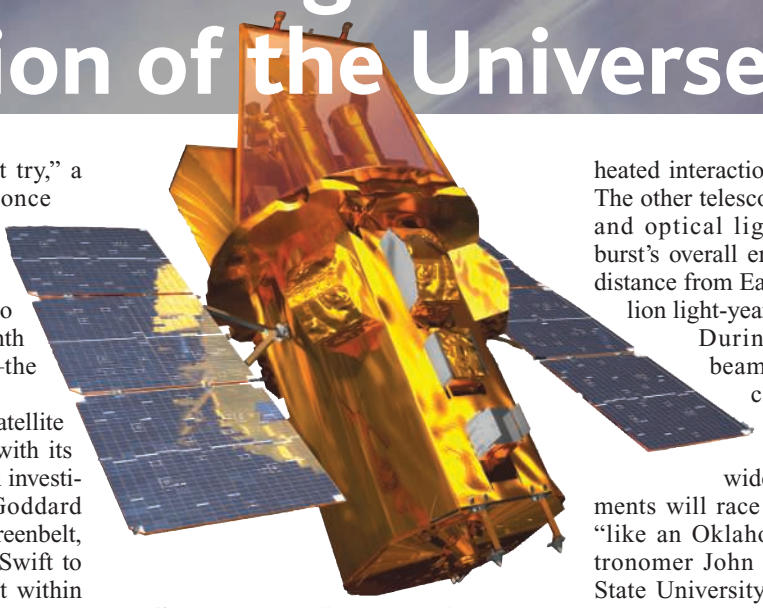

Bird's eye. Swift will pivot in orbit to view evanescent gamma ray bursts.

CREDIT: NASA

BAT's eyes

The $250 million mission, a collaboration between NASA and institutions in Italy and the United Kingdom, was scheduled to take flight in December 2003 before several delays—most seriously, a 5-month overhaul of electronic components to make them more resistant to radiation. Recent damage to Florida's Kennedy Space Center from hurricanes Frances and Jeanne then pushed the launch from September to early November.

The mission features a compact assembly of three telescopes. Swift will catch gamma ray bursts with its Burst Alert Telescope (BAT), which Gehrels calls "the most sensitive gamma ray imager ever." Like someone staring upward to watch for meteors, BAT's gaze will encompass a large swath of the heavens (about 1/6) at any one time. An array of 32,768 cadmium-zinc-telluride detectors, covering a half-meter square, will register electronic blips from incoming gamma rays.

Because gamma rays are so energetic, they would pierce through the optics of a traditional telescope. Instead, BAT will interpret a geometrical pattern created by a "coded aperture mask": a screen above the detectors with randomly placed square lead tiles. "A burst from a particular point on the sky will cast a unique shadow [through the tile pattern] onto the detectors," says astrophysicist Craig Markwardt of GSFC. The satellite's software will calculate the location well enough for Swift to reorient itself toward the burst within about a minute.

After the adjustment, the satellite's two other telescopes will zero in on the burst's rapidly changing cascade of energy. One telescope will gather x-rays to scrutinize the burst's internal chaos and its superheated interaction with material around it. The other telescope, sensitive to ultraviolet and optical light, will help gauge the burst's overall energy and its approximate distance from Earth—typically, several billion light-years.

During each step, Swift will beam the burst's location and characteristics to the ground for e-mail flashes to astronomers worldwide. With each alert, instruments will race to that parcel of the sky "like an Oklahoma land rush," says astronomer John Nousek of Pennsylvania State University, University Park, site of the mission control center. "All scientists will get all of the information as fast as is robotically possible."

The rush could happen often: Mission scientists estimate that Swift will spot 100 to 150 gamma ray bursts a year. But its two research telescopes aren't likely to observe the first critical seconds of many explosions. The sun, moon, or Earth could be too close for a safe view, and the satellite's pivot speed will be too slow to catch the initial flare for all but a few events.

Ground patrol

For the fastest response, the Swift team will rely on automated telescopes now deployed across the globe. Teams on six continents have built small new telescopes or have adapted larger existing telescopes to respond to Swift's electronic prompts—often within mere seconds. The web of ground teams, 39 and counting, will compose the most sweeping coordinated response to a satellite's observations. "It's become a cottage industry," says astronomer Kevin Hurley of the University of California, Berkeley, who coordinates the follow-up effort. "Everything is now in place to reap all of the benefits of studying bright new sources that last only a half-day or so."

One such ambitious project is the Robotic Optical Transient Search Experiment (ROTSE), which has identical autonomous telescopes in Australia, Namibia, Turkey, and Texas. At least one of the 0.45-meter telescopes should be able to zip to a Swift

Published by AAAS

position in less than 10 seconds. That's an advantage because efforts to track a burst's optical or infrared emissions from the ground must take place at night. "With apologies to our British colleagues, the sun never rises on the ROTSE array," quips astronomer Donald Smith of the University of Michigan, Ann Arbor.

Similar efforts in California, Chile, Europe, Hawaii, Japan, and elsewhere will provide global coverage of any given burst as Earth rotates. Even well-equipped amateur astronomers could provide useful results, says Hurley. But everyone expects the squadron of automatons to have growing pains. "These robotic telescopes are incredibly hard to operate and to keep running," Smith says. "It's like Whack-a-Mole: As soon as you fix one thing, something else pops up."

Provided that some of the robots work as advertised, astronomers expect to see the first fires of gamma ray bursts more clearly than ever. That's critical for unraveling what happens at the heart of a titanic supernova, says astronomer Derek Fox of the California Institute of Technology in Pasadena. "At very early times, you observe the blast wave a short distance from the central engine," he says. "The later you look, the less memory it has of the initial explosion."

Although the robots will have the best shot to catch a burst's first sparks, the world's largest telescopes will join the act, too. Plans call for one of the 8.2-meter telescopes of the European Southern Observatory's Very Large Telescope array in Chile to swing to a new burst within 15 minutes or so, when feasible. One of the 10-meter Keck Telescopes in Hawaii will respond to some bursts as well. These mammoth mirrors gather so much more light than other instruments do that they will nail down the distances to the explosions—especially the faintest ones near the edge of the observable universe.

CREDIT: NASA

Coded pattern. A lead-tile mask will cast a unique gamma ray shadow on Swift's detector for each burst.

Gamma Ray Bursts: New Cosmic Rulers?

One class of stellar explosions, called type Ia supernovas, erupts with surprising uniformity. They probably arise from white dwarfs that explode when they exceed a well-known threshold of mass. By correcting for subtle variations, astrophysicists turned the supernovas into "standard candles": cosmic light bulbs of similar brightness (*Science*, 24 November 1995, p. 1295). That property has made type Ia supernovas the premier probes of the accelerating expansion of space, one of astronomy's landmark finds in recent years.

At first glance, it seems unlikely that gamma ray bursts could serve the same purpose. Gigantic spinning stars—the favored progenitors of gamma ray bursts—have wildly varying masses, spin rates, heavy elements, and other properties. When the stars die, those factors apparently spawn bursts whose energies vary as much as 100,000 times from one burst to the next.

But astrophysicists have found a physical pattern hidden within that drastic range. Each burst churns out light that peaks at a unique frequency. A spectral plot reveals that crescendo as a bump in the number of photons at that energy. Each burst also has a total output of energy: its "wattage." For the best-studied bursts, researchers can derive that output by accounting for whether the explosion channeled its emissions toward us along a needlelike cone or a wider spray (*Science*, 30 November 2001, p. 1816).

Those two quantities—peak frequencies of energy and total energy—are tightly correlated for gamma ray bursts, according to astronomer Giancarlo Ghirlanda of the Brera Observatory in Italy and his colleagues. "There is a very small scatter. It convinces us that something significant is going on," Ghirlanda says, although theorists have no idea why the relation exists.

Still, the correlation is so striking that just 15 gamma ray bursts already reveal the mass content of the universe and its expansion nearly as well as type Ia supernovas and other techniques, Ghirlanda says. His team confidently calls gamma ray bursts "new rulers to measure the universe" in the 20 September *Astrophysical Journal Letters*. A team from Nanjing University in China, led by Zigao Dai, reached a similar conclusion.

Other astrophysicists are wary. A couple of noteworthy bursts don't fit the correlation, and the overall statistics are still shaky, say CfA astrophysicist Joshua Bloom and graduate student Andrew Friedman. "The biggest problem is the small number of bursts so far," Friedman says. Swift's cornucopia of bursts should settle the debate, both sides agree.

–R.I.

The deepest probes?

Indeed, the prospect of detecting such faint bursts is the stuff of dreams for astrophysicists. Currently, quasars—the active cores of galaxies, powered by supermassive black holes—are the brightest steady sources that astronomers can see in the young universe. These reach back to within about 1 billion years of the big bang. But in its first 20 minutes of raging energy, a gamma ray burst is 1000 times brighter than any quasar, says Bloom of CfA. "We may see when the first stars were dying," Bloom says. Such a burst, far earlier than the quasar era, would illuminate all other matter between it and Earth to give astronomers the deepest possible cosmic probe.

But it's not clear that the universe's earliest stars actually unleashed gamma ray bursts. Such stars were different beasts, with virtually no heavy elements and perhaps far more mass than later generations. If Swift sees no bursts within the first few hundred million years after the big bang, it will have revealed something fundamental about how those stars lived and died, Bloom notes.

Another profound riddle that Swift may address is the origin of the shortest gamma ray bursts. A whole class of bursts flashes for fractions of a second, then vanishes (*Science*, 30 November 2001, p. 1817). Astrophysicists speculate that these events might arise from something never before observed, such as two neutron stars crashing together. "We're all really curious about what these are," says Hurley. "No one has found a [glowing remnant] yet." If Swift can do that, it may open a new window on the violent universe.

With such rewards ahead, the Swift scientists are itching to fly. "It will be like waiting for the next firework to go off on the Fourth of July," says Nousek of Penn State. "It's going to be a treat."

–ROBERT IRION

Published by AAAS

Robotic Telescopes Give Kids A Cosmic Classroom

Thanks to the Internet, schoolchildren can view the heavens via professional-caliber remote-controlled observatories. But are they ready for astronomical prime time?

CAMBRIDGE, U.K.—At the mountaintop Haleakala Observatory on the Hawaiian island of Maui, a gleaming new telescope waits to peer deep into the cosmos. With a mirror only 2 meters wide, it is not in the front rank of such instruments, but it is a serious piece of research equipment. It is also entirely robotic: It can be controlled from a computer anywhere in the world, and no one need be on site from one week to the next. But astronomers eager to get their hands on it will have to wait their turn; this telescope was designed and built to be used by schoolchildren in the United Kingdom.

The telescope and a twin still undergoing final tests and adjustments at Siding Springs in Australia are part of the Faulkes Telescope Project, an unprecedented effort to get children excited about astronomy in the hope that they will stick with science and mathematics as their education progresses. "It's not just about getting kids into astronomy. It's very rich in all sorts of disciplines," says Dill Faulkes, the cosmologist turned software entrepreneur who put up $18 million to create the project.

Faulkes is not alone. Another new British scope is setting aside observing time for schools' use. In the United States, a handful of long-standing projects are putting smaller scopes into the hands of schoolchildren and laying grand plans for networks of telescopes spanning the globe. "We can compete with MTV and get them hooked into something useful," says astronomer Carl Pennypacker, founder of the U.S.-based Hands-On Universe.

Astronomers may get a piece of the action, too. The Faulkes project hopes to team groups of students with professional astronomers to do some real science. The challenge "is to find a way of bringing kids and teachers up to a professional level," says David Bowdley, educational programs manager for the Faulkes project. "And I'm sure professionals would like to get their hands on [the scopes] too."

Faulkes's motivation was simple. He was grateful for the free state education he'd received up to doctorate level, which led first to postdoctoral work and then to a successful career in the software industry. About 5 years ago he decided to give some of the wealth he'd created back to education. "I was concerned about children moving away from science in schools," he says. After discussion with the U.K.'s astronomy funding body and staff at the Royal Greenwich Observatory, he settled on building a telescope in Hawaii so that children could see the night sky live during school hours. "Being able to observe in class time is a tremendous advantage," says Bowdley.

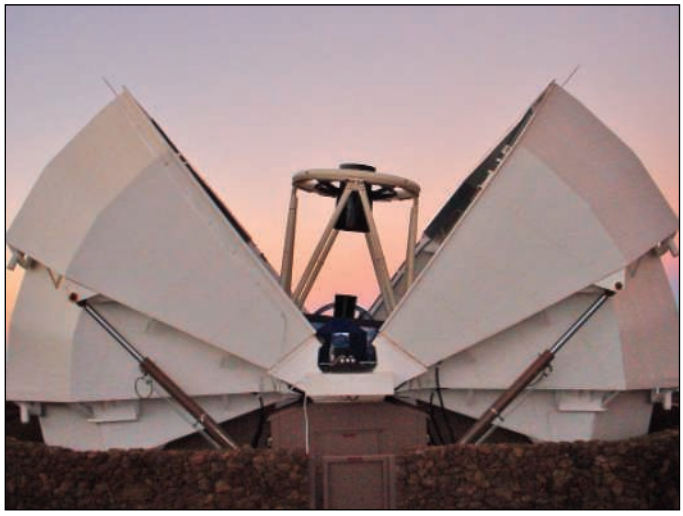

No toy. The Faulkes Telescope on Maui takes real astronomy into schools.

The scopes are provided by the Liverpool-based company Telescope Technologies Ltd., which has pioneered building 2-meter instruments using a production-line approach to reduce costs (*Science*, 22 March 2002, p. 2203). The company's prototype instrument, the Liverpool Telescope, is sited in the Canary Islands. Its owner, Liverpool John Moores University, is devoting 5% of observing time to school groups through a project called the National Schools Observatory (NSO). The Liverpool Telescope became fully operational over the summer, and now NSO hopes to begin enlisting schools in earnest this term. "I haven't spoken to a teacher yet who doesn't want to do it," says NSO's Andy Newsam.

The Faulkes project also plans to ramp up its operations. It has been working with about a dozen schools to iron bugs out of the software and develop curriculum materials. Any school can sign up for the project. For about $340 they get three half-hour sessions, during which they can do what they like with the telescope, plus some offline observing time.

Just before the summer vacation, Tim O'Brien, an astronomer at the Jodrell Bank Observatory near Manchester, tried the system out in a weeklong astronomy project with a class of 10-year-olds. "You have to prime them what to expect," he says. "They're used to seeing things on a computer. You need to show them that this is a live telescope." The class rifled through star charts, catalogs, and books and then picked a handful of objects to observe, including a supernova that exploded only a few weeks before. With the help of Webcams, the children get to see exactly what's going on. "When you move the scope, a light comes on in the dome, and you get a view of it changing position. That got a 'Woooo,' " he says. "It's a field trip in your classroom," says Faulkes's operations manager, Edward Gomez.

Projects in the United States have been getting that sort of reaction for years. Philip Sadler of the Harvard-Smithsonian Center for Astrophysics (CfA) in Cambridge, Massachusetts, was one of the founders of the MicroObservatory project, which has taken a different approach from the Faulkes project by creating a network of four 15-centimeter scopes that snap pictures all night from a list of requests from students. "We found ease of use was important," Sadler says. "They really want pictures of objects with which they have a connection: the sun, the moon, planets, and constellations." Begun some 15 years ago, the MicroObservatory now takes about 50,000 pictures per year. A full half of the pictures taken, Sadler says, are of the moon: "It's a way in for them to the mysteries of astronomy." The young observers also take a lot of pictures of the dirt around the telescope and of nearby cacti, Sadler says, but they soon learn that the object they're after has set: "It's important to fail. You learn more from failure than from success."

The Hands-On Universe (HOU), based at the Lawrence Hall of Science at the University of California (UC), Berkeley, grew out of a research project hunting for supernovae and has been operating since the 1990s,

CREDIT: FAULKES TELESCOPE PROJECT

Published by AAAS

mostly using a 60-centimeter scope at the Yerkes Observatory in Williams Bay, Wisconsin. But Pennypacker, a scientist and educator at UC Berkeley and Lawrence Berkeley National Laboratory, says the project is "on the verge of a major expansion." HOU has begun setting up 36-centimeter scopes in far-off locales so that students can use them live during class. The project now has one each in Hawaii and Australia and hopes to have another two in Australia within months. "In 10 years there will be hundreds," Pennypacker predicts.

Telescopes in Education (TIE) took a similar tack. It started in 1993 by automating a retired 60-centimeter telescope at the Mount Wilson Observatory in Southern California, which was donated by NASA, and making it accessible through the Internet. Now the project relies largely on 36-centimeter scopes at Mount Wilson as well as in Australia and Chile. TIE director Gilbert Clark is a firm believer in giving direct control of the scopes to students, comparing it to driving a Ferrari rather than taking a taxi ride. "You learn a lot behind that wheel," he says.

Is that learning mainly inspirational, or can schoolchildren do real science? "Most teachers are not interested" in research, Clark says. But if students have ambitious plans, TIE puts them in touch with astronomers. "They produce rather miraculous things sometimes," he says. For the Faulkes project, doing science is part of the plan. Bowdley says that over the summer, secondary-school students, under supervision, made measurements of asteroids accurate enough to be submitted to the International Astronomical Union's Minor Planet Center, which keeps track of such objects. School groups can do valuable work making follow-up observations of fast-changing objects such as supernovae and gamma ray burst afterglows. "The more data you can get, the better, and they can make as good measurements as [those of] a professional astronomer," says O'Brien.

High hopes. Dill Faulkes says sky-watching can spur a broad interest in science.

The astronomers and educators involved in these projects have little doubt that they are helping forge the scientists of the future. Sadler gets a kick out of meeting young astronomers at CfA who got their first taste of the stars through the MicroObservatory. Even so, most of the projects struggle to keep going on shoestring funding provided by the likes of NASA, the National Science Foundation, and the departments of Energy and Defense. TIE, for one, has had to cut back the number of students it can handle over the past several years. Says Pennypacker: "It's been hard, but it's been fun and it's been worth it."

–DANIEL CLERY

CREDITS (TOP TO BOTTOM): FAULKES TELESCOPE PROJECT; EUROPEAN MOLECULAR BIOLOGY LABORATORY

European Science

Institute Sparks an Italian Renaissance in Mouse Biology

A young lab in the hills north of Rome is making its mark in mouse genetics—and in the science landscape of Italy

MONTEROTONDO—Coffee, beer, and genetically altered mice are the staples of many modern biology labs, but in an up-and-coming institute outside of Rome, they have been raised to an art form. At the European Molecular Biology Laboratory (EMBL) campus in Monterotondo, Italy, a top-of-the-line espresso machine fuels work throughout the day, top German brews available at Friday beer hours provide a weekly chance to unwind, and the mice dwell in a sleek new 900-square-meter addition to the lab.

The campus is home to six research teams and more than 20,000 mice, which bear genetic defects in dozens of genes. The groups study a grab bag of biological themes, including genetic influences on anxiety, the role of inflammatory genes in atherosclerosis, and the effect of cytoskeletal genes on brain development. "We're free to do anything we want as long as it has to do with the mouse," says director Nadia Rosenthal, a developmental geneticist who left Harvard to lead the fledgling lab in 2001.

After initial growing pains, the young laboratory in the Tiber Valley 20 kilometers north of Rome is starting to make its mark on mouse biology. "They're definitely hitting the international community," says developmental biologist Marianne Bronner-Fraser of the California Institute of Technology in Pasadena, who visited the campus earlier this year. The lab still has to prove its value in the long term, says geneticist H. Lee Sweeney of the University of Pennsylvania in Philadelphia, who collaborates with Rosenthal. "It needs to be productive over a period of time, and they haven't been fully functioning long enough. But I think people recognize now that it's going to work and there's tremendous potential," he says.

A few years ago, the picture was not so rosy. The institute was started in 1996 more out of political than scientific necessity: Italian authorities had complained they weren't getting their money's worth from participation in EMBL and had threatened to withdraw from the 17-country organization. As an incentive to keep Italy on board, EMBL proposed opening a campus outside Rome that would be devoted to mouse biology. At the beginning, there was funding for only three groups. The initial director, Klaus Rajewsky, kept his main lab in Cologne and was on site only part time. Few people even knew the campus existed. "We went through

Bright outlook. Nadia Rosenthal has led the EMBL outpost in Monterotondo since 2001.

Published by AAAS

some rough times," says EMBL director Fotis Kafatos. "It was difficult to recruit when funds were so limited."

Rosenthal says she received plenty of discouraging advice as she contemplated moving to Monterotondo. "I had heard that efforts to establish the campus were not going according to plan, and everyone had an excuse for why it wasn't working," she says. High on the list was what both Italians and outsiders see as an unfriendly climate for science in the country, with labs burdened by layers of bureaucracy and limited funding. "Even my Italian scientist friends said, 'Don't go there. It's suffering from necrosis,' " Rosenthal says. But a sense of adventure and a minor midlife crisis—she had just turned 50—prompted her to take the plunge, she says.

Mouse house. Genetically modified mice (*inset*) make their home at the Monterotondo campus.

The risk has paid off handsomely. Rosenthal has overseen the expansion of the institute's size and international profile. In combination with the European Union–funded European Mutant Mouse Archive, which moved in next door in 1999, Monterotondo is increasingly seen as a center for mouse biology in Europe. "It is playing a significant role in the international scene" working to make mouse models of human disease, says Bob Johnson, head of the British Medical Research Council's new Mary Lyon Centre in Harwell, U.K.

And Rosenthal is enjoying herself. She and her nine-member group probe the effects of the hormone insulin-like growth factor-1 (IGF-1) and related molecules on muscle growth and regeneration. She continues to work on the muscle-bound "Schwarzenegger mice" that grabbed headlines several years ago. The mice carry an extra copy of a gene that codes for IGF-1, which not only bulks up their leg muscles but also seems to aid in wound healing and delay some signs of aging. She is now focusing on the role of the gene in heart muscle repair and regeneration. "This is exactly the kind of place where I want to come to work every morning," she says. "I love it."

Stem cell biologist Claus Nerlov, who arrived just after Rosenthal, notes that the atmosphere has changed radically since the early days. "It used to be considered Siberia by people in Heidelberg [EMBL's headquarters]," he says. "Now they're starting to get jealous, which is good."

Kafatos is also pleased. "The campus is incredibly stimulating and abuzz with excitement, and it has gained the respect of the scientific community," he says. "As far as I'm concerned, it has been a great success." Kafatos, who has known Rosenthal since she was an undergraduate student in his lab and who helped recruit her to the post, attributes much of the success to her "ambitious but cooperative" leadership style. Bronner-Fraser agrees. "There's an interactive spirit there you don't see many places. They're all doing different things, but they're all somehow working together."

The newest recruit, Cornelius Gross, says it was largely Rosenthal's enthusiasm and collegial attitude that persuaded him to turn down university positions in the United States and join the Monterotondo campus. Gross studies the interaction of environmental and genetic factors, especially those related to serotonin signaling, in brain development and anxiety. He has found an unlikely collaborator on the campus in Walter Witke, who studies the genes that code for cell structure proteins. Witke's team found that one of those genes, *profilin 2*, is expressed only in neurons, and that mice with that gene knocked out had a strange phenotype: They seemed normal until they gave birth, when mouse mothers lacking the gene turned out to be completely uninterested in their offspring. The researchers suspect that the mutation affects the release and uptake of neurotransmitters, and the Gross team is now helping to characterize the mice using a battery of behavioral tests.

Such unexpected collaboration is exactly what Rosenthal hopes to see. The wireless Internet network that enables lab members to answer e-mail or download research articles while enjoying the sunshine in the lab's courtyard encourages mixing among the groups. "You see two students sitting and talking in the courtyard, and soon two mice are getting mated that I never would have dreamed of," Rosenthal says.

Each group gets 500 free cages for their mice, and all receive most of their funding from hard money from EMBL, freeing them from pressures of grant writing. As at the main lab in Heidelberg, group leaders have a limited tenure at EMBL. They receive an initial 5-year contract that can be renewed only once for up to four more years. "All that fits into a 'paradise for a decade' idea," Rosenthal says. "The promotional pressure is gone. There is deliberately no ladder to climb," which also helps encourage a collaborative spirit, she says.

It hasn't all been paradise. Although as an EMBL outstation the lab is free from much of the Italian government's notorious bureaucracy, Rosenthal has faced plenty of red tape while importing equipment and building the new mouse house. However, says Andrea Ballabio of the Telethon Institute of Genetics and Medicine in Naples, the Monterotondo lab sets a good example for science in Italy, where many researchers complain bitterly that fossilized organizational structures keep young scientists from getting ahead and stifle innovative research. "It's very important to Italy to have an EMBL campus," he says. "They have the potential to influence Italian science" by recruiting top young scientists to the region and by "establishing a model" of an institute free from most of the constraints of government bureaucracy.

The growth may continue. The campus received enthusiastic reviews from an international review team in September, and Kafatos says that it is possible the facility could expand in coming years. Bronner-Fraser says that would help strengthen the institute's remaining weak points. "They need to recruit a few more top postdocs," she says, and they still need to work to become better known outside Europe.

Although Italian politicians wanted a concrete return for their contributions, EMBL had its own reasons for establishing a foothold in Italy, Kafatos says. "We were keen to see a Europeanization of the research activities in Italy. The fact that we were able to inject [the EMBL] culture and let it take over so fast is really extraordinary," he says. The espresso may have helped. **–GRETCHEN VOGEL**

CREDITS: EUROPEAN MOLECULAR BIOLOGY LABORATORY

Published by AAAS

Risky Business

Can the U.S. government do a better job of betting on long shots in science? NSF and NIH hope the answer is yes

Duke University neuroscientist Erich Jarvis won the National Science Foundation's (NSF's) prestigious Waterman Award for outstanding young researchers 2 years ago. But despite his early success, the assistant professor sounds like a battle-hardened veteran of the struggle for federal funding—in his case, for work on vocal learning. He certainly knows what it's like to have his ideas shot down.

For example, Jarvis has cracked the code used by reviewers to undercut a grant proposal, especially the one that begins, "This is a very ambitious proposal. …" He's learned that those words, seemingly in praise of a novel scientific idea, are actually the kiss of death. And he sees irony in being penalized for trying something that nobody else has attempted—in other words, for proposing the sort of cutting-edge science that federal agencies profess to welcome. "You learn the hard way not to send high-risk proposals to NSF or [the National Institutes of Health], because they will get dinged by reviewers. Instead, you're encouraged to tone down your proposal and request money for something you're certain to be able to do."

That iron rule may be changing, however, at least for a few scientists. On 22 to 23 September, Jarvis was one of 15 outside scientists who spent 2 days telling a few members of NSF's oversight body and agency staff exactly what's wrong with the current system. They also suggested how NSF might become more receptive to the handful of ideas that have the potential to set the scientific establishment on its ear.

Although the fruits of that meeting may not show up for years, if at all, on 29 September nine scientists received a more immediate payoff from NIH: $500,000 a year (in direct costs) for 5 years, with no strings attached. The money is part of a new program, the Director's Pioneer Awards, meant to allow researchers to pursue innovative ideas (nihroadmap.nih.gov/highrisk/initiatives/pioneer). NSF and NIH are also working together on a separate initiative, mandated by Congress, to foster interdisciplinary research with long horizons. That work is inherently high risk, say government officials, who have scheduled a meeting next month to ask outside scientists how best to achieve that goal.

Together, these efforts represent a small but potentially significant move to alter conventions in grant reviewing, which many say favor timid, incremental steps over profound leaps of intuition. At the same time, the initiatives are quite modest, highlighting just how hard it is for federal agencies to encourage risk taking while remaining responsible stewards of taxpayer dollars. "We've been hearing for years that our process doesn't recognize work on the fringes," says NIH Director Elias Zerhouni, whose $25-million-a-year Pioneer Awards program is a tiny piece of his road map initiative to reform the $28 billion biomedical behemoth. "So rather than continuing to debate it, I said, 'Let's test that hypothesis and see how many scientists have good ideas that are not part of our portfolio.' "

> "You learn the hard way not to send high-risk proposals to NSF or NIH." —Erich Jarvis

Real-time feedback

Zerhouni is concerned that scientists don't even bother to submit their best ideas to government agencies anymore. This is part of the larger question of whether those agencies—and the outside reviewers they rely upon to help make funding decisions—would even recognize what the NSF workshop participants labeled "potentially transformative research." Indeed, anecdotal evidence from the Pioneer Awards suggests that NIH may be missing the boat. "None of the 21 finalists thought that NIH peer review was ready for their idea," says Stephen Straus, director of the National Center for Complementary and Alternative Medicine, who helped plan and implement the program. Indeed, several of the winners told *Science* that, despite receiving NIH funding for other projects in their labs, they had been forced to scrape together meager funding for their big idea.

"I never even put in a proposal because the chances of getting an R01 [NIH's bread-and-butter award for investigator-initiated research] would have been zero," says Steven McKnight, who is studying how the metabolic cycle in yeast influences circadian (or more frequent) cycles within the cell. "It's a new and unpopular idea, and it has no sex appeal—metabolism is boring—but I think it's pretty important," says McKnight, chair of the biochemistry department at the University of Texas Southwestern Medical Center in Dallas.

Another winner, Rob Phillips of the California Institute of Technology in Pasadena, suspects that he may have benefited from instructions to all reviewers to "suspend their usual paradigm" because of the risky nature of the proposals they were judging. A theoretical physicist now working on biological questions, Phillips is hoping to complete a "mathematicized" version of classic texts, including *The Molecular Biology of the Cell* by Bruce Alberts *et al.*, that will illustrate how the laws of physics can be used to explain cellular behavior. "It's a scary project," he says, "and I feel like a salmon swimming upstream, with the bears ready to rip me out of the water. But I'm committed to doing it, and this award gives me the resources."

The NSF workshop, held in Santa Fe, New Mexico, was convened by a task group of the National Science Board (NSB), which is mulling a formal study of the issue. The participants—some of them junior faculty members, some distinguished professors and national community leaders—offered heaps of personal testimony that parallels what NIH has learned on its own about the difficulty of funding novel ideas. But to their credit, the researchers heeded the advice of NSB member and workshop chair Nina Federoff, a biologist at Pennsylvania State University, University Park, and avoided turning the meeting into a mass whine about funding disappointments. Instead, the scientists suggested several ways to send the community a message that NSF wants to fund more transformative research.

Many speakers endorsed a scheme to have the agency take a second look at unsuccessful proposals receiving both high and low scores, suggesting that some reviewers may have missed the significance of the idea being pitched. Another popular idea was to put investigators on call for reviewers to query during the course of a panel meeting, or give applicants a chance to respond to questions from an initial mail review before their proposal was taken up

CREDIT: COURTESY OF ERICH JARVIS

Published by AAAS

by a second panel. In each case, the proposed changes are driven by the assumption that high-risk research, because of its novelty, requires a more careful assessment by the agency.

One ongoing experiment by NSF's biology directorate offers a partial answer to Zerhouni's concern about being ignored. Since 2000, program managers in the division of molecular and cellular biology have asked reviewers to flag any proposal that they believe is high risk. Although the percentage is very low (see graphic, right), there was a sudden leap this year in the number of such projects reviewers identified; the spike could mean that more scientists now think the agency will be receptive to risky ideas. In addition, the data show that a high-risk proposal stands a better chance of being funded than a run-of-the-mill submission. Maryanna Henkart, division director, hopes to understand the factors affecting those success rates, including any characteristics of the investigators themselves.

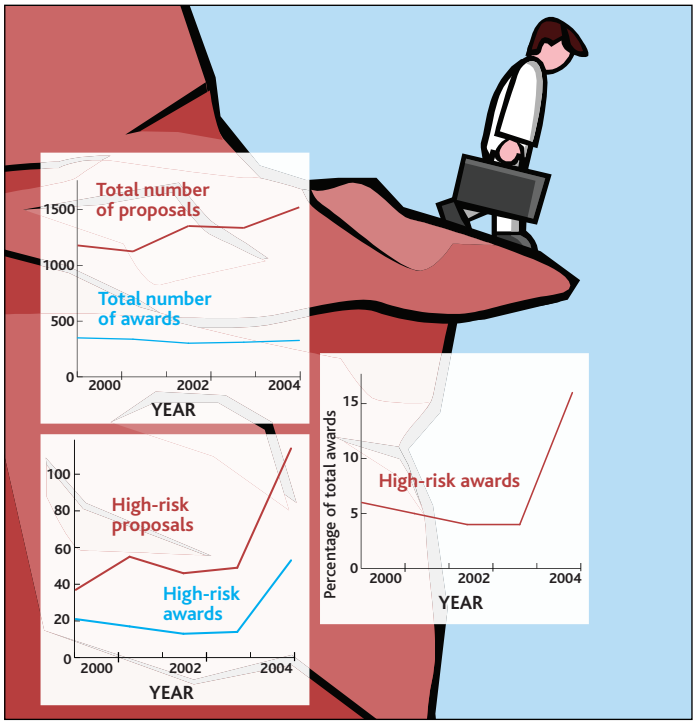

At the edge. NSF biology reviewers saw a spike this year in the number of proposals that they considered high risk.

CREDITS (TOP TO BOTTOM): SOURCE: DIVISION OF MOLECULAR AND CELLULAR BIOLOGY; NSF; COURTESY OF STEVEN MCKNIGHT

Nitpicking conformists

The shortcomings of the review process were a big concern to both NSF workshop participants and NIH officials designing the Pioneer Awards program. The peer-review system that allocates most public monies for basic research tends to reward scientists for finding flaws in the work of others rather than encouraging them to take risks. Two obvious reasons for that behavior, say researchers, are that scarce resources create a zero-sum game and that experts can prove their preeminence by tearing down other proposals in their field. "We profess to be seekers of truth," says biomedical engineer and workshop participant Gerry Pollack of the University of Washington, Seattle. "But our scientific culture reinforces the idea that opposing the mainstream is bad."

Aware of peer review's leveling effect, NIH officials took steps to neutralize it when they designed a process for choosing the Pioneer Awards. First they created a separate pot of money—a total of $125 million, if Zerhouni keeps the competition going for 5 years, as promised. That eased concerns that the awards were siphoning off money from existing programs.

The second change was to request short summaries—two pages in round one, and up to five pages for the second round—describing the new idea and its significance. "We felt it was important to focus on people, not projects," Zerhouni explains. Unlike a 25-page R01 proposal, the Pioneer Awards' submissions were not critiqued for their methodology or technique because none of the proposals contained that level of detail.

The biggest change from business as usual was in the selection of reviewers and what they were asked to do. Rather than assemble panels steeped in the proposer's subdiscipline, NIH chose distinguished scientists from across many areas. Then they told the reviewers to rely on their wisdom and weigh the project's contribution to the big picture.

This advice dovetailed with NIH's invitation to applicants to think big. That's in stark contrast to the work described in a typical R01 grant application, where a scientist is likely asking for support for an incremental piece of a project that is largely done. "NIH has funded great people over the years," says Straus. "But we tend to fund the next step, and then the step after that. It's a slow and risk-averse strategy."

"[The metabolic cycle] has no sex appeal, but I think it's pretty important." —Steven McKnight

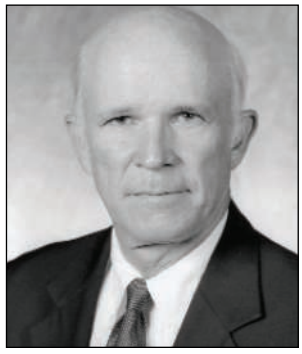

The Pioneer Awards will let a few scientists take giant steps into the unknown. Some 1300 people applied, and 240 moved on to the second round after an up-or-down vote by at least two reviewers. After a second winnowing, the finalists were then flown to NIH for face-to-face interviews with a panel of luminaries.

The nine winners, all men, are in their 40s and 50s. Most are tenured professors at elite institutions, and all but two have current NIH grants, in some cases as many as three. Straus notes that two winners owe their good fortune to decisions by individual institute directors to supplement the director's pot of money.

The vanishingly small success rate—0.7%—has led some scientists to accuse NIH of tokenism. And whether even that handful are true pioneers won't be apparent for several years, Straus says. Asked what an acceptable rate of failure might be for the program, Zerhouni replied that "one big win" might well justify the total expenditures on 50 or so scientists. However, he promised that "they will be monitored more closely than any other project" because of the compelling interest in knowing whether the federal government can become more hospitable to innovative research ideas.

Jarvis is also paying close attention to the Pioneer Awards, which he learned about only after his Duke colleague, biochemist Homme Hellinga, received one. He's also got a big idea—teaching a chicken, say, to imitate sounds as part of an effort to develop new tools for vocal learning, a subset of human language, that can be used to repair speech problems. Jarvis figures that it's too radical for NSF's current funding mechanisms, but he's hoping that the NIH program will spur NSF to come up with something similar. In the meantime, he's thinking about competing for the next round of Pioneer Awards, to be announced this winter. "I think it's a great idea," he says, "and I'd love to get one."

–JEFFREY MERVIS

Published by AAAS

Westerners Put Their Chips on 2007 Indian Moon Mission

Developing countries have started their own moon race, and scientists from cash-strapped developed countries are hoping to hitch a ride

NEW DELHI—Western researchers often beat a path to developing countries to study endangered species, ancient civilizations, or traditional medicine, among other subjects. Now it's time to add planetary science to that list. Five scientists from around the world are jostling to get their experiments aboard an Indian spacecraft, Chandrayaan-1, that is slated to fly to the moon in September 2007.

Mission to India. Scientists from these five countries hope their experiments will be aboard Chandrayaan-1 when it's launched by India's Polar Satellite Launch Vehicle (*inset*).

"Chandrayaan offers a very cost-effective means to gather critical and unique data on the moon while forging new cooperative relationships in lunar exploration," says one of the finalists, Paul Spudis of the Johns Hopkins University Applied Physics Laboratory in Laurel, Maryland. Another finalist, Manuel Grande of the Rutherford Appleton Laboratory in Chilton, U.K., says he welcomes "the increasing opportunities for flying experiments on emerging space-nation launch vehicles and satellites."

The Indian probe is part of a second race to the moon, and this time the competition is not limited to two superpowers. The Indian Space Research Organization (ISRO) is reserving a 10-kg slot for a foreign research team aboard Chandrayaan-1 (Hindi for Voyage to the Moon), which will orbit 100 km above the lunar surface for a minimum of 2 years. The four Indian instruments will map the lunar topography and conduct x-ray and gamma ray spectroscopic studies. Some 30 scientists from 11 countries responded to an ISRO solicitation earlier this year to join the mission, and last month the list was whittled to five.

The 525-kg Chandrayaan is a bit larger than the 367-kg European Space Agency Smart-1 mission launched last year, but much less ambitious than the 1600-kg, 13-instrument orbiter Japan intends to send to the moon in 2006. However, it is not clear if Japan can meet that launch date. China is also planning a mission for as early as 2007, although details about the experiments and scope of the project are not known. NASA intends to launch a lunar orbiter in 2008 as part of a new initiative to return humans to the moon. But funding for the project is in question, and last week a congressional panel expressed concern that the orbiter plan might shortchange science.

Given these uncertainties, space researchers say they welcome the chance to vie for a spot on the Indian probe. And the benefits cut both ways. The competition is designed to ensure "maximum scientific knowledge about the moon," says ISRO chair Gopalan Madhavan Nair. Former ISRO chief Krishnaswamy Kasturirangan says it should also "enhance India's status as a potential partner in future space exploration."

Madhavan says that there may be room for more than one foreign payload on the mission, depending on size and power requirements. A decision is expected later this fall. Still in the running are:

• Spudis, who proposes a radio technology instrument to measure scattering properties of the surface; this experiment can confirm the presence of water ice in the lunar polar regions up to a depth of a few meters. These deposits were first detected by the U.S. military's Clementine mission in 1994 and again by NASA's Lunar Prospector in 1998, although their total volume, thickness, and composition remain unknown.

• Tsvetan Dachev of the Solar-Terrestrial Influences Laboratory at the Bulgarian Academy of Sciences in Sofia, wants to measure solar wind particle flux and map radiation around the moon. His instrument is cheap, small, and uses little power, he says.

• Stas Barabash of the Swedish Institute of Space Physics in Kiruna has a joint proposal with India's Anil Bhardwaj of the Vikram Sarabhai Space Centre in Thiruvananthapuram to image the moon's surface composition and magnetic anomalies.

• Urs Mall of the Max Planck Institute for Solar System Research in Katlenburg-Lindau, Germany, wants to build a near-infrared spectrometer to study the geological and mineralogical aspects of the lunar surface. It is aimed at the mysterious asymmetry that gives the moon a thicker crust on the far side and a thinner crust on the side facing Earth.

• Grande, who proposes a high-quality x-ray spectroscopic map of the moon to shed light on "the key questions of the origin and evolution of the moon."

The winner must bring his own funds to the table to build and deliver the hardware to ISRO by early 2007, says Subash Chandra Chakravarty, program director of ISRO's space sciences office. The entire mission is expected to cost just under $100 million.

Foreign scientists don't seem concerned about partnering with an organization that has never flown beyond Earth's orbit. "ISRO has the full capability to carry out the Chandrayaan-1 mission successfully," says Barabash. And Barabash is spreading his risks. He also is working with China on a joint European-Chinese experiment called the Double Star Polar Satellite, which currently is studying the effects of the sun on Earth's environment. "I do have the experience of working with an 'untried' space program. And this experience is very positive indeed," he says.

—**PALLAVA BAGLA**

With reporting by Andrew Lawler in Boston.

CREDITS: K. BUCKHEIT/*SCIENCE*; PHOTO INSET: P. BAGLA

Published by AAAS

CREDIT: P. BAGLA

Imperiled scavengers. Flocks of *Gyps* vultures are now becoming a rare sight in India.

Circling In on a Vulture Killer

Scientists blame Asian vulture declines on a veterinary drug

In the 1980s, Oriental white-backed vultures (*Gyps bengalensis*) were probably the world's commonest large birds of prey, circling India's skies in the millions. By devouring dead livestock, they and other vultures perform a vital task in many Asian countries: removing rotting carcasses that could spread disease to humans.

Today, this cleanup squad is imperiled: Numbers of white-backed and long-billed vultures (*Gyps indicus*) have declined by more than 99% and 97% respectively in India since 1992, with similarly drastic declines recorded in Pakistan and Nepal and among the rarer slender-billed vultures (*Gyps tenuirostris*). It's "one of the fastest population declines recorded for any bird species," says Rhys Green, a conservation biologist with the Royal Society for the Protection of Birds (RSPB) in Bedfordshire, U.K.

After years of seeking an explanation for the vulture deaths, a surprising theory emerged in May 2003 at a conference in Hungary: Researchers identified a veterinary drug used on hoofed livestock as lethal to the scavenging birds. The hypothesis remains controversial, but a new study out this month offers further support for it. And last month, one of India's states announced that it would phase out the drug. But no one knows if it is too late to save the birds.

Scientists initially suspected that vultures were succumbing to a viral disease, explains veterinary pathologist Andrew Cunningham of the Zoological Society of London (ZSL). In 2003, however, a consortium of scientists from the United States and Pakistan linked diclofenac—an anti-inflammatory drug used to treat livestock on the Indian subcontinent since the 1990s—to vulture deaths in Pakistan. Postmortems of 259 white-backed vulture carcasses from the Punjab province found that 85% had visceral gout—a condition caused by buildup of uric acid crystals on the internal organs, usually as a result of kidney failure. Tests on a subsample showed that those with gout had residues of diclofenac in their kidneys, and 13 of 20 captive vultures fed diclofenac-treated livestock also developed gout and died.

"This was the first veterinary drug implicated in a large-scale effect on wildlife populations," says Green. The results, published this February in *Nature*, were met with initial skepticism, particularly in India. It "was not intuitively apparent that there could be enough contaminated carcasses to cause a massive population decline," says study leader J. Lindsay Oaks, a veterinary microbiologist at Washington State University, Pullman.

But further work by a consortium of scientists from the U.K., India, and Nepal—published online 21 July in *Biology Letters*—found tell-tale gout and diclofenac residues in a high proportion of dead and dying white-backed and long-billed vultures collected in India and Nepal. This demonstrated that the diclofenac problem reached beyond Pakistan, says Green.

He and colleagues at RSPB, ZSL, and the Bombay Natural History Society (BNHS) in Mumbai have now used computer models of vulture demography to confirm that the rapid decline in populations of white-backed and long-billed vultures in India, Pakistan, and Nepal could be largely, if not entirely, attributed to diclofenac poisoning. According to their calculations, reported in the October issue of the *Journal of Applied Ecology*, less than 1% of carcasses would have to carry a lethal dose of diclofenac to account for the declines. "Every time a vulture feeds on a carcass, it's like Russian roulette," says Green. "The trigger is pulled about 120 times per year, so even if a small proportion of the chambers are loaded, a lot of vultures are going to get killed."

But some raise questions about diclofenac usage. "There are large areas of India where vulture declines have been reported, but where there is minimal veterinary care for livestock," veterinarians Joshua Dein of the National Wildlife Health Center in Madison, Wisconsin, and P. K. Malik of the Wildlife Institute of India in Dehradun told *Science* in an e-mail.

Green discounts that argument as unsubstantiated. Estimates of total diclofenac sales by Vijay Teng, vice president of Indian pharmaceutical company Neovet, suggest that the drug is widely used in India, with 20 million large-animal doses sold per year, the equivalent of 5 million large animals treated.

Some Indian scientists, like P. R. Arun and P. A. Azeez of the Sálim Ali Centre for Ornithology and Natural History in Coimbatore, India, maintain that it is "premature" to conclude that diclofenac is the sole cause of vulture declines. Other factors may be contributing, they say, and more needs to be known about how diclofenac affects the birds.

"You don't need to know the mechanism to prove it's killing vultures," counters Cunningham. Vultures may be particularly prone to diclofenac poisoning because they eat the liver and kidney of livestock, where the drug is likely to be more concentrated, he suggests.

At summit meetings in Kathmandu, Parwanoo, and Delhi earlier this year, veterinarians, scientists, government officials, and representatives of conservation groups and pharmaceutical companies agreed that diclofenac should be phased out. The state government of Gujarat, India, was the first to act, announcing last month that it will cease purchasing veterinary diclofenac. There is hope that safe alternatives could be on the market "within months rather than years," says Deborah Pain, head of RSPB's international department.

Even as researchers try to nail down whether diclofenac is the only vulture killer, there's a major effort to establish captive breeding programs to rebuild the bird populations. A breeding center in Haryana state, India, already houses 39 vultures, and there are plans to build centers in West Bengal, Pakistan, and Nepal by early 2005. There's no time to waste: Finding enough birds to stock the Haryana center is already proving tough, warns ornithologist Vibhu Prakash of BNHS.

Indeed, with some vulture populations halving each year, "the possibility to do anything to conserve them is rapidly disappearing," says Green.

–FIONA PROFFITT AND PALLAVA BAGLA

Published by AAAS

LETTERS

Tropical Ecosystems into the 21st Century

WE ENDORSE THE ECOLOGICAL SOCIETY OF America's (ESA) call to shift its primary focus from the study of undisturbed ecosystems to interdisciplinary studies of human-influenced ecosystems for the betterment of human societies (*1*, *2*). At the 2004 annual meeting of the Association for Tropical Biology and Conservation (ATBC) in Miami, Florida, we released a report ("Beyond Paradise: Meeting the Challenges in Tropical Biology in the 21st Century"), which also makes a plea for an interdisciplinary, participatory, and socially relevant research agenda to study and conserve human-impacted as well as pristine tropical ecosystems (*3, 4*). Here, we highlight the similarities and differences of the ESA and ATBC reports.

The ATBC report, like that of ESA, recognizes the increasing impact of humans on tropical ecosystems. Since 1980, 288 million hectares (21%) of tropical forest areas have been deforested, while the population in tropical countries has nearly doubled. Rapid economic growth in several tropical areas exacerbates pressures on tropical forests. A unique feature of tropical regions is that millions of rural people rely on local ecosystem goods and services, often paying a high opportunity cost to maintain biodiversity.

Tropical research thus must be rooted in a more inclusive set of social values. Conservation must become part of the larger agenda of sustainable and equitable development, with the development needs of local communities receiving the same consideration as preservation goals. At the same time, interdisciplinary approaches that accord respect to alternative knowledge systems will be needed to address the effects of human activities on tropical ecosystems, the social drivers of ecosystem degradation, and the social responses to the conservation of those ecosystems. Furthermore, tropical biology will have to increasingly incorporate policy-oriented research to mitigate threats to biodiversity.

The critical knowledge needed to usher tropical ecosystems through the environmental transformations of the 21st century must focus on three components. First, human impacts on tropical ecosystems will increase dramatically. Tropical forest conversion, the effects of climate change, nutrient deposition, spread of alien species, and extraction of ecosystem products on the structure and functioning of undisturbed and managed ecosystems must be understood. The second component pertains to social drivers of change and social responses to conservation. Conflicts and continued poverty around protected areas suggest that existing approaches to conservation lack understanding of links between maintenance of diversity and human well-being. The third component, understanding the structure and function of tropical ecosystems, including cataloging tropical diversity, is fundamental to comprehend and mitigate consequences of the biodiversity loss in human-impacted ecosystems. The equal emphasis in the ATBC report on the study of pristine and human-impacted systems (distinct from the "synthetic" ecosystems described in the ESA report) stems from the uniqueness of tropical ecosystems. The latter contain substantial amounts of undescribed biodiversity, espe-

Letters to the Editor

Letters (~300 words) discuss material published in *Science* in the previous 6 months or issues of general interest. They can be submitted through the Web (www.submit2science.org) or by regular mail (1200 New York Ave., NW, Washington, DC 20005, USA). Letters are not acknowledged upon receipt, nor are authors generally consulted before publication. Whether published in full or in part, letters are subject to editing for clarity and space.

CREDITS: (TOP AND BOTTOM) W. J. KRESS; (MIDDLE) C. CLARK

Published by AAAS

cially in forest canopies and soils, and tropical ecosystems harbor 65% of the world's 10,000 endangered species.

The ATBC proposes four broad recommendations for immediate action. First, research institutions, biological collections, scientific journals, and information infrastructure in the tropics must be strengthened and multiplied by forging partnerships among institutions and collaborators. Second, society must support an expanded system of field stations that are electronically linked, include relatively pristine areas and human-impacted landscapes, and generate and apply knowledge to conserve and sustainably use tropical nature through local networks or coalitions of government agencies, academic institutions, nongovernment organizations, and policy-makers. Third, completing the inventory of existing life is basic to human welfare, especially in tropical regions of mega-diversity. Traditional biology must be combined with advanced technologies to rapidly develop new ways to assemble, organize, and disseminate information about diversity of life in the tropics. Fourth, interdisciplinary research by implementing cross-disciplinary training programs in biology and social sciences should be encouraged to address complex issues that lie at the interface of science and society.

Both the ESA and the ATBC statements, along with reports from other programs (e.g., Millennium Ecosystem Assessment, DIVERSITAS), demonstrate an exciting convergence of interests by tropical biologists, conservationists, and social scientists. This convergence should engender support from international environmental development agencies, national agencies, and private donors for linked studies of ecological and social systems. Such support is critical to understand tropical ecosystems and enhance the welfare of human societies that depend on them.

KAMALJIT S. BAWA,[1,2]* W. JOHN KRESS,[3,4] NALINI M. NADKARNI,[5] SHARACHCHANDRA LELE,[6] PETER H. RAVEN,[7] DANIEL H. JANZEN,[8] ARIEL E. LUGO,[9] PETER S. ASHTON,[10] THOMAS E. LOVEJOY[11]

[1]Department of Biology, University of Massachusetts, Boston, 100 Morrissey Boulevard, Boston, Massachusetts 02125, USA. [2]Ashoka Trust for Research in Ecology and the Environment, No. 659, 5th A Main Road, Hebbal, Bangalore 560024, India. [3]Department of Botany, MRC-166, National Museum of Natural History, Smithsonian Institution, Post Office Box 37012, Washington, DC 20013–7012, USA. [4]Xishuangbanna Tropical Botanical Garden, Chinese Academy of Sciences, Mengla, Yunnan 666303, China. [5]The Evergreen State College, Olympia, WA 98505, USA. [6]Centre for Interdisciplinary Studies in Environment and Development, ISEC Campus, Nagarabhavi, Bangalore 560-072, India. [7]Missouri Botanical Garden, Post Office Box 299, St. Louis, MO 63166–0299, USA. [8]Department of Biology, University of Pennsylvania, Philadelphia, PA 19104, USA. [9]International Institute of Tropical Forestry/USDA Forest Service, Jardín Botánico Sur, 1201 Calle Ceiba, San Juan, PR 00926-1119, Puerto Rico. [10]Center for Tropical Forest Science–Arnold Arboretum Asia Program, Harvard University Herbaria, 22 Divinity Avenue, Cambridge, MA 02138, USA. [11]The H. John Heinz III Center for Science, Economics and the Environment, 1001 Pennsylvania Avenue, NW, Suite 735 South, Washington, DC 20004, USA.

*To whom correspondence should be addressed: kamal.bawa@umb.edu

References and Notes

1. M. A. Palmer *et al.*, "Ecological science and sustainability for a crowded planet: 21st century vision and action plan for the Ecological Society of America" (Ecological Society of America, Washington, DC, 2004) (available at http://esa.org/ecovisions/).
2. M. A. Palmer *et al.*, *Science* **304**, 1251 (2004).
3. K. S. Bawa, W. J. Kress, N. M. Nadkarni, S. Lele, *Biotropica*, in press.
4. ATBC's report (available at http://www.atbio.org/) is based on an international effort initiated in 2000 to review the state of tropical biology and to explore opportunities for future advances in the field. We thank over 150 tropical biologists who participated in the discussions from 2000 to 2004. A. Fiala and A. Das helped in locating statistical figures and sources of information. This report has been prepared with the support of tropical research groups and funding agencies, including the Association for Tropical Biology and Conservation (www.atbio.org), the Ashoka Trust for Research in Ecology and the Environment (www.atree.org), the Smithsonian Institution (www.si.edu), the National Science Foundation (www.nsf.gov), and the British Ecological Society (www.britishecologicalsociety.org).

Changing Strategies in Science Education

AS J. HANDELSMAN *ET AL.* NOTE IN THEIR Policy Forum "Scientific teaching" (23 Apr., p. 521), recent educational research has shown that a variety of active-learning strategies are superior to the teaching methods that many of us experienced in our own training. That is, the traditional approach of lecturing to a room full of students seems to be less effective than engaging these students in the process of thinking about the information.

A particular challenge, which was not noted by Handlesman *et al.*, is reorienting our role in the training of secondary science teachers—indeed, in training teachers throughout the K–12 enterprise. In general, the science courses through which K–12 teachers learn their science are taught by scientists. It is incumbent upon us as scientists to ask ourselves how well we serve as role models for the teachers we train.

In general, we tend to teach the way we were taught ourselves. It is only after we become more comfortable with our teaching expertise, and more comfortable in our other roles as scientists, that some of us may begin to investigate alternate pedagogical approaches. The same can be said for the students whom we teach. If we instruct our future K–12 teachers by the traditional approach of lecturing about scientific facts, we may expect that they will use the same methods in their own classes.

But science is not the memorization of facts. It is an ongoing, investigative endeavor. It requires thinking deeply about subjects, and continuously assessing whether the data support the current understanding. Actually doing science requires a world view that is quite different from that which we portray in our classes.

As scientific literacy has declined, we have considered a variety of ways to address it. One very important effort has been the development of the National Science Education Standards (*1*, *2*). Built into the Standards is the expectation that the teaching of science should be realigned to match more closely the doing of science. That is, K–12 instruction should, wherever possible, use methods of active learning and of inquiry-based learning. The typical response to reading this, I suspect, will be "good, that is as it should be."

Thus, we have a paradox. We applaud the Standards' exhortation to teach science as an investigative endeavor and to use inquiry-based methods where possible. Yet, we, ourselves, tend to teach the way we were taught and use didactic lecturing—through which we train future K–12 teachers the avoidance of inquiry-based methods. Consequently, it is exceedingly difficult for K–12 teachers to incorporate inquiry-based teaching into their courses. This realization suggests that it is essential that we move our own teaching methods into the current century, pay attention to the educational literature, and use active learning, problem-based learning, and inquiry-based learning in our own classes.

Handelsman *et al.* have offered recommendations for how we might improve the Culture of Science to put greater weight on the teaching enterprise. I suspect, however, given the vast inertia of our scientific and educational systems, that a single Policy Forum will be insufficient. It will be necessary to give educational innovations the same degree of attention that we give to basic research. Given the prestige and wide readership of *Science*, I ask that a new section of the journal be created to discuss teaching issues. We need open and frequent discussion of this tremendously important issue.

J. JOSE BONNER

Professor of Biology, Director of Science Outreach, Indiana University, Bloomington, IN 47405, USA. jbonner@bio.indiana.edu

References

1. National Research Council, *National Science Education Standards* (National Academy Press, Washington, DC, 1996).
2. National Research Council, *Inquiry and the National Science Education Standards: A Guide for Teaching and Learning* (National Academy Press, Washington, DC, 2000).

Universities and the Teaching of Science

IN THEIR POLICY FORUM "SCIENTIFIC TEACHING" (23 Apr., p. 521), J. Handelsman *et al.* call for reform of science teaching at research universities. It is ironic to find that the best practices for science teaching described in the article are considered innovative and noteworthy. At predominantly undergraduate colleges and universities, where teaching is a significant part of the professional lives of faculty, these approaches are now common and pervasive. It is unfortunate that the authors fail to recognize this, because there are implications for policy in higher education. More time spent on innovation in teaching typically means less time available for conducting research. For example, faculty at undergraduate colleges and universities publish about one paper every 2 years (*1*). Although it is noteworthy that these professors maintain modest research programs under challenging research conditions, this level of productivity is likely to be unacceptable at research universities. Indeed, administrators at research universities should be striving for greater faculty productivity in research.

The critical policy issue is not how we get research faculty to pay more attention to teaching. Nor is the critical issue how to get teaching faculty to publish more papers. The critical issue is faculty productivity and the alignment of this productivity with the various university missions. If, as the authors posit, undergraduate science education at the research universities is in need of a reform, then it may be more realistic to ask for accurate public descriptions of the strengths and weaknesses of the research university concept. Potential undergraduate students can then make informed choices about where to spend their tuition dollars.

JAMES LUKEN

Department of Biology, Coastal Carolina University, Conway, SC 29528–6054, USA. E-mail: joluken@coastal.edu

Reference

1. *Academic Excellence: The Sourcebook* (Research Corporation, Tucson, AZ, 2001) (available online at www. rescorp.org).

Response

WE AGREE THAT MANY INDIVIDUALS AND programs at primarily undergraduate institutions are leaders in teaching innovation. However, national reports and agencies indicate that the majority of undergraduates are not becoming scientifically literate members of society, and that science education reform is overdue at all undergraduate institutions, regardless of size (*1–8*).

On the basis of these reports, education reform should be on the agenda of all colleges and universities. As Luken points out, teaching could be construed as a conflict of interest at research universities (and vice versa at smaller colleges), but all of these institutions have multiple missions. The mission statement of most research universities includes educating undergraduate students; both research laboratories and classrooms contribute to that goal. If research universities didn't educate, they would be research institutes. Moreover, research universities already practice the effective joining of research and teaching in graduate education. It is the responsibility of research universities to prepare future faculty for careers in research and teaching. Teaching is not incidental at a research university—it's essential.

The goal of our Policy Forum was to impress upon scientists the importance of

scientific teaching at research institutions, to provide evidence that reform is needed, and to offer examples of innovative teaching resources. We acknowledge practices of scientific teaching at small colleges, and would be interested to know of any data about teaching and learning at these schools that could be applied to research institutions. Ideally, instructors at large and small universities will work together to share results and evidence-based explanations of teaching experiences that foster student learning.

JO HANDELSMAN,[1] ROBERT BEICHNER,[2] PETER BRUNS,[3] AMY CHANG,[4] ROBERT DEHAAN,[5]* DIANE EBERT-MAY,[6] JIM GENTILE,[7] SARAH LAUFFER,[1] JAMES STEWART,[8] WILLIAM B. WOOD[9]

[1]Howard Hughes Medical Institute Professor, Department of Plant Pathology, University of Wisconsin-Madison, Madison, WI 53706, USA. [2]Department of Physics, North Carolina State University, Raleigh, NC 27695, USA. [3]Howard Hughes Medical Institute, Chevy Chase, MD 20815, USA. [4]American Society for Microbiology, Washington, DC 20036, USA. [5]National Research Council, Washington, DC 20001, USA. [6]Department of Plant Biology, Michigan State University, East Lansing, MI 48824, USA. [7]Dean of Natural Sciences, Hope College, Holland, MI 49423, USA. [8]Department of Curriculum and Instruction, University of Wisconsin–Madison, Madison, WI 53706, USA. [9]Department of Molecular, Cellular, and Developmental Biology, University of Colorado at Boulder, Boulder, CO 80309, USA.
*Present address: Division of Educational Studies, Emory University, Atlanta, GA 30322, USA.

References

1. House Committee on Science, Unlocking Our Future: Toward a New National Science Policy: A Report to Congress, 24 Sept. 1998.
2. Howard Hughes Medical Institute, Howard Hughes Medical Institute Grants and Fellowships: HHMI Professors (available at www.hhmi.org/grants/awards/indiv/prof/index.html).
3. National Research Council, *Bio2010* (National Academy Press, Washington, DC. 2003).
4. National Research Council, *How People Learn: Brain, Mind, Experience, and School,* (National Academy Press, Washington, DC, 2000).
5. National Research Council, *National Science Education Standards* (National Academy Press, Washington, DC, 1996).
6. National Research Council, Committee on Undergraduate Science Education, *Transforming Undergraduate Education in Science, Mathematics, Engineering, and Technology* (National Academy Press, Washington, DC, 1999).
7. National Science Foundation (NSF), *Shaping the Future, Volume II: Perspectives on Undergraduate Education in Science, Mathematics, Engineering, and Technology* (NSF, Arlington, VA, 1998).
8. NSF, *Shaping the Future: New Expectations for Undergraduate Education in Science, Mathematics, Engineering, and Technology* (NSF, Washington, DC, 1996).

TECHNICAL COMMENT ABSTRACTS

COMMENT ON "How the Horned Lizard Got Its Horns"

Salvatore J. Agosta, Arthur E. Dunham

Young *et al.* (Brevia, 2 April 2004, p. 65) purported to identify the mechanism behind the origin and maintenance of horns in horned lizards. Unfortunately, they asserted rather than demonstrated the current function of horns and failed to recognize the crucial distinction between adaptation and exaptation. As a result, the question implied in the title of their article—how the horned lizard got its horns—remains unanswered and, in the absence of an historical perspective, is unanswerable.

Full text at
www.sciencemag.org/cgi/content/full/306/5694/230a

RESPONSE TO COMMENT ON "How the Horned Lizard Got Its Horns"

Edmund D. Brodie III, Kevin V. Young, Edmund D. Brodie Jr.

Our study of the effect of natural selection on the horns of horned lizards focused on current function, not historical origins of the trait as described by the phylogenetic definition of adaptation. We explain why studies of current function are important for understanding adaptation and why a purely historical perspective on adaptation is unproductively limiting.

Full text at
www.sciencemag.org/cgi/content/full/306/5694/230b

Response to Comment on "How the Horned Lizard Got Its Horns"

Agosta and Dunham (*1*) argue that our study (*2*) did not consider the phylogenetic definition of adaptation and therefore cannot reveal the origin of horns in the larger group of horned lizards. Because we neither presented phylogenetic evidence nor made claims about the historical origin or past selection on horns in this group, this criticism is generally accurate, if somewhat extraneous. We suspect that the misunderstanding stems from the paper's title, which was meant as a humorous allusion to the just-so stories of Kipling (*3*) rather than as a literal description of our work. We expected that the title's intent would be clear and regret that we confused some readers. A more accurate title, perhaps, would have been "How the Flat-Tailed Horned Lizard Got Its Long Horns." Our brief article (*2*) addressed only the current function and adaptation of horn length in modern populations of the flat-tailed horned lizard and clearly stated that "[o]ur study does not show that other agents and forms of selection do not play a role in the evolution of horn size." Nonetheless, the critique by Agosta and Dunham (*1*) does underscore the contentiousness of concepts of adaptation, as well as the inability of either ecological or phylogenetic approaches to the problem to fully satisfy all critics.

Agosta and Dunham argue that we have not demonstrated adaptation of horned lizard horns and could not do so without a phylogenetic perspective. This interpretation is based on a historical definition of adaptation that emphasizes the exaptation/adaptation dichotomy (*4*–*6*). This is one important aspect of adaptation, but not the only one (*7*, *8*). In the parlance of Gould and Vrba (*4*), and those that followed, an exaptation differs from an adaptation in that the former is a feature whose "origin cannot be ascribed to the direct action of natural selection" for its current use. Subsequent attempts to outline methodology for distinguishing exaptation from adaptation (*5*, *6*, *9*, *10*), including the four-part paradigm repeated by Agosta and Dunham, have used phylogenetic frameworks to determine when a character changes state in relation to the selective environment. Although the historically based definition of adaptation has been productive, and we wholeheartedly support its application, we also believe that the blind subscription to this ideal as the only way to understand the phenomenon of adaptation is limiting and masks important aspects of the process of adaptation in natural populations.

First, the process of evolution, and as a part of it adaptation, is dynamic and continuous. A purely historical perspective on adaptation obfuscates the reality that selection continues to occur and modify phenotypes in a way that leads to increased fitness. Historical definitions of adaptation include current selection (*9*, *10*) but commonly view it as a force that maintains a character state and increases fitness by eliminating less fit mutations. However, directional selection of the sort described in our paper actually changes the state of a character and thereby is a force generating adaptation. As pointed out by Price in his famous covariance equations (*11*), selection can be defined as a statistical relation between phenotypic variance and fitness. The extension of this relation to evolutionary theory (and before that to artificial selection by way of the "breeders' equation") demonstrates that current selection on any heritable trait leads to phenotypic change (*12*). For the flat-tailed horned lizard, selection by shrikes leads to a covariance between survival probability and horn length. This selection alone would lead to a change of approximately 10% in only 20 to 30 years, assuming a moderate heritability. Certainly many biologists would view such a phenotypic change as an example of adaptation, regardless of the ancestral origin of horns. To ignore the role of current function in driving adaptation is to assume that evolution is something that has occurred only in the past.

This example also illustrates the second shortcoming of the phylogenetically restrictive definition of adaptation: It is inherently a statement about character states distributed across clades and thus has limited applicability to continuous change on short time scales. Phylogenetic frameworks have been developed to analyze continuous characters, but these necessarily emphasize the contrast between clades and taxa rather than observable change through time within a given lineage (*10*, *13*). Empirical studies of evolution have repeatedly demonstrated "rapid" phenotypic change over a time scale well short of that observable in a phylogenetic context (*14*), and geographic variation within species often equals or exceeds what is present among clades (*15*, *16*). If we focused only on phylogenetic patterns of phenotypic change, we would never have learned that a few generations of altered selection regime can dramatically change the life history of guppies (*17*), the shape of finch bills (*18*), or the mating morphology of salmon (*19*). In the case of horned lizards, analyses at both phylogenetic and contemporary levels undoubtedly will be productive. Species of horned lizards within the genus *Phrynosoma* vary greatly in the size and shape of horns emanating from the skull. The most derived species group within the genus includes three of the species with the longest relative horn sizes (*20*, *21*). Of these taxa, the flat-tailed horned lizard has the longest parietal (rear) horns of any species (*20*), but populations vary. Thus, within the genus *Phrynosoma*, evolution appears to have led to a derived condition of quantitatively longer parietal horns, without a change in character state of presence or absence of these horns. The historical forces that led to this quantitative elaboration of horn length are lost to us; even the strongest historical reconstructions of selective context are at best correlative and speculative regarding how selection operated at some point in deeper phylogenetic time (*22*). It is clear, however, that selection by shrikes generates the relationship necessary to continue to drive the elongation of horns in the short term.

The very definition of exaptation leads to a third problem with the historically based definition of adaptation. Because selection is a process that works with available material and existing variation only, all character states that are modified by natural selection by definition already exist in a population. By the strict application of Gould and Vrba's original definition, all traits could be labeled exaptations if we look at a generation-by-generation process [although Larson and Losos (*10*) disagree, preferring to call such traits "nonaptive or disaptive"]. New mutations arise before selection can act upon them, yet few would be expected to spread through a population if selection did not favor them. On the other hand, if current selection leads to the modification of traits, such as shrike predation driving the elongation of horns in flat-tailed horned lizards, then selection is in fact altering the trait as required by the strict definition of adaptation. If we look at biodiversity through a diffraction lens that only allows us to see discrete differences in character state or species identity, then it appears that the distinction between current and past function is clear. However, if we study selection at a microevolutionary level, this distinction becomes more arbitrary. Much as the disagreement over punctuated equilibrium as an evolutionary process reduces to a perspective of time scale and consequent questions (*23*), the issue of adaptation versus

exaptation depends on the scale of biodiversity and evolutionary time that we seek to explore.

Finally, Agosta and Dunham offer some criticism of the interpretation of current function that we do present in our paper. They argue that we are unsuccessful in identifying the function of horned-lizard horns because we do not know why the covariance between horn length and survival exists. As with all nonmanipulative studies of selection, this is strictly true (*24*). However, in this case we believe that we have strong inferential evidence. Behavioral observations of flat-tailed horned lizards captured in the wild reveal that individuals twist their heads to the back or side to drive their parietal or squamosal horns into any physical restraint (e.g., human fingers, forceps). The horns are sharp enough and the defensive behavior vigorous enough that in many cases lizards draw blood from "attacking" human fingers. Paired wounds and scars from presumed bird attacks on the bodies of some live lizards (illustrated in figure 1B of Young *et al.*) further suggest that this sort of behavior is effective in successfully deterring predation attempts. The most reasonable explanation for why shrikes kill relatively short-horned individuals is that they are less effective at deterring predation than are their longer horned conspecifics. Agosta and Dunham further criticize the use of size-adjusted horn length in our analysis because shrikes do not consume the heads of lizards. In the behavioral scenario described above, it is actually relative, not absolute, horn length that matters, because this measure determines how much of its vulnerable neck region—the favored attack site of shrikes (*25*)—a lizard can protect with its horns. A large lizard with large absolute horns but short horns relative to its body length might not be able to stab an attacking bird, but still might deter a gape-limited predator, as suggested by Agosta and Dunham. In any case, the purpose for analyzing relative horn length was to be conservative and eliminate the possibility that we would confound selection against small lizards with selection against small horns.

We believe we have presented a compelling example of selection in action, and one that identifies an agent and cause of selection that leads to adaptation (*2*). Contrary to the comments of Agosta and Dunham (*1*), our paper did not attempt to distinguish adaptation from exaptation or to reveal the ancestral origin of the horns in the genus *Phrynosoma*. Although we find the historically based definition of adaptation useful in many cases, and suspect that it will be a productive direction of research on horned lizards, we do not believe that it is obligatory or even relevant in all cases, nor should it be exclusive of studies of current function. Microevolutionary studies of the continuing process of natural selection are just as important to understanding how adaptation occurs as are the macroevolutionary studies that reveal their distribution in time and phylogeny.

Edmund D. Brodie III*
Department of Biology
Indiana University
Bloomington, IN 47405–3700, USA

K. V. Young
E. D. Brodie Jr.
Department of Biology
Utah State University
Logan, UT 84322–5305, USA
**To whom correspondence should be addressed.*
E-mail: edb3@bio.indiana.edu

References

1. S. J. Agosta, A. E. Dunham, *Science* **306**, 230 (2004); www.sciencemag.org/cgi/content/full/306/5694/230a.
2. K. V. Young, E. D. Brodie Jr., E. D. Brodie III, *Science* **304**, 65 (2004).
3. R. Kipling, *Just So Stories* (Doubleday, New York, 1902).
4. S. J. Gould, E. S. Vrba, *Paleobiology* **8**, 4 (1982).
5. D. A. Baum, A. Larson, *Syst. Zool.* **40**, 1 (1991).
6. H. W. Greene, *Fieldiana Zool.* **31**, 1 (1986).
7. M. R. Rose, G. V. Lauder, Eds., *Adaptation* (Academic Press, New York, 1996).
8. G. V. Lauder, A. M. Leroi, M. R. Rose, *Trends Ecol. Evol.* **8**, 294 (1993).
9. R. N. Brandon, *Adaptation and Environment* (Princeton Univ. Press, Princeton, NJ, 1990).
10. A. Larson, J. B. Losos, in *Adaptation*, M. R. Rose, G. V. Lauder, Eds. (Academic Press, New York, 1996), pp. 187–220.
11. G. R. Price, *Nature* **227**, 520 (1970).
12. D. S. Falconer, T. Mackay, *Introduction to Quantitative Genetics* (Longman, New York, 4th ed., 1996).
13. E. P. Martins, *Phylogenies and the Comparative Method in Animal Behavior* (Oxford Univ. Press, Oxford, 1996).
14. A. P. Hendry, M. T. Kinnison, *Evolution* **53**, 1637 (1999).
15. J. N. Thompson, *The Coevolutionary Process* (Univ. of Chicago Press, Chicago, 1994).
16. E. D. Brodie Jr., B. J. Ridenhour, E. D. Brodie III, *Evolution* **56**, 2067 (2002).
17. D. N. Reznick, F. H. Shaw, F. H. Rodd, R. G. Shaw, *Science* **275**, 1934 (1997).
18. P. R. Grant, *Ecology and Evolution of Darwin's Finches* (Princeton Univ. Press, Princeton, NJ, 1986).
19. A. P. Hendry, J. K. Wenburg, P. Bentzen, E. C. Volk, T. P. Quinn, *Science* **290**, 516 (2000).
20. R. R. Montanucci, *Contrib. Sci. Nat. Hist. Mus. Los Angeles Cty.* **390**, 1 (1987).
21. T. W. Reeder, R. R. Montanucci, *Copeia* **2001**, 309 (2001).
22. A. M. Leroi, M. R. Rose, G. V. Lauder, *Am. Nat.* **143**, 381 (1994).
23. B. Charlesworth, R. Lande, M. Slatkin, *Evolution* **36**, 474 (1982).
24. E. D. Brodie III, A. J. Moore, F. J. Janzen, *Trends Ecol. Evol.* **10**, 313 (1995).
25. S. M. Smith, *Behaviour* **44**, 113 (1973).

7 July 2004; accepted 16 September 2004

EXHIBITS: ART AND GENOMICS

Engaged with Sequences

R. Scott Winters

Eduardo Kac's installation piece *Genesis* (1999) is a disturbing amusement. Viewers activate an ultraviolet light to illuminate and mutate transgenic bacteria that contain a Bible-inspired artificial gene (*1*). The work transcends its technology to address deeper issues of social responsibility in the wake of the Human Genome Project. Following a long tradition of contemporary art, *Genesis* both interprets and catalyzes discourse on humanity's relationship with science and technology.

Gene(sis)
Contemporary Art Explores Human Genomics
Robin Held, curator

Organized by the Henry Art Gallery, the University of Washington, Seattle, WA, in affiliation with the Berkeley Art Museum, Berkeley, CA. At the Mary and Leigh Block Museum of Art, Northwestern University, Evanston, IL, through 28 November 2004. www.gene-sis.net. CD-ROM catalogue, $24.95.

Artifacts from the *Genesis* installation are included in the traveling museum exhibition *Gene(sis): Contemporary Art Explores Human Genomics*, which appears at the Mary and Leigh Block Museum of Art in Evanston, Illinois, through 28 November. (The Block Museum is the show's fourth and final venue since its 2002 debut at the Henry Art Gallery in Seattle, Washington.) Ostensibly, the exhibition has three goals: to present to lay audiences technological advances associated with the Human Genome Project, to focus attention on ethical issues raised by genomic research, and to promote an ongoing dialog concerning the impact of genomic research on our daily lives.

Gene(sis) comprises nearly 60 works contributed by 24 artists (individuals, ensembles, or organizations). The pieces span media from photography and painting through installation and performance. The exhibition is organized into four sections, each with its own general theme: sequence (the genome as coded text), specimen (DNA as property or medical panacea), boundary (the erosion of species delimiters and the consequences of transgenics), and subject (how does one define human attributes, identity, or social constructs). The pieces on display are augmented by a CD-ROM catalogue that also contains eight original essays, which are as varied as the works themselves.

Kac's second contribution to the exhibit, *GFP Bunny: Paris Intervention* (1999-present), concerns a rabbit, affectionately nicknamed "Alba," that is the world's most (in)famous object of transgenic art. With the help of French geneticists, a variant of the bioluminescence gene from the jellyfish (*Aequorea victoria*) was spliced into an albino rabbit. The result is a bunny that fluoresces in 488-nm light and redefines the boundaries of artistic media. Although documents and relics related to her creation are displayed, Alba remains in a French laboratory. It is the absence of the piece's archetype that makes the work so powerful.

GFP Bunny transcends experiment, chimera, and installation-piece to herald a new form of socially engaged art. It forces us to argue the delimiters of species, the nature of art, and the ethics of technology. As such, it goes beyond the role of icon or index to become a symbol and signifier of a complex social predicate. Few works of art approach this level of semiosis or catalyze as much debate as Alba. However, with the Human Genome Project as both signifier and referent, one would expect artist-pundits to be exploring this shifting landscape of ethical thorns more vigorously. Given its scale and ambition, the exhibit's greatest weakness is inconsistency. Some pieces are hackneyed and simply fail to rise above mere technophilia, novelty, or iconography.

Although it would be unrealistic to expect all pieces to have the impact of *GFP Bunny*, there are a number of other memorable highlights. *The Garden of Delights* (1998) by Iñigo Manglano-Ovalle seamlessly marries icon, aesthetic, and discourse. This impressive installation is composed of 48 autoradiograph portraits arranged in 16 family triptychs. By atomizing his subjects into genomic fragments, Manglano-Ovalle focuses our attention on the beauty of similarities and differences that exist among individuals while boundaries such as sex, race, and belief become indiscernible.

The most interesting "piece" is the exhibit itself: program as meta-installation. Curator Robin Held's catalogue essay (*2*) chronicles the struggle to mount a unique and nontraditional exhibition. After 9/11, the specters of bioterrorism and anthrax haunted the exhibition's planning. *Gene(sis)* was required to register as a "laboratory activity" with the National Institutes of Health, and works for inclusion had to pass a safety review process. As a result of these restrictions, a number of exhibits had to be modified (e.g., dried blood removed) or abandoned (e.g., Critical Art Ensemble's *Cult of the New Eve*). Public safety issues transmogrified into an institutional perception of the public's perception of public safety issues.

During the exhibition's development, the University of Washington's biosafety committee raised some interesting—even if irrelevant to their charge—questions (*2*): Why would anyone want to do this? Why is this art? But prompting questions is the legacy that has made *Gene(sis)* successful. The exhibition encourages social commentary by bridging the gap between the public and the complex social experiment of the Human Genome Project. It provides us with a perspective, however fragmented, of the issues and implications of genomic research. And, it facilitates our path toward bio-ethics via a new bio-aesthetics.

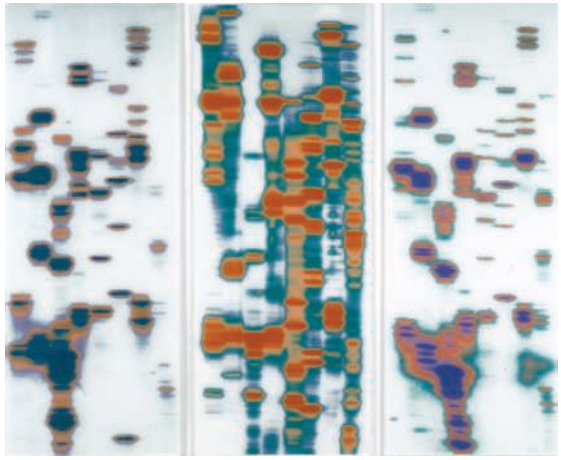

Lu, Jack, and Carrie. C-print of DNA analyses, from Iñigo Manglano-Ovalle's *The Garden of Delights* (1998).

CREDIT: COURTESY OF THE MAX PROTETCH GALLERY, NEW YORK

The reviewer is in the Division of Oncology, Children's Hospital of Philadelphia, 34th Street and Civic Center Boulevard, Philadelphia, PA 19104, USA. E-mail: winters@genome.chop.edu

References and Notes

1. Kac transcribed *Genesis* 1:28 into Morse code and then translated the message into a nucleic acid sequence. The artist interprets the biblical passage as: "Let man have dominion over the fish of the sea and over the fowl of the air and over every living thing."
2. R. Held, "Generating *Gene(sis)*: A Contemporary Exhibit for the Genomic Age." (The text of the essay on the CD-ROM differs slightly from that on the exhibit's Web site.)

Published by AAAS

EDUCATION

The Evolution of Postdocs

Maxine Singer

Four years ago, the National Academies' Committee on Science, Engineering, and Public Policy (COSEPUP) published its guide on enhancing the postdoctoral experience (*1*). Since then, the smoldering "postdoc problem" has transformed into lively constructive activities (*2*). In the United States, research institutions are creating and staffing postdoctoral offices, supporting postdoctoral associations, and improving compensation packages (*3*). Funding organizations are raising stipends and sponsoring transitional grants. The Postdoc Network was founded by *Science*'s Next Wave (*4*). Sigma Xi has launched a large-scale survey of postdocs (*5*). The National Postdoctoral Association (NPA) was formed (*6*).

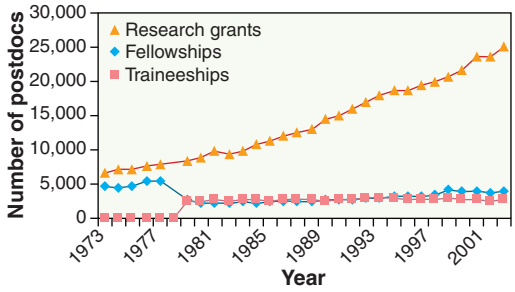

Mechanisms of postdoctoral support (*1*). Traineeship support did not exist before 1981, and there is no NSF data on the support mechanism for 1978.

Although stipends and benefits have improved, they remain a concern. There is continuing frustration at the lack of data on postdocs supported on research grants, data that can only be collected by federal agencies. However, the greatest continuing concern is the quality of mentoring from advisers, especially support and guidance in the transition to independent careers. Here, the first principle identified in COSEPUP's guide [(*1*), p. ii] remains primary: "the postdoctoral experience is first and foremost an apprenticeship whose purpose is to gain scientific, technical, and professional skills that advance the professional career of the postdoc." Mentors must be honest with each postdoc about her/his talents, accomplishments, and potential. They must impart the realities, and variety, of scientific careers, and should encourage experiences outside the laboratory to broaden postdocs' aspirations.

However, such roles are often inconsistent with mentors' expectations, especially because principal investigators (PIs) are already overburdened with responsibilities. Particularly in the biomedical sciences, many PI's view postdocs not as apprentices but as skilled, bargain-rate assistants, who become increasingly valuable with time. Given the career challenges they face, postdocs agree to lengthy extensions in the hope of eventually publishing a highly visible paper that can help them land a good job. This relationship too often confers benefit to the mentor at the cost of the postdoc's career goals.

As years go by, postdocs tend to see their positions as semipermanent "jobs" rather than defined periods in which to advance their careers. Their primary responsibilities become carrying out research defined by their supervisor and training students and new postdocs. In this way, they rightfully acquire a certain status, but it is without a foundation in independence. The title "postdoc" no longer conveys their skills, knowledge, and contributions. In time, they establish families and roots in the community that, together with the lack of academic opportunities elsewhere, make moving away unattractive.

In a positive step, some institutions have adopted a 5-year limit on the postdoctoral period. After that, a postdoc must either leave or be internally promoted to staff scientist or research professor positions with appropriate compensation, retirement benefits, and performance expectations (*7*, *8*).

In earlier times, postdocs were expected to have independent research projects, with guidance from mentors. Many postdocs were supported by portable, competitive fellowships awarded to them directly and limited to 2 or 3 years. This arrangement balanced power between the postdoc and mentor: The mentor still largely controlled the postdoc's future opportunities, but the postdoc controlled the research topic and could shop a proposal to the most suitable mentor.

Today, 80% of postdocs are paid from a PI's research grant (see figure). This shift has advantages and disadvantages, but the important question is how well it serves science and the education of new generations of scientists. At least in biomedical sciences, the shift in funding parallels the increased age at time of first independent grant (*9*).

I worry about the costs to the advancement of science when junior researchers postpone independence and are thwarted in energetically developing original ideas. We all know many scientists who broke new ground when considerably younger than the current median age for postdocs (*10*).

During the COSEPUP-sponsored postdoc convocation last April, MIT Professor Mildred Dresselhaus (*11*) described the postdoc situation as a systems problem. No one designed the current system; it evolved over time. If we clarify the goals of scientific training, we could design strategies and incentives that will promote constructive continued change. Meanwhile, several measures can go a long way toward providing students training for a variety of careers, reducing time to degree (*12*), and promoting earlier independence for postdocs. These include written appointment letters for postdocs with clearly outlined expectations and compensation; at least annual conversations between postdoc and PI to evaluate progress and provide career guidance; tracking of career outcomes by institutions and, tracking of grantees including postdocs supported on investigator awards, by funding agencies. Such changes will also help graduate students and undergraduates see a career in science or engineering as an exciting and rewarding prospect.

The author is chair of the Committee on Science, Engineering, and Public Policy, National Academies, and president emerita, Carnegie Institution of Washington, Washington, DC 20005–1910, USA. E-mail: msinger@pst.ciw.edu

References and Notes

1. National Research Council (NRC), *Enhancing the Postdoctoral Experience for Scientists and Engineers* (National Academy Press, Washington, DC, 2000).
2. B. L. Benderly, *Science*'s Next Wave, 7 May 2004; http://nextwave.sciencemag.org/cgi/content/full/2004/05/05/1.
3. L. Haak, *Science*'s Next Wave, 16 Aug 2002; http://nextwave.sciencemag.org/cgi/content/full/2002/08/13/1.
4. See http://nextwave.sciencemag.org/pdn/.
5. See http://postdoc.sigmaxi.org/.
6. See www.nationalpostdoc.org/.
7. For example, A Sreenivasan, *Science*'s Next Wave, 21 March 2003; http://nextwave.sciencemag.org/cgi/content/full/2003/03/20/4.
8. Office of Postdoctoral Services, "Postdoc Options for Promotion" (Univ. of North Carolina, Chapel Hill, 2003); http://www.unc.edu/ops/policies.htm.
9. NRC, *Trends in Early Careers of Life Scientists* (National Academy Press, Washington, DC, 1988).
10. G. J. Feist, M. E. Gorman, *Rev. Gen. Psychol.* **2**(1), 3 (1998).
11. M. Dresselhaus, personal communication.
12. National Science Foundation, *Survey of Graduate Students and Postdocs in Science and Engineering, 1973–2002*; accessed by using WebCASPAR (www.webcaspar.nsf.gov).

Published by AAAS

MOLECULAR BIOLOGY

RNAs Turn On in Tandem

Michael Famulok

Proteins often carry out their cellular functions at a defined time and place, requiring that their activity be precisely regulated. An important mechanism for controlling protein activity is allosteric regulation by a small molecule that binds to the protein at a location remote from the active site. Binding of this regulatory compound to the allosteric site induces structural rearrangements in the protein that are relayed to the active site, which then becomes either stable or unstable. In allosteric proteins, multiple subunits act cooperatively: Once a regulator is bound to one subunit, another subunit responds with dramatically enhanced affinity, allowing the protein's activity to be modulated as a function of slight changes in the regulator's concentration (see the figure). On page 275 of this issue, Mandal *et al*. (*1*) report that activity regulation by cooperative binding is not restricted to proteins but also is a feature of RNA molecules. They describe a bacterial messenger RNA (mRNA) element, a so-called riboswitch, in which two allosteric RNA subunits are triggered cooperatively by the amino acid glycine. This cooperative activation regulates the expression of genes involved in glycine metabolism without the need for any additional proteins.

The glycine-responsive riboswitch joins a series of recently identified natural RNA motifs that are controlled by other small-molecule regulators (*2*). In all of them, the highly selective binding of small molecules to the RNA motifs activates or represses expression of nearby genes by inducing conformational changes in their mRNAs that interfere with transcription or translation. The RNA elements of the new glycine-responsive riboswitch are embedded within the untranslated regions of genes encoding a protein complex that enables bacteria to cleave glycine for consumption as an energy source—but only if the glycine concentration exceeds a certain level. Accordingly, the expression of the components of the glycine cleavage system must remain in an off-state when the amount of glycine is limited. If not, a resource that is indispensable for vital processes, such as maintenance of protein synthesis, would be invested in energy production, which could just as easily be accomplished with other available molecules. Conversely, if regular fuels such as carbohydrates or fats are scarce, an organism would be at a selective advantage if it could derive energy from sources that are not easily accessible to its competitors. Thus, the glycine riboswitch has to fulfill two important criteria: to act as a genetic "on-switch," and to be able to reliably sense glycine with high specificity within a narrow concentration window. Both of these abilities are far from trivial to achieve even for a protein, and thus set the new riboswitch apart from most other riboswitches. The mechanism of action of the new riboswitch is remarkable and provides a further demonstration of the power of RNA as a regulatory element.

Riboswitches are actually natural versions of a class of artificial ligand-binding nucleic acids known as aptamers. Aptamers were first isolated from complex mixtures of trillions of synthetic sequences by in vitro evolution methods (*3*, *4*). They form binding pockets that recognize a huge variety of small organic molecules with high affinity and specificity. In various cases, different aptamer sequences have been identified for the same ligand (*5*, *6*). The glycine riboswitch consists of two different aptamer types that individually bind to a single molecule of glycine (see the figure). Interestingly, both aptamers are always joined in tandem—separated only by short linker sequences—in the genes of many different bacterial species (see the figure). An individual RNA motif requires about a 100-fold increase in glycine concentration to arrive at nearly complete saturation when starting at concentrations where binding is just about detectable. But in the complete tandem-arranged riboswitch, cooperative glycine binding narrows this concentration range to only 10-fold. Indeed, as Mandal *et al*. note (*1*), the extent of cooperation between the two glycine binding sites in the *Vibrio cholerae* riboswitch compares favorably with that of the four oxygen binding sites in hemoglobin, a star among those proteins exhibiting cooperativity.

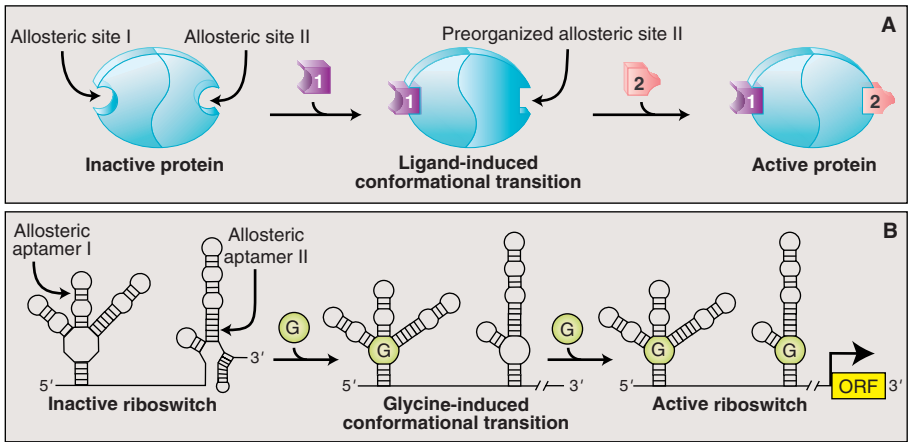

The benefits of cooperation. (**A**) In certain proteins, two distant binding sites for positive regulator molecules 1 and 2 are conformationally coupled. Binding of molecule 1 to allosteric site I triggers conformational changes that result in reorganization of a distant second site, allosteric site II, enabling molecule 2 to bind more efficiently to this site. The protein is active when both molecules are bound. (**B**) Activation of a riboswitch, which consists of the allosteric glycine-binding RNA aptamers I and II, might occur by a similar mechanism. Here, too, binding of one glycine molecule (G) to aptamer I helps a second glycine to bind to aptamer II. Only then is the riboswitch activated, resulting in transcription of genes that encode components of the glycine cleavage system.

From an evolutionary point of view, it is fascinating that nature has evolved several different glycine-binding aptamer motifs and arranged them in tandem to function together in vivo as regulators that sense glycine within a narrower concentration window than either aptamer alone. Also remarkable is the fact that RNA molecules that comprise only 86 to 126 nucleotides are capable of binding to an organic ligand of 75 daltons with such impressive specificity that glycine can be effectively discriminated from closely related amino acids and their derivatives.

Perhaps even more notable, however, is

The author is at the Kekulé Institut für Organische Chemie und Biochemie, D-53121 Bonn, Germany. E-mail: m.famulok@uni-bonn.de

the fact that for virtually every mechanism harnessed by riboswitches to control gene expression, it is possible to cite an analogous artificial system that was first constructed in the laboratory. In vitro selected aptamers that affect translation of reporter genes in cells (*7*) preceded the discovery of similar natural riboswitches (*2*). Engineered allosteric ribozymes regulated by small organic molecules (*5*) antedated the recent discovery of the first catalytic riboswitch regulated by glucosamine-6-phosphate (*8*). There is even an example of an allosteric ribozyme construct in which two aptamers specific for flavine mononucleotide and theophylline are aligned in tandem to act as a cooperative "on-switch" for ribozyme cleavage (*9*). For decades, scientists have been guided in the construction of synthetic model systems that mimic functional principles applied by the corresponding archetypes of nature. It is rewarding to see that in the case of riboswitches, engineering of functional nucleic acid molecules inspired the search for and discovery of closely related natural counterparts.

Is the principle of gene regulation by riboswitches restricted to bacteria, or is it also found in eukaryotes? These regulators appear to be widespread in bacteria, but candidates are also likely to be present in the eukaryotic genes of plants, as suggested by their evolutionary conservation (*10*). It will be interesting to see whether they can also be found in higher eukaryotes, even in humans. If so, completely new avenues of pharmaceutical research would be opened up with the exploration of RNAs as worthwhile drug targets.

References

1. M. Mandal *et al.*, *Science* **306**, 275 (2004).
2. E. Nudler, A. S. Mironov, *Trends Biochem. Sci.* **29**, 11 (2004).
3. C. Tuerk, L. Gold, *Science* **249**, 505 (1990).
4. A. D. Ellington, J. W. Szostak, *Nature* **346**, 818 (1990).
5. M. Famulok, *Curr. Opin. Struct. Biol.* **9**, 324 (1999).
6. J. M. Carothers *et al.*, *J. Am. Chem. Soc.* **126**, 5130 (2004).
7. G. Werstuck, M. R. Green, *Science* **282**, 296 (1998).
8. W. C. Winkler *et al.*, *Nature* **428**, 281 (2004).
9. A. M. Jose *et al.*, *Nucleic Acids Res.* **29**, 1631 (2001).
10. N. Sudarsan *et al.*, *RNA* **9**, 644 (2003).

PHYSICS

The Active Site in Nanoparticle Gold Catalysis

Charles T. Campbell

Most pollution from U.S. automobiles is emitted in the first 5 min after startup. This is because Pt- or Pd-based catalysts currently used in automobile exhaust cleanup are inactive below about 200°C. Gold-based catalysts present a potential solution to this cold-startup problem. Gold nanoparticles dispersed across the surfaces of certain oxides have been shown to be amazingly active and selective as catalysts for a variety of important reactions. There is intense interest in these catalysts for carbon monoxide oxidation, because they are active at room temperature. Interestingly, the low-temperature gold catalysts are totally inactive unless the gold is in the form of particles smaller than ~8 nm in diameter (*1*–*3*). Though gold nanoparticles have been perhaps the most widely studied catalyst system in the last 2 to 3 years, the structure of the active site has remained elusive. On page 252 in this issue, Chen and Goodman (*4*) take an important step toward characterizing the active site.

The problem has been that the active sites are on or near tiny gold particles that are themselves difficult to structurally characterize, and the gold-coated surface is very heterogeneous and thus structurally ill-defined. Chen and Goodman (*4*) have produced a highly active model gold catalyst where the gold is incorporated in a crystalline film, spread uniformly over a Ti_2O_3 surface like icing on a cake. The coated surface is therefore amenable to structural elucidation with quantitative low-energy electron diffraction and other surface crystallographies. The gold appears to be a pure, crystalline film, two atomic layers thick, with an epitaxial relationship to the underlying oxide support, itself a crystalline thin film of Ti_2O_3. The authors prepared this Ti_2O_3 as an ultrathin film on the (112) surface of a molybdenum single crystal using elegant synthetic strategies pioneered previously (*5*–*7*). The very high catalytic turnover rate for this gold film raises the exciting possibility of an ~50-fold improvement in the performance of realistic, high-area catalysts.

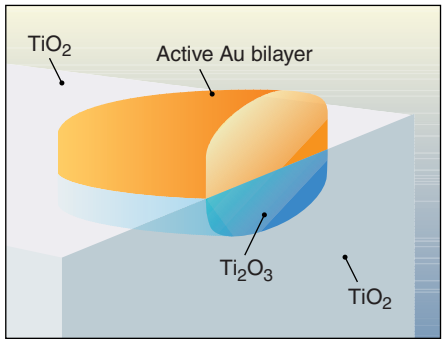

Gold that works: Proposed structure of active gold nanoparticles in which reduced TiO_2 accumulates under gold islands, as first shown in (*19*).

Previous work on oxide-supported gold nanoparticle catalysts has provided evidence used to support a wide range of active-site structures. Some researchers have proposed that the active sites are on the surface of the oxide (usually defects), possibly modified by the presence of nearby gold, and function together with sites on the gold nanoparticles (*8*–*10*). Others attribute the catalytic activity entirely to the presence of neutral gold atoms on the gold nanoparticles. These neutral atoms differ from atoms on bulk gold in three ways that might enhance their catalytic activity: (i) They have fewer nearest-neighbor atoms (that is, a high degree of coordinative unsaturation) (*11*–*14*) and also possibly a special bonding geometry to other gold atoms that creates a more reactive orbital (*15*). (ii) They exhibit quantum size effects that alter the electronic band structure of gold nanoparticles (*3*). (iii) They undergo electronic modification by interactions with the underlying oxide that cause partial electron donation to the gold cluster (*16*). Another proposal is that positively charged gold ions on the oxide support are the key to the catalytic activity of these gold catalysts (*17*, *18*).

The Chen and Goodman study (*4*) marks an important step toward identification of the active site. Although the atomic resolution crystal structure of this highly active gold thin film has not yet been determined, the authors have provided strong evidence for the broad features of its structure using a powerful combination of surface analysis techniques (qualitative low-energy electron diffraction, x-ray photoelectron and Auger electron spectroscopies, high-resolution electron energy loss spectroscopy, and low-energy ion-scattering spectroscopy). Their results imply that the active site, at least for low-temperature CO oxidation, involves gold atoms that are nearly electrically neutral and bound to the surface via Au-Au covalent bonds and Au-Ti bonds. The authors find that the gold film completely covers the oxide and that reactants are sterically hindered from chemical bonding directly with the underlying Ti_2O_3.

This exciting work raises a number of important questions. What is the crystal structure of this Au/Ti_2O_3 film? Why are the gold atoms in this thin gold film different from the atoms on bulk gold? Will this

The author is in the Chemistry Department, University of Washington, Seattle, WA 98195–1700, USA. E-mail: campbell@chem.washington.edu

CREDIT: PRESTON HUEY/*SCIENCE*

structure be stable for extended reaction times, and will it also have activity for other reactions catalyzed by supported gold nanoparticles? Clearly, these questions will inspire much research from experimentalists and theoreticians alike.

The authors characterize the active gold film as a bilayer. In the strictest sense this may be true, but it is also confusing, because the total number of gold atoms per unit area in this film is 20% less than that in the topmost atomic layer of Au(111). This implies that the nearest-neighbor coordination sphere of the surface gold atoms includes many Ti and O neighbors, and not only gold atoms. Such a scenario may explain why the reactivity of the neutral gold atoms differs from that of bulk gold. Furthermore, it even leaves room for reactants to bond directly to O or Ti atoms, so that their direct participation in the reaction cannot be fully excluded. Determining the crystal structure of the gold film would go a long way toward clarifying many of these issues, and would greatly aid future theoretical studies of the catalytic mechanism. We also look forward to the next step—determining the structure of the gold film in the presence of adsorbed reactants.

References and Notes

1. M. Haruta, *Catal. Today* **36,** 153 (1997).
2. T. Hayashi, K. Tanaka, M. Haruta, *J. Catal.* **178**, 566 (1998).
3. M. Valden, X. Lai, D. W. Goodman, *Science* **281**, 1647 (1998).
4. M. S. Chen, D. W. Goodman, *Science* **306**, 252 (2004).
5. M. C. Wu, J. S. Corneille, C. A. Estrada, J. W. He, D. W. Goodman, *Chem. Phys. Lett.* **182**, 472 (1991).
6. J. Libuda *et al.*, *Surf. Sci.* **318**, 61 (1994).
7. T. Schroeder, J. B. Giorgi, M. Baumer, H. J. Freund, *Phys. Rev. B* **66**, 165422 (2002).
8. J.-D. Grunwaldt, A. Baiker, *J. Phys. Chem. B* **103**, 1002 (1999).
9. M. M. H. Schubert *et al.*, *J. Catal.* **197**, 113 (2001).
10. L. M. Molina, B. Hammer, *Phys. Rev. Lett.* **90**, 206102 (2003).
11. V. Bondzie, S. C. Parker, C. T. Campbell, *Catal. Lett.* **63**, 143 (1999).
12. C. Lemire, R. Meyer, S. Shaikhutdinov, H. J. Freund, *Angew. Chem. Int. Ed.* **43**, 118 (2004).
13. N. Lopez *et al.*, *J. Catal.* **223**, 232 (2004).
14. R. Zanella *et al.*, *J. Catal.* **222**, 357 (2004).
15. G. Mills, M. S. Gordon, H. Metiu, *J. Chem. Phys.* **118**, 4198 (2003).
16. A. Sanchez *et al.*, *J. Phys. Chem. A* **103**, 9573 (1999).
17. J. Guzman, B. C. Gates, *J. Phys. Chem. B* **106**, 7659 (2002).
18. Q. Fu, H. Saltsburg, M. Flytzani-Stephanopoulos, *Science* **301**, 935 (2003).
19. J. A. Rodriguez *et al.*, *J. Am. Chem. Soc.* **124**, 5242 (2002).

20. Supported by the U.S. Department of Energy, Office of Basic Energy Sciences, Chemical Sciences Division.

ASTRONOMY

Astronomical Masers

Mark Claussen

Maser emission from molecules such as water, hydroxyl (OH), and silicon monoxide (SiO) is an important tracer of the gas kinematics and magnetic field strength in astrophysically interesting regions. Since their discovery in 1965, these emissions have provided clues about the molecular gas in and around young stellar and protostellar objects, around stars at the end of their life, at the interface of supernova remnants and molecular clouds, and near the black holes at the centers of active galaxies. Because they are bright, they can be observed with the finest angular resolution currently possible in astronomy. They can thus be used to probe much smaller physical scales than with other astronomical methods, and to infer accurate distances to objects within and outside the Milky Way.

Enhanced online at www.sciencemag.org/cgi/content/full/306/5694/235

The first interstellar masers were discovered from the ground state of OH (at a wavelength near 18 cm) but were not recognized as such initially (*1*). It was only because laboratory masers had already been invented [see accompanying Perspective by Walsworth (*2*)] that the discoverers could understand the physical mechanism of the maser. Many early observations characterized the emission from OH masers as time-variable, polarized (both linearly and circularly), and having narrow line widths. These characteristics are typical of most astronomical masers.

As radio telescopes became more sensitive and able to look at a broader range of frequencies, and interferometry provided much better angular resolution, more molecular masers were discovered and their sizes were measured. Brightness temperatures (the temperature that they would have if they were emitting as thermal sources) of $>10^9$ K and sizes of <0.001 arc sec (1 arc sec = ~1/2000 of the angular diameter of the Sun as seen from Earth) were found to be typical of these natural masers. Masers have been found in transitions of OH, SiO, water, methanol, ammonia, and other molecules, and also in recombination lines of hydrogen.

The study of masers has gone hand-in-hand with the development of very long baseline interferometry (VLBI), which enables angular resolutions of 0.0001 arc sec at the highest radio frequencies. The Very Long Baseline Array (VLBA), built and operated since 1993 by the National Radio Astronomy Observatory, has provided the lion's share of recent maser observations.

Masers occur in several places in the universe: in the vicinity of newly forming stars and regions of ionized hydrogen (H II regions) (OH, water, SiO, and methanol masers); in the circumstellar shells of stars at the end of their life—that is, red giants and supergiants (OH, water, and SiO masers); in the shocked regions where supernova remnants are expanding into an adjacent molecular cloud (OH masers); and in the nuclei and jets of active galaxies (OH and water masers).

The brightest water masers seen in the direction of forming stars and H II regions in the Milky Way were used in the 1980s to measure the distances of such objects from Earth by purely geometric and kinematic methods (*3*). This and other procedures were used to model the motions of the water maser spots in a star-forming region at the center of the Milky Way, and thus make an independent measurement of the distance to the galactic center. More recently, water masers in low-mass young stellar objects have been used to trace the collimated outflows from these "protostars" at unprecedentedly small physical scales (*4*). Polarization measurements of OH masers near H II regions have allowed an estimate of the magnetic field throughout the spiral arms of the Milky Way (*5*). Water masers can also be used to trace magnetic fields through the Zeeman effect; with sufficient-

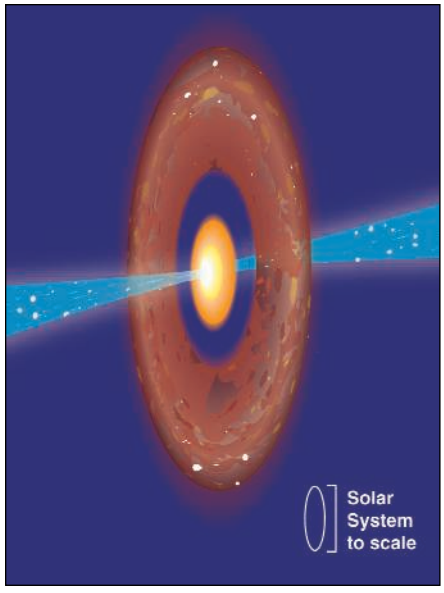

Artist's impression of masers in the outflow from a protostar.

CREDIT: ADAPTED FROM (*9*)

The author is at the National Radio Astronomy Observatory, Post Office Box O, Socorro, NM 87801, USA. E-mail: mclausse@aoc.nrao.edu

ly bright water masers, line-of-sight magnetic fields have been measured in forming low-mass stars.

Masers from different molecules in the circumstellar shells of red giant and supergiant stars probe different regions of the shells. OH masers are found far out in the shell, whereas water masers are found at intermediate radii and SiO masers within the innermost few stellar radii. The latter are likely to be in the "acceleration zone," where gas and dust are accelerated away from the star by radiation pressure coming from the star. Repeated VLBI observations over the light cycle of such variable stars have allowed astronomers to make "movies" of the motions of the SiO masers. A particularly striking movie (*6*) of the red giant star TX Camelopardalis shows that the maser motion appears to pulsate, in line with what stellar astronomers expect the AGB star's atmosphere itself to do. A detailed look at the movie, however, shows some surprises: The masers also perform nonradial motions, and some maser spots move inward when most other masers in the ring are moving away from the star.

In the past decade, OH masers in supernova remnants have received renewed attention. These masers were first discovered in 1966 but were largely forgotten until recent Very Large Array (VLA) observations stimulated new studies. Very recent VLBI observations of these OH masers, together with modeling studies of their excitation, have shown that they trace transverse shocks as the supernova remnant runs into the adjacent molecular cloud (*7*). The magnetic fields on small (a few hundred astronomical units) scales can be traced in these interaction regions and have been found to be rather strong (~0.001 to 0.002 G, up to 10 times the strength found in the surrounding interstellar medium).

Water masers have also been detected and mapped in the nuclei of active galaxies, which are thought to harbor a black hole in their centers. These intrinsically bright masers are thought to lie in the accretion disk of matter that is rotating around and falling into the black hole. In one galaxy, NGC 4258, mapping the velocities of the masers indicated a nearly perfect Keplerian rotation of the disk (*8*). This observation allowed a highly accurate calculation of the central mass within the disk of 4×10^7 solar masses, strongly suggesting the presence of a black hole. Further analysis, assuming a disk model, yields the distance to the masers based only on simple geometric considerations. Thus, the distance to NGC 4258 has been measured to better than 5%, providing an independent estimate of the distance scale of the universe and therefore of the Hubble constant (the ratio of velocity to distance in the expansion of the universe).

With the construction and routine operation of the VLBA, observations of masers have become easier and more accurate. The resulting improved observations of maser emission, with much better positional accuracies, will allow astronomers to measure distances to many weaker masers and their associated astronomical objects out to more than 10 kiloparsecs from the Sun. Because distance measurements are both fundamental and difficult to make (especially for objects farther than a few parsecs from the Sun), these results will be a dramatic step forward in understanding many aspects of stars and stellar evolution in the Milky Way. In addition, the use of masers to trace the outflow and perhaps accretion and associated magnetic fields during the formation of Sun-like stars will yield important clues to stellar and planetary system formation.

References

1. H. Weaver, D. R. W. Williams, N. H. Dieter, T. W. Lum, *Nature* **208**, 29 (1965).
2. R. L. Walsworth, *Science* **306**, 236 (2004).
3. R. Genzel, M. J. Reid, J. M. Moran, D. Downes, *Astrophys. J.* **244**, 884 (1981).
4. M. J. Claussen, K. B. Marvel, A. Wootten, B. A. Wilking, *Astrophys. J.* **507**, L79 (1998).
5. V. L. Fish, M. J. Reid, A. L. Argon, K. M. Menten, *Astrophys. J.* **596**, 328 (2003).
6. P. J. Diamond, A. J. Kemball, *Astrophys. J.* **599**, 1372 (2003).
7. I. M. Hoffman *et al.*, *Astrophys. J.* **583**, 272 (2003).
8. M. Miyoshi *et al.*, *Nature* **373**, 127 (1995).
9. D. S. Shepherd, M. J. Claussen, S. E. Kurtz, *Science* **292**, 1513 (2001).

APPLIED PHYSICS

The Maser at 50

Ronald L. Walsworth

In 1954, Gordon, Zeiger, and Townes (*1*) developed the ammonia maser (see the figure, top), the first device to demonstrate "microwave amplification by stimulated emission of radiation" from atoms or molecules. The maser and its younger optical cousin, the laser, remain prototypical examples of the powerful technologies inspired by quantum mechanics and 20th-century physics. Today, masers are extending the reach of quantum mechanics to revolutionary new methods of computation and communication and are probing theories that seek to unify quantum mechanics with general relativity—the other major part of 20th-century physics.

Enhanced online at www.sciencemag.org/cgi/content/full/306/5694/236

Masers produce coherent, monochromatic electromagnetic radiation at a characteristic frequency and wavelength. All share a few general features:

1) A "population inversion"—that is, a larger population in the higher energy of two selected quantum states of an ensemble of atoms, molecules, or ions—is created in the maser medium. Through stimulated emission, the population inversion amplifies electromagnetic fields that are resonant with the transition frequency between the two quantum states.

2) A surrounding electromagnetic resonator is tuned to the maser medium's transition frequency. The resonator typically has low electromagnetic loss at its resonant frequency, and thereby enhances the ability of electromagnetic fields to induce stimulated emission by the maser.

3) Some fraction of the radiated electromagnetic field is released from the resonator to provide the output signal.

4) In many masers, a steady, continuous output is desired. Such "active oscillation" has two requirements: There must be a continuous means of creating a population inversion, and the time for self-induced maser action (the radiation damping time) must be shorter than the decay time for the radiating electromagnetic moment of the maser medium (that is, the decay time for a coherent superposition of the two quantum states).

These conditions are met in a wide variety of systems. Indeed, the definition of a maser has expanded since 1954 to include the entire audio-to-microwave range of the electromagnetic spectrum, corresponding to wavelengths of millimeters to kilometers.

To operate at these long wavelengths, masers usually exploit magnetic dipole transitions (such as hyperfine or Zeeman transitions) in atoms, molecules, and other media. Because magnetic dipoles interact weakly with each other, with electromagnetic fields, and with environmental perturbations, masers typically provide weak but spectrally pure and temporally stable signals. [An important exception to this weak signal behavior is the electron cyclotron maser, which can be used to create very high power signals—up to hundreds of thousands of watts—in the millimeter wavelength regime (*2*).] When placed in a very cold environment, masers can also

The author is at the Harvard-Smithsonian Center for Astrophysics, 60 Garden Street, Cambridge, MA 02138, USA. E-mail: rwalsworth@cfa.harvard.edu

amplify applied resonant signals with very little added noise beyond the small effects of spontaneous emission and remnant thermal (blackbody) radiation.

The widely used ruby and hydrogen masers are two devices that illustrate the properties and applications of masers over the past 50 years.

The ruby maser (*8*) uses electron spin (Zeeman) levels of Cr^{3+} ions embedded in ruby crystals. A population inversion is created between two Zeeman levels, typically by applying strong microwave pump fields to saturate the population difference between the lower energy maser level and one or more levels of greater energy than the higher energy maser level. Because electron Zeeman levels are used, the maser transition frequency can be tuned over many tens of gigahertz through application of an appropriate magnetic field. The ruby maser generally operates near liquid helium temperature (4.2 K) and below the active oscillation threshold [see requirement 4) above]. It can provide a tunable, low-noise microwave amplifier with a gain of ~40 dB, very low noise temperature (~4 K), and moderately broad bandwidth (~100 MHz). Ruby masers have been widely used as amplifiers in radio astronomy antennas and related applications, such as the detection of weak signals sent back to Earth by distant space probes.

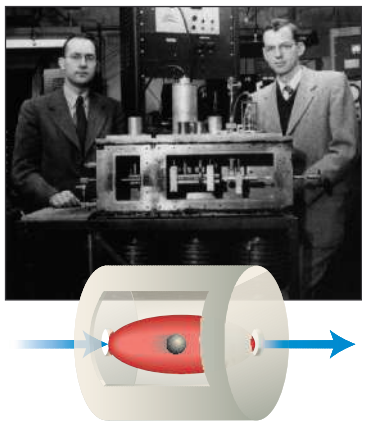

Masers then and now. (**Top**) Inventors Charles Townes (left) and James Gordon pose with the first maser, which used large ensembles of ammonia molecules. (**Bottom**) The Rydberg maser can sustain active maser oscillation with, on average, 1 or less atoms streaming through the resonant cavity at any given time.

The hydrogen maser, first demonstrated by Ramsey and colleagues in 1960 (*3*), was later developed by several groups into a high-stability active oscillator of outstanding robustness and reliability. It uses the hyperfine transition of ground state atomic hydrogen (the "21-cm line" of radio astronomy) to produce 1.42-GHz radiation. Atomic beams are used to create a steady flow of population-inverted hydrogen atoms into a storage bulb inside a microwave cavity that is resonant with the desired hyperfine transition. The inside wall of the bulb is coated with Teflon, which interacts weakly with hydrogen atoms. During the time of their stimulated emission, the atoms make thousands of bulb crossings, thereby averaging out inhomogeneities and enabling a narrow spectral width of ~1 Hz in the hyperfine transition.

The hydrogen maser produces a microwave output signal that is highly stable for seconds to hours. Hydrogen masers are large devices (the size of a small refrigerator), but can operate with minimal maintenance for many years in typical room conditions. They serve as "workhorse" high-stability oscillators for ensembles of atomic clocks in standards laboratories, tests of relativity and fundamental physical laws, very long baseline interferometry for radio astronomy, measurements of continental drift, and—together with the ruby maser amplifier—navigation and tracking of spacecraft in NASA's Deep Space Network of radio antennae in Australia, California, and Spain.

In recent decades, a novel form of maser—the Rydberg maser—has been developed and used in careful studies of the quantum mechanics of interacting atoms and photons (*4*). Unlike most masers, the Rydberg maser uses strongly interacting electric dipole transitions between two metastable states (typically separated by tens of gigahertz) in "Rydberg atoms," in which a single electron is in a highly excited electronic quantum state far from the atomic core. A population inversion is created by sending a beam of Rydberg atoms in the higher energy metastable level through a resonant cavity that is made of superconducting metal and maintained at very low temperatures. The combination of a strongly interacting electric dipole transition and a cavity that ensures very low losses enables active maser oscillation with very few atoms in the cavity.

With recent advances in Rydberg maser technology, the average number of atoms in the microwave cavity can be 1 or less while maintaining active maser oscillation (see the figure, bottom). This "one-atom maser" is a powerful tool in the field of cavity quantum electrodynamics—for example, in the preparation of pure-photon-number states (that is, states containing a specific number of photons) (*5*). The one-atom maser is currently being applied to the study of new techniques and protocols for manipulating quantum information, such as controllably creating quantum correlations among chains of atoms. Such "entangled" states might be used in future quantum computers.

In recent years, masers have also been used in sensitive searches for new phenomena suggested by leading theories of quantum gravity, such as string theory and loop quantum gravity. These theories suggest that quantum fields may have "frozen out" soon after the Big Bang and still permeate the universe. These "background" fields can give an orientation and velocity dependence to the properties of matter and light, and as such would constitute a violation of Lorentz symmetry (*6*). Sensitive measurements could reveal a faint echo of quantum gravity through a temporal modulation of basic physical properties—such as the speed of light, the mass difference of particles and their antiparticles, and the Zeeman splitting of atomic spin energy levels—when the orientation and velocity of the laboratory are changed relative to the background quantum fields.

One of the most sensitive searches for such effects has been performed at audio frequencies with colocated noble gas Zeeman masers (*7*). Population inversions on the nuclear spin transitions of ^{3}He and ^{129}Xe atoms are created in a separate chamber by spin-exchange collisions with optically pumped Rb vapor, followed by diffusion of the state-selected ^{3}He and ^{129}Xe atoms into the maser chamber. The use of two colocated species largely eliminates the confounding effects of magnetic fields. Also, noble gases interact very weakly during collisions with walls or other atoms; thus, noble gas masers can have narrow spectral widths of ~10^{-3} Hz. They have been used to probe for sidereal modulations of the ^{3}He and ^{129}Xe Zeeman splitting down to ~5×10^{-8} Hz, with no such effect yet observed. This sensitive measurement sets a limit of less than 10^{-31} GeV on the magnitude of the coupling of the neutron to background quantum fields—about 50 orders of magnitude below the Planck scale (the energy scale of ~10^{19} GeV at which quantum gravity effects are expected to become dominant).

Ongoing efforts to improve the sensitivity of masers and related devices may soon enable an improvement of several more orders of magnitude in tests of Lorentz symmetry. These advances may provide severe constraints for string and other theories of quantum gravity, and may even usher in an era of quantum gravity as a laboratory science.

References

1. J. P. Gordon, H. J. Zeiger, C. H. Townes, *Phys. Rev.* **95**, 282 (1954).
2. K. R. Chu, *Rev. Mod. Phys.* **76**, 489 (2004).
3. H. M. Goldenberg, D. Kleppner, N. F. Ramsey, *Phys. Rev. Lett.* **5**, 361 (1960).
4. J. M. Raimond, M. Brune, S. Haroche, *Rev. Mod. Phys.* **73**, 565 (2001).
5. B. T. H. Varcoe, S. Brattke, M. Weidinger, H. Walther, *Nature* **403**, 743 (2000).
6. See http://physics.indiana.edu/~kostelec/faq.html for an extensive list of references for this emerging field.
7. D. Bear *et al.*, *Phys. Rev. Lett.* **85**, 5038 (2000).
8. G. Makhov, C. Kikuchi, J. Lambe, R. W. Terhune, *Phys. Rev.* **109**, 1399 (1958).

ECOLOGY

Keeping an Eye on the Neighbors

Steven Buskirk

For decades ecologists have sought to understand the principles underlying how mammals optimize their space requirements. It is intuitive that mammals need home ranges: areas they routinely traverse that are large enough to meet their energy needs, but small enough to be protected from intrusions by same-species neighbors that occupy adjacent home ranges. Early attempts to understand the relation between body mass and home-range area suggested that home-range area increases at the same rate as metabolism (*1*). As metabolic rate is proportional to body mass raised to the $^3/_4$ power, then home-range size should also have the same proportion to body mass (*2*). However, abundant data on the home ranges of mammals, primarily derived from wildlife telemetry studies, suggest that this is not the case. Indeed, the home-range area increases at a higher rate than metabolic rate and, in fact, scales almost linearly with body mass (*3*, *4*). Yet parallel evidence from mammalian population density studies is consistent with a metabolic explanation of individual spatial requirements in that the reciprocal of population density (area per animal) appears to scale to the $^3/_4$ power of body mass (*5*). As large mammals have home ranges bigger than would be predicted from their energetic needs, this implies a maintenance cost that goes beyond the acquisition of essential resources. On page 266 of this issue, Jetz and co-workers (*6*) coalesce all of these findings by deriving a general model of mammalian spatial requirements that incorporates body mass, energy requirements, home-range size and, crucially, interactions with same-species neighbors. Cleverly, the authors use an equation from physics for collisions among gas particles to predict the frequency of interactions between home-range owners and intrusive neighbors. They show that large mammals require a home range that is larger than predicted by resource needs because they share resources with their neighbors to a greater extent than do small mammals (see the figure). This forced sharing is the result of body size–dependent processes, such as whether the mammal is able to traverse its home range often enough to exclude its neighbors.

Jetz *et al.*'s general approach falls within the realm of allometric macroecology, which attempts to explain biological differences among species by examining patterns over a wide range of body sizes (*7*). For terrestrial mammals, this range is represented by the six orders of magnitude that separate the body masses of shrews and elephants. Metabolic rate, the most fundamental of physiological attributes, was shown by Kleiber (*1*) to be proportional to the $^3/_4$ power of body mass in mammals across an entire range of body sizes, rather than the $^2/_3$ power predicted by a simple surface area to volume relation. Recently the $^3/_4$ exponent was derived from first principles by West and co-workers (*8*). Home range is one of the most integrative of ecological variables, and so several confounding factors must be taken into account when calculating home-range size. For example, carnivores have larger home ranges than do herbivores of the same size, so that data sets in which trophic level and body size are correlated produce biased scaling exponents. Species living at high latitudes and altitudes have disproportionately larger home ranges, so correlations between body size or trophic level and latitude must be considered. In addition, the fact that sociality varies with body size in mammals needs to be taken into account. Large mammals, such as moose, giraffes, elephants, and bison, tend to live in groups; shrews and mice are mostly solitary. Thus, for large mammals, a group of animals needs to be considered as the "occupant" of the home range.

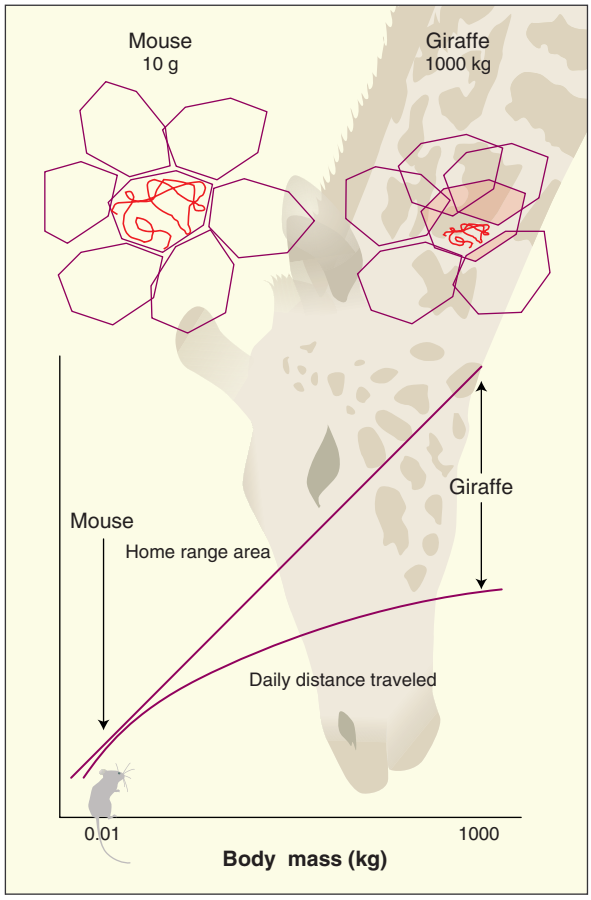

The mathematics of personal space. The ability of mammals to traverse their home ranges (polygons) and exclude same-species neighbors scales with body size. Small mammals, such as the mouse, cover their home ranges (red path) in a short time, interact with neighbors, and maintain exclusive home ranges. Large mammals, such as the giraffe, take longer to cover their home ranges, so that frequent interactions with neighbors is impossible. As a result, large mammals are unable to maintain an exclusive home range and must share parts of the home range (pink shaded area) and resources with intrusive neighbors. Such forced sharing means that the home ranges of larger mammals need to be bigger than that predicted from their resource requirements.

CREDIT: PRESTON HUEY/*SCIENCE*

The most problematic factor, however, is the allometric dependence of home-range maintenance behaviors, including interactions by occupants—individuals or groups—with same-species neighbors. These interactions temporarily deter neighbors from forays into the occupant's home range, so that home-range overlap is reduced. The more frequently an occupant patrols its home range, the better the opportunity to maintain the exclusivity of the home range, and limit home-range size to the energetic optimum. The ability to traverse the home range and deter visits by neighbors decreases rapidly with increasing body size: Daily distance traveled scales with a body-size exponent $^1/_4$ of that for home-range area. So, large mammals are unable to cover the home range often enough to exclude their neighbors (see the figure). Sharing parts of the home range with neighbors means sharing resources, necessitating a larger home range to ensure that energy requirements are met. It might seem that home-range boundaries would completely break down at

The author is in the Department of Zoology and Physiology, University of Wyoming, Laramie, WY 82071, USA. E-mail: marten@uwyo.edu

some body size, but such a shift to nomadism has not been observed.

An ingenious aspect of the approach taken by Jetz *et al*. is their adaptation of a model of molecular collisions in gas to the allometry of encounters between home-range occupants and their neighbors. In the adapted model, frequency of interaction is a function of population density, speed of movement, and the distance at which two animals may be said to have "collided"—that is, the interaction distance. They evaluated each of these factors with regard to its potential relation to body size. In the case of the interaction distance, evidence is accumulating that mammals detect and communicate with each other at distances that scale with a body-mass exponent of less than 1 (*9*). Previous workers (*4*) have not considered the scaling of interaction distance, but Jetz and co-workers assume that a body-mass exponent of $^1/_4$—typical for ecological distances—might approximate this relation. Using this value, home-range size should be proportional to body mass raised to the power of 1, which is very close to the observed values.

Jetz and co-workers have made the most recent contribution to the emerging field of metabolic ecology (*7*), which aims to explain population, landscape, and ecosystem patterns in terms of basic mathematical and physical principles. They also have resolved long-standing confusion about how to scale the spatial needs of mobile animals. Their elegant model will guide future exploration and hypothesis testing in this area. An important remaining task is to more accurately measure the scaling of neighbor detection—that is, the maximum distance apart that mammals of different sizes can be and yet still detect their same-species neighbors. Happily, the Jetz study is not without implications for conservation. Those planning viable mammalian populations should attend more closely to the scaling of population density than to the scaling of home-range size. Concentrating on the scaling of home-range size, a common approach, drastically overestimates the spatial requirements for populations. This unnecessarily constrains planning for viable mammalian populations, especially of the largest mammals.

References

1. M. Kleiber, *The Fire of Life* (Wiley, New York, 1961).
2. B. K. McNab, *Am. Nat.* **97**, 133 (1963).
3. A. S. Harestad, F. L. Bunnell, *Ecology* **60**, 389 (1979).
4. S. L. Lindstedt *et al.*, *Ecology* **67**, 413 (1986).
5. J. Damuth, *Biol. J. Linn. Soc.* **31**, 193 (1987).
6. W. Jetz *et al.*, *Science* **306**, 266 (2004).
7. J. H. Brown *et al.*, *Ecology* **85**, 1771 (2004).
8. G. B. West *et al.*, *Science* **276**, 122 (1997).
9. R. A. Kiltie, *Funct. Ecol.* **14**, 226 (2000).

DEVELOPMENT

ES Cells to the Rescue

Kenneth R. Chien, Alessandra Moretti and Karl-Ludwig Laugwitz

Unlocking the therapeutic potential of embryonic stem (ES) cells has remained a tantalizing but elusive goal. In this new era of "regenerative medicine," the central experimental game plan has been predicated on driving the differentiation of ES cells along specific cell lineages (for example, neural, cardiac, endocrine), expansion and purification of the cell type of interest, and in vivo repopulation of damaged or degenerating organs by ES cell–derived differentiated cells. However, there are numerous hurdles to using ES cells as therapeutic tools. These include the need for reliable ES cell differentiation protocols for different cell lineages, purification techniques for the differentiated progeny, as well as ways to circumvent the immunological rejection of transplanted cells. Given the complexity of these multiple steps, it is not surprising that there are few clear examples of in vivo ES cell therapy for treating disease-related phenotypes. On page 247 of this issue, an exciting new study by Fraidenraich and co-workers (*1*) expands the potential therapeutic repertoire of ES cells (*2*). These investigators provide direct evidence that ES cells can rescue otherwise lethal cardiac defects in mouse embryos. Intriguingly, the rescue effect is not subject to the differentiation of ES cells into the cardiac cell lineages that are normally associated with heart regeneration. Rather, the therapeutic effect of the transplanted ES cells depends on their secretion of defined factors that act either locally within the embryonic heart, or at a distance via the maternal circulation, to trigger fetal myocyte proliferation in utero.

In the new study, Fraidenraich and colleagues (*1*) report a prominent cardiac phenotype in mouse embryos that harbor a double or triple deletion (knockout) of the *Id1*, *Id2*, and *Id3* genes. The proteins encoded by these genes are transcriptional regulators that affect the differentiation of multiple cell types. The mutant Id embryos die at mid-gestation due to a marked thinning of the myocardial wall. This cardiac defect has been found in a number of mutant mouse embryos, including those lacking RXR-α (*3*–*5*), gp 130 (*6*), or other signaling proteins (*7*). In all of these cases, the signals that link these proteins to thinning of the myocardial wall appear to arise from noncardiac muscle cells, and many of these proteins are not expressed in myocardial cells. Previously, approaches such as chimera rescue (*8*) and cardiac lineage–restricted knockout of target genes (*9*, *10*) indicated that a non–cell autonomous pathway causes the onset of "thin myocardial wall" syndrome (that is, the defect does not involve myocardial cells). Indeed, several of these studies implicate another section of heart tissue called the epicardium in myocardial wall thinning (see the figure).

In the new work, Fraidenraich and coworkers report that their mutant Id mouse embryos display a loss of myocardial proliferative capacity, and marked dysregulation of a panel of cardiac genes revealed by gene profiling (*1*). The *Id* gene family is not expressed in the myocardium, but is expressed in the epicardium. The investigators note that conditioned medium from primary cultures of epicardial cells derived from wild-type embryos rescue the proliferative defect in cultured heart cells from the mutant mice. In contrast, conditioned medium derived from the Id mutant embryos had no activity, showing that the rescue effect is specific. Their chimeric embryo studies also support a non–cell autonomous pathway that links the loss of Id signals from outside the myocardium with the cardiac defect. The authors found that injection of mutant blastocyst embryos with as few as 15 wild-type ES cells rescued a subset of the cardiac defects and prevented death of the embryos. Surprisingly, the authors go on to show that the intraperitoneal injection of ES cells into female mice prior to conception also partially rescued the cardiac phenotype and prevented embryonic lethality (see the figure). A brain vascular defect that causes brain hemorrhaging also was rescued, suggesting that the secreted rescue factors act from a distance on at least two distinct target tissues of the embryo. By using ES cells with reduced *Id* gene expression, the authors show that the rescue effect is specific for Id-related pathways. Through microarray analyses, they went on to pinpoint two factors that exhibit partial rescue of the cardiac defect: Wnt5a and IGF-1 (insulin-like growth factor 1). Wnt5a is a local paracrine factor produced in the epicardium of the fetal heart that directly promotes the proliferation of neighboring embryonic cardiac

The authors are in the Institute of Molecular Medicine, University of California San Diego, La Jolla, CA 92037, USA. E-mail: kchien@ucsd.edu

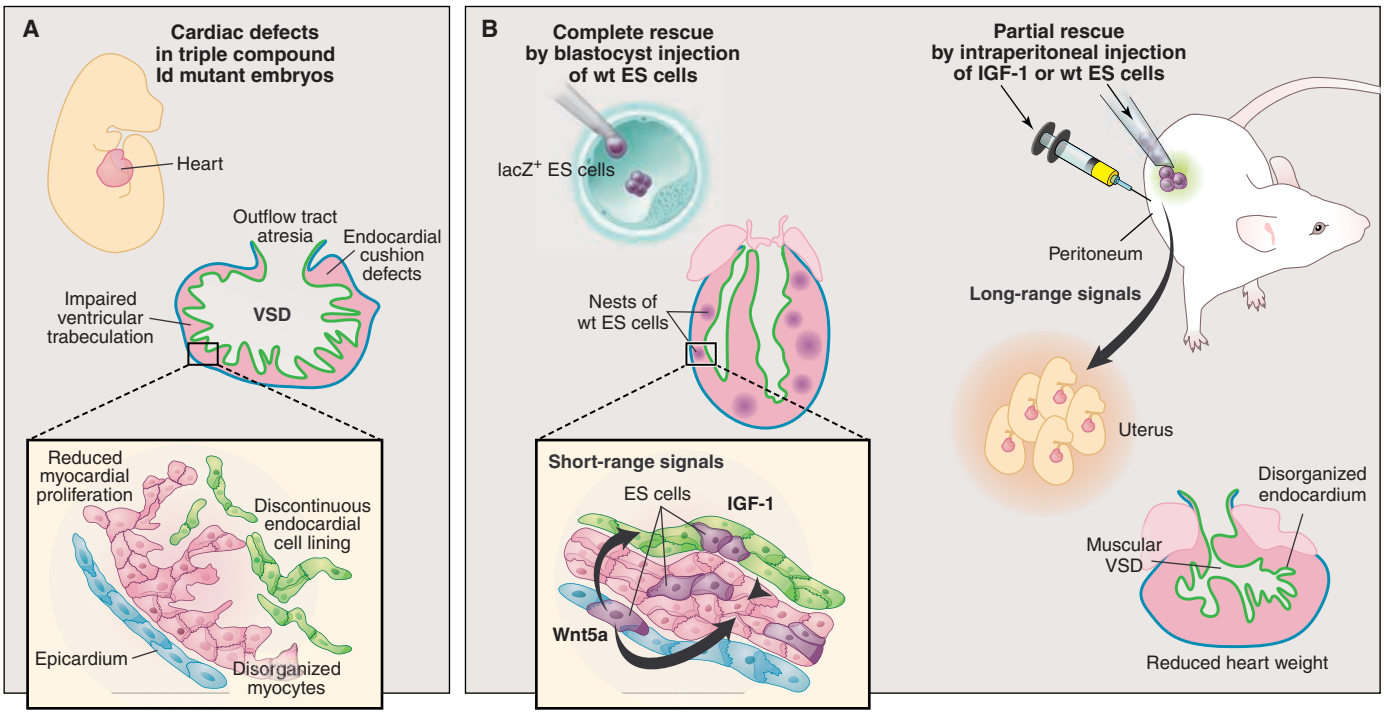

Rescue of cardiac malformations in mutant mouse embryos by ES cells. (**A**) Embryos lacking the *Id1*, *Id2*, and *Id3* genes display multiple cardiac abnormalities and die around embryonic day 13.5. The complex cardiac phenotype includes ventricular septal defects (VSD), thinning of the myocardial wall, outflow tract atresia, and endocardial cushion defects. Additionally, these hearts display reduced cell proliferation by disorganized sheets of myocytes and a discontinuous endocardial lining. (**B**) Injection of a small number of wild-type (wt) ES cells carrying a lacZ marker into Id mutant blastocysts resulted in about 20% chimerism of heart tissue and complete rescue of the Id mutant phenotype. Intraperitoneal injection of wild-type ES cells into female mice (*Id1*–/–, *Id3*+/–) prior to conception that were mated with males (*Id1*–/–, *Id3*+/–) partially rescued the cardiac phenotype of Id mutant embryos without incorporation of ES cells into the fetal heart tissue. Short- and long-range signals emanating from the ES cells reversed the myocardial defect in a non–cell autonomous manner. Two signaling molecules secreted by ES cells—Wnt5a, a locally secreted factor, and IGF-1, a bloodstream factor that promotes myocyte proliferation—were identified as potential candidates involved in the rescue process.

muscle cells. IGF-1, secreted by ES cells implanted in the maternal peritoneal cavity, crosses the placenta and triggers myocardial proliferation. The Fraidenraich *et al*. study provides the first clear demonstration of ES cell–based rescue of an embryonic lethal cardiac defect in vivo via defined secreted factors. ES cells may serve as a source to identify factors that can rescue defined disease-related phenotypes.

Given the potential of ES cells to induce the formation of teratomas (defective embryonic tissue), these findings do not necessarily suggest that administering ES cells to pregnant mothers will become a new therapeutic approach for treating congenital heart disease. However, given that a subset of maternal factors can cross the placenta, there remains a possibility that a subset of embryonic cardiac defects could be partially corrected by the careful delivery of the necessary proteins in the maternal circulation. Increasingly, congenital heart defects can be diagnosed accurately in utero with noninvasive imaging technology (*11*). In addition, ES cell–based assay systems may ultimately allow for the identification of likely candidate maternal factors that could correct a subset of severe human congenital heart defects.

For those of us interested in the potential of stem cell therapy for treating adult heart disease, the Fraidenraich *et al*. study serves as a sort of scientific parable. We may need to move beyond the design of binary experiments that simply evaluate whether the transplantation of bone marrow or mesenchymal-derived stem cells rescues cardiac dysfunction. Instead, we should seek an understanding of whether any observed beneficial effect reflects the real transdifferentiation of stem cells into viable cardiac muscle cells, or whether the beneficial effect is due to the secretion of therapeutic factors that trigger desirable surrogate phenotypes, such as neoangiogenesis, contractility, physiological hypertrophy, or improved myocardial survival following acute injury. Approaches similar to those used by Fraidenraich *et al*. for ES cell rescue of an embryonic cardiac defect could be taken to identify the molecular basis for any potential therapeutic effect of stem cell transplantation in the adult heart (*12*–*14*). Recent studies have documented a relatively low or perhaps negligible level of transdifferentiation of bone marrow progenitor cells into viable cardiac muscle in multiple experimental model systems of cardiac injury (*15*–*18*). Consequently, a renewed effort should be placed on studies to determine whether secreted factors from these cells could form the mechanistic basis for the in vivo rescue of heart failure. Modern tools of bioinformatics, genomic databases, and microarrays could then be used to identify the factors. Ultimately, cell transplantation may be replaced by direct delivery of the factors responsible for the therapeutic effect. In this way, ES cells may fulfill the long-term promise of cardiovascular stem cell therapy for treating adult cardiac diseases.

References

1. D. Fraidenraich *et al*., *Science* **306**, 247 (2004).
2. W. M. Rideout III *et al*., *Cell* **109**, 17 (2002).
3. H. M. Sucov *et al*., *Genes Dev.* **8**, 1007 (1994).
4. P. Kastner *et al*., *Cell* **83**, 859 (1995).
5. E. Dyson *et al*., *Proc. Natl. Acad. Sci. U.S.A.* **92**, 7386 (1995).
6. K. Yoshida *et al*., *Proc. Natl. Acad. Sci. U.S.A.* **93**, 407 (1996).
7. K. R. Chien, E. N. Olson, *Cell* **110**, 153 (2002).
8. C. M. Tran, H. M. Sucov, *Development* **125**, 1951 (1998).
9. J. Chen *et al*., *Development* **125**, 1943 (1998).
10. H. Hirota *et al*., *Cell* **97**, 189 (1999).
11. J. P. Kovalchin, N. H. Silverman, *Pediatr. Cardiol.* **25**, 299 (2004).
12. D. Orlic *et al*., *Nature* **410**, 701 (2001).
13. B. Assmus *et al*., *Circulation* **106**, 3009 (2002).
14. A. Bel *et al*., *Circulation* **108** (suppl.), 247 (2003).
15. L. B. Balsam *et al*., *Nature* **428**, 668 (2004).
16. C. E. Murry *et al*., *Nature* **428**, 664 (2004).
17. J. M. Nygren *et al*., *Nature Med.* **10**, 494 (2004).
18. K. R. Chien, *Nature* **428**, 607 (2004).

Avian H5N1 Influenza in Cats

Thijs Kuiken,* Guus Rimmelzwaan, Debby van Riel, Geert van Amerongen, Marianne Baars, Ron Fouchier, Albert Osterhaus

The relationship between avian influenza A virus and its hosts has changed markedly in recent years, with important consequences for human health (*1*). The most recent example is the 2003 to 2004 avian influenza A (H5N1) virus outbreak in Asia, which not only caused vast mortality in poultry, but also resulted in 39 officially reported cases of direct bird-to-human transmission, of which 28 were fatal (*2*). During this outbreak, there were also anecdotal reports of fatal H5N1 virus infection in domestic cats and zoo felids after they had fed on virus-infected chickens (*3*). This is unusual, because domestic cats are generally considered to be resistant to disease from influenza A virus infection (*4*).

To determine the pathogenicity of this virus for domestic cats, we experimentally infected 4- to 6-month-old European Shorthair cats with H5N1 virus by different routes and examined them by virological and pathological techniques. Each group of cats was placed in a separate, negatively pressurized isolator.

First, we intratracheally inoculated three cats with 2.5×10^4 times the median tissue culture infectious dose ($TCID_{50}$) of a H5N1 virus isolated from a fatal human case in Vietnam (A/Vietnam/1194/04). The cats showed clinical signs, including significantly raised body temperature from 1 day post-infection (dpi) onwards ($P < 0.05$, one-way analysis of variance) (fig. S1) and decreased activity, protrusion of the third eyelid, conjunctivitis, and labored breathing by 2 dpi. One cat died unexpectedly at 6 dpi. The cats excreted virus by 3 dpi at relatively low titers (Fig. 1A), likely because the infection predominantly involved the lower respiratory tract. On necropsy at 7 dpi, they had multiple or coalescing foci of pulmonary consolidation (Fig. 1B), which consisted histologically of diffuse alveolar damage, resembling that from H5N1 virus infection in humans and nonhuman primates (Fig. 1C) (*5*). H5N1 virus infection was confirmed as the cause of these lesions by virus isolation and immunohistochemistry (Fig. 1D). In contrast, three cats inoculated with an influenza A (H3N2) virus isolate from a human case in the Netherlands (A/Netherlands/18/94)—the most prevalent subtype of influenza A virus in humans—showed no evidence of virus infection or disease. These results show that this H5N1 virus can productively infect domestic cats, cause diffuse alveolar damage, and result in clinical disease or death.

Second, we tested whether cats could be infected with H5N1 virus through horizontal transmission by placing two sentinel cats in contact with the intratracheally inoculated cats above at 2 dpi. Third, we determined whether cats could by infected with H5N1 virus by feeding on virus-infected birds. To test this, we inoculated 1-day-old chicks intratracheally with 2.5×10^4 $TCID_{50}$ of H5N1 virus and, after euthanasia at 1 dpi, fed one chick to each of three cats. In both the sentinel cats and the cats fed on infected chicks, virus excretion (Fig. 1A), clinical signs (fig. S1), and pulmonary changes were similar to those of intratracheally inoculated cats. In contrast, two cats fed on chicks inoculated with phosphate-buffered saline (PBS) solution showed no evidence of virus infection or disease (Fig. 1, A to D, and fig. S1). These results show that cats can be infected with H5N1 virus both by horizontal transmission and by feeding on virus-infected birds.

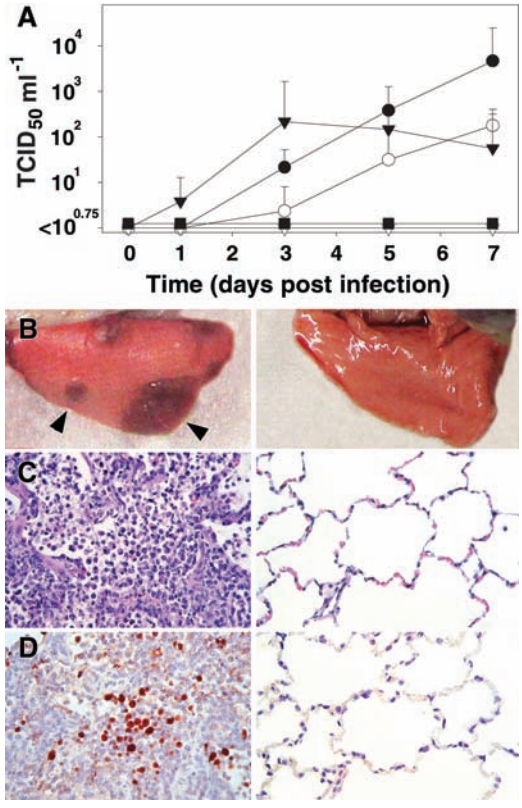

Fig. 1. Virus excretion and pulmonary lesions in cats infected with influenza A (H5N1) virus. (**A**) Pharyngeal virus excretion (mean and standard deviation) in cats inoculated with H5N1 virus either intratracheally (solid circles), by contact with H5N1 virus–inoculated cats (open circles), or by feeding on chicks inoculated with H5N1 virus (solid triangles). Control animals were either fed chicks inoculated with PBS solution (open triangles) or inoculated intratracheally with H3N2 virus (solid squares). (**B** to **D**) Left: The lung of a cat fed with an H5N1 virus–inoculated chick has (B) multiple foci of consolidation (arrowheads), consisting histologically of (C) diffuse alveolar damage, with (D) expression of influenza virus antigen in inflamed tissue, shown by immunohistochemistry. Right: The lung of a cat fed with a PBS-inoculated chick.

The implications of these findings are, first, that during H5N1 virus outbreaks, domestic cats are at risk of disease or death from H5N1 virus infection, either because of feeding on infected poultry or wild birds (*6*) or because of contact with infected cats. Second, the role of cats in the spread of H5N1 virus between poultry farms, and from poultry to humans, needs to be reassessed. Third, cats may form an opportunity for this avian virus to adapt to mammals, thereby increasing the risk of a human influenza pandemic.

References and Notes

1. R. J. Webby, R. G. Webster, *Science* **302**, 1519 (2003).
2. World Health Organization, "Confirmed human cases of avian influenza A (H5N1), 7 September 2004," available at www.who.int/csr/disease/avian_influenza/country/cases_table_2004_09_07/en/print.html.
3. ProMED Mail, "Avian influenza H5N1, mammals—East Asia" (Archive number 20040221.0560, 21 February 2004), available at www.promedmail.org.
4. V. S. Hinshaw, R. G. Webster, B. C. Easterday, W. J. Bean Jr., *Infect. Immun.* **34**, 354 (1981).
5. G. F. Rimmelzwaan *et al.*, *J. Virol.* **75**, 6687 (2001).
6. K. M. Sturm-Ramirez *et al.*, *J. Virol.* **78**, 4892 (2004).
7. We thank W. Lim for kindly providing the H5N1 virus isolate, W. Beyer for assistance with statistical analysis, and T. Bestebroer, E. de Wit, R. Dias d'Ullois, F. Read, and F. van der Panne for technical assistance. R.F. is a fellow of the Royal Dutch Academy of Arts and Sciences. This study was partly funded by the EU Framework V program Novaflu.

Supporting Online Material
www.sciencemag.org/cgi/content/full/1102287/DC1
Fig. S1

2 July 2004; accepted 6 August 2004
Published online 2 September 2004;
10.1126/science.1102287
Include this information when citing this paper.

Department of Virology, Erasmus Medical Center, 3015 GE Rotterdam, Netherlands.

*To whom correspondence should be addressed. E-mail: t.kuiken@erasmusmc.nl

Controlling the Dynamics of a Single Atom in Lateral Atom Manipulation

Joseph A. Stroscio* and Robert J. Celotta

We studied the dynamics of a single cobalt (Co) atom during lateral manipulation on a copper (111) surface in a low-temperature scanning tunneling microscope. The Co binding site locations were revealed in a detailed image that resulted from lateral Co atom motion within the trapping potential of the scanning tip. Random telegraph noise, corresponding to the Co atom switching between hexagonal close-packed (hcp) and face-centered cubic (fcc) sites, was seen when the tip was used to try to position the Co atom over the higher energy hcp site. Varying the probe tip height modified the normal copper (111) potential landscape and allowed the residence time of the Co atom in these sites to be varied. At low tunneling voltages (less than ~5 millielectron volts), the transfer rate between sites was independent of tunneling voltage, current, and temperature. At higher voltages, the transfer rate exhibited a strong dependence on tunneling voltage, indicative of vibrational heating by inelastic electron scattering.

Manipulation of single atoms and molecules on surfaces with the use of a scanning tunneling microscope (STM) (*1*) encompasses lateral processes, which transfer atoms and molecules parallel to the surface, as well as vertical processes, which transfer atoms and molecules between the tip and surface (*2*). Lateral atom manipulation experiments (*1*, *3*, *4*) and theory (*5*, *6*) have focused on the importance of the tunable chemical bond interaction between the tip and adatom, whereas vertical manipulation experiments (*7*, *8*) and theory (*9*–*12*) stress the importance of inelastic electron tunneling in stimulating atom transfer via vibrational excitation of the adatom-substrate bond. Vibrational excitation induced by tunneling electrons has also been used to induce rotations of single molecules (*13*).

We report a study of the dynamics of a single metal atom during lateral manipulation. We first discuss the dynamics of the manipulated Co atom in the context of a novel type of STM image—which we refer to as a "manipulated atom" image—that reveals the binding sites of the substrate. This image is obtained by the rastering of a Co atom over the Cu(111) surface, using the tip-induced local potential to trap the Co atom under the rastering probe tip. We then study the dynamics of the manipulated Co atom, which switches between neighboring (and almost equivalent) fcc and hcp sites of the Cu(111) surface at cryogenic temperatures. This switching appears as a periodic noise pattern in the manipulated atom images and as telegraph noise in tunnel current measurements. Measurements of the atom transfer rate as a function of tunneling current and tip height show the importance of vibrational excitation via inelastic electron tunneling in lateral atom manipulation. We demonstrate detailed control of single-atom switching by tuning the local potential landscape with the tip-adatom interaction. The control we can obtain suggests the development of sophisticated procedures to facilitate bond-breaking and greatly enhance lateral atom manipulation processes.

Listening to atoms move. We studied the lateral manipulation of a Co atom residing on a single-crystal Cu(111) surface (Fig. 1A) (*14*). On this surface, the fcc site has no Cu atom below it in the lower Cu layer and, as a consequence, is energetically favored over the hcp site as a binding site for Co (*15*, *16*).

Imaging with the STM typically places the probe tip sufficiently far from the sample so that tip-sample interactions do not initiate atomic movement. To move a Co adatom (fig. S1A) (*17*), we first bring the tip closer to the adatom by adjusting the tunneling junction resistance R (R is set by the ratio of the tunneling voltage V to the tunneling current I). This interaction creates a highly localized potential well that traps the adatom under the tip (*2*). For simple point-to-point adatom repositioning, the STM tip first moves laterally to the adatom while at the greater tip height Z used in normal STM imaging, where Z is the relative distance between the STM probe tip and the surface of the substrate. The STM then traps the adatom by decreasing R (decreasing Z), moves the tip laterally while maintaining I constant, and finally releases the adatom at the destination by reverting to the value of R used in normal imaging (increasing Z). As shown by Bartels *et al.* (*3*), recording Z while repositioning an adatom provides a measure of how well the adatom is following the tip motion.

The underlying atomic lattice is needed as a template to construct nanostructures by atom manipulation, but for the Cu(111) surface, it cannot be observed in a conventional tip height image (fig. S1A) (*17*) because of the very small electron lattice corrugation. We therefore devised what we call a manipulated atom image as a way to observe substrate lattice structure. We form this image by rastering the tip over the surface in the normal topographic imaging mode, except now with a Co adatom trapped in the moving tip–induced potential well that exists at lower R values (Fig. 2A) (fig. S1B) (*17*). Details, on a lateral scale of a fraction of a lattice constant, are visible in this manipulated atom image that cannot be seen in the normal STM image, even when such images are taken at the lower R values (fig. S1C) (*17*). The difference is that in a manipulated atom image, the trapped Co atom can move laterally relative to the tip in response to the local potential surface; this motion is recorded as changes in Z, because the STM servo is trying to maintain I constant. Using the motion of the Co atom to image the local binding sites is an example of a new class of measurements based on single-atom transducers sensing their local environments; we refer to this as "atom-based metrology."

Surprisingly, the manipulated atom image (Fig. 2A) shows three-fold symmetry with three distinct features, labeled A, B, and C, which is only possible if more than the top layer is contributing to the imaging process. At first glance, this image looks like a replica of the surface model of Cu(111) shown in Fig. 1A. However, a detailed analysis reveals that the binding site of Co on Cu(111) is always at the site labeled A in Fig. 2A in our low-temperature STM measurements. This fact—together with manipulated atom image measurements of Co on Cu(111) with different tips with various resolving functions, as well as atom-manipulation simulations (*6*)—indicates that the feature at A is an image of a

Electron Physics Group, National Institute of Standards and Technology, Gaithersburg, MD 20899-8412, USA.

*To whom correspondence should be addressed. E-mail: joseph.stroscio@nist.gov

stationary Co adatom at the fcc site (*15*, *16*). The Co atom remains stationary in the fcc site as the tip begins to move laterally (Fig. 1C); a lateral force begins to develop as the tip continues to move away from the Co atom (Fig. 1D). When the lateral force becomes large enough, the Co atom hops to the nearest binding site within the trapping range of the tip (Fig. 1E). This switching motion produces the manipulated atom image in Fig. 2A. This switching is unlike the so-called sliding mode of atom manipulation (*2*, *4*, *6*) in which the adatom follows exactly the tip motion at sufficiently low R. Instead, the Co atom does not precisely follow the tip (over the tunneling resistance range of 50 to 180 kilohms), but hops to the fcc or hcp binding site nearest the moving tip.

The maximum Z is roughly the same at the center of features A and B in Fig. 2A. Therefore, we assign feature B to Co in the hcp site, as one would expect from the geometric similarity of the fcc and hcp sites (Fig. 1A), which leaves the on-top site for assignment to feature C. Feature C is lower than features A and B, because the Co atom is unstable on the on-top site and switches to the nearest fcc site (site A in Fig. 2A), and the tip height decreases in response. This tip motion is borne out by simulations (*6*) and is similar to that observed in experiments of the manipulation of Ag atoms on Ag(111) (*4*). For these measurement conditions, the manipulated atom image can be thought of as a binding site image for Co on Cu(111). Note that in the manipulated atom images, site B, the hcp site, is noisy (Fig. 2A). This speckle suggests that a dynamic process is occurring at the hcp site during atom manipulation.

Audio-frequency components of the tunneling current have been monitored with an audio system and used as a real-time diagnostic of the atom manipulation process (*18*). The origin of such ''sounds'' in the tunneling current during atom manipulation has remained largely unexplored. In our work, an audio-frequency modulation of the tunneling current can be ''heard'' as a manipulated atom image is recorded (movie S1) (*17*). An examination of the tunneling current signal shows that the noise density increases when the Co atom is positioned over the hcp sites (Fig. 2B). It is this increase in current noise that gives rise to the ''sound'' of atom manipulation when the tunneling current is used to provide audio feedback.

To measure the current noise, we measured the time dependence of I (*19*) at the hcp site during a manipulated atom image, as in Fig. 2A. The tip position was held fixed at a selected lateral location on the surface by pausing the raster, and the tip height was fixed by disabling the STM servo. The tunneling signal was measured as a function of time for several values of V. After the measurement, the STM servo was turned back on and the raster was continued until another selected position was reached. The time dependence of I at two different locations (Fig. 3A) near the center of the hcp site is shown in Fig. 3, B and D. Random two-state telegraph noise, switching between a high level of ~35 nA and a low level of ~23 nA in Fig. 3B, results from the Co atom switching between the hcp site under the tip location and the nearest fcc site, labeled as #1 in Fig. 3A. The corresponding tunneling current distribution (Fig. 3C) shows that, for the choice of interaction parameters used in this measurement, the Co atom spends most of its time in the fcc site. The measurement in Fig. 3B was obtained at a location ~0.2 Å away from the center of the hcp site. Only two states were observed because the tip-

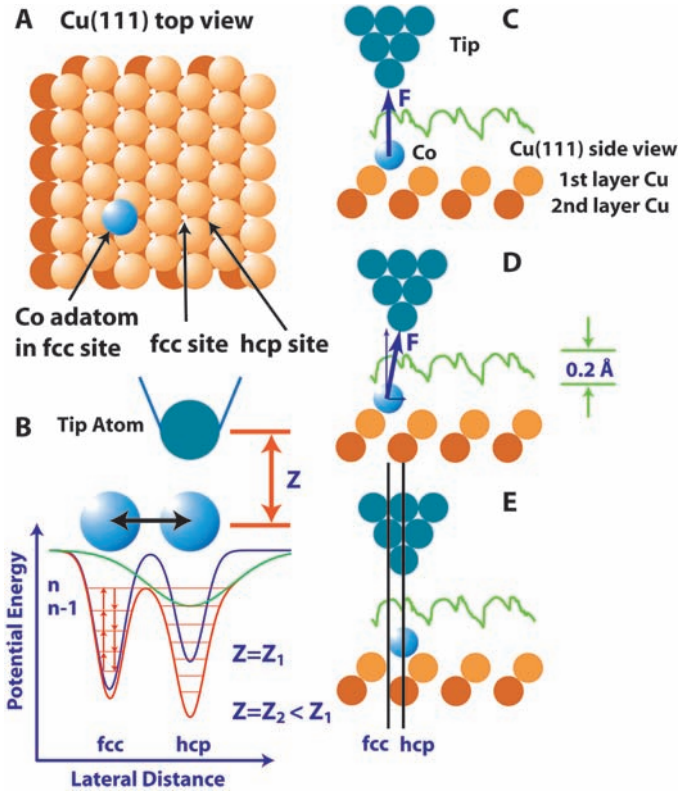

Fig. 1. (**A**) Top view of the Cu(111) surface with the Co adatom shown in its natural fcc binding site. (**B**) Schematic potential well for the Co atom in fcc and hcp sites: blue curve, native potential well, no tip-Co interaction; green curve, tip-induced potential well; red curve, native potential with added tip-induced potential. The potential at the hcp site increases in depth because of the increase in tip-Co interaction as the tip-Co distance decreases. The tip-induced potential well over the hcp site causes the Co atom to switch between the fcc and hcp sites, producing discrete changes in the tunnel current. (**C** to **E**) Schematic of manipulated atom tip height trace. Initially, with the tip over the fcc site, the force on the Co atom is vertical and the tip images the Co atom. As the tip moves down the side of the Co atom, a lateral force develops (D). When the tip reaches the hcp site, the lateral force is large enough to induce the Co atom to hop to the hcp site (E). The green curve is the measured tip height trace from the manipulated atom image in Fig. 2A.

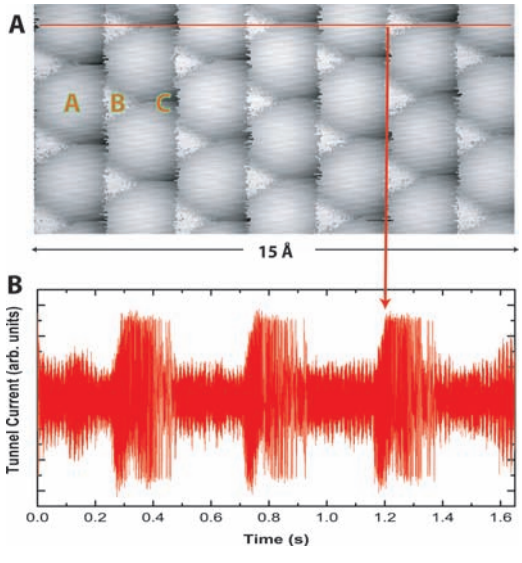

Fig. 2. (**A**) Manipulated atom image of Co over Cu(111) surface. Tunnel current, 50 nA; sample bias, –5 mV; T = 4.3 K. The labels A, B, and C denote fcc, hcp, and top sites, respectively. (**B**) Tunnel current recorded during manipulated atom image going through the hcp and fcc sites as indicated by the horizontal line in (A). The arrow shows the increased noise in the tunnel current corresponding to the position of the hcp site.

induced potential well is closest to the fcc site labeled #1 in Fig. 3A.

When the tip was positioned closer to the center of the hcp site (Fig. 3D), we observed four different levels in *I* corresponding to the Co atom switching between the hcp site and all three neighboring fcc sites. In the *I* distribution (Fig. 3E), a single high current level corresponds to the Co atom in the hcp site, but the lower *I* level splits into three sublevels corresponding to the fcc sites labeled #1 to #3. Note that the current transitions are always between the hcp level and an fcc level, and never between two fcc levels directly.

The data in Fig. 3 show that the tip–Co atom interaction modifies the unperturbed multiwell surface potentials, as shown schematically in Fig. 1B. Because we observed atom switching only with the tip at close tip–Co atom distances (low tunneling resistances), we can conclude that the original potential well at the fcc site is deeper than the original well at the hcp site, consistent with previous experiments and calculations (*15*, *16*). The presence of the tip–Co atom interaction deepens the potential well at the hcp site (Fig. 1B), which makes it favorable for the Co atom to switch back and forth at these temperatures. The residence times for each state can be varied from being predominantly at the fcc site to being predominantly at the hcp site by varying the strength of the tip–Co atom interaction. We next consider the exact mechanisms of atom switching for the case of an ideal double-well potential.

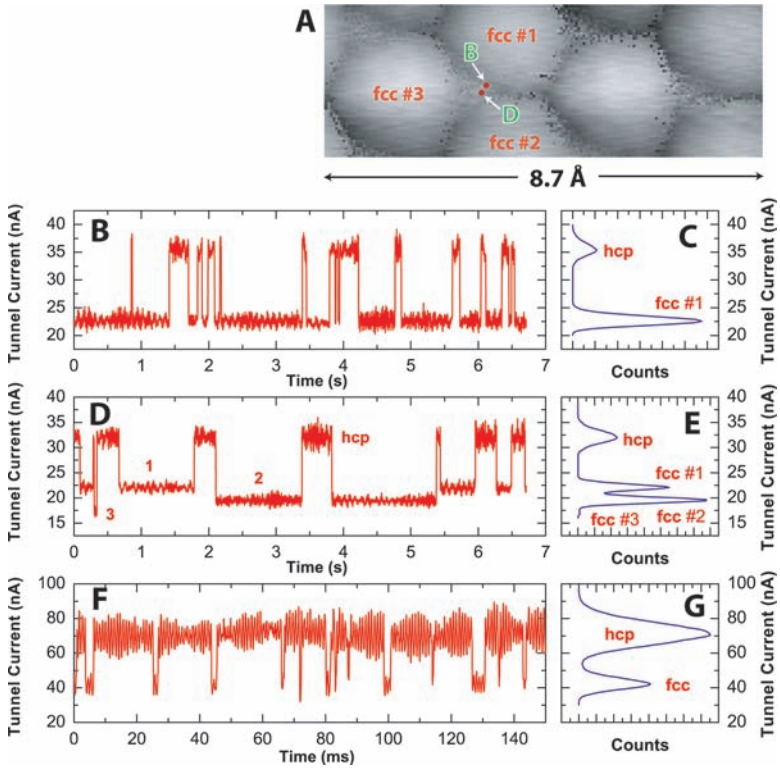

Fig. 3. (**A**) Co manipulated atom image on Cu(111). Tunnel current, 100 nA; sample bias, 11.0 mV; junction resistance, 110 kilohms; T = 2.3 K. (**B** and **D**) Tunnel current versus time measurements recorded at the positions indicated by the corresponding red spots in (A) near the hcp site. Sample bias, 3.3 mV. (**C** and **E**) The corresponding histograms of the current distributions. (**F**) Tunnel current versus time measurement showing two-state random telegraph noise near the hcp site for Co on Cu(111) measurement at junction resistance of 120 kilohms. Sample bias, 8.4 mV; T = 2.3 K. (**G**) Corresponding histogram of the current distribution.

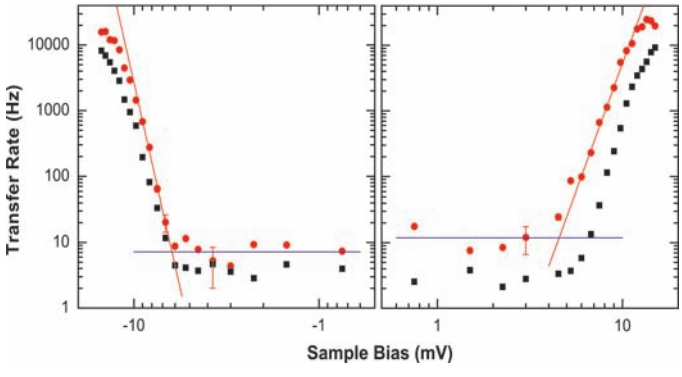

Fig. 4. Transfer rate versus sample bias at constant tip height, obtained by measuring the distribution of residence time in the hcp and fcc states from two-state random telegraph noise in the tunnel current. Junction resistance = 150 kilohms; T = 2.3 K. R_{hcp}, red circles; R_{fcc}, black squares. Solid red line shows a power-law fit to the initial threshold region; blue horizontal line shows the average transfer rate for the low-bias region for the hcp transfer rate.

An ideal two-state fluctuator. Two-state fluctuating systems are fundamental in the theory of $1/f$ noise in solids (*20*, *21*), but in many of these systems the exact identity of the two-state object is unknown. Here, we can use the STM probe tip to modify the potential landscape to create a known two-state fluctuating system on the basis of the position of a single atom.

Figure 3F shows random two-state telegraph noise, with its associated current distribution shown in Fig. 3G, for a measurement obtained at a tunneling voltage of 8.4 mV. The transitions are about an order of magnitude more frequent than in Fig. 3, B and C, where V was 3.3 mV. We examined this difference quantitatively by determining the average transition rate for the Co atom to switch sites from hcp to fcc, R_{hcp}, and from fcc to hcp, R_{fcc}. The Co atom has no memory of the time it spent at a given site; therefore, these events can be described by a two-state discrete Markov process with an exponentially distributed residence time probability density given by

$$P_{hcp,fcc}(t) = R_{hcp,fcc}\ \exp(-R_{hcp,fcc}t) \qquad (1)$$

(*20*). The residence time distributions for the hcp and fcc sites (fig. S2, A and B) (*17*) are well described by an exponential distribution, in agreement with Eq. 1. The transition rates were determined to be 184.6 ± 3.0 Hz and 568 ± 8.6 Hz (*22*) for the hcp and fcc sites, respectively, for the tunneling parameters used in the measurement.

The transfer rates for the two-state fluctuator, corresponding to a double-well potential of the hcp and fcc sites and measured at constant Z, span four orders of magnitude as the voltage is varied from 1 to 15 mV, which corresponds to a current variation of ~5 to 100 nA (Fig. 4) [see movie S2 to listen to audio recordings of this single-atom switching (*17*)]. The transfer rates are nearly symmetrical with tunneling voltage polarity and are characterized by two distinct regimes. For voltage magnitudes less than ~5 mV, the transfer rate is relatively independent of V followed by a crossover to a regime strongly dependent on V. This behavior is seen in all our measurements, irrespective of tunneling resistance, temperature, or tip used.

A model for the atom switching observed in Fig. 4 can be based on the theory developed to explain the vertical Xe atom switch experiment by Eigler *et al*. (*7*). A vibrational heating mechanism (*9*–*11*) was invoked to reproduce the power-law dependence observed in the Xe switch experiment. With vibrational heating, the atom overcomes the potential barrier through stepwise climbing of a vibrational ladder of the adatom-substrate bond excitations (Fig. 1B) through a competition between gaining energy from inelastic tunneling electrons and losing energy to electron-hole pairs and phonons. Gao *et al*. (*12*) showed that the power-law behavior results from an Arrhenius-like expression for the transfer rate,

$$R_{VH} \approx n\Gamma_{\uparrow} \exp[-(\tilde{V}_B/k_B T_v)] \qquad (2)$$

where Ω is 2π times the vibrational frequency, $\tilde{V}_B$ is defined as $(n-1)\hbar\Omega$ (which is close to the actual barrier height V_B), n is the number of vibrational levels in the well with spacing $\hbar\Omega$, $\Gamma_{\uparrow}$ and $\Gamma_{\downarrow}$ are the vibrational excitation and deexcitation rates between nearest neighbor levels of the harmonic oscillator potential (which contain a thermal contribution and a contribution due to inelastic electron tunneling), k_B is Boltzmann's constant, and $\hbar$ is Planck's constant divided by 2π. Because of the nonthermal population of the vibrational system excited through inelastic electron tunneling, the vibrational temperature $T_v = (\hbar\Omega/k_B)[\ln(\Gamma_{\downarrow}/\Gamma_{\uparrow})]^{-1}$ can be higher than the substrate temperature T. This model yields a transfer rate $R \propto I^n$ or V^n, because I and V are linearly related by the junction resistance. At lower I and V values, a crossover to a thermally activated regime is predicted (*12*) but has not been observed experimentally.

The transfer rate data in Fig. 4 do not follow a pure power law, varying as V^n, as predicted by the vibrational heating models. We found an initial fast turn-on of the transfer rate (Fig. 4). Fitting a power law to the hcp transfer rates for voltages between –7 and –9 mV gives an exponent of 12.5 ± 1.2 (*22*) (solid red line in Fig. 4). At higher V, the power-law behavior is followed by a gradual decrease in slope. In the vibrational heating model, deviations from a pure power law are expected when the inelastic tunneling rate, I_{in}/e, is comparable to the vibrational relaxation rate, γ. For our experiment, this crossover should occur at a total current of about 100 nA, taking $\gamma \approx 10^{10}$ s^{-1} (*12*, *23*) and the inelastic tunneling current to be 1% of the total current. This is approximately where we observe deviations from a pure power law (Fig. 4). Such deviations can also result from a number of competing paths for the barrier crossing, as discussed by Walkup *et al*. (*10*).

For applied potentials within ~5 meV of the Fermi energy, we observed a finite background rate of atom switching in the range of 1 to 20 Hz that is independent of tunneling voltage and current (Fig. 4). Two possible mechanisms for this transfer are thermal activation and quantum tunneling of the Co atom between the hcp and fcc sites. For thermal activation, a very strong variation of the transfer rate would be expected over the temperature range from 2 to 4 K (fig. S3A) (*17*), assuming preexponential factors corresponding to typical vibrational frequencies ranging from 10^{10} to 10^{13} Hz. However, the measurements shown in fig. S3, A and B (*17*) show relatively little variation in the transfer rate with T, requiring an alternate explanation.

Although quantum tunneling might seem improbable given the large mass of the Co atom, atomic-scale distances together with a barrier height less than ~50 meV can result in appreciable tunneling rates for large-mass atoms (*24*, *25*). The rate for quantum tunneling can be estimated with the Wentzel-Kramer-Brillouin (WKB) approximation,

$$R_{QT} = \nu \exp\{[-d(2mV_B)^{1/2}]/\hbar\} \qquad (3)$$

(*26*), where ν is on the order of the vibrational frequency, d is an effective distance between wells, m is the mass of the Co atom, and V_B is the potential barrier. With the barrier estimated from calculations (*15*), V_B = 37 meV, $\nu = 10^{12}$ s^{-1}, and d = 0.75 Å (*27*), we estimate a transfer rate of 30 Hz, which is comparable to the rate seen in our measurements for low V and supports the quantum tunneling mechanism for atom transfer in this regime.

Controlling atom dynamics. To gauge the importance of the tip-adatom interaction on the adatom dynamics, we varied the probe tip height Z at a constant V. For this measurement, we created a two-state fluctuator by pausing during a manipulated atom image when the Co atom was in the vicinity of the hcp site. At this location, while tunneling at the resistance used for the manipulated atom image, we turned the STM servo off to allow direct control of Z. We then recorded time sequence data of the tunneling current at a series of Z values set by positioning the tip with a calibrated piezo transducer.

As we increased Z, we expected a weaker tip-Co interaction to create a shallower potential well at the hcp site (Fig. 1B). An increase in Z corresponds to an increase in R and a reduction in I (fig. S4). The transfer rates, computed from the tunneling current time sequence data, depend strongly on Z both in the quantum tunneling and vibrational heating regimes (Fig. 5, A and B). The hcp rates (Fig. 5A) increased with Z, whereas the fcc rates (Fig. 5B) showed a similar decrease. The increases in the hcp rates may at first seem surprising, because the current is decreasing with Z and the transfer rate due to vibrational heating is a strong function of I. The explanation lies in the even stronger effect of the changes in the local potential energy surface, which leads to an increase in the transfer rate that overcomes the decrease in the transfer rate due to vibrational heating over the range of tip heights used in this measurement.

A series of current histograms plotted as a function of the tip height (Fig. 5C) shows

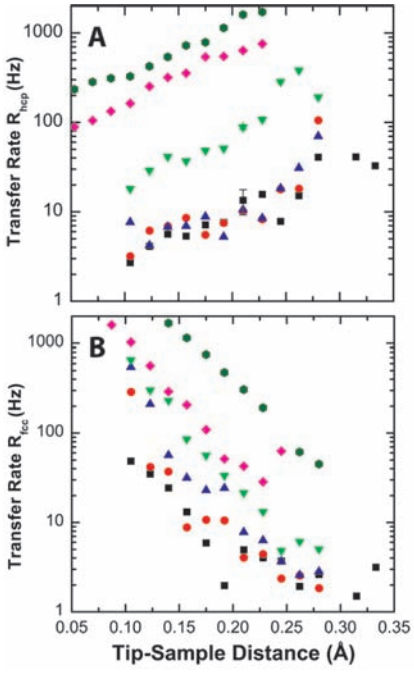

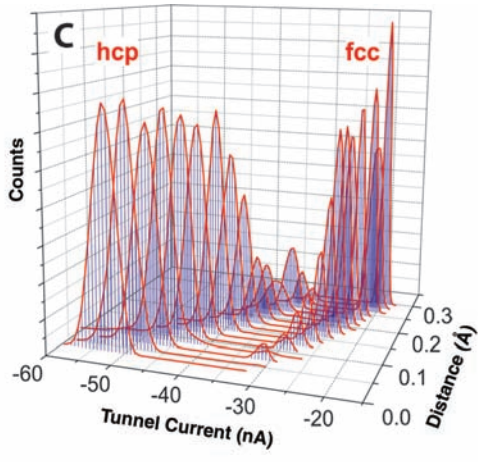

Fig. 5. (**A**) hcp transfer rate, (**B**) fcc transfer rate versus tip-sample distance at constant sample bias. Black squares, sample bias V = –5 mV; red circles, V = –6 mV; blue triangles, V = –7 mV; green inverted triangles, V = –8 mV; magenta diamonds, V = –9 mV; green circles, V = –10 mV. (**C**) Current distribution from two-state telegraph noise obtained near the hcp site during a Co manipulated atom measurement as a function of tip-sample distance. Zero tip-sample distance corresponds to the initial set point at junction resistance of 90 kilohms; Z = 0.35 Å corresponds to 180 kilohms (fig. S4). Sample bias, –5 mV; T = 2.3 K.

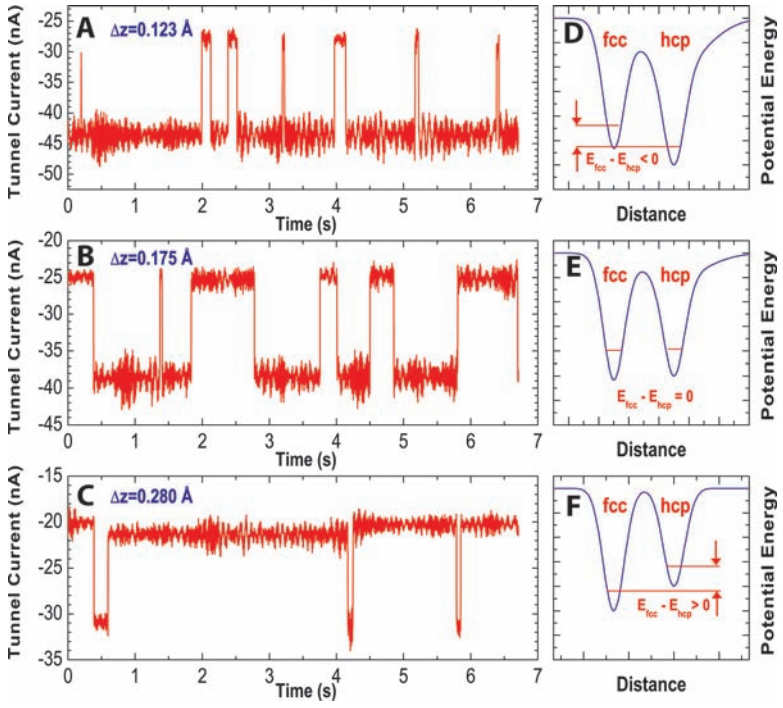

Fig. 6. Telegraph noise measurements near the hcp site during a Co manipulated atom measurement as a function of tip-sample distance. Tip-sample distance was increased (**A**) 0.123 Å, (**B**) 0.175 Å, and (**C**) 0.280 Å relative to the initial set point at junction resistance of 90 kilohms. Sample bias, –5 mV; T = 2.3 K. Corresponding current histogram distributions for these data are shown in Fig. 5C. (**D** to **F**) Schematic potential diagrams showing the relative variation of the potentials that give rise to the change in duty cycle between the hcp and fcc signals observed in (A) to (C).

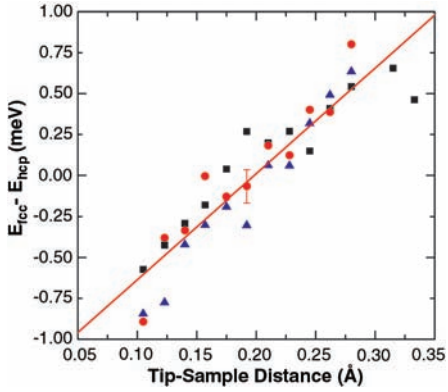

Fig. 7. Energy difference between the hcp and fcc potentials obtained from the detailed balance expression in Eq. 4, using the transfer rates for the hcp and fcc sites as a function of tip-sample distance. T = 2.3 K. The symbols correspond to separate measurements at different sample bias: squares, V = –5 mV; circles, V = –6 mV; triangles, V = –7 mV. The solid line is a linear fit to all three data sets.

that at low R the Co atom can be completely trapped in the hcp site. As Z is increased and the tip-adatom interaction weakens, the hcp population continuously decreases and the fcc population increases. Finally, at the largest Z the Co atom resides at the fcc site. Thus, the tip-adatom potential is strong enough to completely reverse the relative binding energy of the fcc and hcp sites (Fig. 6). Snapshots of the two-state telegraph noise are shown in Fig. 6, A to C, for the circumstances where the hcp potential is deeper than, approximately equal to, and higher than the fcc potential.

The difference in energy between the hcp-site and fcc-site ground states, schematically shown in Fig. 6, D to F, can be obtained from the measured transfer rates at low voltage (Fig. 5, A and B) by using the detailed balance condition

$$R_{\mathrm{fcc}} = \exp[-(E_{\mathrm{fcc}} - E_{\mathrm{hcp}})/k_{\mathrm{B}}T]R_{\mathrm{hcp}} \quad (4)$$

(*12*). Figure 7 shows the energy difference, which varies linearly with tip height with a slope of 6.5 ± 0.9 meV/Å (*22*). The data in Figs. 6 and 7 reflect an induced 2-meV shift in the relative energies of the hcp and fcc ground states. Although this corresponds to only a 5% variation of the 37-meV potential well depth (*15*), it is sufficient to completely reverse the binding characteristics of the two sites. This conveniently allows us to tune the atom switching to an appropriate time scale for observation and to ''listen'' to the atom dynamics within the audio range.

Conclusions. We have separately studied the two most important factors in atom manipulation: vibrational heating of the adatom-substrate bond and the tip-adatom interaction. We see how the tip-adatom potential effectively constrains the Co atom to within a nearest neighbor distance of the tip position. The tip-adatom interaction can be tuned to distort the potential surface and control the atom's dynamics. The vibrational excitation acts effectively to raise the atom within its potential well, bringing it closer to the activation barrier for transfer between sites. Control of the two independent processes of vibrational heating and guiding the adatom by tuning the potential landscape with the tip-adatom interaction can greatly enhance lateral atom manipulation processes and their applicability.

We believe the ability to control the transfer of a single atom between lattice sites can lead to the ability to switch and control electrical signals in atomic-scale devices built by atom manipulation. This capability expands on the concept of the atomic switch first discovered by Eigler *et al*. (*7*), where in the original geometry the atom switches vertically between the sample and tip. In a lateral atom switch, the metal atom can remain bound to the substrate, which allows it to control conductance through atomic-scale devices. A number of different atomic-scale devices can be realized given the ability to control a lateral single-atom switch (*28*). Of course, there are difficult challenges to overcome, such as extending these concepts to semiconductor substrates where the potential corrugations are larger, before the control of electrical conductance with this type of atomic switch is possible.

References and Notes

1. D. M. Eigler, E. K. Schweizer, *Nature* **344**, 524 (1990).
2. J. A. Stroscio, D. M. Eigler, *Science* **254**, 1319 (1991).
3. L. Bartels, G. Meyer, K.-H. Rieder, *Phys. Rev. Lett.* **79**, 697 (1997).
4. S. W. Hla, K.-F. Braun, K.-H. Rieder, *Phys. Rev. B* **67**, 201402 (2003).
5. X. Bouju, C. Joachim, C. Girard, *Phys. Rev. B* **59**, R7845 (1999).
6. A. Kühnle, G. Meyer, S. W. Hla, K.-H. Rieder, *Surf. Sci.* **499**, 15 (2002).
7. D. M. Eigler, C. P. Lutz, W. E. Rudge, *Nature* **352**, 600 (1991).
8. T. C. Shen *et al.*, *Science* **268**, 1590 (1995).
9. S. Gao, M. Persson, B. I. Lundqvist, *Solid State Commun.* **84**, 271 (1992).
10. R. E. Walkup, D. M. Newns, Ph. Avouris, *Phys. Rev. B* **48**, 1858 (1993).
11. M. Brandbyge, P. Hedegård, *Phys. Rev. Lett.* **72**, 2919 (1994).
12. S. Gao, M. Persson, B. I. Lundqvist, *Phys. Rev. B* **55**, 4825 (1997).
13. B. C. Stipe, M. A. Rezaei, W. Ho, *Science* **280**, 1732 (1998).
14. This system was realized experimentally as follows: A Cu(111) sample was cleaned by repeated cycles of Ne sputtering and annealing to 600°C while reflection high-energy electron diffraction was used to monitor sample quality. We then transferred the substrate, along with an Ir probe tip prepared using a field ion microscope, to a low-temperature STM. Co adatoms were then deposited onto the Cu(111) substrate at 7 K. All preparation, transfers, and measurements took place in an ultrahigh-vacuum system containing a low-temperature STM of our design that operates over a temperature range of 2.3 to 4.3 K.

15. D. V. Tsivlin, V. S. Stepanyuk, W. Hergert, J. Kirschner, *Phys. Rev. B* **68**, 205411 (2003).
16. V. S. Stepanyuk *et al.*, *Phys. Rev. B* **68**, 205410 (2003).
17. Video clips and additional data are available on *Science* Online.
18. Although we know of no mention in the published literature, we believe D. M. Eigler was the first to use the tunnel current for audio feedback during atom manipulation.
19. We measured the time dependence of I at the hcp site as a function of V at fixed Z, and as a function of Z at fixed V, during atom manipulation. These two measurements are interrelated through the tunnel junction relation (and elucidate different aspects of the switching dynamics), where, at low voltages, $I = V/R$, at fixed Z, and $I = A \exp(-2\kappa Z)$, for fixed V; here, κ is the tunneling barrier decay constant. See (*29*).
20. Sh. Kogan, in *Electronic Noise and Fluctuations in Solids* (Cambridge Univ. Press, Cambridge, 1996).
21. M. B. Weissman, *Rev. Mod. Phys.* **60**, 537 (1988).
22. Errors reported in this article represent two standard deviations of the statistical uncertainty in the measurement.
23. B. N. J. Persson, *Phys. Rev. B* **44**, 3277 (1991).
24. A. J. Heinrich, C. P. Lutz, J. A. Gupta, D. M. Eigler, *Science* **298**, 1381 (2002).
25. J. Repp, G. Meyer, K.-H. Rieder, P. Hyldgaard, *Phys. Rev. Lett.* **91**, 206102 (2003).
26. L. D. Landau, E. M. Liftshitz, in *Quantum Mechanics* (Pergamon, New York, ed. 3, 1977).
27. We take the effective distance to be half the fcc-hcp distance for a constant barrier approximation that would yield the same WKB barrier integral.
28. Y. Wada, *Optoelectronics Devices Technol.* **10**, 205 (1995).
29. J. A. Stroscio, W. J. Kaiser, Eds., *Scanning Tunneling Microscopy*, vol. 27 of *Methods of Experimental Physics* (Academic Press, Boston, 1993).
30. We thank A. Fein and S. Blankenship for their assistance, and W. Gadzuk, M. Stiles, and N. Zimmerman for very fruitful discussions. Supported in part by the Office of Naval Research.

Supporting Online Material
www.sciencemag.org/cgi/content/full/1102370/DC1
Figs. S1 to S4
Movies S1 and S2

6 July 2004; accepted 25 August 2004
Published online 9 September 2004;
10.1126/science.1102370
Include this information when citing this paper.

Rescue of Cardiac Defects in *Id* Knockout Embryos by Injection of Embryonic Stem Cells

Diego Fraidenraich,[1] Elizabeth Stillwell,[1] Elizabeth Romero,[1] David Wilkes,[3] Katia Manova,[2] Craig T. Basson,[3] Robert Benezra[1]*

We report that Id knockout mouse embryos display multiple cardiac defects, but mid-gestation lethality is rescued by the injection of 15 wild-type embryonic stem (ES) cells into mutant blastocysts. Myocardial markers altered in Id mutant cells are restored to normal throughout the chimeric myocardium. Intraperitoneal injection of ES cells into female mice before conception also partially rescues the cardiac phenotype with no incorporation of ES cells. Insulin-like growth factor 1, a long-range secreted factor, in combination with WNT5a, a locally secreted factor, likely account for complete reversion of the cardiac phenotype. Thus, ES cells have the potential to reverse congenital defects through Id-dependent local and long-range effects in a mammalian embryo.

The Id proteins are dominant negative antagonists of basic helix-loop-helix (bHLH) transcription factors and regulate differentiation in multiple lineages (*1*). Previous studies have shown that Id1 to Id4 are expressed in embryonic tissues during development in partially overlapping patterns (*2*) and that Id1 and Id3 are detected at mid-gastrulation in the three germ layers (*3*). In the developing heart, Id1 to Id3 are detected in the endocardial cushion (EC) mesenchyme from embryonic day 10.5 (E10.5) through E16.5 (*2*), but Id4 is absent (*2*). Here, we show that Id1 to Id3 are also expressed in the epicardium and endocardium but are absent in the myocardium [fig. S1, A to C, for Id1; fig. S1, D and E, for Id3; (*4*) for Id2]. Id1 to Id3 expression becomes confined to the leaflets of the cardiac valves as the atrioventricular (AV) EC tissue myocardializes (*4*). Id1 and Id3 expression persists in the cardiac valves, endocardium, endothelium, and epicardium at postnatal day 7 (P7) (*4*).

Double– and triple–*Id* knockout embryos display severe cardiac defects and die at mid-gestation. *Id1*, *Id2*, or *Id3* knockout (KO) embryos do not exhibit developmental abnormalities, but ablation of two Id genes in any combination (*Id1/Id2*, *Id2/Id3*, or *Id1/Id3*) leads to embryonic lethality by E13.5 (table S1). *Id1/Id3* KO embryos display a collapse of brain vasculature with associated hemorrhage and enhanced expression of p16 and bHLH neural factors in the neighboring neuroepithelium by E12 or E13 (*5*). We wanted to identify the cause of embryonic lethality common to all KO embryos. Embryos lacking four or five copies of *Id1*, *Id2*, and *Id3* displayed multiple cardiac abnormalities at E11.5 to E13.5 (Fig. 1, A, B, D, E, G, H, J, K, M, and N for $Id1^{-/-}Id3^{-/-}$; fig. S2C for $Id1^{-/-}Id2^{-/-}$; fig. S2D for $Id1^{-/-}Id2^{+/-}Id3^{-/-}$; and fig. S2F for $Id1^{+/-}Id2^{+/-}Id3^{-/-}$). Embryo size was reduced by 10 to 30%. KO embryos displayed ventricular septal defects (VSDs) associated with impaired ventricular trabeculation and thinning of the compact myocardium. Trabeculae had disorganized sheets of myocytes surrounded by discontinuous endocardial cell lining. Cell proliferation in the myocardial wall was defective [percentage 5-bromo-2′-deoxyuridine (BrdU) ± SD: wild type (WT): 38 ± 4%; $Id1^{-/-}Id3^{-/-}$: 23 ± 3%; (Fig. 1, J to L and L inset)]. Outflow tract (OT) atresia was apparent (Fig. 1, M and N). OT and AV ECs displayed low cellularity at E11.5, which resulted in hypoplastic ECs in $Id1^{+/-}Id2^{+/-}Id3^{-/-}$ embryos at E13.5 (fig. S2, E and F). The epicardium appeared normal, and EC apoptosis was unaffected [terminal deoxynucleotidyl transferase–mediated deoxyuridine triphosphate nick end labeling (*4*)]. The impaired development of the myocardium in Id KO animals even though Ids are not expressed there suggests that Ids might participate in molecular signaling between myocardium and the Id^+ epicardium, endocardium, and EC. Alternatively, loss of Id expression in early myocardial precursors might lead to myocardial defects.

Id1/Id2/Id3 KOs have severe cardiac malformation as early as E9.5 (fig. S2, A and B). The overall size of the embryo and heart was reduced by 40 to 60%. The atrium did not separate from the ventricle, and ventricular trabeculation was rudimentary (fig. S2, A and B). No hemorrhage was observed in *Id1/Id2/Id3* KO brains at E9.5 (*4*). No triple-KO embryos survived to E11.5 (table S1). These observations suggest that a defective heart is the primary cause of mid-gestation lethality.

Injection of ES cells into Id KO blastocysts corrects cardiac defects and rescues embryonic lethality. Cardiac defects and embryonic lethality was reversed by injecting 15 β-galactosidase (*LacZ*)–marked ES Rosa 26 (R26) cells into *Id* KO blastocysts. In the resultant embryos, LacZ-positive cells were detected in the heart and forebrain (Fig. 1C). At E11.5, all cardiac structures in rescued embryos were identical to those of WT embryos. No endocardial, myocardial, or EC defects were observed (Fig. 1, C, F, I, L, and O) (*4*), and cell proliferation was restored [percentage BrdU in compact myo-

[1]Cancer Biology and Genetics Program, [2]Molecular Cytology Core Facility, Memorial Sloan-Kettering Cancer Center, [3]Molecular Cardiology Laboratory, Greenberg Cardiology Division, Department of Medicine, Weill Medical College of Cornell University, New York, NY 10021, USA.

*To whom correspondence should be addressed. E-mail: r-benezra@ski.mskcc.org

cardium: 34 ± 4% (Fig. 1L, inset)]. We determined that 25% of the litter of *Id1*$^{-/-}$ *Id3*$^{+/-}$ (or *Id1*$^{-/-}$*Id2*$^{+/-}$) or 43.75% of the litter of *Id1*$^{-/-}$*Id2*$^{+/-}$*Id3*$^{+/-}$ intercrosses should carry a null mutation in at least two Id genes, but double KOs never survive past E13.5 (table S1). However, 15 out of 75 animals (20%) of the litter of *Id1*$^{-/-}$*Id3*$^{+/-}$ and *Id1*$^{-/-}$*Id2*$^{+/-}$*Id3*$^{+/-}$ intercrosses with ES cell injection into blastocysts carried the genotype *Id1*$^{-/-}$*Id3*$^{-/-}$*:R26*, *Id1*$^{-/-}$*Id2*$^{-/-}$*:R26*, *Id1*$^{-/-}$*Id2*$^{+/-}$*Id3*$^{-/-}$*:R26*, or *Id1*$^{-/-}$*Id2*$^{-/-}$*Id3*$^{+/-}$*:R26* past E13.5 (1 out of 6 at E14.5, 5 out of 25 at E17.5, and 9 out of 45 after birth). The appearance of double-KO animals is therefore due to the presence of ES cells ($P < 0.0001$).

Rescued hearts were structurally and functionally indistinguishable from those of WT embryos by histology and echocardiography (Fig. 1, P to Z_2, and table S2). The chamber walls, septum, OT, and valves were normal (Fig. 1, P to Z_2) (*4*). Unlike *Id1/Id3* KO embryos, a continuous lining of endocardial cells apposed the myocardium in rescued pups, despite most endocardial cells not being ES-cell derived (Fig. 1, Z_1 and Z_2). In rescued pups, body and heart sizes were severely reduced during the first 3 weeks, in some cases by 50 to 70% [P15 WT, 8.33 g and 65 mg of body and heart weights, respectively; P15 *Id1*$^{-/-}$*Id3*$^{-/-}$*:R26*, 3.11 g (63% reduction) and 25 mg (62% reduction) of body and heart weights, respectively], and 44% of the rescued pups died during the first 4 weeks. The surviving rescued adult animals (5 out of 9) displayed correction of these parameters (10 to 30% reduction relative to that of WT animals by 5 to 6 weeks) (Fig. 1, X and Y). The heart/body weight ratio in WT or rescued animals was constant [heart/body ratio (±SD): $7.9 \times 10^{-3} \pm 0.5 \times 10^{-3}$], and all organs were small and grossly normal (*4*).

The average fraction of WT LacZ^{+} cells per heart was 20% (range of incorporation: 5 to 45%) and blue cells were grouped in clusters (Fig. 1, Q, U, W, and Y). The percentage of ES cell incorporation [in X-galactosidase (X-Gal) staining of tail sections] was confirmed by Southern analysis from adjacent tissue (fig. S3A). An E14.5 *Id1*$^{-/-}$*Id3*$^{-/-}$*:R26* rescued embryo with 15 ± 5% of X-Gal–positive cells displayed a WT band 80% less intense than the mutant band (Southern, fig. S3A). To rule out that X-Gal–negative cells are ES-derived cells which had lost their ability to express LacZ, individual X-Gal–negative cells were laser-captured from heart sections of an E17.5 *Id1*$^{-/-}$*Id2*$^{-/-}$*:R26* rescued embryo and shown to be *Id2*$^{-/-}$ (fig. S3B). R26 E17.5 heterozygous embryos stained uniformly blue after X-Gal staining, indicating that the result was not due to incomplete staining (Fig. 1P, inset).

In rescued hearts, a small subset of R26 cells from the epicardium, endocardium, and EC was the source of Id1/Id3 expression (fig. S1, H to J and M) (*4*). R26 cells also populated the myocardium (fig. S1, K and L), but no Ids were detected (fig. S1M) (*4*). Although it is likely that the rescue by ES cells is Id dependent, it is formally possible that ES cells incorporated into the heart provide Id-independent signals. To test this, ES cells with reduced Id1 levels by small interfering (siRNA) knockdown (fig. S3C) were injected into Id KO blastocysts. Id1 knockdown ES cells incorporated in the embryos (fig. S3D), but failed to rescue *Id1*$^{-/-}$*Id3*$^{-/-}$ blastocysts (fig. S1E).

Gene expression profiles in *Id* KO hearts are altered. Microarray analysis of E11.5 WT and *Id1/Id3* double-KO hearts (table S3) showed skeletal myosin alkali light chain (*6*) (skMLC) up-regulated 2.83-fold in mutant hearts. The enhanced signal was confirmed by Northern analysis (+2.9-fold) (Fig. 2E, inset) and ISH (Fig. 2, E and F) (*4*). Cardiac α-myosin heavy chain (α-MHC), the adult isoform, was up-regulated (+2.0-fold) (table S3). No other sarcomeric isoform was misregulated in Id-defective hearts (table S3). A switch to a complete skeletal muscle program does not occur, because the myotome-specific

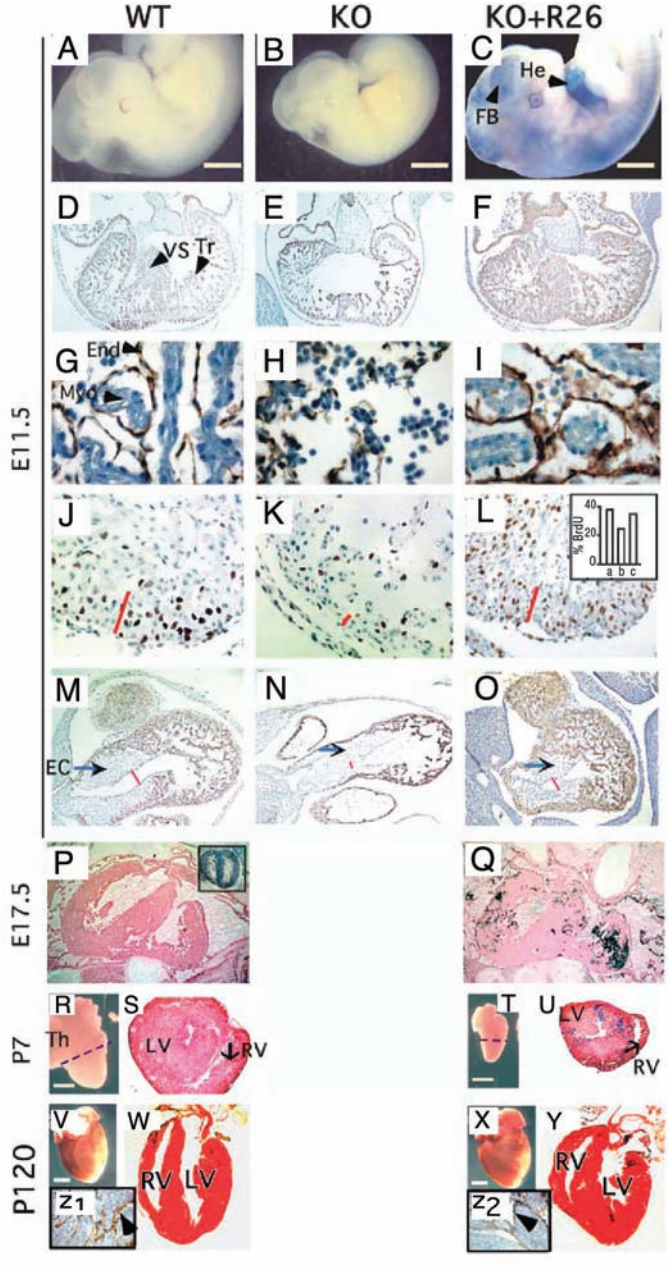

Fig. 1. Cardiac defects in *Id* KO embryos are rescued by injection of 15 ES cells. [(A) to (O)] A WT (**A**, **D**, **G**, **J**, and **M**), *Id1*$^{-/-}$*Id3*$^{-/-}$ (**B**, **E**, **H**, **K**, and **N**), or *Id1*$^{-/-}$*Id3*$^{-/-}$*:R26* (**C**, **F**, **I**, **L**, and **O**) E11.5 embryo was X-Gal stained [(A) to (C)] or transversely sectioned at the ventricle [(D) to (L)] or OT level [(M) to (O)]. (D) to (F) are magnified by 50× and (M) to (O) are magnified by 80×, desmin immunodetection. (G) to (I) show CD31 immunodetection at 200×. (J) to (L) show BrdU immunodetection at 100×. The inset in (L) shows the percentage of BrdU from (J) to (L). [(P) and (Q)] A WT (**P**), *ROSA*$^{+/-}$ [(P), inset], or *Id1*$^{-/-}$*Id3*$^{-/-}$*:R26* (**Q**) E17.5 embryo was X-Gal and eosin stained (magnified by 50×). [(R) to (Z_2)] A WT (**R** and **S**), WT:R26 (**V** and **W**), *Id1*$^{-/-}$*Id2*$^{+/-}$*Id3*$^{-/-}$*:R26* (**T** and **U**), or *Id1*$^{-/-}$*Id3*$^{-/-}$*:R26* (**X** and **Y**) P7 [(R) to (U)] or P120 [(V) to (Z_2)] heart was sectioned (dashed lines), X-Gal and eosin stained [(S) and (U), 25×; (W) and (Y), 15×) or CD31 immunostained [(Z_1) and (Z_2), 50×). He, heart; FB, forebrain; VS, ventricular septum; Tr, trabeculae; End, endocardium; Myo, myocardium; Th, thymus; LV, left ventricle; RV, right ventricle; blue arrow, outflow tract EC; KO, Id KO; red bar in (J) to (L), myocardial wall thickness; red bar in (M) to (O), luminal thickness; black arrowhead in (Z_1) and (Z_2), CD31^{+} cells. Scale bar, 500 μm [(A) to (C)]; 2 mm [(R), (T), (V), and (X)].

bHLH factors MyoD and myogenin were not detected in the *Id* KO myocardium, and α-cardiac actin was normally expressed (*4*). Stra13, a member of the Hey family of bHLH proteins (*7*, *8*) was up-regulated 4.92-fold in Id KO hearts (table S3), with enhanced Stra13 expression in the myocardium (Fig. 2, A and B). Stra13 was also detected in the neuroepithelium of the forebrain ganglionic eminence, and its expression was enhanced in the hemorrhagic *Id1/Id3* KO embryos (Fig. 2, I and J). skMLC contains E-box motifs in its enhancer (*9*). *Stra13* contains E-box motifs in the promoter and is regulated by Sharp-1, another bHLH member (*10*). α-MHC is regulated by the bHLH protein dHand. Id loss may lead to ectopic activation of bHLH proteins that in turn activate Stra13, skMLC, and α-MHC.

ES cells correct gene expression profiles in a non–cell autonomous manner. Of the misregulated markers, 82% (60 out of 74), including skMLC, α-MHC, and Stra13, were corrected in chimeric rescued hearts (table S4 and Fig. 2, C and G). The myocardium not only displayed normal skMLC or Stra13 transcript levels in R26 cells but also in *Id* KO cells (Fig. 2, C, D, G, and H). Thus, signals emanating from the R26 cells (EC, endocardium, epicardium, myocardium, or distally outside the heart) revert the myocardium in a non–cell autonomous manner.

Most of the brain endothelium was composed of *Id* KO cells (Fig. 2L). However, no collapse of the endothelium and associated hemorrhage was observed in rescued embryos (Fig. 2, K and L). Stra13 was also corrected in the neuroepithelium (Fig. 2K). Although we cannot rule out that very few R26 endothelial cells account for the rescue, a non–cell autonomous mechanism must operate because the whole of the brain endothelium appears normal.

Supernatants of epicardial cultures containing R26-derived cells rescue proliferation defects of the *Id* KO hearts. To determine whether secreted factors from *Id* KO:R26 epicardium correct proliferation defects in the *Id* KO myocardium, we derived epicardial primary cells from WT, *Id1*$^{-/-}$*Id3*$^{+/-}$, and *Id1*$^{-/-}$*Id3*$^{+/-}$*:R26* adult hearts (*11*) [reverse transcription polymerase chain reaction (RT-PCR), Fig. 3L] and collected conditioned medium (epiCM). WT and *Id1*$^{-/-}$*Id3*$^{+/-}$*:R26* but not *Id1*$^{-/-}$*Id3*$^{+/-}$ epicardial cells expressed Id1 (*4*). *Id1*$^{-/-}$*Id3*$^{+/-}$ E17.5 whole hearts were cultured for 48 hours with epiCM and BrdU and then sectioned and analyzed. WT and *Id1*$^{-/-}$*Id3*$^{+/-}$*:R26* but not *Id1*$^{-/-}$*Id3*$^{+/-}$ epiCM improved the proliferation rate of the Id KO compact myocardium relative to controls without epiCM (Fig. 3, E to H for Ki67 and insets in E to G for BrdU; compare with Fig. 3, A to D). Because *Id1*$^{-/-}$*Id3*$^{+/-}$ epiCM has little effect relative to controls with no epiCM (Fig. 3H), the R26 component of the KO:R26 epiCM (Fig. 3L, inset) accounts for the proliferation rescue. These results support the existence of an epicardial-to-myocardial rescue, through secretion of extracellular factors. We asked if misregulated myocardial markers could also be reversed. However, epiCM from WT or *Id1*$^{-/-}$*Id3*$^{+/-}$*:R26* failed to correct skMLC in E12.5 *Id1/Id3* KO hearts (Fig. 3, I to K).

Injection of ES cells into females before conception partially corrects cardiac defects and rescues embryonic lethality of the *Id* KO offspring. To investigate whether myocardial proliferation is rescued by secretion of long-range ES cell–dependent factors, 3-month-old *Id1*$^{-/-}$*Id3*$^{+/-}$ females

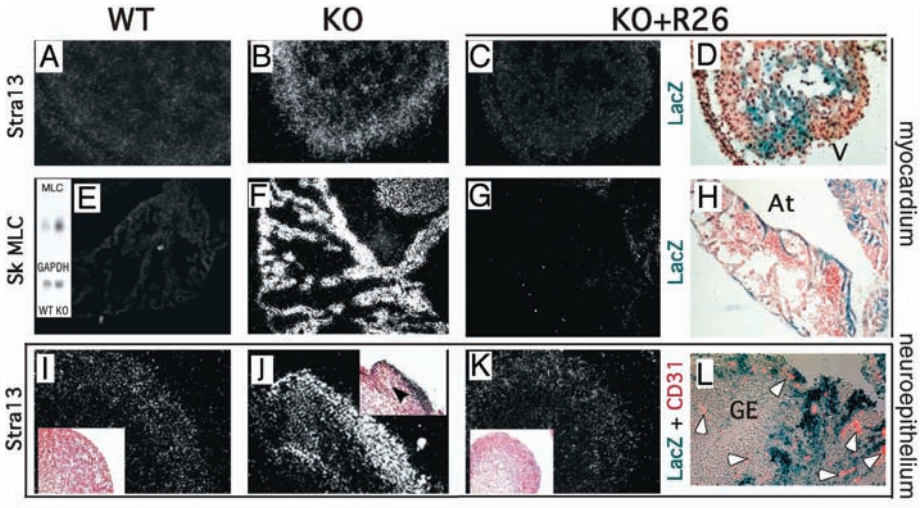

Fig. 2. R26 cells rescue *Id1*$^{-/-}$*Id3*$^{-/-}$ cells non–cell autonomously. (**A** to **C** and **I** to **K**) A WT [(A) and (I)], *Id1*$^{-/-}$*Id3*$^{-/-}$ [(B) and (J)], or *Id1*$^{-/-}$*Id3*$^{-/-}$*:R26* [(C) and (K)] E11.5 embryo was subjected to ISH for Stra13 (100×). (**D**) Adjacent section of (C), X-Gal stained. (**L**) An *Id1*$^{-/-}$*Id3*$^{-/-}$*:R26* E14.5 embryo was X-Gal and CD31 immunostained (100×). [(E) to (G)] A WT (**E**), *Id1*$^{-/-}$*Id3*$^{+/-}$ (**F**), or *Id1*$^{-/-}$*Id2*$^{+/-}$*Id3*$^{-/-}$*:R26* (**G**) P7 heart was subjected to ISH for skMLC (50×). (**H**) Adjacent section of (G), X-Gal stained. [(E), inset] Northern blot from a WT or *Id1*$^{-/-}$*Id3*$^{+/-}$ E13.5 heart probed for skMLC. Insets in (I) to (K) show bright field. V, ventricle; At, atrium; GE, ganglionic eminence; black arrowhead in (J) inset, hemorrhage; white arrowheads (L), CD31^{+} cells.

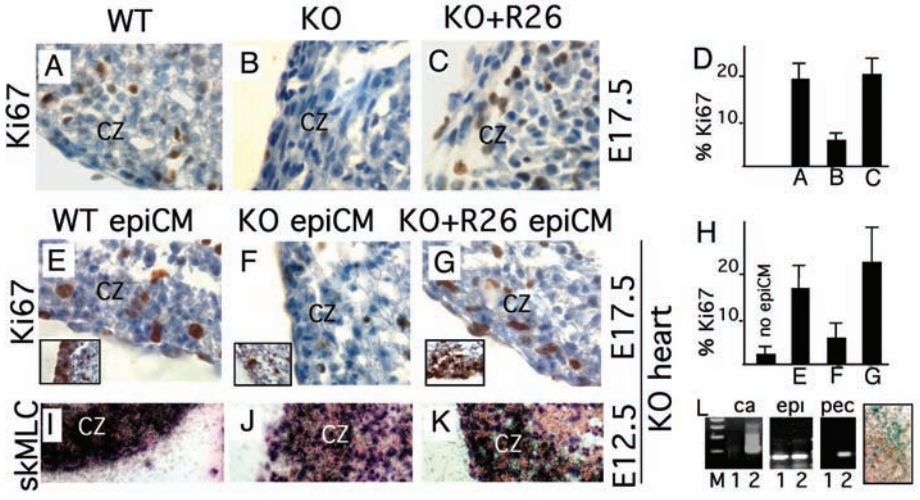

Fig. 3. Conditioned medium from *Id* KO:R26 epicardial cells (epiCM) corrects myocardial proliferation defects in *Id* KO hearts. (**A** to **C**) A WT, *Id1*$^{-/-}$*Id3*$^{+/-}$, or *Id1*$^{-/-}$*Id3*$^{+/-}$*:R26* E17.5 embryo was sectioned at heart level and Ki67 immunostained. (**D**) Percentage of Ki67^{+} cells of (A) to (C). Error bars show mean + SD. (**E** to **G** and **I** to **K**) An *Id1*$^{-/-}$*Id3*$^{+/-}$ E17.5 [(E) to (G)] or *Id1*$^{-/-}$*Id3*$^{-/-}$ E12.5 [(I) to (K)] heart was cultured with BrdU and WT [(E) and (I)], *Id1*$^{-/-}$*Id3*$^{+/-}$ [(F) and (J)], or *Id1*$^{-/-}$*Id3*$^{+/-}$*:R26* [(G) and (K)] epiCM, sectioned, and Ki67 [(E) to (G)] or BrdU [(E) to (G), insets] immunostained or subjected to ISH for skMLC [(I) to (K)]. (**H**) Percentage of Ki67^{+} cells of (E) to (G) and control with no epiCM. Error bars show mean + SD. (**L**) RT-PCR [cardiac actin (ca), epicardin (epi), and pecam (pec)] of *Id1*$^{-/-}$*Id3*$^{+/-}$*:R26* epicardial-derived cells (lane 1) or E13.5 heart (lane 2). [(L), inset] *Id1*$^{-/-}$*Id3*$^{+/-}$*:R26* epicardial-derived cells were X-Gal stained. KO, Id1$^{-/-}$Id3$^{+/-}$. Magnification: 630× in (A) to (C) and (E) to (G); 400× in (I) to (K). CZ, myocardial compact zone; M, markers.

were injected with 10^5 R26 cells intraperitoneally, and, after a week, mated with *Id1*$^{-/-}$*Id3*$^{+/-}$ males. Floating cells isolated from the intraperitoneal (IP) cavity and cultured formed ES cell outgrowths (fig. S3F) and embryoid bodies (*4*). R26 cells also adhered to connective tissue in the external side of the uterine wall, but no X-Gal–positive cells were detected inside the uterus or in placenta or any part of the embryo, including the yolk sac (*4*). Of newborn pups, 18% (7 out of 40) carried the *Id1*$^{-/-}$*Id3*$^{-/-}$ genotype, whereas no double-KO pups have been observed in over 10 years of breeding ($P < 0.001$). Double-KO pups contained no X-Gal–positive cells (Fig. 4G) (*4*) and tail DNAs were *LacZ* negative (PCR). Injection of supernatants from R26 cultures also rescued the lethality of *Id1/Id3* embryos (3 out of 35), although at lower rates (9%). The Id1/Id3 double-KO newborn pups, however, died by P2 and displayed enlarged hearts (body weight of *Id1*$^{-/-}$*Id3*$^{-/-}$ or WT P1 pups: 1.4 ± 0.1 g; heart weight of *Id1*$^{-/-}$*Id3*$^{-/-}$ P1 pups: 16 ± 1 mg; heart weight of WT P1 pups: 10 ± 1 mg; *Id1*$^{-/-}$*Id3*$^{-/-}$ P1 heart/body ratio: 11.4 × 10^{-3} ± 1.1 × 10^{-3} compared with WT heart/body ratio: 7.1 × 10^{-3} ± 0.6 × 10^{-3}; *Id1*$^{-/-}$*Id3*$^{+/-}$*:R26* heart/body ratio at P1 was 7.3 × 10^{-3} ± 0.5 × 10^{-3}) with muscular VSDs (Fig. 4G), little endocardium, and disorganized endothelium (Fig. 4H) (compare with a WT P1 heart, Fig. 4, D and E). As with the *Id* KO hearts (with no injection), E11.5 rescued hearts (IP injection) displayed incomplete VS and discontinuous endocardium (Fig. 4, A and B). However, the thickness of the compact myocardium was corrected (Fig. 4C; compare with Fig. 1, J to L) with increased myocardial proliferation (35 ± 4% BrdU incorporation at E11.5, Fig. 4, F and I insets, for E18.5). P1 *Id1/Id3* double-KO hearts, no longer influenced by the R26 cells after birth, showed severe proliferation defects in the inner myocardium (Fig. 4, F and I).

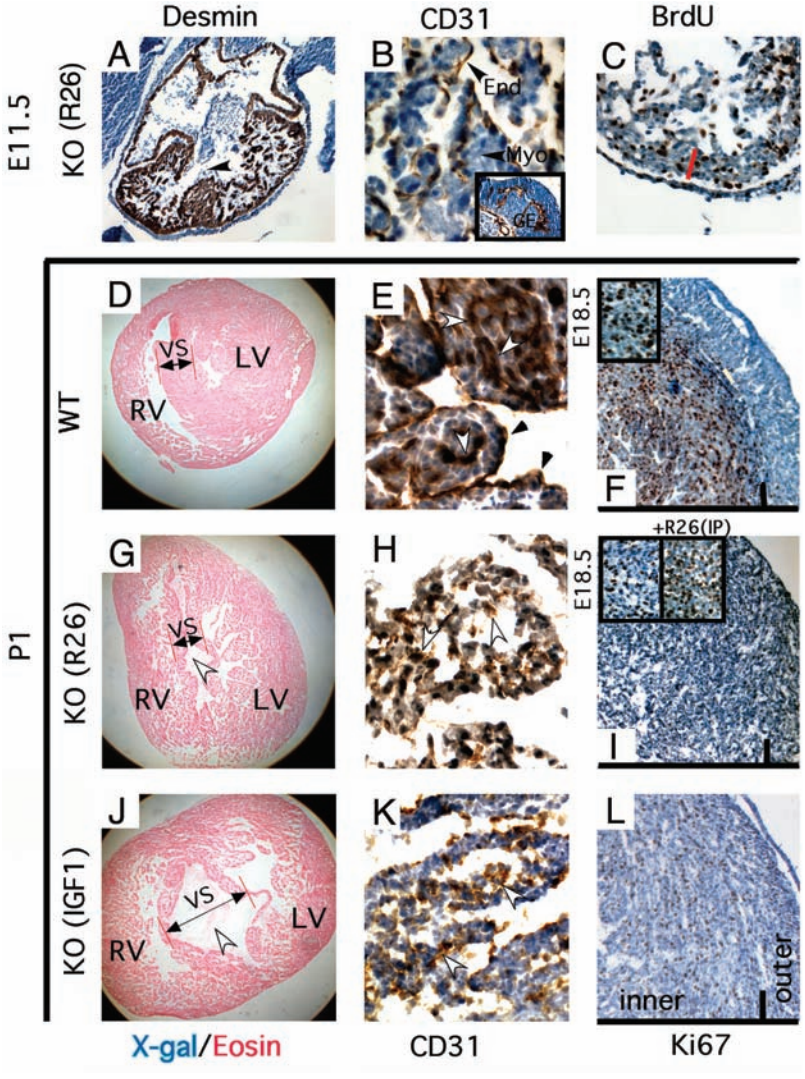

Fig. 4. *Id1/Id3* double KO pups are born from mice intraperitoneally injected with ES cells or IGF-1. (**A** to **C**) An *Id1*$^{-/-}$*Id3*$^{-/-}$ E11.5 embryo from an ES-injected female was sectioned at heart [(A) to (C)] or brain [(B), inset] level and Desmin [(A), 50×], CD31 [(B), 200× and (B), inset, 100×] or BrdU [(C), 100×] immunostained. [(D) to (L)] A WT (**D** to **F**), an *Id1*$^{-/-}$*Id3*$^{-/-}$ from an ES-injected female (**G** to **I**), or an *Id1*$^{-/-}$*Id3*$^{-/-}$ from an IGF-1–injected female (**J** to **L**) P1 heart was transversely sectioned and stained with X-Gal and eosin [(D), (G), and (J), 25×], CD31 [(E), (H), and (K), 200×], or Ki67 [(F), (I), and (L), 50×]. [(F) and (I), insets] A WT [(F), inset, 400×] or an *Id1*$^{-/-}$*Id3*$^{+/-}$ E18.5 heart from a noninjected or from an R26 injected female [(I), insets, 400×] was sectioned and Ki67 immunostained. KO(R26), Id KO embryos (pups) from R26-injected females; KO (IGF-1), *Id* KO pups from IGF-1–injected females; End, endocardium; Myo, myocardium; RV, right ventricle; LV, left ventricle; VS, ventricular septum; GE, ganglionic eminence; arrowhead (A), VS defect; red bar (C), thickness of compact myocardium; white arrowhead (G), VS defect; black arrowheads (E), CD31$^+$ endocardial cells; white arrowheads (E), CD31$^+$ endothelial cells; white arrowheads [(H) and (K)], disorganized endothelial cells.

Of the markers misregulated in *Id1/Id3* KO hearts, 64% (47 out of 74) were corrected at E11.5 after ES cell IP injection, but 36% (27 out of 74) failed to be restored (table S4). skMLC was not corrected (table S4). Mating of the same *Id1*$^{-/-}$*Id3*$^{+/-}$ parents without additional R26 injections rendered no double-KO pups. However, a subsequent mating with a second R26 injection led to a rescue, suggesting a reversible effect. WT murine embryonic fibroblasts (MEFs) were injected every 3 days in pregnant females, but no double-KO pups were born. Although the brain vasculature of the *Id* double-KO embryos (from IP rescue) formed an endothelial cell aggregate at E11.5 (Fig. 4B, inset), no macroscopic hemorrhage was observed.

In support of the mode of action of ES cells at a distance, *Id1*$^{-/-}$*Id3*$^{-/-}$*:R26* female chimeras were fertile, and when crossed with *Id1*$^{-/-}$*Id3*$^{+/-}$ males, 44% of the litter (4 out of 9) carried the *Id1*$^{-/-}$*Id3*$^{-/-}$ genotype (PCR), although these neonates died soon after birth. Thus, ES-derived cells in chimeric mothers provide distal signals during pregnancy that rescue embryonic lethality.

Identification of IGF-1 as the ES cell–secreted factor that partially corrects cardiac defects and rescues embryonic lethality of the *Id* KO offspring. To identify ES cell–secreted factors responsible for the partial cardiac rescue, we performed microarray analyses from WT, KO, or KO:R26 epicardial cultures. Because *Id* KO cultures (unlike WT or KO:R26 cultures) failed to rescue myocardial proliferation defects, we searched for secreted factors in WT or chimeric cultures with proliferation-promoting capacity, whose expression was down-regulated in *Id* KO cultures. We identified several secreted factors that showed Id-dependent regulation [table S5 (WT versus KO): IGF-1, +2; bone morphogenetic protein 4 (BMP4), –4.29; endothelin I, –3.25; table S6 (chimera versus KO): IGF-1, +1.62; BMP4, –1.52; endothelin-I, –1.62-fold). Of particular interest was IGF-1;

because it is down-regulated in *Id* KO cultures, it promotes cardiomyocyte proliferation (*12*), it is released in the bloodstream (*13*), *Id1/Id3* and *IGF-1* KO embryos are small, and Id rescued chimeras as well as *IGF-1* KO pups are small with a variable rate of postnatal lethality (*14*, *15*). IGF-1 was also down-regulated in E11.5 $Id1^{-/-}Id3^{-/-}$ hearts (–1.3-fold, according to data from microarrays).

As in the case of Ids, IGF-1 was observed at E11.5 in nonmyocardial layers of developing hearts (EC, endocardium, and epicardium) but not in the myocardium (Fig. 5, A, C, and E). IGF-1 expression was compromised in the endocardium and epicardium of $Id1^{-/-}Id3^{-/-}$ E11.5 hearts. (Fig. 5, B, D, and F). Because IGF-1 expression is not fully abrogated by Id1/Id3 loss, it is possible that Id2 sustains basal levels of IGF-1 expression. We also observed down-regulation of the 8-Kb message of IGF-1 in $Id1^{-/-}Id3^{-/-}$ E11.5 livers (Fig. 5G), the main source of circulating IGF-1. IGF-binding protein 4 (IGFBP4), an inhibitor of IGF-1 activity, was up-regulated in *Id1/Id3* KO tissues [Fig. 5G and table S5 (WT versus KO): –1.85-fold; table S7 (KO versus WT): +4.59).

We hypothesized that IGF-1 from ES cells (fig. S3G) is released into maternal circulation, passes through the placenta, and accounts for the partial rescue of $Id1^{-/-}Id3^{-/-}$ embryos. We injected IGF-1 (700 ng/day) intraperitoneally into $Id1^{-/-}Id3^{+/-}$ pregnant females, resulting in an increase in serum levels of IGF-1 (fig. S3H). Of newborn pups, 6 out of 41 (15%) carried the $Id1^{-/-}Id3^{-/-}$ genotype ($P < 0.001$). Thus, maternal injection of IGF-1 recapitulates the effect observed by maternal injection of ES cells. To test specificity of the effect and because loss of Id1 down-regulates expression of parathyroid hormone (PTH) in ES cells (*4*), we injected recombinant PTH intraperitoneally, but no *Id1/Id3* pups were born (0 out of 15). Similar to IP injection of R26 cells, pups born from IGF-1–injected mothers died by P2, and the rescued hearts were hypertrophic, with muscular VSDs and compromised endocardium and endothelium but with normal myocardial wall (Fig. 4, J to L). Thus, IGF-1 is one of the Id-dependent non–cell autonomous factors responsible for the rescue of myocardial proliferation defects.

WNT5a corrects cardiac gene expression profiles. Although maternal injection of ES cells (or IGF-1) rescues embryonic lethality and proliferation defects in *Id1/Id3* KO hearts, *Id1/Id3* KO neonates display cardiac abnormalities with altered gene expression profiles. Because the rescue in chimeric hearts generated by injection of WT ES cells in blastocysts is complete, we hypothesized that a local requirement for ES cells, which is missing in the IP rescue experiment, was critical for a full rescue. We therefore searched for locally secreted factors up-regulated in the chimeric epicardial arrays relative to *Id* KO controls. WNT5a, a noncanonical WNT, is a lipid-modified glycoprotein associated with the cell membrane and extracellular matrix (*16*) and was up-regulated 2.3-fold in chimeric versus KO as well as WT epicardial cultures (tables S5 and S6), suggesting a possible neomorphic effect of ES cells incorporated in the epicardium. Consistently, WNT5a expression was enhanced in the epicardium of E16.5 chimeric rescued hearts (fig. S4). To determine whether WNT5a corrects gene expression profiles, we performed coculture experiments in which heart explants [P1 $Id1^{-/-}Id3^{-/-}$ hearts partially rescued by maternal IP injection of R26 cells (IP R26)] were grown on MEFs overexpressing WNT5a (threefold up-regulation, according to data from microarrays). We found 653 genes misregulated between WT and *Id1/Id3* KO (IP R26) heart explants in the presence of mock-infected MEFs (table S7), including components of the WNT pathway [table S7 (KO versus WT): β-catenin, –2.64; β-catenin interacting protein, +2.3; Dkk3, –2.14-fold). Out of 653 genes, 554 (85%) were corrected when Id1/Id3 KO (IP R26) heart explants were cultured on WNT5a-overexpressing MEFs, including β-catenin, β-catenin interacting protein, and Dkk3. The adult isoform of cardiac MHC (–12.13-fold down-regulated in the Id KO explants) was corrected in the presence of WNT5a-overexpressing MEFs (table S7). It is likely that ES cells circumvent Id loss in embryonic hearts by providing WNT5a locally, which can normalize gene expression profiles.

Discussion. In this report, we demonstrate that compound *Id1/Id3* KO embryos have severe cardiac defects that result from a failure in signaling between the Id-expressing epicardium and endocardium and the Id-negative myocardium. This failure results in a thinning of the myocardial wall due to proliferation defects, VSDs, endocardial and EC defects, and OT atresia. We have been able to show that cardiac defects can be rescued by the incorporation of WT ES cells into the heart with as little as 20% chimerism. Transcriptional alterations observed in myocardial cells of *Id* KO hearts are largely restored to normal in *Id* KO cells of the chimeric hearts, indicating a non–cell autonomous rescue by WT ES cells. As in the case of Id mutant embryos, other congenital heart malformations appear to partially result from non–cell autonomous defects in cell proliferation (*17*–*19*). Although injection (aggregation) experiments with KO ES cells and WT blastocysts (morulas) have been previously reported with non–cell auton-

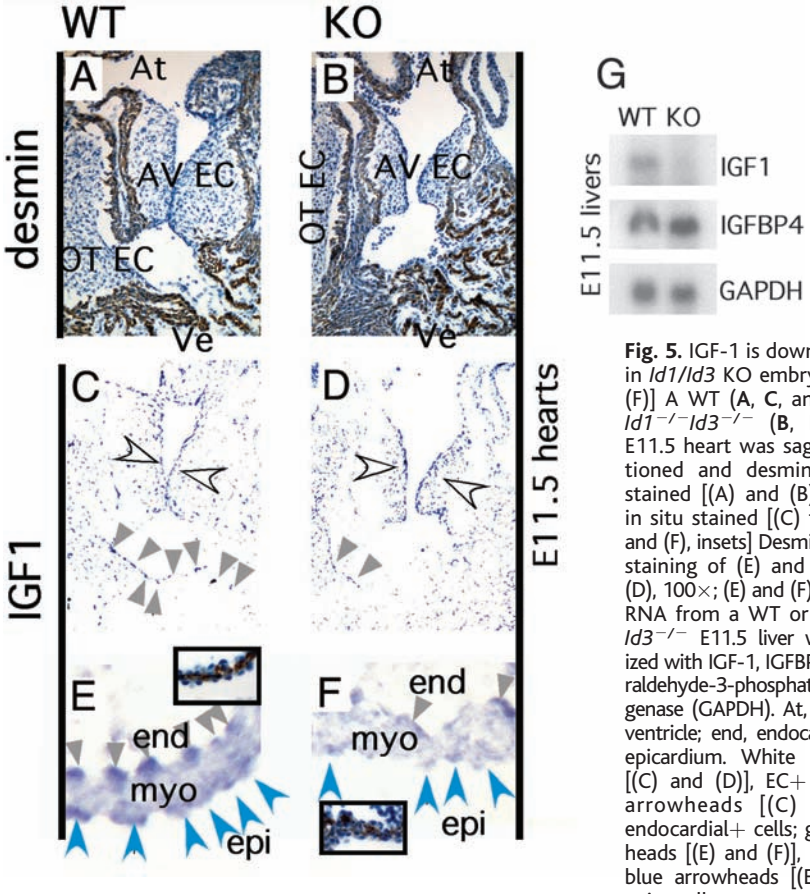

Fig. 5. IGF-1 is down-regulated in *Id1/Id3* KO embryos. [(A) to (F)] A WT (**A**, **C**, and **E**) or an $Id1^{-/-}Id3^{-/-}$ (**B**, **D**, and **F**) E11.5 heart was sagittally sectioned and desmin immunostained [(A) and (B)] or IGF-1 in situ stained [(C) to (F)]. [(E) and (F), insets] Desmin immunostaining of (E) and (F). (A) to (D), 100×; (E) and (F), 200×. (**G**) RNA from a WT or an $Id1^{-/-}Id3^{-/-}$ E11.5 liver was hybridized with IGF-1, IGFBP4, or glyceraldehyde-3-phosphate dehydrogenase (GAPDH). At, atrium; Ve, ventricle; end, endocardium; epi, epicardium. White arrowheads [(C) and (D)], EC+ cells; gray arrowheads [(C) and (D)], endocardial+ cells; gray arrowheads [(E) and (F)], end+ cells; blue arrowheads [(E) and (F)], epi+ cells.

omous correction of cardiac defects (*17*, *20*, *21*), this is the first time that low numbers of WT ES cells have been injected into blastocysts fated to die with the resultant production of viable and fertile adult animals.

The rescue we show results from a combination of long-range and short-range effects of the injected ES cells. IGF-1, secreted by ES cells, is lower in *Id* KO embryos relative to those of the WT and is restored by ES cells in chimeras or by IP injection of ES cells into mothers bearing *Id1/Id3* compound mutant embryos before conception. This latter result suggests that IGF-1 is a long-range acting factor because ES cells do not cross placenta. However, the rescue by IP injection of ES cells and direct injection of recombinant IGF-1 is incomplete with enhanced proliferation of the myocardium observed but many of the structural cardiac defects still remaining, including ventricular septal and endocardial and endothelial defects. Thus, the VS, endocardial, and endothelial defects and myocardial proliferation defects are separable, and even if VS, endocardial, and endothelial defects contribute to a defect in myocardial proliferation, this contribution can be overcome by IGF-1 administration.

Reversion of transcriptional defects of *Id* KO myocardial cells and repair of the structural defects is not achieved with IGF-1 or ES cell IP injection alone. Rather, short-range effects of ES cells incorporated into chimeric hearts are required to see this full rescue of the Id mutant heart phenotype. We have identified WNT5a, a noncanonical member of the WNT signaling family, as likely playing a key role in the rescue, given that MEFs expressing WNT5a are capable of reverting myocardial markers from KO to WT levels in 85% of the loci examined in coculture experiments. Interestingly, ES cells in chimeras are probably producing a neomorphic effect with respect to WNT5a expression because the chimeric rescued embryos have a broader WNT5a expression pattern than observed in WT embryos. Whether this broadening of WNT5a expression is required for the near complete marker reversion observed in most of the *Id* KO cells in chimeric hearts has not been demonstrated.

The ES cell rescue reported here is dependent on the expression of the Id genes, because ES cells treated with Id1 siRNA fail to effect the rescue. Interestingly, the Ids have been shown to be sufficient for self-renewal in ES cells in culture (*22*). Although the levels at which Id is required in ES cells for the cardiac rescue observed have yet to be fully elucidated, maintenance of IGF-1 expression and expansion of the WNT5a expression pattern are likely to be critical components. In any event, it is clear from these studies that ES cells can provide factors missing from mutant mammalian embryos and induce neomorphic effects that can compensate for the effects of the mutation. Such properties may imbue ES cells with a greater therapeutic value than previously imagined.

References and Notes

1. M. B. Ruzinova, R. Benezra, *Trends Cell Biol.* **13**, 410 (2003).
2. Y. Jen, K. Manova, R. Benezra, *Dev. Dyn.* **207**, 235 (1996).
3. Y. Jen, K. Manova, R. Benezra, *Dev. Dyn.* **208**, 92 (1997).
4. D. Fraidenraich *et al.*, data not shown.
5. D. Lyden *et al.*, *Nature* **401**, 670 (1999).
6. R. Kelly, S. Alonso, S. Tajbakhsh, G. Cossu, M. Buckingham, *J. Cell Biol.* **129**, 383 (1995).
7. P. Bouillet *et al.*, *Dev. Biol.* **170**, 420 (1995).
8. M. Boudjelal *et al.*, *Genes Dev.* **11**, 2052 (1997).
9. R. G. Kelly *et al.*, *Dev. Biol.* **187**, 183 (1997).
10. S. Azmi, H. Sun, A. Ozog, R. Taneja, *J. Biol. Chem.* **278**, 20098 (2003).
11. T. H. Chen *et al.*, *Dev. Biol.* **250**, 198 (2002).
12. K. Reiss *et al.*, *Proc. Natl. Acad. Sci. U.S.A.* **93**, 8630 (1996).
13. M. Adamo, W. L. Lowe, Jr., D. LeRoith, C. T. Roberts Jr., *Endocrinology* **124**, 2737 (1989).
14. L. Powell-Braxton *et al.*, *Genes Dev.* **7**, 2609 (1993).
15. J. P. Liu, J. Baker, A. S. Perkins, E. J. Robertson, A. Efstratiadis, *Cell* **75**, 59 (1993).
16. K. M. Cadigan, R. Nusse, *Genes Dev.* **11**, 3286 (1997).
17. C. M. Tran, H. M. Sucov, *Development* **125**, 1951 (1998).
18. C. J. Hatcher *et al.*, *Dev. Biol.* **230**, 177 (2001).
19. J. Chen, S. W. Kubalak, K. R. Chien, *Development* **125**, 1943 (1998).
20. H. Wu, S. H. Lee, J. Gao, X. Liu, M. L. Iruela-Arispe, *Development* **126**, 3597 (1999).
21. D. E. Clouthier, S. C. Williams, R. E. Hammer, J. A. Richardson, M. Yanagisawa, *Dev. Biol.* **261**, 506 (2003).
22. Q. L. Ying, J. Nichols, I. Chambers, A. Smith, *Cell* **115**, 281 (2003).

23. We thank J. Massague and members of the Benezra lab for critically reading the manuscript, W. Mark, J.-H. Dong (Transgenic Facility), A. Viale (Microarray Facility), S. Curelariu (technical assistance), P. Soriano (R26 cells), Y. Yokota (Id2-deficient mice), V. Mittal and S. Gupta (Id1 knockdown ES cells), and the Molecular Cytology Core Facility. D.F. and R.B are funded by NIH grants KO1HL076568-01 and R01CA107429, respectively. C.T.B. is an AHA established investigator and supported by the Snart Cardiovascular Fund.

Supporting Online Material

www.sciencemag.org/cgi/content/full/306/5694/247/DC1
Material and Methods
Figs. S1 to S4
Tables S1 to S7
References

12 July 2004; accepted 13 August 2004

REPORTS

The Structure of Catalytically Active Gold on Titania

M. S. Chen and D. W. Goodman*

The high catalytic activity of gold clusters on oxides has been attributed to structural effects (including particle thickness and shape and metal oxidation state), as well as to support effects. We have created well-ordered gold monolayers and bilayers that completely wet (cover) the oxide support, thus eliminating particle shape and direct support effects. High-resolution electron energy loss spectroscopy and carbon monoxide adsorption confirm that the gold atoms are bonded to titanium atoms. Kinetic measurements for the catalytic oxidation of carbon monoxide show that the gold bilayer structure is significantly more active (by more than an order of magnitude) than the monolayer.

Highly dispersed Au particles exhibit exceptional catalytic activity for several reactions, including CO oxidation (*1*, *2*). On the basis of kinetic studies and scanning tunneling microscopy (STM) data, the most active structures of Au have been shown to consist of bilayer islands (*2*–*4*) that have distinctive electronic (*4*) and chemical (*5*, *6*) properties compared to bulk Au. Other explanations based on the Au particle shape or perimeter (*7*), the Au-oxide contact area (*8*), the metal oxidation state (*9*), and support effects (*7*, *10*) have also been proposed to account for the special catalytic properties of nanostructured Au particles (*11*, *12*). We now report an atomic-level, structure-activity relation for the catalytic activity of supported Au. Specifically, two well-ordered Au films, a (1×1) monolayer (ML) and a (1×3) bilayer, completely wet an ultrathin titanium oxide (titania) surface that was grown on a Mo(112) surface. Unprecedented catalytic activity for CO

Department of Chemistry, Texas A&M University, College Station, TX 77842–3012, USA.

*To whom correspondence should be addressed. E-mail: goodman@mail.chem.tamu.edu

oxidation was observed for the Au bilayer structure (Fig. 1).

We prepared the Mo(112)-(8×2)-TiO_x support by depositing ~1 ML of Ti from a filament source onto a Mo(112)-c(2×2)-[SiO_4] surface (*13*, *14*), which was then oxidized at 800 K and annealed at 1200 K (each step for 10 min in 5×10^{-8} torr of O_2). A subsequent anneal at 1400 K in 1×10^{-8} torr of O_2 for an additional 5 min completely removed the c(2×2)-[SiO_4] film and any residual Si (*15*, *16*). The TiO_x film so formed exhibited a sharp (8×2) low energy electron diffraction (LEED) pattern (Fig. 2) [The high-resolution electron energy loss (HREEL) spectra are shown in fig. S1.] This film synthesis is self-limiting, in that different initial Ti coverages upon annealing lead to TiO_x films with an identical Ti/Mo Auger electron spectroscopic (AES) ratio, corresponding to 1 ML. Furthermore, various Ti coverages when annealed to 1400 K show a single phonon feature at 84 meV, related to the Ti-O stretching mode and consistent with the (8×2)-TiO_x structure that corresponds to 1 ML (Fig. 3A, curve b). Because the 84-meV single phonon feature is considerably lower in energy loss than the 95-meV mode observed for bulk TiO_2 (*17*) and the ~103-meV mode for three-dimensional (3D) TiO_2 clusters on the Mo(112) surface, this mode likely originates from Ti^{3+}-O-Mo and/or Ti^{3+}-O-Ti^{3+} species anticipated to have a mode close to this value (*18*). Indeed, recent x-ray photoelectron spectroscopic data indicate a Ti oxidation state of +3 (fig. S2). A possible arrangement of Ti on the Mo(112) surface (Fig. 2A) has seven Ti atoms for every eight Mo atoms in the Mo(112) trough (the $[\bar{1}\bar{1}1]$ direction), bonded to the surface by Ti-O-Mo bonds and to each other by Ti-O-Ti linkages.

Gold disperses on the Mo(112)-(8×2)-TiO_x surface for submonolayer coverages when deposited at room temperature, as reflected by the linear relation of the Au/Mo AES ratio versus deposition time (Fig. 4) and also by the quenching of the Ti-O phonon feature in HREELS (Fig. 3A, curve c, and fig. S1). Upon annealing to 900 K, this disordered surface restructures to a well-ordered (1×1) structure, as indicated in its sharp LEED pattern (Fig. 2B). The marked increase in the Au/Mo and Au/Ti AES ratio after a 900 K anneal (Fig. 4, inset) is consistent with a strong interaction (i.e., with wetting of the TiO_x surface by Au). Wetting of the TiO_x surface by Au is also consistent with recent STM, and temperature-programmed desorption studies (figs. S2 and S3). Because the clean Mo(112) and 1-ML Au/Mo(112) surfaces annealed at 900 K in O_2 at ~10^{-8} torr exhibit a well-ordered p(2×3) and a poorly ordered p(1×3) LEED pattern (fig. S4), respectively, the (1×1) pattern is not due to the bare Mo(112) surface with Au and/or TiO_x clusters or to a Au/Mo(112) surface with TiO_x clusters, but rather arises from Au-TiO_x/Mo(112). The (8×2)-TiO_x surface was stable when annealed to 900 K in ultrahigh vacuum or in 5×10^{-9} torr of O_2 with respect to the observed LEED pattern and the appearance of the Ti-O phonon feature.

The formation of a Au film was confirmed by the appearance of a pronounced CO vibrational feature [$\nu_{(CO)}$] at 261 meV (2088 cm^{-1}) upon CO adsorption at 90 K (Fig. 3B, inset, and fig. S5), whereas no CO-related feature was observed after an identical exposure of CO to the Mo(112)-(8×2)-TiO_x surface. The observed CO frequency is very near the value of 2100 cm^{-1} found for CO on Au(332) (*19*) and on Au/TiO_2 (*20*). CO adsorbed on positively charged Au ($Au^{\delta+}$)

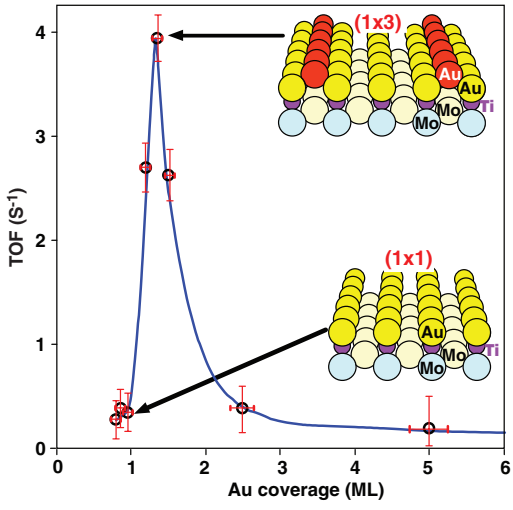

Fig. 1. Activity for CO oxidation at room temperature as a function of Au coverage above the monolayer on Mo(112)-(8×2)-TiO_x. The CO:O_2 ratio was 2:1, and the total pressure was 5 torr. The data represent initial rates derived by extrapolating the rate data to zero time. The TOF frequency for the (1×1) Au structure was calculated with the total number of Au atoms in the structure; we computed the TOF for the (1×3) structure by dividing the overall rate minus two-thirds the (1×1) rate (those reactive atom sites blocked by the second-layer Au) by the number of Au atoms in the second layer of the structure; for Au coverages >2.0 ML, the TOFs are based on total Au due to the formation of 3D clusters. Insets: Schematic models for the (1×1) and (1×3)-Au/TiO_x surfaces.

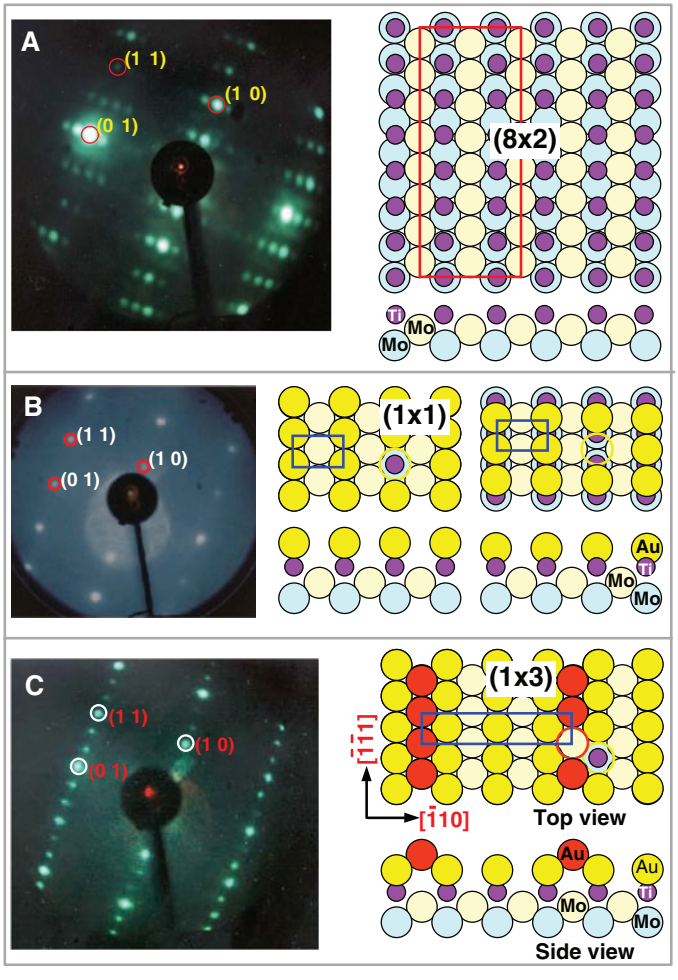

Fig. 2. LEED patterns and structural models, top and side views for (**A**) the Mo(112)-(8×2)-TiO_x; (**B**) the Mo(112)-(1×1)-(TiO_x, Au); and (**C**) the Mo(112)-(1×3)-(TiO_x, $Au_{1.33}$). The oxygen atoms are omitted from the models for clarity.

exhibits a feature at 2125 cm^{-1} (*20*), therefore; it is unlikely that Au in the structure shown in Fig. 2B is bonded to Ti by oxygen. It is more likely that Au bonds directly to a Ti atom that is coordinatively unsaturated, as reported for Au on TiO_2(110) (*21–23*). The direct bonding between Ti and Au is evident in the significant blue shift and broadening of the Ti-O phonon feature (Fig. 3A, curve d, and fig. S6) (*14*). This feature can be qualitatively deconvoluted into two components, one at ~90 meV and another at ~100 meV, which correspond to asymmetrical stretching of Ti^{4+}-O-Mo and Ti^{4+}-O-Ti^{4+} species, respectively. These data imply that the TiO_x layer, in bonding to Au and rearranging from the (8×2) to the (1×1) structure, is oxidized, consistent with the formation of $Au^{\delta-}$ (*3*, *4*, *21–23*). Two structures are possible, Au bonded directly over a Ti site or Au bridge-bonded between two Ti sites, each with a (1×1) unit cell containing one Au and one Ti atom (Fig. 2B). The arrangement of the Au atoms is similar to that in the Au(110) surface, but with the nearest Au-Au distance compressed to 2.73 Å from the 2.88 Å in Au(110) to fit the Mo(112) lattice. CO remains adsorbed on this Au surface up to ~150 K (fig. S5) (*14*), corresponding to a significant stabilization compared to 100 and 125 K for Au(111) and Au(110), respectively (*24*, *25*).

Sequential deposition of Au onto the (8×2)-TiO_x surface with a 900 K anneal after each deposition yields a (1×1) LEED pattern at a Au coverage of ~0.7 ML. With increasing Au coverages up to 1 ML, the (1×1) pattern becomes progressively sharper; 1 ML is defined by the AES break point at a deposition time of 36 min (Fig. 4). A (1×3) LEED pattern (Fig. 2C) is observed with an increase in the Au coverage from 1.0 to 1.2 ML and is apparent up to a Au coverage of 2.5 ML, suggesting that 3D clustering of Au occurs on top of the well-ordered (1×3) structure. A plot of the Au/Mo AES ratio versus deposition time (Fig. 4) is linear, with a second break point at 54 min. These break points coincide with the formation of the (1×1) and (1×3) Au structures at the first and second layers, respectively. The (1×1) and (1×3) Au surfaces are stable at 900 K and an oxygen pressure of 2×10^{-8} torr.

Because the (1×3) structure appears after deposition of an additional 0.2 to 0.5 ML of Au onto the (1×1) structure, the coverage of the (1×3) structure is assumed to be four-thirds ML (Fig. 2C). In the (1×3) structure, a second row of Au atoms is located above the first layer of Au atoms. Upon formation of this bilayer structure, the $\nu_{(CO)}$ blue-shifts slightly to a frequency very near that of metallic Au (Fig. 3B, inset). The intensity of the CO band relative to the Ti-O phonon feature for saturation CO coverage at 90 K increases with increasing Au coverages up to 1 ML, then decreases (Fig. 3B). A second maximum with a two-thirds intensity of that at 1 ML is observed at a Au coverage of 1.4 ML [corresponding to the Au-(1×3) structure].

To test the catalytic efficacy of the discrete (1×1) and (1×3) structures of Au on TiO_x-Mo(112), CO oxidation was investigated at realistic reaction conditions (*26*) as a function of the Au coverage (Fig. 1). The initial turnover frequencies (TOFs) for CO oxidation at room temperature over the (1×1) Au (monolayer) structure were significantly lower than the rate over the (1×3) Au (bilayer) structure. The specific rate per unit area found for the Au-(1×3) surface was >45 times that previously reported for the most active high-surface-area Au/TiO_2 catalysts (*27*). If we assume that the Au-(1×3) structure is the optimum catalytic morphology, a factor of ~45 then represents the potential for improvement in existing supported Au catalysts for CO oxidation. At Au coverages in excess of 1.33 ML, the reaction rate falls sharply from its maximum for the Au-(1×3) structure. This decrease is likely a consequence of either (i) the additional Au forming 3D clusters with low activities on the (1×3) structure that partially block access to the active Au-(1×3) surface sites and/or (ii) a decrease in the optimum ratio of the first- and second-layer Au sites. The specific rates measured in this study for the Au-(1×3) sites agree closely with the rates reported previously for Au clusters supported on TiO_2(110), where an activity maximum was observed for Au structures with two atomic layers in thickness (*2*).

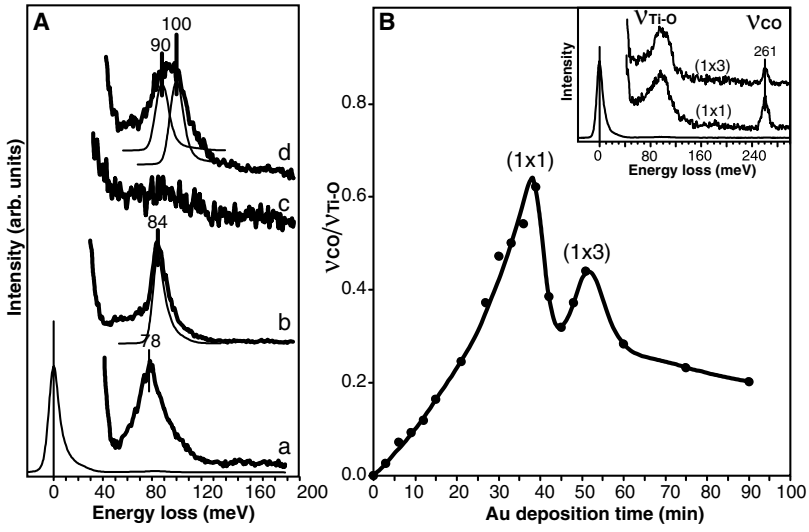

Fig. 3. (**A**) HREEL spectra for (a) annealing the Mo(112) at 800 and 1200 K in 5×10^{-8} torr of O_2 for 10 min each, then at 1400 K in 1×10^{-8} torr of O_2 for an additional 5 min; (b) the Mo(112)-(8×2)-TiO_x; (c) 1-ML Au deposited on the Mo(112)-(8×2)-TiO_x at room temperature; and (d) the material in (c) after annealing at 900 K for 10 min. (**B**) Relative intensities of $\nu_{(CO)}/\nu_{(Ti-O)}$ versus Au deposition onto the Mo(112)-TiO_x surface; CO was adsorbed to saturation at 90 K. Inset: HREEL spectra after CO adsorption on the (1×1) and (1×3) surfaces.

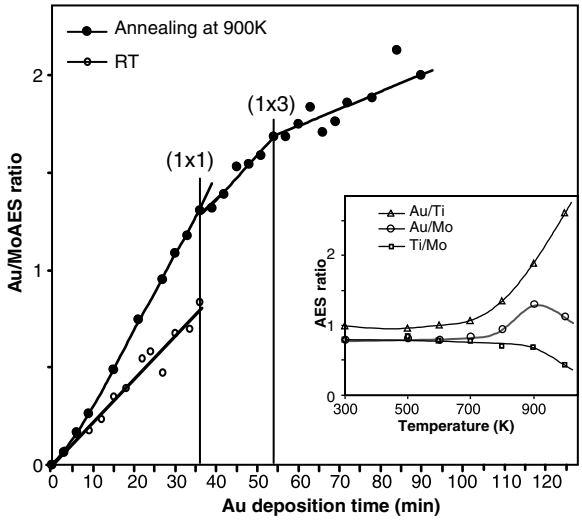

Fig. 4. Plots of Au/Mo AES ratios versus deposition time. Inset: A plot of the indicated AES ratios as a function of the anneal temperature for 1-ML Au on Mo(112)-(8×2)-TiO_x. RT, room temperature.

Explanations for the exceptional activity of Au nanostructures often include a direct role played by the support, such as at the perimeter of the Au-support interface (*7*, *9*, *28*, *29*). Our data show that the TiO_x support is crucial as a dispersant and a promoter of the Au overlayer, but that TiO_x itself cannot be directly involved in the bonding of O_2 or CO, because in the Au-(1×1) and -(1×3) structures, the Au overlayer precludes access to the Ti cation sites by the reactants. That an optimum reactivity is seen for the (1×3) Au structure strongly suggests that a combination of the first- and second-layer Au sites is necessary to promote reaction between CO and O_2. The interaction of the first-layer Au with Ti^{3+} of the support, yielding $Au^{\delta-}$, likely is crucial for activation of O_2 (*3*, *4*, *21–23*). CO, however, has been shown to adsorb strongly on the Au bilayer structure (*5*, *6*). For the more general case of Au/TiO_2, mono- and bilayer Au islands in the <4-nm diameter range form as a result of Au atoms nucleating initially at Ti^{3+} defect sites (*2*), then with the addition of more Au, evolve into Au bilayer islands stabilized by the bonding between the interfacial Au atoms and Ti^{3+} defects that accumulate at the Au-TiO_2 interface (*21–23*, *30*). The mono- and bilayer Au islands seen for Au on TiO_2(110) (*2*) have also been observed for Au supported on high-surface-area TiO_2 by Lupini and co-workers (*31*). These mono- and bilayer Au structures appear to be truncated analogs of the extended Au-(1×1) and Au-(1×3) structures described here. In the arrangement of the (1×3) surface, all the first-layer atoms of the bilayer Au structure are accessible to the reactants, a morphology that may very well contribute to its exceptional catalytic activity.

Recent density functional theoretical calculations have shown that O_2 adsorbs preferentially and readily dissociates at the Au-TiO_2 interface (*32*). However, as we noted earlier, for the Au-(1×3) structure, access by O_2 to the Au and Ti interface is precluded. In any case, if O_2 activation is promoted by the Au-(1×1) sites and CO adsorbs on the Au-(1×3) sites, theory predicts a relatively small barrier for the CO-O_2 reaction (*33*).

References and Notes

1. M. Haruta, N. Yamada, T. Kobayashi, S. Ijima, *J. Catal.* **115**, 301 (1989).
2. M. Valden, X. Lai, D. W. Goodman, *Science* **281**, 1647 (1998).
3. D. W. Goodman, *J. Catal.* **216**, 213 (2003).
4. C. Chusuei, X. Lai, K. Luo, Q. Guo, D. W. Goodman, *Top. Catal.* **14**, 71 (2001).
5. D. C. Meier, D. W. Goodman, *J. Am. Chem. Soc.* **126**, 1892 (2004).
6. V. A. Bondzie, S. C. Parker, C. T. Campbell, *Catal. Lett.* **63**, 143 (1999).
7. M. Haruta, *CATTECH* **6**, 102 (2002).
8. J. J. Pietron, R. M. Stroud, D. R. Rolison, *Nano Lett.* **2**, 545 (2002).
9. J. Guzman, B. C. Gates, *J. Am. Chem. Soc.* **126**, 2672 (2004).
10. M. M. Schubert *et al.*, *J. Catal.* **197**, 113 (2001).
11. A. T. Bell, *Science* **299**, 1688 (2003).
12. N. Lopez *et al.*, *J. Catal.* **223**, 232 (2004).
13. M.-S. Chen, A. K. Santra, D. W. Goodman, *Phys. Rev. B* **69**, 155404 (2004).
14. Materials and methods are available as supporting material on *Science* Online.
15. M.-S. Chen, D. W. Goodman, in preparation.
16. Annealing multilayer Ti_2O_3 or TiO_2 on a Mo(112)-c(2×2)-[SiO_4] surface induces an interface restructuring of the [SiO_4] surface followed by decomposition or desorption at 1200 K.
17. Q. Guo, W. S. Oh, D. W. Goodman, *Surf. Sci.* **437**, 49 (1999).
18. The Mo-O phonon feature is at 78 meV, as deduced from the Mo(112) surface (Fig. 3A, curve a); the comparable feature for Ti_2O_3 is at 88 meV (*17*). A single phonon at 70 meV, corresponding to Ti^{2+}-O-$Pd^{\delta+}$, was observed on a Pd-TiO_x complex (*34*) (fig. S7). This feature for a Ti^{3+}-O-Mo species should appear between 78 and 88 meV.
19. C. Ruggiero, P. Hollins, *Surf. Sci.* **377–379**, 583 (1997).
20. F. Boccuzzi *et al.*, *J. Catal.* **202**, 256 (2001).
21. E. Wahlström *et al.*, *Phys. Rev. Lett.* **90**, 026101 (2003).
22. A. Vijay, G. Mills, H. Metiu, *J. Chem. Phys.* **118**, 6536 (2003).
23. N. Lopez *et al.*, *J. Catal.* **223**, 232 (2004).
24. P. D. Holmes, B. E. Koel, *J. Vac. Sci. Technol. A* **8**, 2585 (1990).
25. D. A. Outka, R. J. Madix, *Surf. Sci.* **179**, 351 (1987).
26. M. Haruta *et al.*, *J. Catal.* **144**, 175 (1993).
27. The factor of 45 is based on a reaction rate for the Au-(1×3) structure of 1.82×10^{-5} mol·s^{-1}·m^{-2} compared to a rate of 4.0×10^{-7} mol·s^{-1}·m^{-2} at comparable reaction conditions for high-surface-area supported Au (*35*).
28. G. C. Bond, D. T. Thompson, *Catal. Rev. Sci. Eng.* **41**, 319 (1999).
29. F. Cosandey, T. E. Madey, *Surf. Rev. Lett.* **8**, 73 (2001).
30. J. A. Rodriguez *et al.*, *J. Am. Chem. Soc.* **124**, 5242 (2002).
31. A. R. Lupini *et al.*, in preparation.
32. Z.-P. Liu, X.-Q. Gong, J. Kohanoff, C. Sanchez, P. Hu, *Phys. Rev. Lett.* **91**, 266102 (2003).
33. L. M. Molina, M. D. Rasmussen, B. Hammer, *J. Chem. Phys.* **120**, 7673 (2004).
34. M.-S. Chen, D. W. Goodman, unpublished data.
35. T. V. Choudhary *et al.*, *J. Catal.* **207**, 247 (2002).

36. We thank Y. Kuroda (Okayama University) for his valuable assistance as a visiting scientist and W. T. Wallace, B. K. Min, K. Gath, E. Ozensoy, C.-W. Yi, Z. Yan, and K. Luo for fruitful discussions, comments, and the supporting data displayed online. Supported by the U.S. Department of Energy, Office of Basic Energy Sciences, Division of Chemical Sciences; the Robert A. Welch Foundation; and the Texas Advanced Technology Program under grant no. 010366-0022-2001.

Supporting Online Material

www.sciencemag.org/cgi/content/full/1102420/DC1
Materials and Methods
Figs. S1 to S7

7 July 2004; accepted 16 August 2004
Published online 26 August 2004;
10.1126/science.1102420
Include this information when citing this paper.

Accelerated Sea-Level Rise from West Antarctica

R. Thomas,[1,2]* E. Rignot,[2,3] G. Casassa,[2] P. Kanagaratnam,[4] C. Acuña,[2] T. Akins,[4] H. Brecher,[5] E. Frederick,[1] P. Gogineni,[4] W. Krabill,[6] S. Manizade,[1] H. Ramamoorthy,[4] A. Rivera,[2,7] R. Russell,[1] J. Sonntag,[1] R. Swift,[1] J. Yungel,[1] J. Zwally[6]

Recent aircraft and satellite laser altimeter surveys of the Amundsen Sea sector of West Antarctica show that local glaciers are discharging about 250 cubic kilometers of ice per year to the ocean, almost 60% more than is accumulated within their catchment basins. This discharge is sufficient to raise sea level by more than 0.2 millimeters per year. Glacier thinning rates near the coast during 2002–2003 are much larger than those observed during the 1990s. Most of these glaciers flow into floating ice shelves over bedrock up to hundreds of meters deeper than previous estimates, providing exit routes for ice from further inland if ice-sheet collapse is under way.

Perhaps half the present increase in global sea level of ~1.8 mm/year is caused by melting of terrestrial ice (*1*). During the 1990s, nonpolar glaciers accounted for an estimated 0.4 mm/year (*2*) and Greenland for ~0.15 mm/year (*3*). Although data from Antarctica are still sparse, they suggest a net loss from West Antarctica equivalent to ~0.2 mm/year and approximate balance in East Antarctica, where uncertainty remains large (*4*). Substantial grounding line retreat (*5*, *6*), thinning (*7*), and acceleration (*8*) have been observed on glaciers flowing into the Amundsen Sea, with small ice shelves now but larger ones in the past (*9*). These glaciers flow into ice shelves over beds well below sea level, and sustained thinning would allow them to float free from bedrock, potentially easing resistive forces acting on upstream ice

[1]EG&G Inc., NASA Goddard Space Flight Center (GSFC)/Wallops Flight Facility (WFF), Building N-159, Wallops Island, VA 23337, USA. [2]Centro de Estudios Científicos (CECS), Avenida Arturo Prat 514, Casilla 1469, Valdivia, Chile. [3]Jet Propulsion Laboratory (JPL), 4800 Oak Grove Drive, Pasadena, CA 91109, USA. [4]Radar Systems and Remote Sensing Laboratory, University of Kansas, Lawrence, KS 66045, USA. [5]Byrd Polar Research Center, Ohio State University, Columbus, OH 43210, USA. [6]Code 972, NASA-GSFC, Greenbelt, MD 20771, USA. [7]Departamento de Geografía, Universidad de Chile, Casilla 3387, Santiago, Chile.

*To whom correspondence should be addressed. E-mail: thomas@osb.wff.nasa.gov

and thereby leading to further glacier acceleration.

The extent to which ice shelves affect the dynamics of tributary glaciers remains an unresolved controversy within glaciology. Early suggestions that ice-shelf weakening would result in increased discharge from the ice sheet (*10*–*12*) require ice-shelf "back forces" to affect glacier dynamics over long distances. If correct, this implies that "marine ice sheets" with beds deep below sea level may be vulnerable to rapid collapse if their deep beds extend to the coast and if buttressing ice shelves are removed. But if glacier behavior is determined mainly by local conditions, it is almost immune to distant perturbations (*13*, *14*). The behavior of the Amundsen Sea glaciers, recent acceleration of tributary glaciers soon after ice-shelf breakup along the east side of the Antarctic Peninsula (*15*), and rapid acceleration of Greenland's fastest glacier, Jakobshavn Isbrae, after thinning and breakup of its floating tongue (*16*, *17*) may help to resolve this issue, which is particularly important because it could imply far more rapid ice discharge than currently predicted (*1*) from Antarctica in a warmer climate.

Understanding these observations and predicting future glacier behavior requires detailed measurements of surface elevation and ice thickness, but the remoteness of the Amundsen Sea glaciers limited comprehensive measurements until late 2002, when surveys were made from Punta Arenas by CECS aboard a Chilean Navy P-3 aircraft equipped with NASA sensors, including a conically scanning laser altimeter (*18*) and ice-sounding radar (*19*). Four flights yielded measurements of surface elevations (to ±0.4 m) at a dense array of 2-m laser footprints within a swath ~500 m wide, and ice thickness to ±20 m, along a total flight track of 3500 km. Surveys included Pine Island (PIG), Thwaites (THW), Haynes (HAY), Pope (POP), Smith (SMI), and Kohler (KOH) glaciers (Fig. 1), where our measurements show much deeper bedrock near the coast than had been estimated earlier (*20*). For the flight running mainly close to the coast between PIG and KOH, the bedrock was on average 400 m deeper than previous estimates (Fig. 2), reaching more than 1 km deeper for the SMI and KOH glacier troughs where no data had previously been obtained, with beds up to 2 km below sea level that may connect to the Byrd Subglacial Basin (BSB). Flights over PIG show its northern side to be shallower than earlier estimates, but its main trunk and particularly its southern tributaries are deeper further inland, suggesting another link to the BSB and the potential for ice-sheet collapse if suggestions that marine ice sheets are susceptible to near-coastal perturbations are correct (*10*–*12*). Using our ice-thickness measurements, together with velocity estimates for 1996 (SMI, HAY, KOH, POP) and 2000 (PIG, THW) derived from interferometric synthetic aperture radar (InSAR), we find that the entire ice-sheet sector [earlier estimates (*4*–*6*) only addressed individual glaciers] bounded by and including PIG and KOH discharged 253 ± 5 km^3/year of ice at the time of the velocity measurements, compared to a total annual snow accumulation equivalent of 160 ± 16 km^3 of ice over a catchment area of 393,000 km^2 (*21*).

Satellite radar altimetry data show all surveyed glaciers to have thinned rapidly during the 1990s (*5*, *22*), with thinning rates decreasing from ~2, 3, and 5 m/year near PIG, THW, and SMI grounding lines, respectively, to ~0.1 m/year hundreds of kilometers inland. Comparison of our measurements with surface elevations derived from satellite laser altimeter data acquired by NASA's ICESat (*22*, *23*) in late 2003 and early 2004 shows thinning for each of the

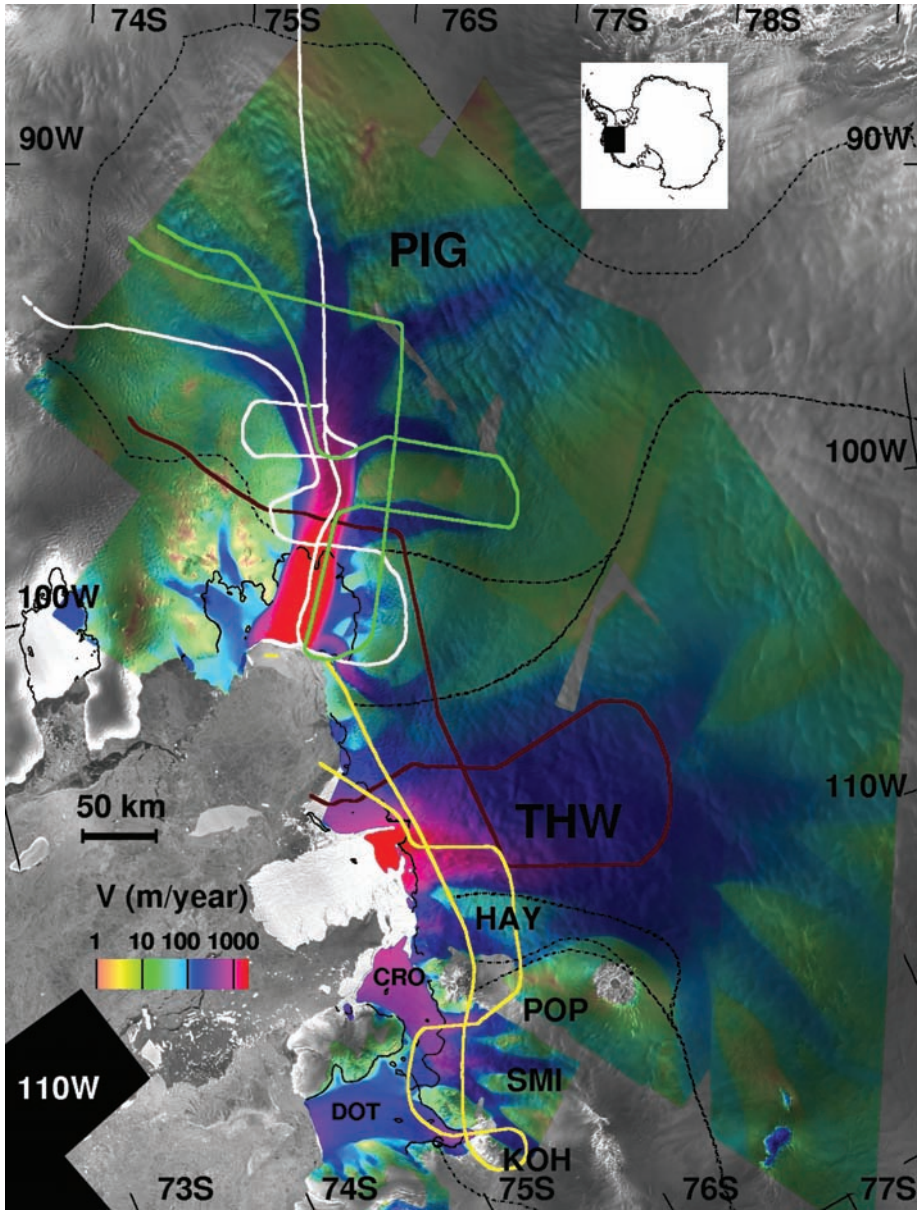

Fig. 1. Part of West Antarctica, showing ice velocities (on a logarithmic scale) derived from 1996 European Remote Sensing Satellites 1 and 2 (ERS-1/2) interferometric radar data (*21*), overlaid on a radar image from Radarsat (*28*). The four CECS/NASA flight lines over Pine Island (PIG), Thwaites (THW), Haynes (HAY), Pope (POP), Smith (SMI), and Kohler (KOH) glaciers, and Crosson (CRO) and Dotson (DOT) ice shelves, are shown in white, brown, yellow, and green lines. Boundaries of catchment basins are marked as thin broken black lines. Grounding line positions in 1996 inferred from ERS-1/2 are shown as thin continuous black lines. Inset shows location in Antarctica.

four flight lines (Fig. 3), with average values ranging from 0.4 m/year (for the flight primarily over PIG tributaries) to 1.8 m/year (for the flight crossing the seaward ends of THW, HAY, POP, SMI, and KOH), and a mean value of 1.0 m/year for all flights. Although the short time interval implies that elevation changes less than a few tens of centimeters per year may simply reflect natural fluctuations in snow accumulation rates, our results show many areas with changes greater than 1 m/year and a pattern of rapid thinning over fast-moving parts of surveyed glaciers. If the 1 m/year average thinning typifies conditions within the ~60,000 km^2 encompassed by our survey, this alone represents a volume loss of ~60 km^3/year from only 15% of the total catchment area. Although this estimate is approximate, it is consistent with losses inferred from mass-budget calculations if average thinning over the rest of the catchment area is 0.1 m/year, as inferred from satellite radar altimetry data (*22*).

Thinning rates near the grounding lines of all surveyed glaciers reach local maxima exceeding 5 m/year, but with high spatial variability resulting from rapid forward motion of the undulating surface. These values are much higher than the earlier estimates, partly because of the smoothing effect of large radar footprints (several kilometers, versus laser footprints of ~2 m for aircraft and 60 m for ICESat), which results in underestimation of high thinning rates along narrow channels occupied by some outlet glaciers, and partly because of a real increase in thinning. Our results from 2002–2003 and 2004 show thinning along the entire main trunk of PIG (Fig. 4A), averaging ~1.2 m/year between 100 and 300 km inland from the grounding line, or double the value from satellite radar altimetry (*24*) for the period 1992–1999 in an area of smoother near-horizontal ice where the radar measurements should give reliable estimates. Further west, flights over THW, SMI, and KOH show rapid thinning within 50 km of the coast (Fig. 4B), decreasing with increasing distance from the sea. This follows a similar pattern to that inferred from satellite radar altimetry (*7*), but with higher thinning rates within 50 km of grounding lines. Further inland, within the THW catchment basin, our results agree with those from radar altimetry data (*7*) indicating little change in thinning rates. This region has surface characteristics very similar to those of inland regions of PIG, where our results show thinning rates approximately double those from earlier radar altimetry data, lending confidence to our conclusion that these measurements show a real increase in thinning rates.

Earlier observations (*25*) showed the seaward 25 km of PIG to be a grounded "ice plain" with surface elevation less than 30 m above flotation elevation. Our 2002 measurements include resurvey of a 1998 airborne survey (*25*), with estimated surface elevation errors of ±0.7 m, and show surface lowering by 20 to 30 m across the ice plain during the 5-year interim. Similar high thinning rates are also shown by comparison of our measurements with those from ICESat along an orbit track that followed our flight line across the ice plain (Fig. 4C). If this continues, most of the ice plain should float free from its bed within the next 5 years.

Flotation of parts of the ice plain may have been responsible for a 9% PIG velocity increase (*8*) between 1996 and 2001 (*26*), representing almost half the 22% increase between 1974 and 2000 (*27*). Here, we compared 24-day repeat data collected by RADARSAT-1 in January–February 2003 and in April 2001, using a speckle-tracking technique, to show that PIG velocity increased another 3.5 ± 0.5% during that time period. This new observation of continued velocity increase is consistent with the increase in thinning rates inferred from our

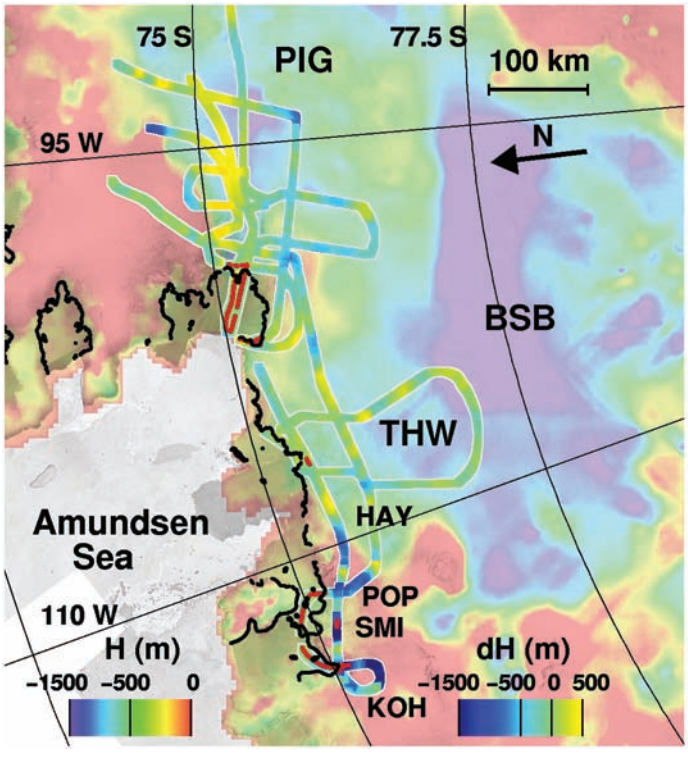

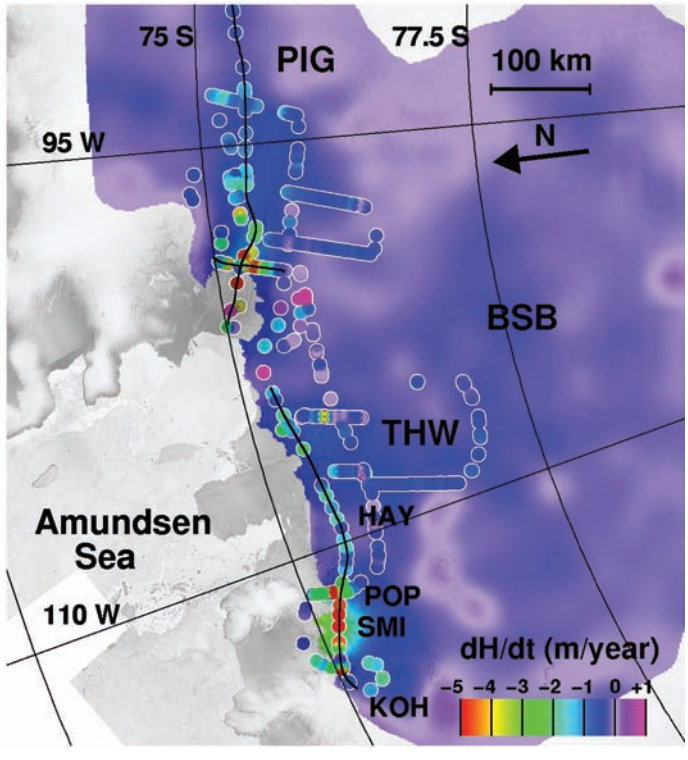

Fig. 2 (left). Bed topography, *H* (*20*), of Amundsen Sea glaciers, omitting elevations above sea level (color scale at lower left), and differences, *dH*, between this and our measurements along flight tracks (color scale at lower right). Sections of floating ice along flight tracks are shown in red. Grounding line positions in 1996 are shown in black. BSB marks the location of the Byrd Subglacial Basin. **Fig. 3 (right).** Thinning rates, *dH*/*dt*, interpolated from ERS-1/2 radar altimetry comparisons (*7*) over Amundsen Sea glaciers, with overlaid values obtained by comparing CECS/NASA airborne and ICESat satellite laser altimetry data. Thin black lines mark locations of profiles shown in Fig. 4.

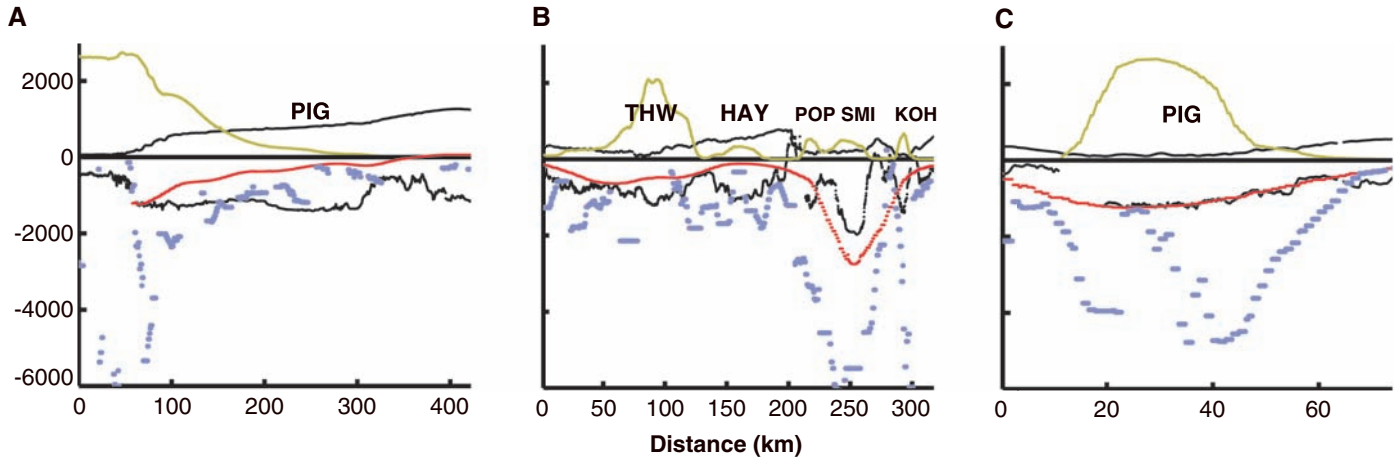

Fig. 4. Surface and bed elevations, shown on the *y* axis in meters (black lines), and rates of elevation change in millimeters per year [red for earlier estimates from ERS-1/2 radar altimetry data (*7*); blue for our results], plotted against distance along sections of flight tracks shown in Fig. 3 for measurements (**A**) along PIG from the ice shelf to the interior; (**B**) along the coast crossing THW, HAY, POP, SMI, and KOH from east to west; and (**C**) across the main trunk of PIG near the grounding line starting from the north. Thinning is largest along the channels of ice discharge occupied by glaciers, as indicated by the ice velocity shown in yellow in meters per year on the *y* axis. High spatial variability in our estimated thinning rates is apparent near the PIG grounding line [(A) and (C)], where down-glacier motion of high-amplitude surface undulations causes excessive local thickening at some locations and thinning at others nearby.

elevation measurements on PIG. Flotation of the entire ice plain is likely to result in further glacier acceleration and additional increases in total ice discharge. The bed of the ice plain deepens from 600 m (below sea level at the grounding line) to 1300 m (25 km further inland) (Fig. 4A). This large thickness slope, together with rapid glacier motion, favors advection thickening by several tens of meters per year as thicker ice moves seaward. Even so, glacier thinning dominates, indicating that thinning by longitudinal stretching exceeds advection thickening. Inland of the ice plain, the bed is almost horizontal for 250 km, and if the grounding line retreats to this deeper region, advection of thicker ice will decrease by an order of magnitude, allowing more rapid thinning. All surveyed glaciers have similar deep beds with ice plains close to flotation in regions more than 10 km upstream from their 1996 grounding-line positions (Fig. 2), making all of them vulnerable to a rapid and widespread response to thickness change.

The catchment regions of Amundsen Sea glaciers contain enough ice to raise sea level by 1.3 m (*6*). Our measurements show them collectively to be 60% out of balance, sufficient to raise sea level by 0.24 mm/year. Although these glaciers are the fastest in Antarctica, they are likely to flow considerably faster once the ice shelves are removed and glacier retreat proceeds into the deeper part of glacier basins.

References and Notes

1. Intergovernmental Panel on Climate Change, *IPCC Third Assessment Report, Climate Change 2001: The Scientific Basis* (Cambridge Univ. Press, Cambridge, 2001).
2. M. Dyurgerov, *Polar Geogr.* **25**, 241 (2001).
3. W. Krabill *et al.*, *Science* **289**, 428 (2000).
4. E. Rignot, R. Thomas, *Science* **297**, 1502 (2002).
5. E. Rignot, *Science* **281**, 549 (1998).
6. E. Rignot, *J. Glaciol.* **47**, 213 (2001).
7. A. Shepherd, D. Wingham, J. Mansley, *Geophys. Res. Lett.* **29** (no. 10), 1364 (2002).
8. E. Rignot, D. Vaughan, M. Schmeltz, T. Dupont, D. MacAyeal, *Ann. Glaciol.* **34**, 189 (2002).
9. T. Kellogg, D. Kellogg, *J. Geophys. Res.* **92**, 8859 (1987) .
10. T. Hughes, *ISCAP Bull.* (Ohio State University), no. 1 (1972).
11. J. Mercer, *Nature* **27**, 321 (1978).
12. R. Thomas, *Geogr. Phys. Quat.* **31**, 347 (1977).
13. P. Huybrechts, *Ann. Glaciol.* **14**, 115 (1990).
14. R. Hindmarsh, *Ann. Glaciol.* **23**, 105 (1993).
15. H. De Angelis, P. Skvarca, *Science* **299**, 1560 (2003).
16. R. Thomas *et al.*, *J. Glaciol.* **49**, 231 (2003).
17. R. Thomas, *J. Glaciol.*, in press.
18. W. Krabill *et al.*, *J. Geodyn.* **34**, 357 (2002).
19. S. Gogineni *et al.*, *J. Geophys. Res.* **106**, 33761 (2001).
20. M. Lythe, D. Vaughan, *J. Geophys. Res.* **106**, 11335 (2001).
21. E. Rignot *et al.*, *Ann. Glaciol.*, in press.
22. J. Zwally *et al.*, *J. Geodyn.* **34**, 405 (2002).
23. NASA's ICESat (Ice, Cloud, and Land Elevation Satellite) was launched into near-polar orbit in February 2003 carrying a laser altimeter (*22*) that operated during February–March and September–November 2003 and during February–March 2004. Some of our aircraft surveys were along ICESat orbits, and all crossed orbit tracks at many locations. Overlapping (by 50%) planar surfaces, or "platelets," were fit to the ~1200 aircraft measurements on each side of the aircraft within a 70-m along-track distance, generally with root-mean-square fit of 10 cm or less. These were compared with ICESat footprint elevations by extrapolating elevations from any platelet within 200 m distance (using the platelet slope), yielding almost 7000 comparisons. The major source of aircraft survey errors was laser pointing, with errors magnified by the 15° off-nadir scan angle. For the ~1000-m altitude flown and a typical maximum roll error of 0.05° (effects of pitch errors are averaged out in the platelet calculation), the resulting elevation error is <0.3 m, with opposite signs on each side of the surveyed swath. Because we averaged about four adjacent ICESat/aircraft comparisons that included data from each side of the aircraft, effects of these roll errors should be largely canceled. Other error sources contribute about ±0.2 m. Accuracy of ICESat measurements is determined mainly by errors in laser pointing and by forward scattering in thin clouds, with the latter edited from the data on the basis of distortion of laser return waveforms. We estimated pointing errors for the September–November 2003 and the 2004 measurements to be <5 arc sec by comparing ICESat data with aircraft surveys over undulating terrain in Antarctica, Greenland, and arid parts of the western United States. Most of our Amundsen glacier surveys were over slopes less than 2°, resulting in slope-induced errors less than ±0.5 m. Consequently, estimated (largely random) errors in elevation changes are less than ±0.6 m. ICESat pointing errors for February–March 2003 data were larger (up to 40 arc sec) and are not included in this analysis.
24. A. Shepherd, D. Wingham, J. Mansley, H. Corr, *Science* **291**, 862 (2001).
25. H. Corr, C. Doake, A. Jenkins, D. Vaughan, *J. Glaciol.* **47**, 51 (2001).
26. R. Thomas, E. Rignot, P. Kanagaratnam, W. Krabill, G. Casassa, *Ann. Glaciol.*, in press.
27. I. Joughin, E. Rignot, C. Rosanova, B. Lucchitta, J. Bohlander, *Geophys. Res. Lett.* **30** (no. 13), 1706 (2003).
28. H. Liu, K. Jezek, B. Li, *J. Geophys. Res.* **104**, 23199 (1999).

29. We dedicate this work to the memory of Niels Gundestrup, who did much to make the project possible despite serious illness. We thank pilots, crew, technicians, and staff from the Armada de Chile, University of Kansas, NASA/WFF, and CECS who helped make the surveys over Antarctica; the British Antarctic Survey, NSF, U.S. Geological Survey, NOAA, Dirección Meteorológica de Chile, and the field team at Base Carvajal for providing weather reports/forecasts and GPS data that made possible the flights and subsequent accurate trajectory calculations; A. Shepherd for estimates of elevation change rates (*7*); NASA's ICESat Project for satellite laser altimeter elevation measurements; and T. Hughes and an anonymous reviewer for suggesting improvements to the paper. Supported by CECS, through Fundación Andes and the Millennium Science Initiative, and by NASA's Cryospheric Processes Program. E.R. performed his work at JPL under a contract with this program.

27 April 2004; accepted 9 September 2004
Published online 23 September 2004;
10.1126/science.1099650
Include this information when citing this paper.

Variable Azimuthal Anisotropy in Earth's Lowermost Mantle

Edward J. Garnero,[1]* Valérie Maupin,[2] Thorne Lay,[3] Matthew J. Fouch[1]

A persistent reversal in the expected polarity of the initiation of vertically polarized shear waves that graze the D″ layer (the layer at the boundary between the outer core and the lower mantle of Earth) in some regions starts at the arrival time of horizontally polarized shear waves. Full waveform modeling of the split shear waves for paths beneath the Caribbean requires azimuthal anisotropy at the base of the mantle. Models with laterally coherent patterns of transverse isotropy with the hexagonal symmetry axis of the mineral phases tilted from the vertical by as much as 20° are consistent with the data. Small-scale convection cells within the mantle above the D″ layer may cause the observed variations by inducing laterally variable crystallographic or shape-preferred orientation in minerals in the D″ layer.

The D″ layer is located at the base of Earth's silicate lower mantle, where it meets the liquid iron outer core. The D″ layer plays a critical role in Earth's dynamical evolution because it acts as the lower boundary layer in the convecting mantle system (*1*, *2*). Seismic wave speed dependence on propagation direction, seismic anisotropy, is present in D″ (*3*) and may trace mineral and structural fabric alignment (*4*). High-resolution investigations of D″ anisotropy are restricted to a few regions as a result of geographical limitations in the distribution of earthquake sources and seismic sensors; these regions are located beneath the Caribbean Ocean, Alaska, the central Atlantic, the central and southern Pacific, central Eurasia, and southern India (fig. S1) (*5*–*12*). Ground velocity recordings (Fig. 1) allow us to distinguish the downward arrival of an impulsive vertically polarized shear wave (SV) having a polarity opposite to that of SKS (an S-wave with a portion of its path as a P-wave in the outer core) and arriving seconds after the onset of the horizontally polarized shear wave (SH). This apparent decoupling of the SH and SV components has been observed in previous studies (fig. S2) (*5*, *13*) and has led to the interpretation of extensive transverse isotropy with a vertical axis of symmetry (VTI) in D″ (*14*). VTI can arise from preferred orientation of anisotropic crystals within the D″ layer or alternatively from fine-scale lamellae of strongly contrasting material properties (*10*, *13*).

However, on ground displacement waveforms there is SV energy with the same polarity as SKS, arriving at the same time as the initial SH motion. This is consistent with a projection of the fast polarization arrival onto SH and SV components, an indication of azimuthal anisotropy (*15*). The SH arrival involves two impulsive ground velocity signals and a correspondingly complex displacement record. This feature can be accounted for by triplication of the S wave as the result of an abrupt 2 to 3% velocity discontinuity at the top of D″. The first arrival involves energy refracting below the discontinuity; the second is energy reflected from the discontinuity (*6*, *16*, *17*).

Source complexity or deconvolution problems are ruled out as the cause of the SV waveform complexity because SKS signals show no corresponding reversed onsets. SV-to-P conversions at the receiver are precluded by the rotation of the three orthogonal components of ground displacement to the incident wavefront and the lack of any precursors for SKS arrivals. Models with complex D″ lamellae and VTI structures (*13*), and with three-dimensional isotropic heterogeneities (*18*), show that it is difficult to produce reversed SV onsets without introducing azimuthal anisotropy. We explore models in which the D″ discontinuity coincides with the onset of anisotropy 250 km above the core-mantle boundary, such that azimuthal anisotropy affects the first arrival, which penetrates into the D″ layer.

We focus on D″ structure beneath the Caribbean, the region with the greatest sampling by high-quality broadband data, provided by S waves from intermediate- and deep-focus South American earthquakes recorded by the Canadian National Seismographic Network (CNSN). The epicentral distance range (87° to 112°) is such that waves graze or diffract horizontally through the D″ layer (fig. S2). Broadband data were deconvolved by the instrument responses to obtain ground surface displacement recordings and then rotated into the reference frame of the incoming S wavefront to obtain SH and SV motion, minimizing crustal SV-to-P conversions (*19*). Data with impulsive signals and favorable signal-to-noise ratios for SH and SV energy were retained, reducing our initial data set from 120 to 16 earthquakes recorded at 19 broadband CNSN stations, comprising 89 individual high-quality displacement traces. Data were corrected for upper-mantle anisotropy by using shear-wave splitting parameters published for CNSN stations (*20*, *21*) and were discarded when corrections did not adequately remove SKS energy from the SH component.

Introduction of azimuthal anisotropy increases the number of model space parameters. Limited azimuthal sampling restricts

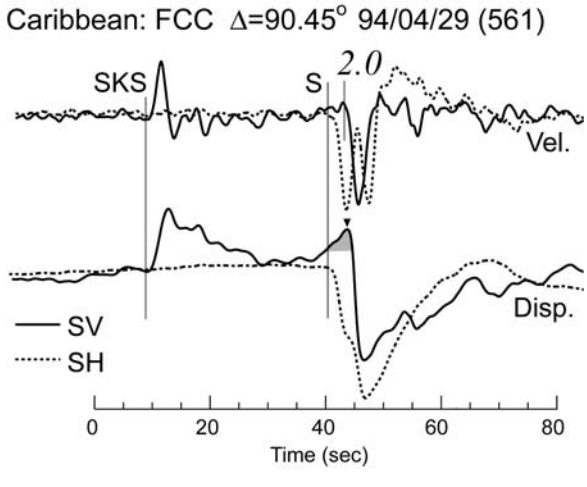

Fig. 1. Broadband shear-wave data from station FCC (Fort Churchill, Canada) for the event of 29 April 1994. SV and SH ground velocity recordings (Vel.) are shown along with ground displacements (Disp.). SKS is isolated on the SV component. The predicted polarity of the SV component of the S arrival is downward in the figure, and the short vertical line indicates an arrival that could be picked as a late SV on the velocity records (delay time noted on record), but in the displacement record there is clearly SV energy arriving at the same time as the strong SH onset (shaded, peak noted by inverted triangle). The SH waveform shows two arrivals, which correspond to interactions with a shear velocity increase at the top of D″.

[1]Department of Geological Sciences, Arizona State University, Tempe, AZ 85287–1404, USA. [2]Department of Geosciences, University of Oslo, Post Office Box 1047, Blindern, Oslo 0316, Norway. [3]Institute of Geophysics and Planetary Physics and Earth Sciences Department, University of California, Santa Cruz, CA 95064, USA.

*To whom correspondence should be addressed. E-mail: garnero@asu.edu

unique resolution to two anisotropic parameters: the direction of polarization of the fast and slow waves in the plane perpendicular to the propagation direction, and the amplitude of the anisotropy. We also have observations of delayed SV signals with no apparent SH-SV coupling as seen in other regions (fig. S3). These features led us to adopt a model space involving transverse isotropy in which the symmetry axis ranges from vertical to tilted, essentially setting VTI as the reference state.

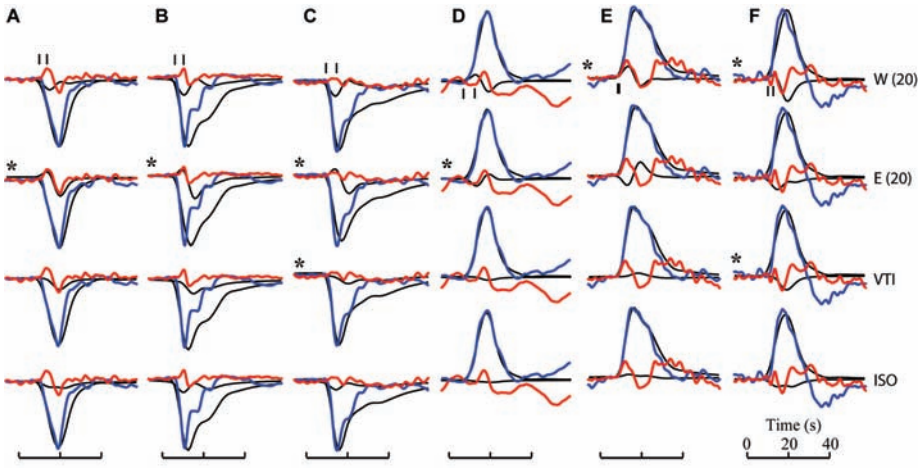

Fig. 2. Observed SH (blue) and SV (red) displacement traces for six event-station pairs. Columns (**A**) to (**F**) correspond to station name, epicentral distance (in degrees), and earthquake date (YYMMDD) information: (A) FRB 91.8 940429, (B) YKW2 99.4 940429, (C) DAWY 109.3 940429, (D) BBB 92.6 000512, (E) INK 98.4 991130, and (F) DLBC 93.6 010629. [Abbreviations represent seismic stations of the Canadian National Seismic Network: Iqaluit (FRB), Yellowknife (YKW2), Dawson City (DAWY), Bella Bella (BBB), Inuvik (INK), and Dease Lake (DLBC), Canada.] The data are shown with original polarities, normalized to the peak SH amplitudes, with the top row having small markers at the onset of SH and correctly polarized SV arrivals. The data are compared with synthetics (black) for four models: top row, W(20) synthetics are for tilted transverse isotropy with T = 20°, Az = 270°; second row, E(20) synthetics are for tilted transverse isotropy with T = 20°, Az = 90°; third row, VTI synthetics are for transverse isotropy with vertical symmetry axis; bottom row, synthetics for isotropic D″ structure (ISO). Asterisks (*) indicate models that best fit the data. Small tick marks in top row indicate SH arrival time and arrival time of SV wave having VTI expected polarity, which governs anisotropy strength for VTI models. ISO and VTI models do not produce the observed SV polarity reversal and underpredict the amplitude of the main part of the anomalous SV waveforms.

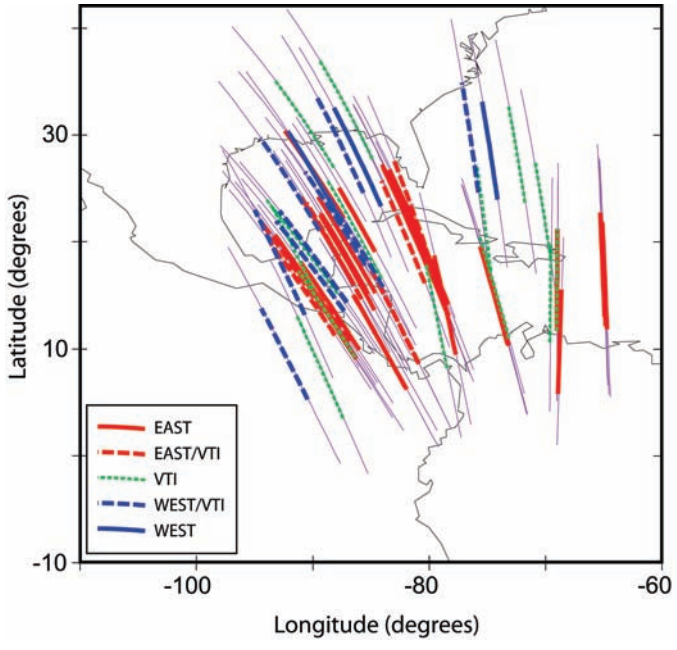

Fig. 3. Map of ray paths and best-fitting anisotropic models. Ray-path segments for the deepest 50 km of the ray path, with the color-coded portions representing the deepest 10 km of each path, are shown to emphasize the short scale nature of the variations. EAST indicates paths for which easterly azimuths of the tilted transverse isotropy symmetry axis match the data (T = 20°, Az = 90°), WEST is for paths for which westerly azimuths of the tilted transverse isotropy symmetry axis match the data (Az = 270°, T = 20°), and VTI is for paths for which vertical transverse isotropy fits the data. VTI and TTI models have anisotropy distributed over a 250-km-thick D″ layer. See (*33*) for paths compatible with ISO models.

Synthetic seismograms (*22*) (fig. S4) for a tilted transverse isotropy (TTI) model, in which the tilt angle is measured from the vertical and azimuth varies in all directions, are capable of producing reversed-onset SV signals. The precursory behavior is dependent on initial S-wave polarization upon entry into the anisotropic D″ layer; thus, every record was individually modeled with the correct source mechanism, omitting records near SV radiation pattern nodes. Although the overall strength of anisotropy is fairly well resolved because it controls the arrival time difference between fast and slow polarizations, the depth distribution of D″ anisotropy is less constrained. The difference in overall SV and SH wave shape is partly a consequence of interference with the S-wave that reflects off the core (ScS) and arrives a few seconds after S, which causes destructive interference on the SV components and constructive interference on the SH components.

Individual waveform modeling for six observations (Fig. 2) for three different models shows that, because of the mixing of fast and slow polarization energy onto the SV and SH waveforms, the relative amplitudes are dependent on the anisotropic properties and are not explained by isotropic models. Goodness of fit is determined by observation and prediction similarity in the front part of the waveform. Four cases show preference for either 20° east or 20° west tilting symmetry axes; it is difficult to distinguish between TTI and VTI for two waveforms, as a result of either weak or complex SV signals. We focus on the modeling of the early part of the waveforms because the later portions depend more strongly on poorly constrained details of the discontinuity structure and the crustal structure at the receivers.

A map of the anisotropy (Fig. 3) shows the predominance of east-dipping TTI in the southeast of the study area and west-dipping TTI in the area to the northwest (totaling 30% of all observations). There is a mixing of observations consistent with VTI throughout the study area (15% of records), with numerous waveforms being compatible with TTI and VTI predictions (20% of records). Only six waveforms are best explained by isotropy, and five waveforms are fit equally well by isotropy and TTI (fig. S5). These patterns are consistent with spatial fluctuations in the macroscopic fabric of the boundary layer caused by small-scale convection.

Prior studies have proposed the existence of azimuthal anisotropy in localized regions of D″, primarily below the Pacific (*15*, *23*, *24*), based on early arrivals of SV or ScSV signals. Those observations can be explained

by TTI models with horizontal symmetry axes (90° tilt) sampled by ray paths at azimuths perpendicular to the symmetry axes. The lack of azimuthal sampling for any region of D″ prevents us from resolving any more complex anisotropy systems, such as those expected for lattice-preferred orientation (LPO) of lower-mantle minerals. MgO has been shown to have anisotropic properties and slip systems that should favor SH velocities that are faster than SV velocities in horizontally sheared portions of D″, but with a 4θ azimuthal variation in relative velocities (*25*–*28*). We calculated synthetic waveforms for shear waves traveling through ferropericlase (Mg,Fe)O with cubic symmetry (*25*) and found that specific crystallographic orientations exist that reproduce the observed waveform behavior. The azimuthal dependence for this system may explain why our data show variations at small scale lengths (~100 km laterally), but this question cannot be robustly resolved because of the lack of good azimuthal coverage.

Deep-mantle anisotropy may be related to mantle circulation, with mid-mantle downwelling currents beneath subduction zones possibly inducing LPO in cooled, high-stress regions of D″ (such as beneath the Caribbean), whereas hot upwelling regions, such as beneath groupings of surface hot spots, could give rise to shape-preferred orientation (SPO) by, for example, aligning melt inclusions (*4*, *10*, *13*, *14*). Three-dimensional flow patterns could account for the spatial pattern in tilting of the symmetry axis imaged here, whether the fundamental cause of the anisotropy is LPO or SPO.

The apparent onset of anisotropy with the velocity jump at the top of D″ suggests a link between the two, which could arise if there is a chemically distinct layer (*1*), a transition to a sheared zone of enhanced velocity heterogeneity (*29*), a change in iron partitioning associated with pressure-induced change in spin state (*30*), or a major phase change (*31*, *32*). Improved azimuthal constraints are required to distinguish among these possibilities and that of MgO above, but we now have unequivocal evidence that extensive regions of D″ anisotropy contain more complex structure than simple VTI, with high-resolution seismic analysis required to detect and map the structure. The lateral variations in the observed azimuthal anisotropy are probably coupled to small-scale dynamics in the deepest mantle.

References and Notes

1. T. Lay, E. J. Garnero, Q. Williams, *Phys. Earth Planet. Inter.* **146**, 441 (2004).
2. E. J. Garnero, *Science* **304**, 834 (2004).
3. T. Lay, Q. Williams, E. J. Garnero, *Nature* **392**, 461 (1998).
4. A. K. McNamara, P. E. van Keken, S.-I. Karato, *Nature* **416**, 310 (2002).
5. J.-M. Kendall, P. G. Silver, *Nature* **381**, 409 (1996).
6. E. J. Garnero, T. Lay, *Phys. Earth Planet. Inter.* **140**, 219 (2003).
7. E. Matzel, M. K. Sen, S. P. Grand, *Geophys. Res. Lett.* **23**, 2417 (1996).
8. E. J. Garnero, M. M. Moore, T. Lay, M. Fouch, *J. Geophys. Res.* **109**, 10.1029/2004JB003004 (2004).
9. S. A. Russell, T. Lay, E. J. Garnero, *Nature* **396**, 255 (1998).
10. J.-M. Kendall, in *Earth's Deep Interior: Mineral Physics and Tomography from the Atomic to the Global Scale*, S. Karato, A. M. Forte, R. C. Liebermann, G. Masters, L. Stixrude, Eds. (American Geophysical Union, Washington, DC, 2000), pp. 133–159.
11. C. Thomas, J.-M. Kendall, *Geophys. J. Int.* **151**, 296 (2002).
12. J. Ritsema, *Geophys. Res. Lett.* **27**, 1041 (2000).
13. M. M. Moore, E. J. Garnero, T. Lay, Q. Williams, *J. Geophys. Res.* **109**, B02319, 10.1029/2003JB002546 (2004).
14. M. Panning, B. Romanowicz, *Science* **303**, 351 (2004).
15. V. Maupin, *Phys. Earth Planet. Inter.* **87**, 1 (1994).
16. J.-M. Kendall, C. Nangini, *Geophys. Res. Lett.* **23**, 399 (1996).
17. T. Lay, D. V. Helmberger, *J. Geophys. Res.* **88**, 8160 (1983).
18. V. Emery, V. Maupin, H. C. Nataf, *Geophys. J. Int.* **137**, 325 (1999).
19. M. G. Bostock, *J. Geophys. Res.* **2**, 8393 (1996).
20. M. G. Bostock, J. F. Cassidy, *Geophys. Res. Lett.* **22**, 5 (1995).
21. C. A. Currie, J. F. Cassidy, R. D. Hyndman, M. G. Bostock, *Geophys. J. Int.* **157**, 341 (2004).
22. We used a full wave-theory method to construct synthetic seismograms (*15*) for general forms of D″ anisotropy in the D″ layer. This is a convenient method for modeling waves diffracted along a spherical boundary.
23. S. A. Russell, T. Lay, E. J. Garnero, *Nature* **396**, 255 (1998).
24. J. Pulliam, M. K. Sen, *Geophys. J. Int.* **135**, 113 (1998).
25. D. Yamazaki, S.-I. Karato, *Phys. Earth Planet. Inter.* **131**, 251 (2002).
26. L. Stixrude, in *The Core-Mantle Boundary Region*, M. Gurnis, M. Wysession, E. Knittle, B. Buffet, Eds. (American Geophysical Union, Washington, DC, 1998), pp. 83–96.
27. B. B. Karki, R. Wentzcovitch, S. de Gironcoli, S. Baroni, *Science* **286**, 1705 (1999).
28. D. Mainprice, G. Barruol, W. Ben Ismail, in *Earth's Deep Interior: Mineral Physics and Tomography from the Atomic to the Global Scale*, S. Karato, A. M. Forte, R. C. Liebermann, G. Masters, L. Stixrude, Eds. (American Geophysical Union, Washington, DC, 2000), pp. 237–264.
29. V. F. Cormier, *Geophys. J. Int.* **136**, 373 (1999).
30. J. Badro *et al.*, *Science* **300**, 789 (2003).
31. M. Murakami, K. Hirose, K. Kawamura, N. Sata, Y. Ohishi, *Science* **304**, 855 (2004).
32. S.-H. Shim, T. S. Duffy, R. Jeanloz, G. Shen, *Geophys. Res. Lett.* **31**, L10603, 10.1029/2004GL019639 (2004).
33. Additional figures are available as supporting material on *Science* Online.

34. We thank M. Bostock for assistance in accessing some of the Canadian National Seismic Network waveform data, S. Ford and D. Wiens for data from the South Pacific, and the Incorporated Research Institutions for Seismology Data Management Center for all other waveform data. This work was supported by the U.S. National Science Foundation. V.M. was on leave to Institut de Physique du Globe de Paris while part of this work was done.

Supporting Online Material

www.sciencemag.org/cgi/content/full/306/5694/259/DC1
Figs. S1 to S5
References

29 July 2004; accepted 3 September 2004

Estimation of Fault Strength: Reconstruction of Stress Before the 1995 Kobe Earthquake

Futoshi Yamashita,* Eiichi Fukuyama, Kentaro Omura

We have estimated the stress field before the 1995 Kobe, Japan, earthquake (moment magnitude 6.9) using in situ post-shock stress measurements obtained from hydraulic fracturing experiments near the fault. We reconstructed the pre-shock stress field using a kinematic source model inverted from seismic waveforms and geodetic deformations. We found that at the center of the fault, two sides of the fault surface coupled completely before the earthquake, with a coefficient of friction of 0.6, which is equivalent to strong crust. At the edge of the fault, a possible aseismic slip is expected to occur from the pre-shock stress orientation.

To determine whether Earth's crust is strong or weak, we need to measure the in situ stress (*1*, *2*). Shear stress in the upper crust is in a critical state, indicating that the crust is near failure, and the coefficient of friction (0.6 to 1.0) for optimally oriented faults is consistent with Byerlee's law (*3*). The most direct way to measure fault strength is to observe the stress field just before an earthquake. Unfortunately, it is difficult to measure in situ stress continuously, making the observation of pre-shock stress nearly impossible.

We used a new method to estimate the pre-shock stress field for the 1995 Kobe (Hyogoken Nanbu), Japan, earthquake [moment magnitude (M_w) 6.9]. The background stress field in this region was consid-

National Research Institute for Earth Science and Disaster Prevention, 3-1, Tennodai, Tsukuba, Ibaraki, 305-0006, Japan.

*To whom correspondence should be addressed. E-mail: yamafuto@bosai.go.jp

ered to be east-west compression, which was determined from the focal mechanisms of small earthquakes (*4*). After the Kobe earthquake, however, the maximum horizontal stress direction was reported to be northwest-southeast (*4–6*), which is perpendicular to the fault. This rotation of the stress field was a result of the fault slip of the Kobe earthquake. Here we reconstruct the stress field just before the Kobe earthquake, using measurements of absolute stress near the fault after the earthquake and a kinematic slip model based on seismic waveforms and geodetic observation.

We used in situ stress measurement data obtained by hydraulic fracturing experiments (*5*, *6*) at Kabutoyama, Iwaya, Hirabayashi, and Toshima (Fig. 1A). The principal stress directions were estimated from the directions of borehole breakouts or hydraulic fractures on the bore wall (Fig. 1C) (*7*). We used the stress measurement data whose principal stress direction was estimated (*8*). The data show that the shear stress was small and maximum principal stress directions were directed northwest-southeast, which is perpendicular to the fault. Unfortunately, the accuracy of horizontal maximum stress (σ_{Hmax}) measured by hydraulic fracturing experiments is still under discussion (*9*). Thus, we considered two possible σ_{Hmax} values: the measurement data from hydraulic fracturing tests, and the estimated value assuming the stress ratio $R = 0.5$ with vertical (σ_v) and horizontal minimum (σ_{hmin}) stress values (*10*). We expect that the actual σ_{Hmax} would be around these two values, depending on the outcome of the discussion about the accuracy of σ_{Hmax}.

There are several kinematic fault models proposed for the 1995 Kobe earthquake (*11–15*). Because the in situ stress measurements were taken about 1 year after the earthquake, we accounted for any post-slip motion that might have occurred after the earthquake (*16*) by using a kinematic fault model (*12*) that employed geodetic data as well as seismic waveforms. In order to reconstruct the pre-shock stress field, we estimated the stress change near the fault due to the fault slip, using a theoretical formulation (*17*) for faults in an elastic half space. To see the contribution of fault slip to the stress change at each observation site, we plotted the distribution of shear stress changes at 1 km depth (Fig. 1B). The pre-shock stress field was then estimated by subtracting the stress change due to the coseismic slip; this technique is similar to the concept of back slip in subduction zones (*18*).

The estimated pre-shock stress field (Fig. 1D) shows that at the center of the fault (Iwaya and Hirabayashi), the maximum principal stress direction was east-west, which is consistent with the background stress before the earthquake. Moreover, large *r* values (*19*) at the center of the fault and the maximum principal stress direction oblique to the fault strike suggest that shear stress on the fault might be

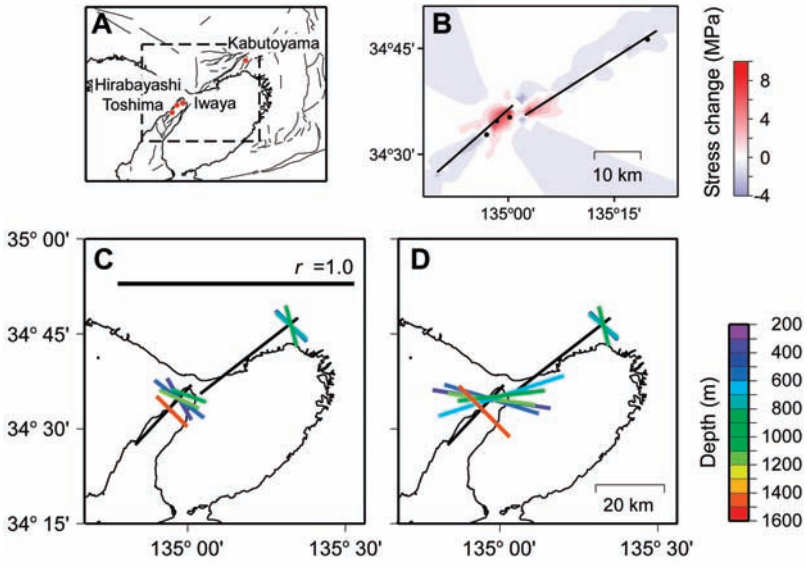

Fig. 1. (**A**) Locations of observation sites of in situ stress by hydraulic fracturing experiments. (**B**) Distribution of shear stress changes at a depth of 1 km associated with coseismic and postseismic slip on the fault. Observation sites are shown by black circles. The computation area is shown by a rectangle with broken lines in (A). The shear stress is calculated with respect to an assumed plane with a strike of N90°E and a dip of 90°. The locations of NE and SW segments are shown in (B) to (D) as black lines. Strike and dip angles of NE and SW segments are N232°E, 85° and N43°E, 75°, respectively. (**C**) Results of in situ stress measurements obtained about 1 year after the Kobe earthquake. The direction, length, and color of each bar show maximum horizontal stress direction, *r* value (*19*), and depth at which stress was measured, respectively. (**D**) Reconstructed pre-shock stress using a kinematic fault model and in situ stress data from the hydraulic fracturing tests. Bar parameters are the same as those in (C).

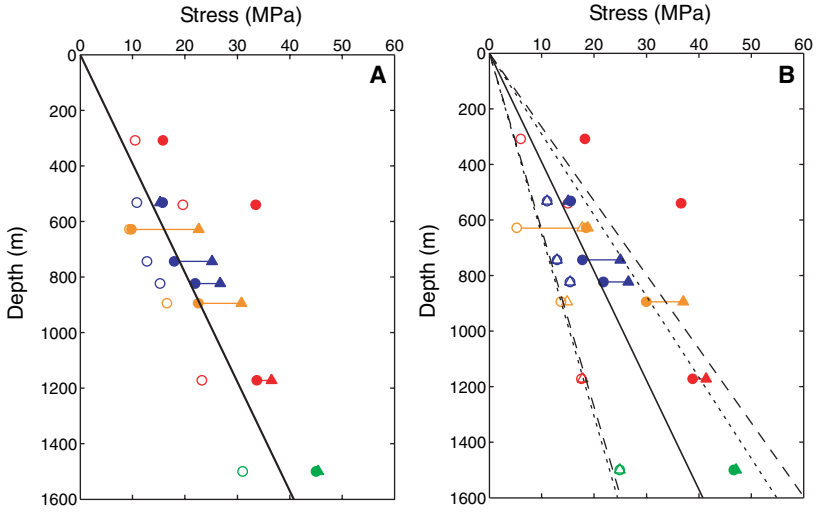

Fig. 2. (**A**) Distribution of σ_{Hmax} and σ_{hmin} with depth obtained by in situ stress measurements about 1 year after the Kobe earthquake at Hirabayashi (red), Iwaya (orange), Kabutoyama (blue), and Toshima (green). Solid and open symbols show σ_{Hmax} and σ_{hmin}, respectively. The circles show the measurement data from hydraulic fracturing tests, and the triangles show σ_{Hmax} estimated by the assumed stress ratio *R* of 0.5 (*10*). The solid black line shows σ_V, assuming lithostatic stress (*20*). (**B**) Depth dependence of the reconstructed σ_{Hmax} and σ_{hmin}. Circle and triangle symbols are the same as those in (A). Dotted lines show the least-square fitting lines of reliable σ_{Hmax} and σ_{hmin}, with circles (*21*). Dashed lines show the stress gradients with triangles. The obtained gradients of σ_{Hmax} and σ_{hmin} of the dotted lines are 34 and 15 MPa/km, respectively. The gradients of the dashed lines are 38 and 16 MPa/km, respectively.

large. On the contrary, at the edge of the fault (Kabutoyama and Toshima), the stress field did not change by the earthquake, and its direction was perpendicular to the fault. The depth dependence of σ_{Hmax} and σ_{hmin} is shown in Fig. 2. After the earthquake, stress values were distributed along σ_V [lithostatic stress (*20*) is indicated by a solid line in Fig. 2A] because both observed (circle) and estimated (triangle) differential stress ($\sigma_{Hmax} - \sigma_{hmin}$) was relatively small (Fig. 2A). But in the reconstruction of the pre-shock state, σ_{Hmax} and σ_{hmin} were typically different, suggesting that a large shear stress was accumulating on the fault. By using estimates at the central part of the fault (Hirabayashi and Iwaya), we determined the depth dependence of σ_{Hmax} and σ_{hmin} (Fig. 2B). If we extrapolate this relation to the hypocentral depth of 14.3 km and assume that the materials were brittle above this depth, we obtain a maximum shear stress at the hypocenter of 136 MPa (*21*, *22*).

After we estimated the stress field just before the earthquake, we were then able to estimate the coefficient of static friction (μ) using the shear (τ) and normal (σ_n) stress on the fault plane. We assumed that one of the principal stresses was vertical and its depth gradient was evaluated by the rock density profile along the depth measured during the experiments (*5*, *6*). At each depth, pore pressure (P_p) was assumed to be hydrostatic (*6*, *23*), so that the coefficient of friction was estimated to be $\mu = \tau/(\sigma_n - P_p)$ (Fig. 3). This is a rough estimate and may correspond to a lower bound of μ, but it characterizes the strength of the fault. We assume that the fault was completely locked before the earthquake, so that the stress field was similar on the fault plane and at the drilling sites close to the fault. The average coefficient of static friction was estimated to be 0.60 (*24*) for a fault with hydrostatic P_p. This estimate is consistent with Byerlee's law (*3*) in the laboratory, and indicates that the fault strength is similar to that of the strong crust in other places (*1*).

The spatial variation of μ was large at the center of the fault and smaller at both edges (Fig. 3). This variation is similar to the *r*-value variation (Fig. 1D). One explanation for this variation is that because the pre-shock friction at the fault edge was small before the earthquake, the fault could not sustain the stress and aseismic slip occurred (*25*). This interpretation is also consistent with our model result that the maximum principal stress direction was perpendicular to the fault before the earthquake. Kinematic models also showed that during the earthquake, the slip on the fault was small (*11*–*15*), and then shear stress due to fault slip was also small in this region (Fig. 1B). These results will contribute to exploring heterogeneous intraplate faults and the mechanism of earthquake occurrence.

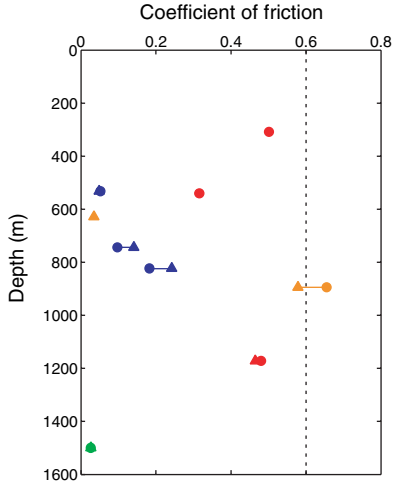

Fig. 3. Depth dependence of the coefficient of static friction (μ). Circles and triangles show the coefficients estimated from σ_{Hmax} with in situ measurements and that estimated by stress ratio, respectively. The coefficient of friction at Iwaya at the depth of 628 m with the circle symbol is estimated at 2.0, which is not plotted in the figure. The dotted line indicates the average coefficient of static friction with original σ_{Hmax} measurement data (*24*). The same coefficient of friction (0.60) was obtained using σ_{Hmax} estimated by assumed *R*. Both estimates are based on a reliable data set (*21*), and the hydraulic P_p effect (*23*) is taken into account.

References and Notes

1. J. Townend, M. D. Zoback, *Geology* **28**, 399 (2000).
2. M. D. Zoback *et al.*, *Int. J. Rock Mining Sci.* **40**, 1049 (2003).
3. J. D. Byerlee, *Pure Appl. Geophys.* **116**, 615 (1978).
4. H. Katao, N. Maeda, Y. Hiramatsu, Y. Iio, S. Nakao, *J. Phys. Earth* **45**, 105 (1997).
5. R. Ikeda, Y. Iio, K. Omura, *Island Arc* **10**, 252 (2001).
6. H. Tsukahara, R. Ikeda, K. Yamamoto, *Island Arc* **10**, 261 (2001).
7. The term "breakout" stands for the region enlarged by the spallation of the bore wall after drilling, due to the compressive stress concentration, appearing along the minimum horizontal stress direction (*26*). On the other hand, during the hydraulic fracturing experiment, fractures were created on the bore wall along the maximum stress direction.
8. To reconstruct the pre-shock stress state, knowledge of the principal stress direction as well as its magnitude is necessary. However, some of the stress data in (*5*, *6*) lacked the principal stress direction data owing to the unclear direction of breakouts or fractures. Such data were not used in our analysis.
9. Some researchers (*27*) have asserted the accuracy of the measurements of σ_{Hmax} in hydraulic fracturing experiments, based on a numerical simulation and indirect estimation. But no one has yet confirmed such a claim in a direct way by field experiments. The inherent error related to the hydraulic fracturing experiment is smaller than the size of plotted symbol.
10. The stress ratio *R* is defined as $(\sigma_1 - \sigma_2)/(\sigma_1 - \sigma_3)$ (*28*), where σ_1, σ_2, and σ_3 are the maximum, intermediate, and minimum principal stress, respectively. Because most aftershocks have strike-slip mechanisms in the present study (*4*), σ_1 and σ_3 correspond to σ_{Hmax} and σ_{hmin}, respectively, and *R* is considered to be close to 0.5. Because at the depths of 308 and 540 m of Hirabayashi σ_{hmin} is not the minimum principal stress, we did not apply these data.
11. H. Sekiguchi, K. Irikura, T. Iwata, Y. Kakehi, M. Hoshiba, *J. Phys. Earth* **44**, 473 (1996).
12. S. Yoshida *et al.*, *J. Phys. Earth* **44**, 437 (1996).
13. M. Hashimoto, T. Sagiya, H. Tsuji, Y. Hatanaka, T. Tada, *J. Phys. Earth* **44**, 255 (1996).
14. D. J. Wald, *J. Phys. Earth* **44**, 189 (1996).
15. S. Ide, M. Takeo, *J. Geophys. Res.* **102**, 27379 (1997).
16. Postseismic deformation of the 1995 Kobe earthquake was observed by the Global Positioning System (GPS) (*29*). Those workers interpreted the postseismic deformation not as a viscoelastic effect but as the post-slip on the fault with a decay time of 50 days. Because the 2-month-long GPS data beginning just before the earthquake were used for the modeling (*12*), the observed post-slip is considered to be included in the slip model.
17. Y. Okada, *Bull. Seismol. Soc. Am.* **82**, 1018 (1992).
18. M. Matsu'ura, T. Sato, *Tectonophysics* **277**, 189 (1997).
19. The *r* value is a shear stress normalized by average stress and is defined by $(\sigma_1 - \sigma_3)/(\sigma_1 + \sigma_3)$.
20. Lithostatic stress stands for the overburden pressure estimated by the rock density distribution along depth.
21. Because the direction of reconstructed σ_{Hmax} at the center of the fault is east-west, we regarded the reconstructed data whose σ_{Hmax} direction is within N90°E ± 10° as reliable. The average shear stress was calculated using such reliable data. The shear stress at the hypocentral depth (14.3 km) is 157 MPa if we use the σ_{Hmax} estimated using an assumed stress ratio of 0.5 (*10*).
22. However, some researchers (*30*) have claimed that linear extrapolation to such a depth is inappropriate.
23. Y. Kitagawa, K. Fujimori, N. Koizumi, *Geophys. Res. Lett.* **29**, 121.1 (2002).
24. On estimating the average coefficient of friction, we assumed that the direction of σ_{Hmax} at the center of the fault was N90°E before the earthquake and that the stress linearly increased with depth. The stress gradient was calculated from the reliable data (*21*) shown in Fig. 2B. The coefficient using σ_{Hmax} estimated from the assumed stress ratio was also calculated and obtained the same coefficient (0.60). The uncertainty of σ_{Hmax} was found not to affect the estimation of the coefficient of friction here.
25. We did not have any evidences for the aseismic slip. Because the recurrence interval of this earthquake is about 2000 years (*31*), the deformation rate before the earthquake might be very small. We did not, unfortunately, have a very dense geodetic observation network to detect such a small change at that time.
26. B. Amadei, O. Stephansson, in *Rock Stress and Its Measurements* (Chapman & Hall, London, 1997), p. 102.
27. T. Ito, K. Evans, K. Kawai, K. Hayashi, *Int. J. Rock Mining Sci.* **36**, 811 (1999).
28. J. W. Gephart, D. W. Forsyth, *J. Geophys. Res.* **89**, 9305 (1984).
29. T. Kato *et al.*, *J. Geod. Soc. Japan* **43**, 181 (1997).
30. P. Spudich *et al.*, *Bull. Seism. Soc. Am.* **88**, 413 (1998).
31. Y. Awata *et al.*, *J. Seismol. Soc. Jpn.* **49**, 113 (1996).

32. We thank S. Yoshida for permission to use their inverted slip data. This work was done under the project entitled Research on Mechanisms of Earthquake Occurrence at the National Research Institute for Earth Science and Disaster Prevention in Japan.

22 June 2004; accepted 7 September 2004

Morphological Disparity of Ammonoids and the Mark of Permian Mass Extinctions

Loïc Villier[1,2]* and Dieter Korn[2]

The taxonomic diversity of ammonoids, in terms of the number of taxa preserved, provides an incomplete picture of the extinction pattern during the Permian because of a strongly biased fossil record. The analysis of morphological disparity (the variety of shell shapes) is a powerful complementary tool for testing hypotheses about the selectivity of extinction and permits the recognition of three distinct patterns. First, a trend of decreasing disparity, ranging for about 30 million years, led to a minimum disparity immediately before the Permian-Triassic boundary. Second, the strongly selective Capitanian crisis fits a model of background extinction driven by standard environmental changes. Third, the end-Permian mass extinction operated as a random, nonselective sorting of morphologies, which is consistent with a catastrophic cause.

The extinctions at the close of the Paleozoic were initially understood as a relatively long process ranging for about 10 million years (My) or more, recording a progressive decline in numerous groups of marine organisms, many of which became extinct before the end-Permian (*1*). Most recent studies emphasize an "instantaneous" extinction event at geological scales—that is, restricted to the several thousand years bracketing the Permian-Triassic boundary (*2*, *3*)—with a distinct mass extinction event at the end-Capitanian, 10 My earlier (*2*, *4*).

Testing the several putative cause(s) of these events would require detailed studies of the rate, timing, and selectivity of the extinction patterns. The resulting data would permit rejection of extinction hypotheses that do not fit observed patterns. In particular, extinction selectivity can be tested using a wide array of methods (*5*–*9*). If we assume that the variety of forms (morphological disparity) reflects the variety of adaptive zones occupied, the analysis of disparity patterns provides a means of differentiating among various extinction models (*10*–*12*).

Ammonoids are suitable subjects for analyses of extinction dynamics because they show high fluctuations in taxonomic diversity during their history and record numerous extinction events and subsequent recovery (*13*). We analyzed diversity dynamics of ammonoids from a distribution of 1965 species ranging from the Late Carboniferous to the Early Triassic. The data are derived from the GONIAT database, a compendium of Paleozoic species of ammonoids encompassing taxonomy, morphological data, and geographical and stratigraphical occurrences (*14*). The database has been extended to include Early Triassic forms and the most recent systematic developments (*15*).

Zhou *et al*. (*16*) interpreted variations in Late Permian ammonoid diversity (Fig. 1) as multi-episodal extinction near the stage boundary, related to sea-level fluctuations. The end-Permian is characterized by the survival of only two or three genera across the Permian-Triassic boundary (*13*). Pseudo-extinction of several paraphyletic taxa certainly overemphasizes the level of extinction, but the Early Triassic forms represent only three surviving superfamilies, the Medlicottiaceae and two in the Ceratitina, implying the demise of three others. However, the measured diversity pattern is strongly constrained by analytical biases and the effect of uneven sampling, preventing a confident interpretation.

Ammonoid species and genera are taxa with a short time range, generally restricted to one stage or part of a stage. This leads to an overestimation of extinction intensity when measured at the stage level. In data for the Permian, taxonomic diversity for particular time intervals is also highly correlated with the number of geographical domains sampled (Spearman rank correlation test, $P = 0.009$ and $P = 0.038$ for genera and species richness, respectively). This indicates that measured diversity is highly sensitive to sampling effort and challenges the reliability of the temporal patterns. The crucial problem is that the critical period of the Late Permian and earliest Triassic (Griesbachian and Dienerian) suffers from a paucity of available fossiliferous sections, which can in itself explain part of the diversity patterns (*17*, *18*).

Analysis of morphological disparity can overcome part of the sampling bias of the fossil record (*19*) and also complements patterns of taxonomic diversity. By focusing on shape differences, morphological disparity is relatively independent of taxonomy and allows the comparison of samples in which a variable proportion of taxa are preserved or sampled (*20*). Estimates of disparity consider the distribution of taxa and proportions of morphological space occupied at successive time intervals.

We constructed an empirical morphospace for Permian and Triassic ammonoids on the

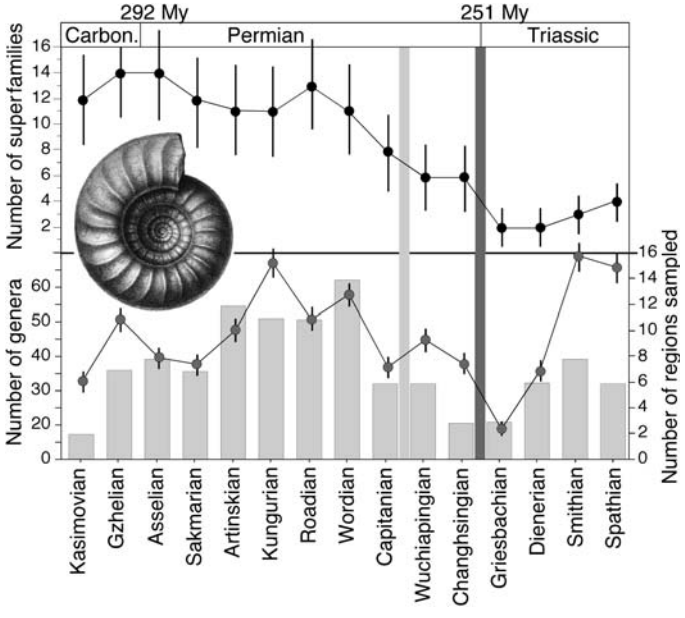

Fig. 1. Patterns of diversity for ammonoids for the interval Late Carboniferous to Early Triassic. The diversity is counted at the stage level; the stratigraphic range of taxa is taken from their first and last occurrence in the fossil record. Error bars indicate square roots of numbers of taxa. Upper panel: Number of superfamilies. Lower panel: Comparison of the number of genera (curve) and the number of regions sampled (histogram). Gray vertical bars indicate the position of mass extinctions at the end of the Capitanian and the end of the Changhsingian.

[1]Centre de Sédimentologie–Paléontologie, FRE CNRS 2761, Université de Provence, 3 place Victor-Hugo, F-13331 Marseille Cedex 3, France. [2]Museum für Naturkunde, Humboldt-Universität zu Berlin, Invalidenstraße 43, D-10115 Berlin, Germany.

*To whom correspondence should be addressed. E-mail: lvillier@up.univ-mrs.fr

basis of conch coiling (whorl expansion rate, umbilical width index, whorl width index, and whorl imprint zone). Two complementary estimates of disparity were calculated: the sum of variance and the sum of range on morphospace axes. Variance measures the dispersal of forms through morphospace. It is sensitive to taxonomic choices but is statistically insensitive to the sample size, except in small samples for which uncertainty increases markedly (*12*). The sum of ranges estimates the amount of morphospace occupied. It is insensitive to taxonomic choices but is sensitive to sample size, the impact of which can be minimized with the use of rarefaction (*20*).

The temporal patterns of disparity (Fig. 2) that we found are broadly similar to the diversity curve for superfamilies (Fig. 1) (Spearman rank correlation test, $P = 0.011$). However, at low taxonomic levels, diversity and morphological disparity are independent (no statistical support for correlation, $P = 0.718$ for genera, $P = 0.740$ for species) and track different information. Disparity increased in the Late Carboniferous to Early Permian and remained stable during the first three Permian stages (Fig. 2). During the period from the Artinskian to the end of the Permian (~30 My), disparity decreases, interrupted only by a brief increase in the Wordian. However, patterns of the two disparity estimates differ substantially. Fluctuations in variance are more pronounced, whereas the decreasing trend of the range exhibits more regularity. The brief disparity increase during the Wordian is related to an increase in disparity in three groups [Neoicoceratacea, Adrianitaceae, Cyclolobina (fig. S4)] that diversified during this interval (*14*). The end-Capitanian crisis is characterized by the loss of a large number of genera (*21*), and the sum of variances decreases more rapidly than does the sum of ranges. The disparity continued to decrease during the two last stages of the Permian and reached the lowest value in the Changhsingian, just before the end-Permian mass extinction. Paradoxically, the level of disparity is similar to that at the beginning of the Triassic, despite a high rate of extinction. The Triassic data show a stagnation in the variance and only a slight expansion of morphospace occupation. The post-crisis diversification of morphologies is delayed relative to the steep increase in taxonomic richness.

According to the models of Foote (*10*), a nonselective extinction should not affect the disparity, whereas selective extinctions should modify the variance and reduce the range (or both), depending on the sensitivity to extinctions among occupants of particular adaptive zones. The progressive long-term decline during the Late Permian—demonstrated by the sum of range, and coeval to the progressive demise of superfamilies—suggests progressive erosion of the morphospace, selectively affecting the marginal morphologies (see fig. S5). This trend is inherent to the ammonoids and reflects a low rate of appearance of morphological novelties that, except for a brief interval in the Wordian, failed to compensate for ongoing background extinction during the Permian. This might be determined either by a constantly filled ecological space or by evolutionary and developmental properties of the organisms (*22*).

The decrease in morphological variance during the Capitanian crisis reflects a reworking of the morphospace whose margins were trimmed back, as expressed by the decrease in the sum of range, leaving surviving forms mainly clustered in its central part (*21*). The end-Capitanian crisis was thus selective, with most of the cases affecting the goniatitic morphologies (Adrianitaceae, Cyclolobina, Thalassoceratacea) and laterally compressed forms (Medlicottiaceae) (*20*). All these clades suffered during the Capitanian event or became extinct. The Wuchiapingian is distinguished from the Capitanian by the high rate of origination but absence of morphological diversification of the Ceratitina subsequent to the extinction event. Calibrated using conodont biostratigraphy, the end-Capitanian is a relatively long time interval, at least recognizable at a geological scale. Various, but not all, groups of marine organisms were affected, selectively at different times within the end-Capitanian or early Wuchiapingian (*2*). Although treated as occurring at the stage boundary, ammonoid extinction peaked during the earliest Wuchiapingian. The selective extinction of ammonoids and other invertebrate organisms (foraminifers, brachiopods, gastropods) can be attributed to gradual changes in environmental conditions (*2*, *5*).

By contrast, the preservation of disparity after the end-Permian mass extinction would be expected only in a context for the nonselective extinctions of whorl morphologies. Although constructed with distinct time scale and taxonomic sampling, the index for suture line complexity (*23*) also provides a measure of morphological disparity of ammonoids. Its changes through time are compatible with a nonselective end-Permian extinction, showing a reduction of the range and the likely preservation of the mean value of the complexity index. Members of the Ceratitina are predominant among the survivors, but this does not reflect selectivity, as they were the taxa most likely to survive. They had the highest morphological disparity and were taxonomically the most diverse group, consisting of more than 100 species (the other clades contained fewer than 10 species each). Simulation using a rarefaction of Changhsingian diversity predicts that the survival of two groups (one being the Ceratitina) has the highest likelihood when 87% of species are randomly killed, which matches previously estimated extinction rates for the end-Permian crisis (*2*).

The end-Capitanian and the end-Changhsingian have been recognized as two distinct mass extinction events, the latter being marked by its intensity, but this model cannot explain all aspects of the end-Permian extinctions. Variation through time of morphological disparity suggests three independent patterns for Permian ammonoids: a long-term reduction in disparity, a high level of selective extinction at the end of the Capitanian, and a nonselective extinction at the end of the Permian. The pattern at the end of the Capitanian corresponds to a model of background extinction

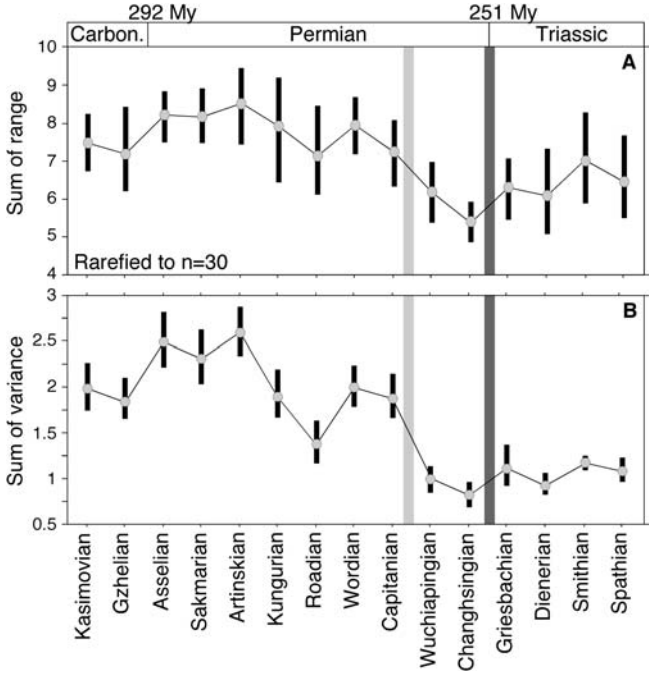

Fig. 2. Patterns of morphological disparity for the ammonoid conch for the interval Late Carboniferous to Early Triassic. (**A**) Disparity estimated as the sum of range measures the amount of morphospace occupied. The values are rarefied to a sample size of 30 species. (**B**) Disparity estimated as the sum of variance approximates the mean dissimilarity between taxa. Plots are the mean value of 500 bootstrap replicates, with 90% confidence intervals as error bars.

despite the high level of extinction. Only the end-Permian event matches the model of a "mass extinction regime" (*5*), arguing for a catastrophic cause consisting of a brief but major event, independent of earlier variations in diversity, with a worldwide effect and, for the most part, the nonselective demise of taxa.

References and Notes

1. D. H. Erwin, *The Great Paleozoic Crisis: Life and Death in the Permian* (Columbia Univ. Press, New York, 1993).
2. D. H. Erwin *et al.*, *Geol. Soc. Am. Spec. Pub. 336,* 363 (2002).
3. M. J. Benton, *When Life Nearly Died: The Greatest Mass Extinction of All Time* (Thames & Hudson, London, 2003).
4. S. M. Stanley, X. Yang, *Science* **266**, 1340 (1994).
5. D. Jablonski, *Science* **231**, 129 (1986).
6. D. M. Raup, in *Evolutionary Paleobiology*, D. Jablonski, D. H. Erwin, J. H. Lipps, Eds. (Univ. of Chicago Press, Chicago, 1996), pp. 419–433.
7. A. B. Smith, C. H. Jeffery, *Nature* **392**, 69 (1998).
8. D. Jablonski, *Proc. Natl. Acad. Sci. U.S.A.* **99**, 8139 (2002).
9. M. Aberhan, T. K. Baumiller, *Geology* **31**, 1077 (2003).
10. M. Foote, *Paleobiology* **19**, 185 (1993).
11. K. Roy, M. Foote, *Trends Ecol. Evol.* **12**, 277 (1997).
12. C. N. Ciampaglio, M. Kemp, D. W. McShea, *Paleobiology* **27**, 695 (2001).
13. W. B. Saunders, D. M. Work, S. V. Nikolaeva, *Paleobiology* **30**, 19 (2004).
14. J. Kullmann, D. Korn, *GONIAT Version 3.1, Paleozoic Ammonoid Database System* (Univ. of Tübingen, 2002).
15. T. B. Leonova, *Paleontol. J.* **36** (suppl. 1) (2002).
16. Z. Zhou *et al.*, *Permophiles* **29**, 195 (1996).
17. S. E. Peters, M. Foote, *Paleobiology* **27**, 583 (2001).
18. S. E. Peters, M. Foote, *Nature* **416**, 420 (2002).
19. M. A. Wills, in *Fossils, Phylogeny, and Form—An Analytical Approach*, J. M. Adrain *et al.*, Eds. (Kluwer Academic/Plenum, New York, 2001), pp. 55–144.
20. See supporting data on *Science* Online.
21. B. F. Glenister, W. M. Furnish, in *The Ammonoidea*, M. R. House, J. R. Senior, Eds. (Academic Press, London, 1981), pp. 49–64.
22. C. N. Ciampaglio, *Evol. Dev.* **6**, 260 (2004).
23. W. B. Saunders, D. M. Work, S. V. Nikolaeva, *Science* **286**, 760 (1999).

24. We thank D. Lazarus, D. Unwin, G. J. Eble, and W. Kiessling for discussions. Supported by a postdoctoral fellowship of the Alexander von Humboldt Foundation (L.V.) and by the Deutsche Forschungsgemeinschaft (D.K.). This is Paleobiology Database publication number 28.

Supporting Online Material

www.sciencemag.org/cgi/content/full/306/5694/264/DC1
Materials and Methods
Figs. S1 to S5
Table S1
References

29 June 2004; accepted 25 August 2004

The Scaling of Animal Space Use

Walter Jetz,[1,2*†] Chris Carbone,[3] Jenny Fulford,[3] James H. Brown[2]

Space used by animals increases with increasing body size. Energy requirements alone can explain how population density decreases, but not the steep rate at which home range area increases. We present a general mechanistic model that predicts the frequency of interaction, spatial overlap, and loss of resources to neighbors. Extensive empirical evidence supports the model, demonstrating that spatial constraints on defense cause exclusivity of home range use to decrease with increasing body size. In large mammals, over 90% of available resources may be lost to neighbors. Our model offers a general framework to understand animal space use and sociality.

Space use in animals is strongly tied to body size and has been a focal point of ecological research (*1–7*). This research has led to the formulation of scaling rules—power law relations between body size and animal area use—in two separate lines of research: population density and home range size. Here we develop a simple model for the use of space by animals that incorporates energy requirements and interactions with neighbors to unify these approaches.

We assume that energy and material resource requirements are determined by the whole-organism field metabolic rate B (in units of kJ/day or watts), which has been shown to scale as

$$B = B_0 M^{3/4} \quad (1)$$

B_0 is a normalization constant that also incorporates the diet-specific assimilation efficiency, which determines the proportion of ingested energy available for activity. Let H be the home range area in km^2 and R the species-specific rate of supply of usable resources available in H, in units of W/km^2. However, intrusions from foraging conspecific neighbors into a portion of the home range may decrease the proportion of R available to the home range owner (*8*). This resource depletion can be put into a spatial context by thinking in terms of a portion of the home range that is used exclusively only by the owner, H_o, and a portion that overlaps with neighbors and whose resources are harvested only by intruders. We use α to designate the proportion of the resource supply rate across a home range that is harvested exclusively by the owner: $\alpha = H_o R/HR$. This can be simplified to

$$\alpha = H_o/H \quad (2)$$

Accordingly, the proportion of resource supply rate taken by the neighbors, or home range overlap, is $1 - \alpha$.

It follows that if an individual uses an area just sufficient to meet its metabolic requirements, it requires a home range of area

$$H = B/\alpha R = B_0 R^{-1} \alpha^{-1} M^{3/4} \quad (3)$$

Population density, N, can be used to empirically quantify α. Its reciprocal, N^{-1} indicates the average area per individual and is equivalent to H_o, and thus from Eq. 2 it follows that

$$\alpha = N^{-1}/H \quad (4)$$

Finally, the scaling of N^{-1} is identical to that of H, without the effect of neighbors on scaling and normalization constant

$$N^{-1} = B/R = B_0 R^{-1} M^{3/4} \quad (5)$$

These equations can serve to illustrate three potential scenarios for the scaling of home range size that are dependent on the examination of the two key parameters, R and α. (i) Both α and R are body size–invariant ($R \propto M^0$ and $\alpha \propto M^0$). This is the hypothesis initially proposed by McNab (*1*). It predicts that home range size should scale as $M^{3/4}$ ($H \propto M^{3/4}$), but it was not supported by subsequent analyses indicating home range scaling close to 1 (*9–12*). (ii) R decreases with body size approximately to the quarter power, whereas α is body size–invariant ($R \propto M^{-1/4}$ and $\alpha \propto M^0$). This predicts the observed $H \propto M^1$. This idea was originally proposed by Harestadt and Bunnell (*13*) and recently refined by Haskell *et al.* (*14*), who modeled the potential interaction between the fractal distribution of resources and foraging mode. This scenario predicts that larger species require larger home ranges than the scaling of their energy needs alone would suggest, because of their lower encounter rates with food items. Because R affects the scaling of both N^{-1} and H equally (compare Eqs. 3 and 5), their scaling lines should have no distinct intersection. (iii) Resource supply rate R does not scale with body size, but proportional access by the home range owner, α, scales approximately to the negative one-

[1]Department of Ecology and Evolutionary Biology, Princeton University, Princeton, NJ 08544–1003, USA. [2]Department of Biology, University of New Mexico, Albuquerque, NM 87131, USA. [3]Institute of Zoology, Zoological Society of London, Regent's Park, London, NW1 4RY, UK.

*To whom correspondence should be addressed. E-mail: wjetz@princeton.edu
†Address as of December 2004: Division of Biological Sciences, University of California, San Diego, La Jolla, CA 92093, USA.

quarter power ($R \propto M^0$ and $\alpha \propto M^{-1/4}$), leading to the observed $H \propto M^1$ and an intersection of the scaling lines. A potential role of home range overlap with neighbors has been pointed out previously (*7*, *15*, *16*), but an understanding of the scaling remains little developed. Here we develop a new theory that quantifies the effect of neighbors, α, and provide an empirical test for all core scenarios for the scaling of animal space use.

Larger home ranges are more difficult to defend from intrusion. This idea is supported by field observations (*8*), but its conceptual basis can be seen by considering the task of defending an increasing area (fig. S1). From Eq. 3, it follows that the minimum area of a home range in the absence of competition scales as $M^{3/4}$. It has been found empirically that the day range, or the average distance traveled in 1 day, scales as $M^{1/4}$ (*16*–*18*). Hypothetically, this is equivalent to a mouse traveling 110 m in a 70–m-diameter home range, versus an elephant traveling 2 km in a 6-km-diameter home range. Clearly, the larger animal faces a more formidable task of detecting and minimizing overlap with intruders.

The magnitude of this task can be modeled quantitatively by using the equation from physics for collisions among gas particles to predict the frequency of interactions between owners and intruders (*19*–*21*). In two-dimensional space, the frequency of interactions f among individuals is

$$f = \frac{4}{\pi} N D d \qquad (6)$$

where N is the population density (in individuals per km^2), D is the average speed (the day range in km traveled per day), and d is the average neighbor interaction distance (in km). We use the above well-established scaling relations to characterize how density and speed of movement vary with body size: $N \propto M^{-3/4}$ (*5*) and $D \propto M^{1/4}$ (*7*, *16*–*18*). Less is known about the scaling of interaction distance, which is likely to vary with communication system and habitat structure. Limited sources indicate a scaling of detection distance between M^0 and $M^{1/2}$ (*17*, *22*, *23*), and here we attempt a first test of its effect using the midpoint, $d \propto M^{1/4}$, the scaling of a typical biological distance (*7*, *24*, *25*).

We assume that interactions with conspecific neighbors lead to temporary reinforcement of exclusive home range use and hence to reduced resource extraction by home range intruders (*2*). All else being equal, neighbors that encounter each other more frequently should be able to maintain more fixed home range boundaries and thus get by with relatively smaller home ranges, because the resources are used more exclusively. Quantitatively, we assume that the proportion of the total resources or proportional home range area that is exclusive to a home range owner, α, is proportional to the neighbor interaction frequency, so $\alpha \propto f$. Substituting the assumed allometric scalings of population density, day range, and interaction distance into Eq. 4 gives the predicted scaling of α

$$\alpha \propto f \propto M^{-3/4} M^{1/4} M^{1/4} \propto M^{-1/4} \qquad (7)$$

The assumption of random movement in Eq. 6 can be relaxed to allow a wide variety of movement patterns without altering Eq. 7; the critical feature is that the way owner and intruder move with respect to each other is independent of body size. We now modify Eq. 3 to model home range area, incorporating the fraction of the total home range whose resources are used by the neighbor. Following scenario (iii) and assuming body size invariance of resource supply rate R this leads to

$$H = B/\alpha R = B_0 R^{-1} M^{1/4} M^{3/4} = B_0 R^{-1} M^1 \qquad (8)$$

The above equations provide a simple general model for how animals use space and interact with neighbors. This model makes a number of predictions that can be tested empirically. We use two extensive compilations on home range size and population density in mammals (*11*, *26*) to test the model predictions. In order to account for the effect of grouping in the context of our model, we perform our analyses with home range size per individual, H = (observed home range/social unit size), as a response (*27*).

A log-log plot of H as a function of M has a slope of 1.07, which is not statistically distinguishable from the value of 1 estimated in Eq. 8 (Fig. 1 and Table 1) but is significantly higher than 0.75, which rejects body size invariance of R and α predicted by scenario (i) (*1*). A log-log plot of N^{-1}, the reciprocal of population density, as a function of M has a slope of 0.76 (Fig. 1 and Table 1), which is almost identical to the value of 3/4 predicted in Eq. 5, given body size invariance of R [see also (*5*, *28*–*30*)]. Across trophic groups, the slopes vary from 0.73 to 0.86 but are never significantly different from 0.75 (t tests, $P > 0.1$ in all cases). This supports the assumption of scenario (iii) that resource supply rate R is body size–independent ($R \propto M^{-0.02}$ to $M^{0.11}$ across trophic levels) and rejects the supply rate–based scenario (ii) for the scaling of home range size (*13*, *14*). The intercepts of the relations in Figs. 1 and 2 at $M = 1$ kg indicate the ratio between energy expenditure and energy supply rate (B_0/R) as a function of body size. Given empirical estimates of mammalian field metabolic rates and assimilation efficiencies, we can estimate how the different area needs point to the highly different resource supply rate experienced across trophic levels. We find that the energy supply rate R is approximately 2188 W km^{-2} in herbivores, 408 W km^{-2} in omnivores, and 32 W km^{-2} in carnivores, independent of body size.

Following Eq. 4, the difference in scaling exponents of H and N^{-1}, or their slopes on the log-log plot with body size (Fig. 1), indicates the value of α, proportional home range exclusivity. We find that α is statistically different from zero in all trophic groups and ranges from 0.26 to 0.39, without any consistent effect of diet (Table 1). These values are not different from those predicted by Eqs. 7 and 8 (t tests, $P > 0.1$ in all cases). Together with the body size independence of R, these results support scenario (iii), the proposed scaling of neighbor interaction, as a general mechanism explaining the scaling of animal space use in the presence of neighbors.

We can further estimate the home range exclusivity at a given body size by synthesizing

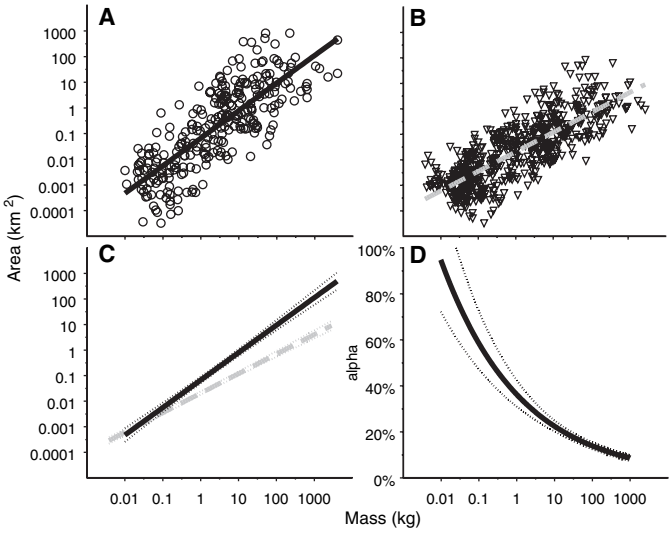

Fig. 1. The body size dependence of individual area use and overlap in mammals. (**A**) Individual home range size H, corrected for grouping. (**B**) Per-individual area use or reciprocal density, N^{-1}. (**C**) The above scaling relations of H (solid line) and N^{-1} (dashed line) plotted together for comparison. (**D**) The resulting scaling of α (in percent); that is, the percentage of resources exclusively taken by the home range owner or percent of home range exclusivity (percent of home range overlap is given as 1–α as percentage). Data points are species; thick lines are least-squares fits; dotted lines are their 95% confidence intervals. For detailed regression results, see Table 1.

Table 1. Observed scaling relations of per-individual area use in mammals. Data are obtained from two measures: the inverse of population density (N^{-1}) and individual home range size (H, corrected for group size). These data are also analyzed by trophic level, herbivores (Herb), omnivores (Omn), and carnivores (Carn). The slope analysis gives the individual scaling exponents m and the scaling exponents for α, proportional home range exclusivity, which are given as $\alpha = m(N^{-1}) - m(H)$, where m refers to the calculated scaling exponents. Numbers in brackets are the 95% confidence intervals. The r^2 values are based on log-transformed data. n indicates sample size (number of species).

		n	Cross over	Intercept	Slope		Model	
			M (kg) at $N^{-1} = H$	Area (ha) at $M = 1$	m	$\alpha \propto M^{x}$	F	r^2
All	H	274	0.022 (0.215)	6.69 (1.68)	1.07 (0.10)	−0.31 (0.11)	464.3	0.63
	N^{-1}	563		2.06 (0.28)	0.76 (0.05)		979.1	0.64
Herb	H	158	0.064 (0.260)	2.05 (0.03)	1.02 (0.09)	−0.26 (0.11)	454.1	0.74
	N^{-1}	327		1.01 (0.01)	0.76 (0.05)		948.7	0.74
Omn	H	44	0.022 (0.187)	15.87 (1.30)	1.12 (0.15)	−0.39 (0.18)	208.5	0.83
	N^{-1}	176		3.62 (0.09)	0.73 (0.09)		228.8	0.57
Carn	H	70	0.299 (0.596)	52.07 (10.87)	1.20 (0.19)	−0.34 (0.28)	157.8	0.70
	N^{-1}	38		34.43 (4.03)	0.86 (0.20)		68.7	0.65

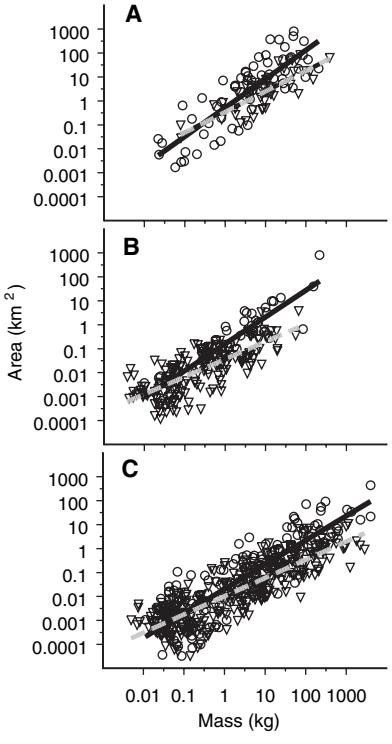

Fig. 2. The scaling across trophic levels of per-individual area (N^{-1}, triangles, dashed line) and individual home range size (H, circles, solid line). (**A**) Carnivores. (**B**) Omnivores. (**C**) Herbivores. Lines are least-squares fits. For detailed regression results, see Table 1.

the data for N and H. In a fully filled landscape, we expect individual home range size to be at least equal to the area per individual, $H \geq N^{-1}$. Because the model predicts increasing overlap in home ranges with increasing size, it follows that log-log plots of H and N^{-1} as function of M should be nearly coincident for the smallest mammals but diverge with increasing body mass. This is exactly what is observed (Figs. 1 and 2). The regression equations for all mammals suggest that although neighbor effects are negligible at the smallest body sizes, already at 1 kg only 31% of home range or resource supply rate is obtained by the owner, and just 7% at 100 kg (Fig. 1). These surprising results are robust to a more restrictive analysis using only species with data on both H and N^{-1} (table S1), and they highlight the so-far–underappreciated magnitude of neighbor effects.

Our finding of extensive home range overlap at all but the smallest body sizes falsifies key assumptions of hypotheses on the scaling of animal space use that assume exclusive access to resources (*12*) or, additionally, a body size dependence of resource supply rate (*13*, *14*). Population estimates of large-bodied species are as much as an order of magnitude higher than suggested by home range size. This finding is counter to the idea that increased census areas and the inclusion of unsuitable habitat have led to underestimates of population densities for large-bodied animals [(*31*), but see (*32*)]. Indeed, the high degree of home range overlap in large mammals suggests that population density rather than home range size is the better measure to use in quantifying individual area needs for conservation purposes.

Our findings resolve a long-standing conflict resulting from two divergent approaches to studying the use of space in animals, based on home range size and population density. Our approach provides a simple and powerful framework for understanding how animal space use reflects the constraints of both harvesting resources and detecting and responding to intruders. It has important applications in other behavioral ecological phenomena, such as group living, mate finding, disease transmission, and predator-prey encounters. Our results show how mechanistic models based on first principles of physics, ecological energetics, and behavioral ecology can make testable predictions and enhance our understanding of macroecological patterns.

References and Notes

1. B. K. McNab, *Am. Nat.* **97**, 133 (1963).
2. L. Witting, *J. Theor. Biol.* **177**, 129 (1995).
3. T. M. Blackburn, K. J. Gaston, *J. Anim. Ecol.* **66**, 233 (1997).
4. R. H. Peters, K. Wassenberg, *Oecologia* **60**, 89 (1983).
5. J. Damuth, *Nature* **290**, 699 (1981).
6. M. Silva, M. Brimacombe, J. A. Downing, *Global Ecol. Biogeogr.* **10**, 469 (2001).
7. W. A. Calder, *Size, Function and Life History* (Harvard Univ. Press, Cambridge, MA, 1984).
8. J. W. A. Grant, C. A. Chapman, K. S. Richardson, *Behav. Ecol. Sociobiol.* **31**, 149 (1992).
9. G. Mace, P. H. Harvey, *Am. Nat.* **121**, 120 (1983).
10. T. W. Schoener, *Ecology* **49**, 123 (1968).
11. D. A. Kelt, D. H. Van Vuren, *Am. Nat.* **157**, 637 (2001).
12. S. L. Lindstedt, B. J. Miller, S. W. Buskirk, *Ecology* **67**, 413 (1986).
13. A. S. Harestad, F. L. Bunnell, *Ecology* **60**, 389 (1979).
14. J. P. Haskell, M. E. Ritchie, H. Olff, *Nature* **418**, 527 (2002).
15. J. Damuth, *Biol. J. Linn. Soc.* **15**, 185 (1981).
16. R. K. Swihart, N. A. Slade, B. J. Bergstrom, *Ecology* **69**, 393 (1988).
17. T. Garland, *Am. Nat.* **121**, 571 (1983).
18. C. Carbone, G. Cowlishaw, N. J. B. Isaac, J. M. Rowcliffe, *Am. Nat.*, in press.
19. P. M. Waser, *Am. Nat.* **110**, 911 (1976).
20. A. Okubo, *Diffusion and Ecological Problems: Mathematical Models; Biomathematics* (Springer-Verlag, Berlin, 1980).
21. L. Barrett, C. B. Lowen, *Funct. Ecol.* **12**, 857 (1998).
22. R. A. Kiltie, *Funct. Ecol.* **14**, 226 (2000).
23. K. Kirschfield, in *Neural Principles in Vision*, F. Zettler, R. Weiler, Eds. (Springer, Berlin, 1976), pp. 354–370.
24. V. M. Savage, J. F. Gillooly, J. H. Brown, G. B. West, E. L. Charnov, *Funct. Ecol.* **18**, 257 (2004).
25. R. H. Peters, *The Ecological Implications of Body Size* (Cambridge Univ. Press, Cambridge, 1983).
26. J. Damuth, *Biol. J. Linn. Soc.* **31**, 193 (1987).
27. Materials and methods are available as supporting material on *Science* Online.
28. C. Carbone, J. L. Gittleman, *Science* **295**, 2273 (2002).
29. P. A. Marquet, *Science* **295**, 2229 (2002).
30. S. K. M. Ernest *et al.*, *Ecol. Lett.* **6**, 990 (2003).
31. T. M. Blackburn, K. J. Gaston, *Oikos* **75**, 303 (1996).
32. C. N. Johnson, *Oikos* **85**, 565 (1999).
33. We are indebted to D. A. Kelt and D. H. Van Vuren for granting us access to their compilation of home range data and to J. Damuth for making his population density data publicly available. We thank A. P. Allen, E. L. Charnov, S. K. M. Ernest, A. P. Dobson, A. B. Herman, D. Rubenstein, R. P. Freckleton, J. L. Gittleman, P. H. Harvey, J. M. C. Hutchinson, N. J .B. Isaac, M. V. McPhee, H. Olff, J. M. Rowcliffe, V. Savage, D. Storch, J. S. Weitz, and E. P. White for inspiring discussions and helpful feedback on the manuscript. W.J. gratefully acknowledges support from the German Academic Exchange Service (DAAD) and the German Research Foundation (Deutsche Forschungsgemeinschaft).

Supporting Online Material

www.sciencemag.org/cgi/content/full/306/5694/266/DC1
Materials and Methods
Fig. S1
Table S1
References

29 June 2004; accepted 12 August 2004

Activating Mutations of *NOTCH1* in Human T Cell Acute Lymphoblastic Leukemia

Andrew P. Weng,[1]*† Adolfo A. Ferrando,[2]* Woojoong Lee,[1] John P. Morris IV,[2] Lewis B. Silverman,[2] Cheryll Sanchez-Irizarry,[1] Stephen C. Blacklow,[1] A. Thomas Look,[2] Jon C. Aster[1]‡

Very rare cases of human T cell acute lymphoblastic leukemia (T-ALL) harbor chromosomal translocations that involve *NOTCH1*, a gene encoding a transmembrane receptor that regulates normal T cell development. Here, we report that more than 50% of human T-ALLs, including tumors from all major molecular oncogenic subtypes, have activating mutations that involve the extracellular heterodimerization domain and/or the C-terminal PEST domain of NOTCH1. These findings greatly expand the role of activated NOTCH1 in the molecular pathogenesis of human T-ALL and provide a strong rationale for targeted therapies that interfere with NOTCH signaling.

T-ALL is an aggressive cancer that preferentially affects children and adolescents. It is commonly associated with acquired chromosomal translocations and other genetic or epigenetic abnormalities, which lead to aberrant expression of a select group of transcription factors (*1*). *NOTCH1* was discovered as a partner gene in a (7;9) chromosomal translocation found in <1% of T-ALLs (*2*). It encodes a transmembrane receptor that is required for the commitment of pluripotent progenitors to T cell fate (*3*) and the subsequent assembly of pre–T cell receptor complexes in immature thymocytes (*4*).

Cleavage of pro-NOTCH1 by a furinlike protease during transit to the cell surface (*5*) produces a NOTCH1 heterodimer comprised of noncovalently associated extracellular (NEC) and transmembrane (NTM) subunits (*6*). The heterodimerization domain (HD) responsible for stable subunit association consists of a 103 amino acid region of NEC (HD-N) and a 65 amino acid region in NTM (HD-C) (*7*). Physiologic activation of NOTCH receptors occurs when ligands of the Delta-Serrate-Lag2 (DSL) family bind to the NEC subunit and initiate a cascade of proteolytic cleavages in the NTM subunit. The final cleavage, catalyzed by γ-secretase (*8*, *9*), generates intracellular NOTCH (ICN), which translocates to the nucleus and forms a large transcriptional activation complex that includes proteins of the Mastermind family (*10*–*12*).

Prior work has shown that enforced NOTCH1 signaling is a potent inducer of T-ALL in the mouse (*13*–*15*) and is required to sustain the growth of a human t(7;9)-positive T-ALL cell line (*16*). To investigate the possibility of a more general role for NOTCH signaling in human T-ALL, we tested T-ALL cell lines lacking the t(7;9) for NOTCH dependency by treating these cells with a γ-secretase inhibitor (*17*). Of 30 human T-ALL cell lines tested, 5 showed a G_0/G_1 cell-cycle arrest that equaled or exceeded that of T6E, a reference NOTCH1-dependent murine T-ALL cell line (Fig. 1A). This drug-induced growth suppression was abrogated by retroviral expression of ICN1 (Fig. 1B) and reproduced (fig. S1) by retroviral expression of dominant negative Mastermindlike-1 (*16*). These results indicated that the growth of these five cell lines depends on NOTCH-transduced signals.

Because physical dissociation of the NOTCH extracellular domain has been linked to receptor activation (*6*, *18*), we reasoned that the HD domain of NOTCH1 (*7*) could be the site of gain-of-function mutations. A second logical candidate region for oncogenic mutations is the negative regulatory PEST sequence lying at the C terminus of the NOTCH1 NTM (*19*), as retroviral insertions that cause deletion of this region have been reported in murine T-ALL (*14*, *15*). Remarkably, sequencing revealed mutations that involve both the HD-N domain and the PEST domain in four of the five NOTCH-dependent cell lines (summarized in Fig. 2). Missense mutations affecting HD-N caused nonconservative changes at amino acid positions that are invariant in vertebrate NOTCH1 receptors (fig. S2). One cell line, DND-41, had two different HD-N mutations within the same *NOTCH1* allele. The PEST mutations were short insertions or deletions causing shifts in reading frame that are predicted to result in partial or complete deletion of the PEST domain (fig. S4). Sequencing of cDNAs revealed that the

[1]Department of Pathology, Brigham and Women's Hospital, Harvard Medical School, Boston, MA 02115, USA. [2]Department of Pediatric Oncology, Dana Farber Cancer Institute, Harvard Medical School, Boston, MA 02115, USA.

*These authors contributed equally to this work.
†Present address: Department of Pathology, British Columbia Cancer Agency, Vancouver, BC V5Z 4E6, Canada.
‡To whom correspondence should be addressed. E-mail: jaster@rics.bwh.harvard.edu

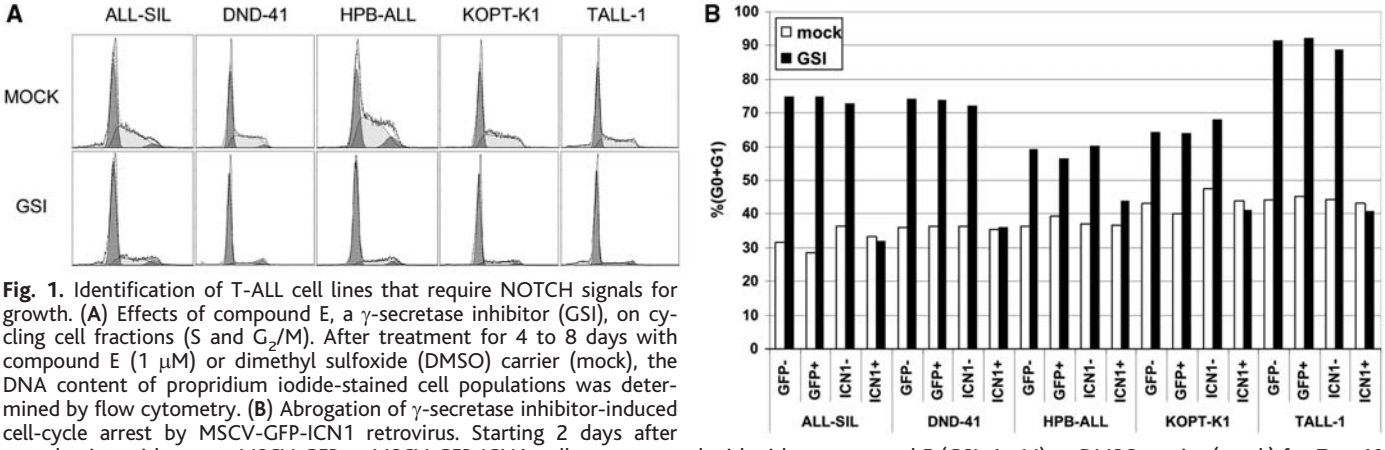

Fig. 1. Identification of T-ALL cell lines that require NOTCH signals for growth. (**A**) Effects of compound E, a γ-secretase inhibitor (GSI), on cycling cell fractions (S and G_2/M). After treatment for 4 to 8 days with compound E (1 μM) or dimethyl sulfoxide (DMSO) carrier (mock), the DNA content of propridium iodide-stained cell populations was determined by flow cytometry. (**B**) Abrogation of γ-secretase inhibitor-induced cell-cycle arrest by MSCV-GFP-ICN1 retrovirus. Starting 2 days after transduction with empty MSCV-GFP or MSCV-GFP-ICN1, cells were treated with either compound E (GSI, 1 μM) or DMSO carrier (mock) for 7 to 10 days. After staining with DRAQ5, the proportion of growth-arrested cells ($G_0 + G_1$ fractions) in the GFP^- and GFP^+ subpopulations was determined by flow cytometry.

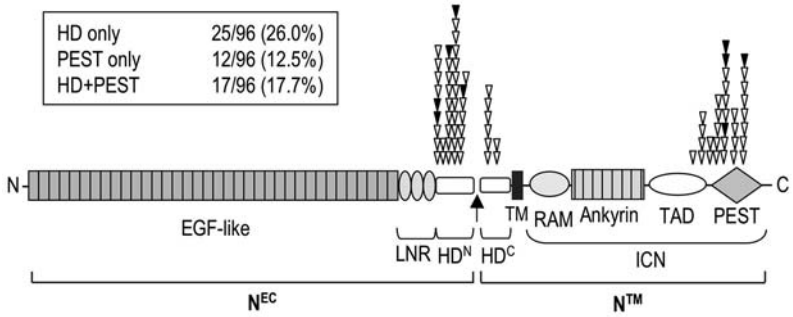

Fig. 2. NOTCH1 HD and PEST domain mutations in human T-ALL. A schematic representation of human NOTCH1 shows the distribution and frequency of HD-N, HD-C, and PEST domain mutations in NOTCH-dependent T-ALL cell lines (black arrowheads) and primary T-ALL samples (white arrowheads). N^{EC}, NOTCH1 extracellular domain; LNR, Lin/NOTCH repeats; HD-N and HD-C, N-terminal and C-terminal halves, respectively, of the heterodimerization domain; N^{TM}, NOTCH transmembrane subunit; TM, transmembrane domain; RAM, RAM domain; ANK, ankyrin repeat domain; TAD, transcriptional activation domain. The arrow denotes the site of furin cleavage.

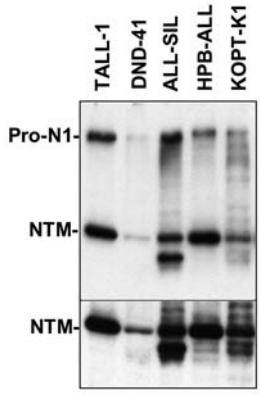

Fig. 3. Western blot analysis of lysates from NOTCH-dependent T-ALL cell lines. Whole-cell extracts were analyzed with a rabbit polyclonal antibody raised against the transcriptional activation domain of NOTCH1 (*13*). The lower panel is a longer exposure of the same blot that accentuates the presence of additional NOTCH1 polypeptides of smaller size than the normal NTM. Each lane contains 25 μg total protein.

HD-N and PEST domain mutations lie in cis in the same *NOTCH1* allele in each of the four cell lines tested (fig. S5). Normal *NOTCH1* cDNA clones were also identified in each cell line, indicating that both alleles are expressed. This is consistent with Western blot analysis (Fig. 3), which revealed that cell lines with HD-N and PEST domain mutations contained a polypeptide of the expected size of NTM and additional smaller polypeptides. We also sequenced a subset of T-ALL cell lines that were insensitive to the γ-secretase inhibitor. This revealed NOTCH1 mutations in 9 out of 19 nonresponsive cell lines, including three lines with dual HD and PEST domain mutations (table S1). The failure of all cell lines with mutations to respond to γ-secretase inhibitors may result from these cell lines having been maintained in tissue culture for many years.

We also identified frequent *NOTCH1* HD and PEST domain mutations in primary T-ALL samples obtained from the bone marrow of 96 children and adolescents at the time of diagnosis (summarized in Fig. 2). At least one mutation was identified in 54 tumors (56.2%). Mutations were seen in tumors associated with misexpression of *HOX11* (2 of 3 cases), *HOX11L2* (10 of 13, or 77%), *TAL1* (12 of 31, or 39%), *LYL1* (9 of 14, or 64%), *MLL-ENL* (1 of 3), or *CALM-AF10* (1 of 2) (table S2), which together define the major molecular subtypes of T-ALL (*1*). The HD domain mutations in primary tumors were clustered in a "hot spot" spanning residues 1574 to 1622 of HD-N and included each of the three L to P missense mutations originally identified in the *NOTCH*-dependent T-ALL cell lines, as well as deletions of 1 to 2 residues and short "in-frame" insertions (fig. S2). In addition, a smaller number of missense mutations were observed in HD-C, which again involved highly conserved residues (fig. S3). PEST domain mutations included insertions or deletions that induced a shift in reading frame and point mutations that created premature stop codons (fig. S4). In contrast with T-ALLs, B cell ALLs (B-ALLs) (n = 89) showed no mutations in these regions of *NOTCH1* (*20*). Mutations were also absent from four remission bone marrow samples obtained from patients whose T-ALLs harbored *NOTCH1* mutations (*20*), indicating that these mutations are acquired within the malignant clones.

To prove that HD domain mutations found in T-ALL patients have effects on function, NOTCH-sensitive reporter-gene assays were conducted in human U2OS cells (Fig. 4). Single L to P mutations within the HD-N domain at residues 1575, 1594, or 1601 caused a 3- to 9-fold increase in luciferase activity, whereas a T-ALL–associated PEST deletion at position 2471 resulted in ~1.5- to 2-fold increase. More strikingly, each HD mutation and the same PEST domain truncation in cis resulted in 20- to 40-fold increases; in contrast, the same mutations in trans produced lesser effects close to the average of each mutation acting alone. The synergistic interaction of HD and PEST domain mutations in cis is consistent with a model (fig. S6) in which (i) HD domain mutations enhance γ-secretase cleavage and increase the rate of production of ICN1 and (ii) truncations that remove the PEST domain increase ICN1 half-life (*19*). The intermediate levels of activation produced by these mutations in trans presumably reflect competition between relatively weak and strong gain-of-function NOTCH1 polypeptides for factors required for processing and signaling. The stimulatory effects of mutated transmembrane NOTCH1 polypeptides were completely abrogated by a γ-secretase inhibitor (Fig. 4), which indicates a requirement for proteolysis at the juxtamembrane site of NTM for signal transduction. In contrast, the stimulation produced by ICN1, which is constitutively nuclear, was unaffected by γ-secretase inhibition (Fig. 4).

Several factors may explain the high frequency of *NOTCH1* mutations in T-ALL. The requirement for NOTCH1 signals during several stages of normal early T cell development provides a functional basis for its frequent involvement. Unlike the t(7;9), which is created during attempted V-D-Jβ rearrangement in committed T cell progenitors, the common point mutations and insertions described here could occur in multipotent hematopoietic progenitors, which normally express *NOTCH1* (*21*). This would be predicted to induce daughter cells to adopt a T cell fate (*22*) and thereby increase the pool of cells at risk for additional leukemogenic events, such as synergistic mutations affecting *NOTCH1* and misexpression of other critical transcription factors. The *NOTCH1* mutations we describe here are currently specific to human T-ALL among vertebrate cancers, but a mutation involving the putative HD domain of the NOTCH homolog GLP-1 causes massive germ-cell proliferation in *Caenorhabditis elegans* (*23*), which suggests that such mutations have a highly conserved capacity to cause abnormal growth in specific cellular contexts.

Of potential clinical relevance, our findings identify the NOTCH pathway as a rational molecular therapeutic target in T-ALL. Although up to 75% of T-ALL patients are currently cured with very intensive cytotoxic chemotherapy regimens (*24*), new therapies are needed for patients with refractory disease, and less toxic, more efficacious drug combinations would be generally beneficial. Potent, specific inhibitors have already been developed (*25*) as a result of the involvement of γ-secretase in the production of amyloidogenic peptides in patients with Alzheimer's disease. On the basis of the results reported

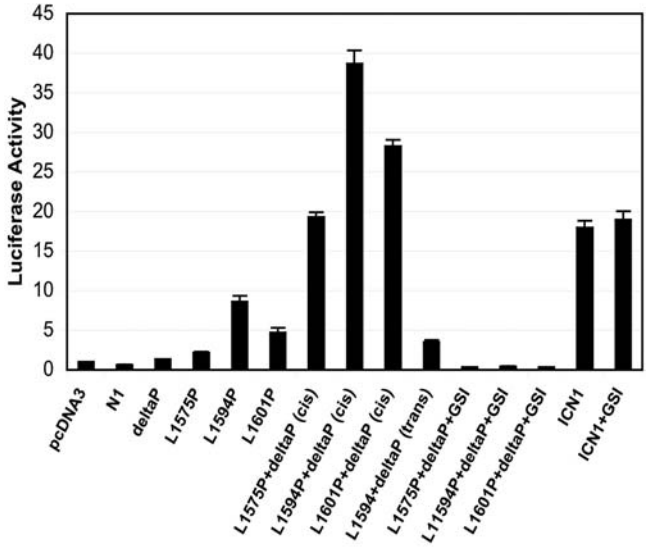

Fig. 4. HD and PEST domain mutations activate NOTCH1 signaling synergistically. Human U2OS cells were transiently cotransfected in 24-well format with the indicated pcDNA3 plasmids, a NOTCH-responsive luciferase reporter gene, and an internal *Renilla* luciferase internal control plasmid, as described previously (*13*). Twenty-five ng of pcDNA3 plasmid was used per well, except for experiments with pcDNA3-ICN1, in which 5 ng of plasmid per well was used. "DeltaP" denotes the presence of a deletion removing NOTCH1 residues 2473 to 2556. Normalized luciferase activities in whole-cell lysates were determined in triplicate and expressed relative to the activity in lysates prepared from vector-transfected cells. Error bars represent standard deviations.

here, clinical trials are warranted to test the efficacy and potential side effects (*26*) of this class of NOTCH-pathway inhibitor in patients with T-ALL.

References and Notes

1. A. A. Ferrando *et al.*, *Cancer Cell* **1**, 75 (2002).
2. L. W. Ellisen *et al.*, *Cell* **66**, 649 (1991).
3. F. Radtke *et al.*, *Immunity* **10**, 547 (1999).
4. A. Wolfer, A. Wilson, M. Nemir, H. R. MacDonald, F. Radtke, *Immunity* **16**, 869 (2002).
5. F. Logeat *et al.*, *Proc. Natl. Acad. Sci. U.S.A.* **95**, 8108 (1998).
6. M. D. Rand *et al.*, *Mol. Cell. Biol.* **20**, 1825 (2000).
7. C. Sanchez-Irizarry *et al.*, *Mol. Cell. Biol.*, in press.
8. R. Francis *et al.*, *Dev. Cell* **3**, 85 (2002).
9. W. T. Kimberly *et al.*, *Proc. Natl. Acad. Sci. U.S.A.* **100**, 6382 (2003).
10. A. E. Wallberg, K. Pedersen, U. Lendahl, R. G. Roeder, *Mol. Cell. Biol.* **22**, 7812 (2002).
11. C. J. Fryer, E. Lamar, I. Turbachova, C. Kintner, K. A. Jones, *Genes Dev.* **16**, 1397 (2002).
12. Y. Nam, A. P. Weng, J. C. Aster, S. C. Blacklow, *J. Biol. Chem.* **278**, 21232 (2003).
13. J. C. Aster *et al.*, *Mol. Cell. Biol.* **20**, 7505 (2000).
14. C. D. Hoemann, N. Beaulieu, L. Girard, N. Rebai, P. Jolicoeur, *Mol. Cell. Biol.* **20**, 3831 (2000).
15. B. J. Feldman, T. Hampton, M. L. Cleary, *Blood* **96**, 1906 (2000).
16. A. P. Weng *et al.*, *Mol. Cell. Biol.* **23**, 655 (2003).
17. Materials and methods are available as supporting material on *Science* Online.
18. H. Kramer, *Sci. STKE* **2000**, pe1 (2000).
19. N. Gupta-Rossi *et al.*, *J. Biol. Chem.* **276**, 34371 (2001).
20. J. C. Aster, A. A. Ferrando, A. P. Weng, unpublished data.
21. L. M. Calvi *et al.*, *Nature* **425**, 841 (2003).
22. D. Allman *et al.*, *J. Exp. Med.* **194**, 99 (2001).
23. L. W. Berry, B. Westlund, T. Schedl, *Development* **124**, 925 (1997).
24. C. H. Pui, M. V. Relling, J. R. Downing, *N. Engl. J. Med.* **350**, 1535 (2004).
25. M. S. Wolfe, *Nature Rev. Drug Discov.* **1**, 859 (2002).
26. G. T. Wong *et al.*, *J. Biol. Chem.* **279**, 12876 (2004).

27. We thank M. Wolfe for compound E and J.-P. Hezel for expert technical assistance. Supported by NIH grants CA82308 (J.C.A.), CA68484 and CA109901 (A.T.L.), CA94233 (S.C.B.), CA98093 (A.P.W.), and CA21765 (St. Jude Cancer Center). A.A.F. is a fellow of the Leukemia and Lymphoma Society.

Supporting Online Material

www.sciencemag.org/cgi/content/full/306/5694/269/DC1
Materials and Methods
Figs. S1 to S6
Tables S1 and S2
References

30 June 2004; accepted 24 August 2004

Jun Turnover Is Controlled Through JNK-Dependent Phosphorylation of the E3 Ligase Itch

Min Gao,[1] Tord Labuda,[1,2] Ying Xia,[1]* Ewen Gallagher,[1] Deyu Fang,[3]† Yun-Cai Liu,[3] Michael Karin[1]‡

The turnover of Jun proteins, like that of other transcription factors, is regulated through ubiquitin-dependent proteolysis. Usually, such processes are regulated by extracellular stimuli through phosphorylation of the target protein, which allows recognition by F box–containing E3 ubiquitin ligases. In the case of c-Jun and JunB, we found that extracellular stimuli also modulate protein turnover by regulating the activity of an E3 ligase by means of its phosphorylation. Activation of the Jun amino-terminal kinase (JNK) mitogen-activated protein kinase cascade after T cell stimulation accelerated degradation of c-Jun and JunB through phosphorylation-dependent activation of the E3 ligase Itch. This pathway modulates cytokine production by effector T cells.

Ubiquitin-dependent proteolysis controls turnover and abundance of transcription factors and other regulatory proteins (*1*). Protein ubiquitination requires the concerted action of ubiquitin-activating enzyme (E1), ubiquitin-conjugating enzymes (E2), and ubiquitin ligases (E3) (*2*, *3*). Extracellular stimuli can regulate protein turnover through inducible substrate phosphorylation which confers recognition by F box–containing E3 ligases (*4*). Such E3 ligases, which are devoid of catalytic activity, recognize only the phosphorylated forms of their substrates (*5*). Transcription factors regulated through ubiquitin-dependent turnover include the Jun proteins, components of the AP-1 transcription factor. The activity of c-Jun and JunB is enhanced by phosphorylation of their transcriptional activation domain by JNKs (*6*, *7*). JNK-dependent phosphorylation can also stabilize c-Jun (*8*, *9*). Recently, however, JNK-mediated phosphorylation was shown to accelerate c-Jun degradation by allowing its recognition by the E3 ligase Fbw7-containing Skp/Cullin/F-box protein complex (SCF^{Fbw7}) (*10*). Here, we provide physiological and biochemical evidence for another pathway through which extracellular stimuli control c-Jun and JunB abundance. This process is based on inducible phosphorylation of an E3 ligase of the homology to the E6-associated protein C terminus (HECT) family, which increases its catalytic activity.

[1]Laboratory of Gene Regulation and Signal Transduction, Department of Pharmacology, School of Medicine, University of California, San Diego, 9500 Gilman Drive, La Jolla, CA 92093–0723, USA. [2]Department of Medical Microbiology and Immunology and Institute of Molecular Biology, University of Copenhagen, 2200 Copenhagen N, Denmark. [3]Division of Cell Biology, La Jolla Institute for Allergy and Immunology, San Diego, CA 92121, USA.

*Present address: Department of Environmental Health, University of Cincinnati Medical Center, Cincinnati, OH 45267–0056, USA.
†Present address: Department of Biological Chemistry, University of Michigan Medical School, Ann Arbor, MI 48109–0606, USA.
‡To whom correspondence should be addressed: E-mail: karinoffice@ucsd.edu

The HECT domain E3 Itch functions in ubiquitin-dependent degradation of both c-Jun and JunB, which accumulate in T cells of *Itchy* mice, lacking Itch activity (*11*). Accumulation of JunB, a transcription factor that promotes differentiation of T helper 2 (Th2) cells and interleukin-4 (IL-4) gene transcription (*12*, *13*), is likely to contribute to excessive Th2 cytokine production in *Itchy* mice (*11*). A similar phenotype is exhibited by T cells lacking JNK1 (*14*) or both JNK1 and JNK2 (*15*), suggesting that JNK activation negatively regulates Th2 cytokine production. It is not known, however, whether this function is related to JNK-dependent modulation of JunB turnover.

To understand how JNK activation regulates Th2 cytokine expression, we examined T cells from *Mekk1*$^{\Delta KD}$ mice that express an inactive form of mitogen and extracellular kinase kinase 1 (MEKK1) (*16*), a mitogen-activated protein kinase (MAPK) kinase kinase (MAP3K) that is a potent activator of JNK signaling (*17*). *Mekk1*$^{\Delta KD}$ mice are viable (*16*) without any obvious defect in generation or survival of T cells or their intrathymic differentiation into CD4$^+$ and CD8$^+$ subsets (fig. S1). Yet, T cells from these mice exhibit reduced JNK activation following engagement of the T cell receptor (TCR) and the CD28 auxiliary receptor (Fig. 1A). *Mekk1*$^{\Delta KD}$ peripheral T cells and thymocytes also hyperproliferated in response to stimulation with antibodies to CD3 and CD28 (fig. S2) and within 4 hours of receptor engagement expressed larger amounts of IL-4 and IL-13 mRNAs relative to those in wild-type (WT) cells, although they expressed normal amounts of IL-2 mRNA (Fig. 1B). IL-4, as the master regulator of Th2 effector T cell differentiation, can induce expression of other cytokines, including IL-5, IL-10, and IL-13 (*18*). Indeed, after 24 hours, activated *Mekk1*$^{\Delta KD}$ T cells expressed increased amounts of IL-5, IL-10, and IL-13 mRNAs in addition to IL-4 mRNA (Fig. 1B). The mRNAs for IL-2 and the Th1 cytokine interferon-γ (IFNγ) remained unchanged. We also cultured naïve WT or *Mekk1*$^{\Delta KD}$ CD4$^+$ T cells under Th1- or Th2-polarization conditions (*18*, *19*) to examine their differentiation into effector cells. Because of the BL6×C129 genetic background (*20*), WT Th2 cells produced relatively small amounts of IL-4, but their amounts were increased in *Mekk1*$^{\Delta KD}$ Th2 cells (Fig. 1C). Production of IFNγ by Th1 cells remained unchanged.

To examine whether the effect of MEKK1 on Th2 cytokine production is JNK dependent, we crossed *Jnk1*$^{-/-}$ mice with *Mekk1*$^{\Delta KD}$ mice. *Mekk1*$^{+/\Delta KD}$*Jnk1*$^{+/-}$ CD4$^+$ T cells expressed increased amounts of IL-4, IL-5, IL-10, and IL-13 mRNAs relative to those in

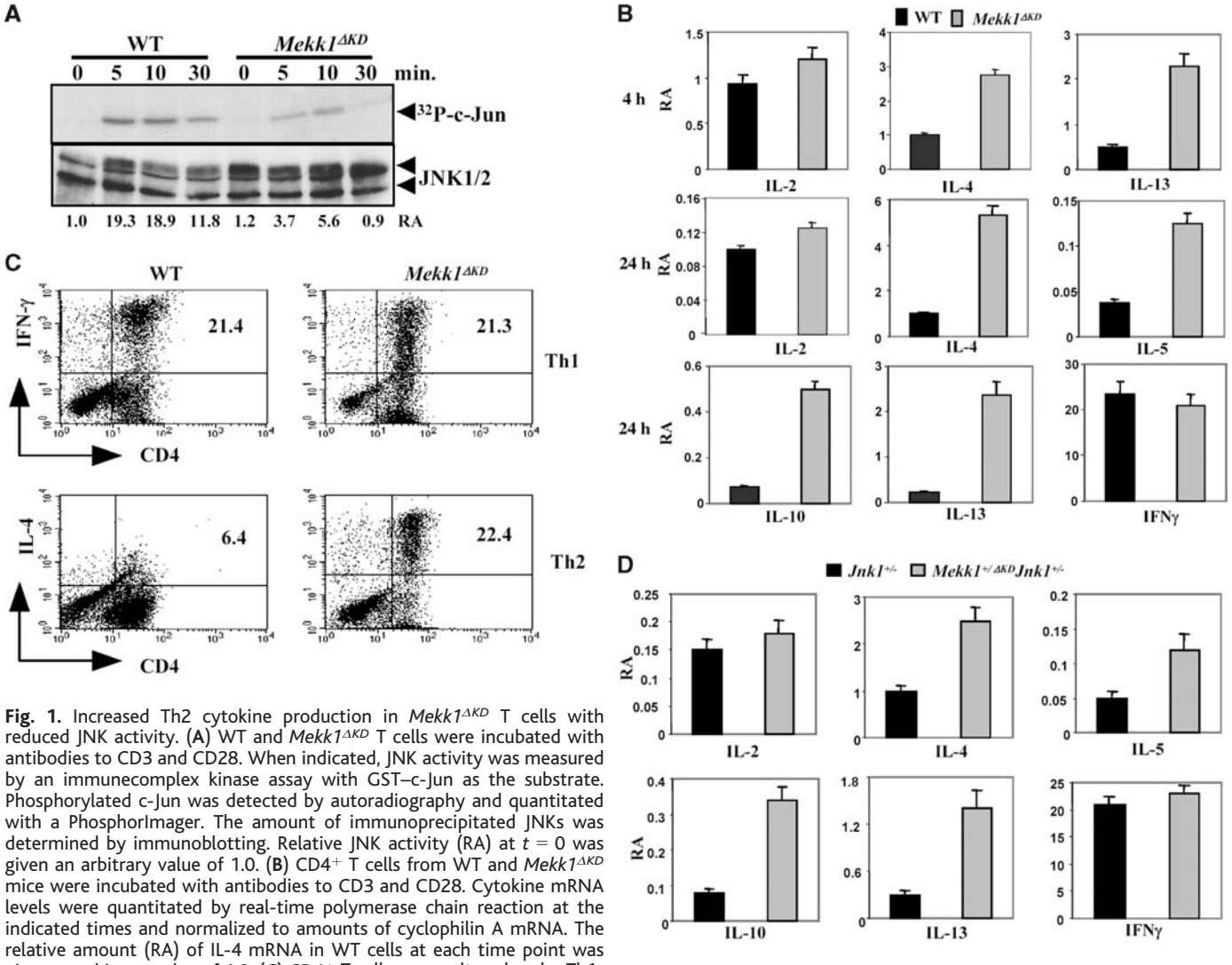

Fig. 1. Increased Th2 cytokine production in *Mekk1*$^{\Delta KD}$ T cells with reduced JNK activity. (**A**) WT and *Mekk1*$^{\Delta KD}$ T cells were incubated with antibodies to CD3 and CD28. When indicated, JNK activity was measured by an immunecomplex kinase assay with GST–c-Jun as the substrate. Phosphorylated c-Jun was detected by autoradiography and quantitated with a PhosphorImager. The amount of immunoprecipitated JNKs was determined by immunoblotting. Relative JNK activity (RA) at $t = 0$ was given an arbitrary value of 1.0. (**B**) CD4$^+$ T cells from WT and *Mekk1*$^{\Delta KD}$ mice were incubated with antibodies to CD3 and CD28. Cytokine mRNA levels were quantitated by real-time polymerase chain reaction at the indicated times and normalized to amounts of cyclophilin A mRNA. The relative amount (RA) of IL-4 mRNA in WT cells at each time point was given an arbitrary value of 1.0. (**C**) CD4$^+$ T cells were cultured under Th1- or Th2-polarizing conditions for 7 days. Th subsets were restimulated with antibodies to CD3 and CD28 and analyzed for cytokine expression by flow cytometry after 6 hours. (**D**) CD4$^+$ T cells from *Jnk1*$^{+/-}$ and *Mekk1*$^{+/\Delta KD}$*Jnk1*$^{+/-}$ mice were stimulated with antibodies to CD3 and CD28 and cytokine mRNAs were quantitated as in (B) after 24 hours. Error bars in (B) and (D) show mean + SD.

Jnk1$^{+/-}$ (Fig. 1D) or *Mekk1*$^{+/\Delta KD}$ (*21*) T cells, indicating JNK1 dependence. These results agree with Dong *et al*., who found hyperproliferation and increased Th2 cytokine production by *Jnk1*$^{-/-}$ T cells (*14*), and differ from those reported by Sabapathy *et al*., who found reduced proliferation of *Jnk1*$^{-/-}$ T cells, attributable to diminished IL-2 expression (*22*). As shown above, the loss of MEKK1 and JNK1 does not affect IL-2 mRNA levels. The elevated Th2 cytokine response of *Mekk1*$^{\Delta KD}$ CD4^{+} T cells was IL-4 dependent, given that it was absent in *Mekk1*$^{\Delta KD}$*IL-4*$^{-/-}$ T cells (fig. S3).

Multiple transcription factors, including nuclear factor of activated T cells (NF-AT), GATA-3, c-Maf, and JunB, regulate *IL-4* gene expression (*19*). We examined the amounts of these transcription factors in WT and *Mekk1*$^{\Delta KD}$ T cells. Both c-Jun and JunB were increased in activated *Mekk1*$^{\Delta KD}$ CD4^{+} T cells, whereas amounts of JunD, another family member, as well as GATA-3, c-Maf, NF-ATc1, and NF-ATc2 were unchanged (Fig. 2A). The effect on c-Jun and JunB resulted from loss of JNK activity, because two different JNK inhibitors—SP600125 (*23*) and JNKI-1, a peptide inhibitor based on the c-Jun docking site for JNK (*24*, *25*)—also increased c-Jun and JunB expression (Fig. 2B). No such effects were observed with the p38 inhibitor SB202190 (*21*). Elevated c-Jun and JunB expression was also found in *Jnk1*$^{-/-}$ T cells, whereas *Jnk2*$^{-/-}$ T cells showed a slight reduction (fig. S4). These results indicate that a JNK1 deficiency rather than a JNK2 deficiency is responsible for the altered expression of c-Jun and JunB in *Mekk1*$^{\Delta KD}$ T cells.

Despite the change in protein abundance, the amounts of *c-Jun* and *JunB* mRNAs remained unchanged (Fig. 2C). We therefore examined whether MEKK1 and JNK promoted c-Jun and JunB turnover. In pulse-chase experiments, in WT T cells, newly synthesized c-Jun and JunB turned over with half-lives ($T_{1/2}$) of 59 and 78 min, respectively, but were more stable in *Mekk1*$^{\Delta KD}$ cells, with $T_{1/2}$s of 109 and 280 min, respectively (Fig. 2D). The turnover of RelA(p65) remained unaltered. After engagement of TCR and CD28 in WT and *Mekk1*$^{\Delta KD}$ T cells, the amounts of *JunB* mRNA were very similar, but the amounts of JunB protein after 1 to 4 days of stimulation were greater in the mutant cells (Fig. 2E). Thus, activation of the JNK MAPK cascade appears to accelerate turnover of JunB in CD4^{+} T cells and may have an instructional role in their polarization into Th1 and Th2 effector cells.

The phenotypic and biochemical similarities between *Mekk1*$^{\Delta KD}$ and *Itchy* T cells raised the possibility that JNK-enhanced JunB and c-Jun turnover is Itch dependent. We examined this in transfected 293T cells because of difficulties in detecting endogenously ubiquitinated proteins in primary T cells. Ectopic expression of MEKK1 in 293T cells promoted polyubiquitination of both c-Jun (*21*) and JunB (Fig. 3A) in an Itch-dependent manner. Overexpression of kinase-deleted MEKK1 did not enhance Itch-dependent Jun polyubiquitination (Fig. 3A). Itch-dependent Jun ubiquitination was enhanced by a constitutively active JNKK2-JNK1 fusion protein, but not by an inactive version (Fig. 3B). JNK-enhanced ubiquitination correlated with accelerated JunB degradation (fig. S5). Treatment with a JNK inhibitor reduced the extent of Itch + MEKK1-induced polyubiquitination of c-Jun and JunB (Fig. 3C). This effect of JNK, however, appeared to be independent of JNK-mediated c-Jun phosphorylation because mutant versions of c-Jun lacking its JNK phosphorylation sites (*8*, *26*) were ubiquitinated as efficiently as WT c-Jun in cells overexpressing Itch and WT MEKK1 (Fig. 3D).

Unlike F box–containing E3 ligases, HECT domain ligases are thought to recognize their substrates independently of their

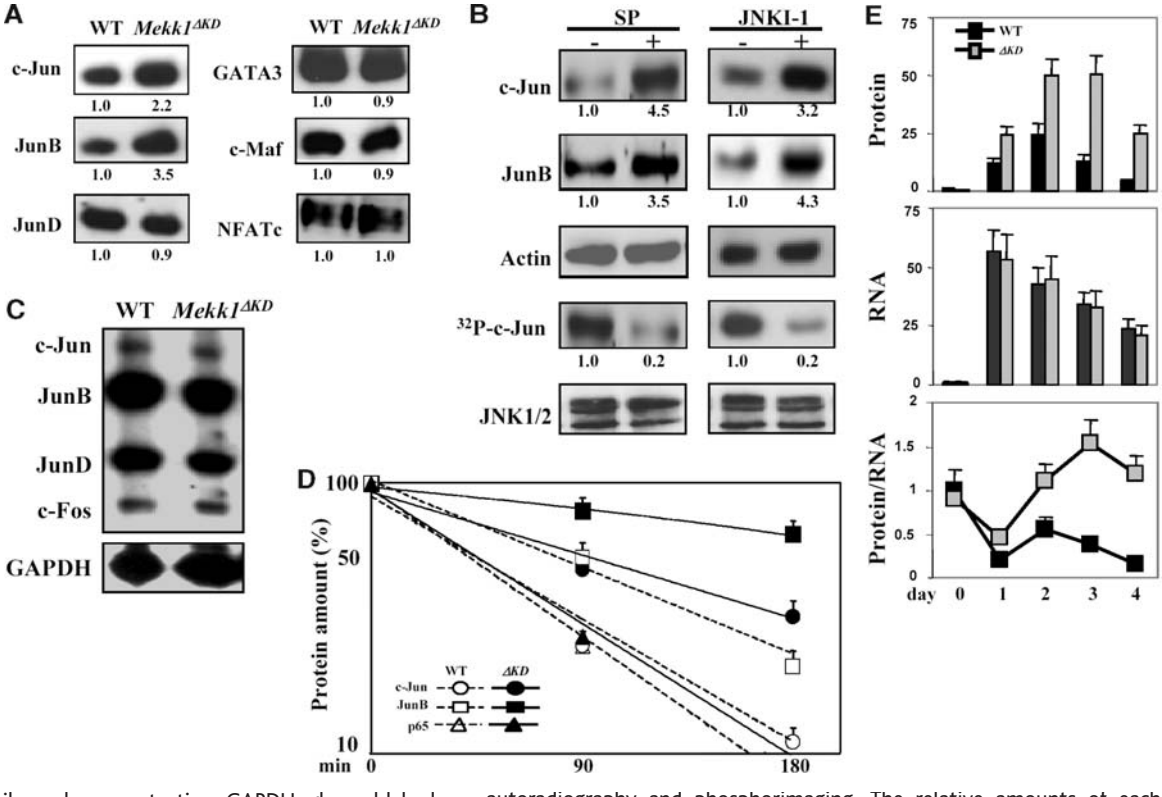

Fig. 2. Decreased turnover of JunB and c-Jun after inactivation of MEKK1 or JNK. (**A**) WT and *Mekk1*$^{\Delta KD}$ CD4^{+} T cells were stimulated with antibodies to CD3 and CD28 for 24 hours. Cell extracts were prepared and the amounts of various transcription factors were measured by immunoblotting and densitometry. The amount of each protein in WT cells was given an arbitrary value of 1.0. (**B**) WT CD4^{+} T cells were stimulated as above in the absence or presence of JNK inhibitors (SP600125 or JNKI-1) for 24 hours. Jun protein levels were analyzed as above and JNK activity was measured by an immunecomplex kinase assay. (**C**) The mRNA amounts of Jun family members and c-Fos in cells from (A) were measured by ribonuclease protection. GAPDH, glyceraldehyde-3-phosphate dehydrogenase. (**D**) WT and *Mekk1*$^{\Delta KD}$ T cells were pulse-labeled with [^{35}S] amino acids and chased with nonlabeled amino acids. Proteins were immunoprecipitated at the indicated times postlabeling, separated by SDS–polyacrylamide gel electrophoresis and analyzed by autoradiography and phosphorimaging. The relative amounts of each [^{35}S]-labeled protein at $t = 0$ were considered to be 100%. (**E**) WT CD4^{+} T cells were stimulated with antibodies to CD3 and CD28. At the indicated time points, the relative levels of JunB mRNA and protein were quantitated as in (A) and (C). Error bars in (E) and (F) show mean + SD.

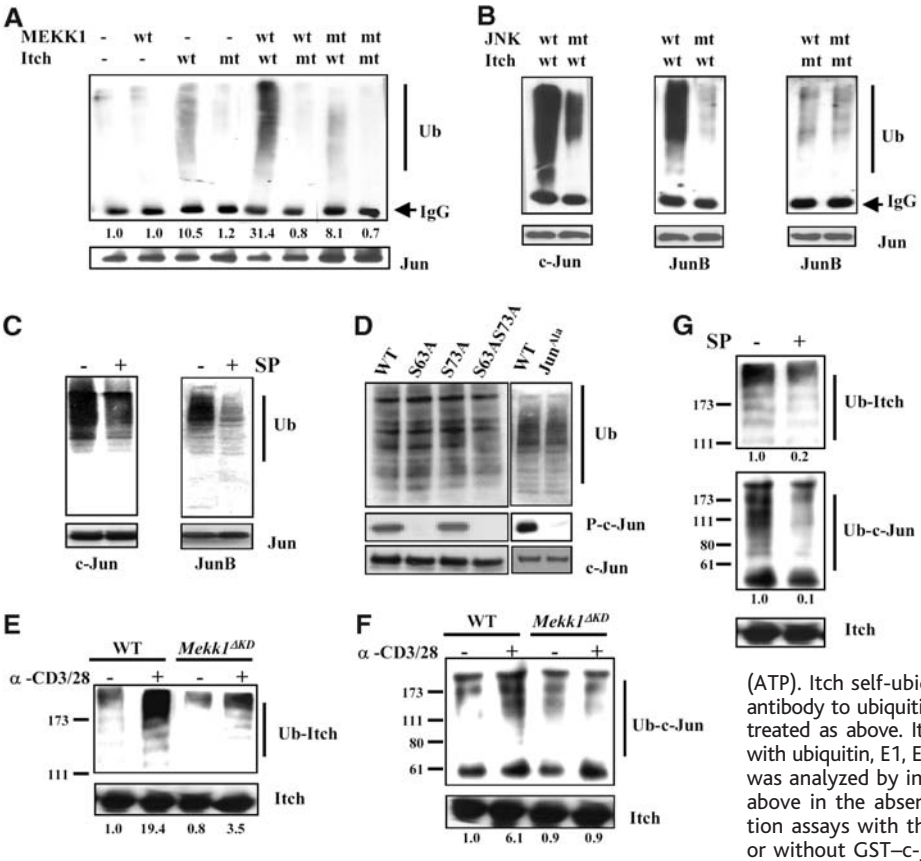

Fig. 3. The MEKK1-JNK cascade promotes c-Jun and JunB ubiquitination by enhancing Itch activity. (**A**) 293T cells were transiently transfected with plasmids encoding hemagglutinin (HA)–tagged ubiquitin, Myc-tagged JunB, WT or a kinase domain–deleted (mt) MEKK1, and WT or catalytically inactive (mt) Itch. Ubiquitin conjugation was examined by immunoblotting with an antibody to HA and quantitated by densitometry. IgG, immunoglobulin G. (**B**) 293T cells were transfected with HA-ubiquitin, Myc-tagged c-Jun or JunB, WT or catalytically inactive (mt) Itch, and WT or inactive (mt) JNKK2-JNK1 fusion proteins. Jun ubiquitination was examined as above. (**C**) 293T cells were transfected with c-Jun or JunB, HA-ubiquitin, Itch, and MEKK1. Cells were incubated with or without JNK inhibitor (SP600125) for 24 hours and analyzed as above. (**D**) 293T cells were transfected as above with WT or phosphorylation-deficient c-Jun constructs, Itch, and MEKK1. Ubiquitin conjugation was analyzed as above and c-Jun phosphorylation was examined by immunoblotting. (**E**) WT and *Mekk1*$^{\Delta KD}$ T cells were left unstimulated or stimulated with antibodies to CD3 and CD28 for 15 min. Itch was immunoprecipitated and incubated with ubiquitin, E1, E2, and adenosine 5′-triphosphate (ATP). Itch self-ubiquitination was analyzed by immunoblotting with antibody to ubiquitin and quantitated by densitometry. (**F**) T cells were treated as above. Itch immunecomplexes were isolated and incubated with ubiquitin, E1, E2, ATP, and purified GST–c-Jun. c-Jun ubiquitination was analyzed by immunoblotting. (**G**) WT T cells were stimulated as above in the absence or presence of SP600125. In vitro ubiquitination assays with the use of immunoprecipitated Itch as the E3 with or without GST–c-Jun as the substrate were done as above.

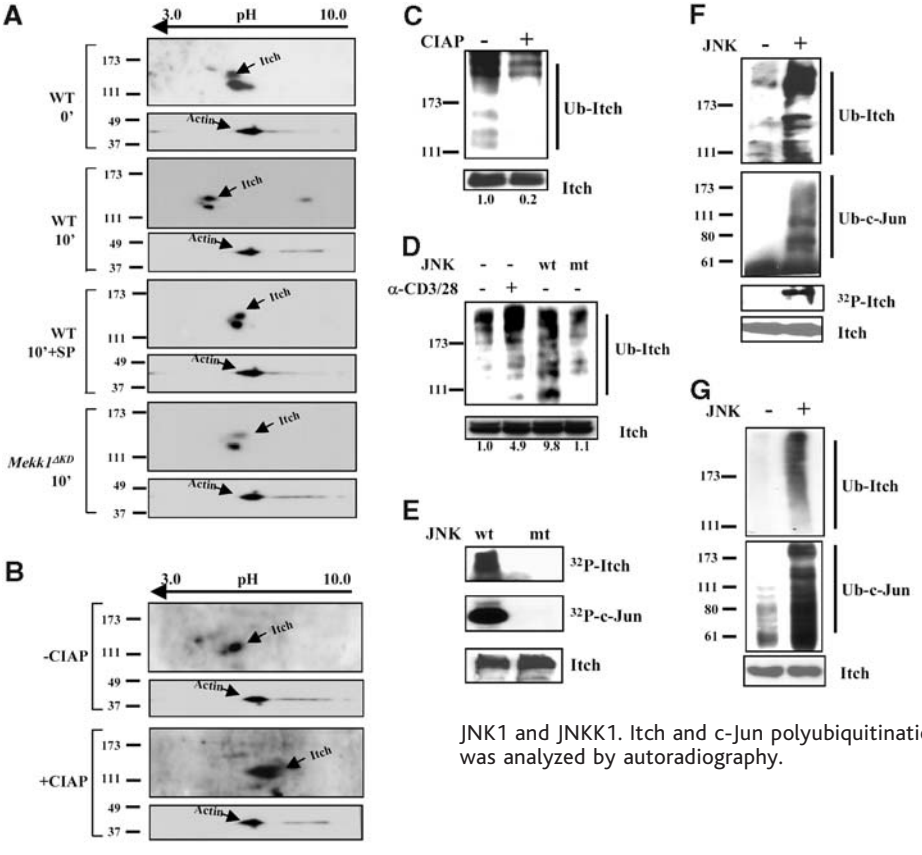

Fig. 4. Increased E3 activity of Itch after JNK-mediated phosphorylation. (**A**) Proteins from non-stimulated (0′) and activated (10′) WT T cells incubated without or with SP600125 were resolved by 2D gel electrophoresis, transferred to membranes, and immunoblotted with antibodies to Itch and actin. Itch migration in activated *Mekk1*$^{\Delta KD}$ cells was similarly analyzed. (**B**) Extracts from activated WT T cells were incubated without or with CIAP before 2D gel electrophoresis and immunoblotting as above. (**C**) Itch was immunoprecipitated from the extracts used in (B) and incubated with ubiquitin, E1, E2, and ATP. Itch ubiquitination was analyzed by immunoblotting with the antibody to ubiquitin and densitometry. (**D**) Immunoprecipitated Itch from nonstimulated T cells was incubated with active (wt) or inactive (mt) JNK1 and JNKK1. Itch ubiquitination was analyzed as above and quantitated by densitometry. (**E**) Immunoprecipitated Itch from nonstimulated T cells was incubated with active or inactive JNK1 and JNKK1 in the presence of [γ-^{32}P]ATP. GST–c-Jun was included as a positive control. Protein phosphorylation was analyzed by autoradiography. The same membrane was probed with antibody to Itch. In vitro translated Itch (**F**) or a recombinant GST-Itch (**G**) was incubated with JNK1 and JNKK1. Itch and c-Jun polyubiquitination were analyzed as above. Itch phosphorylation was analyzed by autoradiography.

phosphorylation. We therefore examined whether JNK activation enhances Jun ubiquitination by modulating the activity of Itch. Itch undergoes self-ubiquitination, and this activity was enhanced if it was isolated from WT T cells activated with antibodies to CD3 and CD28 (Fig. 3E). Little enhancement of Itch self-ubiquitination was observed after activation of *Mekk1*$^{\Delta KD}$ T cells (Fig. 3E). The ability of Itch to promote ubiquitination of a glutathione *S*-transferase (GST)–c-Jun substrate was enhanced in response to T cell activation and this response was also diminished in *Mekk1*$^{\Delta KD}$ cells (Fig. 3F). Both Itch self-ubiquitination and its ability to promote c-Jun polyubiquitination largely depended on incubation with both E1 and E2 (Ubc7) enzymes (fig. S6) and were reduced in activated T cells that were treated with a JNK inhibitor (Fig. 3G).

To examine whether Itch is a target for JNK-mediated phosphorylation, we separated proteins from nonactivated and activated T cells by two dimensional (2D) gel electrophoresis and transferred them to membranes. Following T cell activation, Itch became more negatively charged and displayed a lower isoelectric point (Fig. 4A). These changes are consistent with increased Itch phosphorylation and were reversed by calf intestine alkaline phosphatase (CIAP) (Fig. 4B). The kinetics of Itch phosphorylation correlated with those of JNK activation (fig. S7). Furthermore, when Itch phosphorylation was reduced by treatment with a JNK inhibitor and compared with that of WT cells, less TCR-induced Itch phosphorylation was observed in *Mekk1*$^{\Delta KD}$ cells (Fig. 4A). Similarly, Itch self-ubiquitination and c-Jun polyubiquitination were reduced after CIAP treatment of isolated Itch (Fig. 4C) (*21*). Moreover, incubation of Itch from nonstimulated T cells with activated JNK1 enhanced its self-ubiquitination, but incubation with inactive JNK1 had no effect (Fig. 4D). Incubation of Itch with active JNK1 also led to its efficient phosphorylation (Fig. 4E). Incubation of in vitro translated Itch with JNK1 also increased its self-ubiquitination and its ability to promote c-Jun polyubiquitination (Fig. 4F). Similar results were obtained with recombinant Itch produced in *Escherichia coli* (Fig. 4G). Consistent with the changes in c-Jun and JunB expression seen in *Jnk1*$^{-/-}$ and *Jnk2*$^{-/-}$ T cells (fig. S4), JNK1 is a more efficient Itch kinase than JNK2 and as a result is a more potent activator of Itch (fig. S8). The highly efficient phosphorylation of Itch by JNK1 is due to the presence of a JNK docking site, whose mutational inactivation prevents Itch phosphorylation and activation by JNK1 (*21*).

Extracellular stimuli often affect ubiquitin-dependent proteolysis by inducible target protein phosphorylation, which confers recognition by F box–containing E3 ligases (*5*). Instead, the effect of JNK on Itch-dependent c-Jun and JunB polyubiquitination and turnover is exerted by means of Itch itself. Some members of the HECT domain family are thought to be constitutively active E3 ligases. However, Itch catalytic activity is strongly modulated in response to T cell activation, through JNK-dependent phosphorylation. It is plausible that other members of the HECT domain family may be subject to similar regulation. The regulation is exerted at the level of the enzyme and not the substrate, and as is the case for F box-containing ligases, it allows a simultaneous increase in the turnover of multiple proteins. Disruption of Itch-dependent JunB turnover either through inactivation of Itch or inhibition of JNK results in increased expression of Th2 cytokine genes. Given the importance of JunB for *IL-4* gene transcription and Th2 differentiation (*12*, *13*), one function of JNK-dependent Itch activation is likely to be attenuation of IL-4 production in response to strong T cell activating signals.

References and Notes

1. A. Varshavsky, *Nature Cell Biol.* **5**, 373 (2003).
2. A. Hershko, A. Ciechanover, *Annu. Rev. Biochem.* **67**, 425 (1998).
3. C. M. Pickart, *Annu. Rev. Biochem.* **70**, 503 (2001).
4. M. Karin, Y. Ben-Neriah, *Annu. Rev. Immunol.* **18**, 621 (2000).
5. P. K. Jackson, A. G. Eldridge, *Mol. Cell* **9**, 923 (2002).
6. M. Karin, *J. Biol. Chem.* **270**, 16483 (1995).
7. S. Gupta *et al.*, *EMBO J.* **15**, 2760 (1996).
8. A. M. Musti, M. Treier, D. Bohmann, *Science* **275**, 400 (1997).
9. S. Y. Fuchs, L. Dolan, R. J. Davis, Z. Ronai, *Oncogene* **13**, 1531 (1996).
10. A. S. Nateri, L. Riera-Sans, C. Da Costa, A. Behrens, *Science* **303**, 1374 (2004).
11. D. Fang *et al.*, *Nature Immunol.* **3**, 281 (2002).
12. B. Li, C. Tournier, R. J. Davis, R. A. Flavell, *EMBO J.* **18**, 420 (1999).
13. B. Hartenstein *et al.*, *EMBO J.* **21**, 6321 (2002).
14. C. Dong *et al.*, *Science* **282**, 2092 (1998).
15. C. Dong *et al.*, *Nature* **405**, 91 (2000).
16. L. Zhang *et al.*, *EMBO J.* **22**, 4443 (2003).
17. A. Minden *et al.*, *Science* **266**, 1719 (1994).
18. W. E. Paul, R. A. Seder, *Cell* **76**, 241 (1994).
19. K. M. Murphy *et al.*, *Annu. Rev. Immunol.* **18**, 451 (2000).
20. C. S. Hsieh, S. E. Macatonia, A. O'Garra, K. M. Murphy, *J. Exp. Med.* **181**, 713 (1995).
21. M. Gao, M. Karin, unpublished data.
22. K. Sabapathy *et al.*, *J. Exp. Med.* **193**, 317 (2001).
23. B. L. Bennett *et al.*, *Proc. Natl. Acad. Sci. U.S.A.* **98**, 13681 (2001).
24. T. Kallunki, T. Deng, M. Hibi, M. Karin, *Cell* **87**, 929 (1996).
25. T. Borsello *et al.*, *Nature Med.* **9**, 1180 (2003).
26. T. Smeal, B. Binetruy, D. A. Mercola, M. Birrer, M. Karin, *Nature* **354**, 494 (1991).

27. We thank A. Lin for providing the JNKK2-JNK1 fusion proteins and D. Bohmann for Jun^{Ala} construct. We thank A. Ciechanover and T. Hunter for helpful discussion and critique and L. Chang and J. Park for assistance. M.G. was supported by a postdoctoral fellowship from the Damon Runyon Cancer Research Foundation. T.L. was supported by the Alfred Benzon Foundation and the LEO Pharma Research Foundation, Denmark. Work was supported by the Sandler Family Research Foundation and NIH grants AI43477, ES04151 and ES06376 to M.K. and by NIH grant R21AI48542 and a Research Scholar grant from the American Cancer Society (ACS) to Y.-C.L. M.K. is the Frank and Else Schilling ACS Research Professor.

Supporting Online Material

www.sciencemag.org/cgi/content/full/1099414/DC1
Materials and Methods
Figs. S1 to S8
References

21 April 2004; accepted 18 August 2004
Published online 9 September 2004;
10.1126/science.1099414
Include this information when citing this paper.

A Glycine-Dependent Riboswitch That Uses Cooperative Binding to Control Gene Expression

Maumita Mandal,[1] Mark Lee,[2] Jeffrey E. Barrick,[2] Zasha Weinberg,[3] Gail Mitchell Emilsson,[1] Walter L. Ruzzo,[3,4] Ronald R. Breaker[1]*

We identified a previously unknown riboswitch class in bacteria that is selectively triggered by glycine. A representative of these glycine-sensing RNAs from *Bacillus subtilis* operates as a rare genetic on switch for the *gcvT* operon, which codes for proteins that form the glycine cleavage system. Most glycine riboswitches integrate two ligand-binding domains that function cooperatively to more closely approximate a two-state genetic switch. This advanced form of riboswitch may have evolved to ensure that excess glycine is efficiently used to provide carbon flux through the citric acid cycle and maintain adequate amounts of the amino acid for protein synthesis. Thus, riboswitches perform key regulatory roles and exhibit complex performance characteristics that previously had been observed only with protein factors.

Genetic control by riboswitches located within the noncoding regions of mRNAs is widespread among bacteria (*1*–*3*). About 2% of the genes in *Bacillus subtilis* are regulated by these metabolite-binding RNA domains (*4*). All riboswitches discovered thus far use

a single highly structured aptamer as a sensor for their corresponding target molecules. Selective binding of metabolite by the aptamer causes allosteric modulation of the secondary and tertiary structures of the mRNA 5′-untranslated region (5′-UTR), which changes gene expression by one or more mechanisms that influence transcription termination (*5*, *6*), translation initiation (*7*, *8*), or mRNA processing (*9*, *10*).

The existence of riboswitches in modern cells implies that RNA molecules have considerable potential for forming intricate structures that are comparable to protein receptors. Furthermore, riboswitches do not have an obligate need for additional protein factors to carry out their gene control tasks and thus serve as economical genetic switches that sense and respond to changes in metabolite concentrations. However, higher-ordered functions exhibited by some protein factors have not been observed with natural riboswitches. For example, many protein enzymes, receptors, and gene control factors make use of cooperative binding to provide the cell with a means to rapidly respond to small changes in ligand concentrations [e.g., (*11*–*13*)].

We recently reported the identification of highly conserved RNA motifs in numerous bacterial species that have features similar to known riboswitches (*14*). One of these motifs, termed *gcvT* (Fig. 1A), is found in many bacteria, where it typically resides upstream of genes that express protein components of the glycine cleavage system. In *B. subtilis*, a three-gene operon (*gcvT-gcvPA-gcvPB*) codes for components of this protein complex, which catalyzes the initial reactions for use of glycine as an energy source (*15*, *16*).

Two forms of the *gcvT* RNA motif, type I and type II (Fig. 1A), had been identified on the basis of differences in the sequences that flank their conserved cores (*14*). More sensitive computational scans (*17*) revealed that both motif types reside adjacent to each other, as represented by the architecture of the region immediately upstream of the *VC1422* gene (a putative sodium and alanine symporter) from *Vibrio cholerae* (Fig. 1B). Individually, the type I and type II elements appear to represent separate aptamer domains, wherein each presumably binds a separate target molecule. Furthermore, the linker sequence between the two aptamers exhibits some conservation of both sequence and length, suggesting that the aptamers are functionally coupled (fig. S1).

The metabolite-binding capabilities of *V. cholerae* RNAs were assessed by using a

[1]Department of Molecular, Cellular, and Developmental Biology, [2]Department of Molecular Biophysics and Biochemistry, Yale University, Post Office Box 208103, New Haven, CT 06520–8103, USA. [3]Department of Computer Science and Engineering, [4]Department of Genome Sciences, University of Washington, Post Office Box 352350, Seattle, WA 98195, USA.

*To whom correspondence should be addressed. E-mail: ronald.breaker@yale.edu

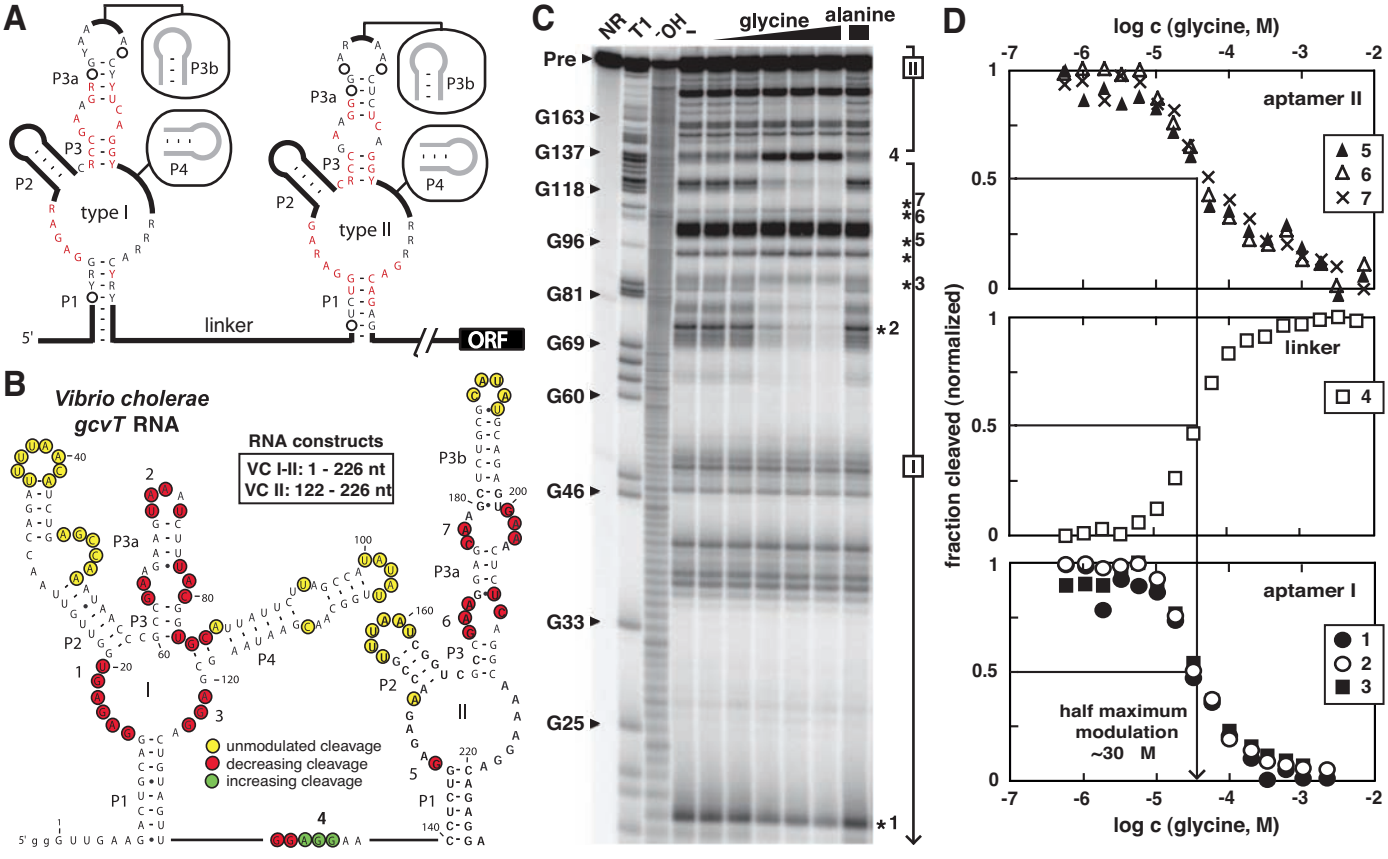

Fig. 1. Type I and type II *gcvT* motifs are natural RNA aptamers for glycine. (**A**) Consensus nucleotides present in more than 80% (black) and 95% (red) of representative sequences were identified by bioinformatics (*17*) (fig. S1). Circles and thick lines represent nucleotides whose base identities are not conserved. P1 through P4 identify common base-paired elements. ORF, open reading frame. (**B**) Patterns of spontaneous cleavage that occur with VC I-II in the absence and presence of glycine are depicted. Numbers adjacent to sites of changing spontaneous cleavage correspond to gel bands denoted with asterisks in (C) and data sets in (D). (**C**) Spontaneous cleavage products of VC I-II upon separation by polyacrylamide gel electrophoresis (PAGE) (*7*, *8*) (fig. S2). NR, T1, and $^{-}$OH represent no reaction, partial digest with RNase T1, and partial digest with alkali, respectively. Pre, precursor RNA. Some fragment bands corresponding to T1 digestion (cleaves after G residues) are labeled. Numbered asterisks identify locations of major structural modulation in response to glycine. The two rightmost lanes carry 1 mM of the amino acids noted. Brackets labeled I and II identify RNA fragments that correspond to cleavage events in the type I and type II aptamers, respectively. (**D**) Plots of the extent of spontaneous cleavage products versus increasing concentrations of glycine for aptamer I (sites 1 through 3), aptamer II (sites 5 through 7), and the linker sequence (site 4). C, concentration.

method termed inline probing (*18*), which can reveal metabolite-induced changes in aptamer structure by monitoring changes in the levels of spontaneous RNA cleavage (*4*, *6*, *7*–*9*). For example, the addition of glycine at 1 mM caused changes in the pattern of spontaneous cleavage of a 226-nucleotide RNA construct (VC I-II) that carries both aptamer types (Fig. 1C), whereas 1 mM L-alanine did not induce change.

Similar results were observed when a 105-nucleotide RNA (VC II) carrying the type II aptamer alone was used for inline probing (fig. S2). Because both type I and type II domains undergo similar structural changes upon introduction of glycine and because VC II alone exhibits ligand-dependent structural change, we conclude that each domain serves as a separate glycine binding aptamer. Furthermore, all three sections of the VC I-II construct (aptamer I, linker, and aptamer II) responded to glycine equally at various concentrations (Fig. 1D). This concerted response to glycine suggests the two aptamers either have perfectly matched affinities for glycine or bind glycine in a highly cooperative manner.

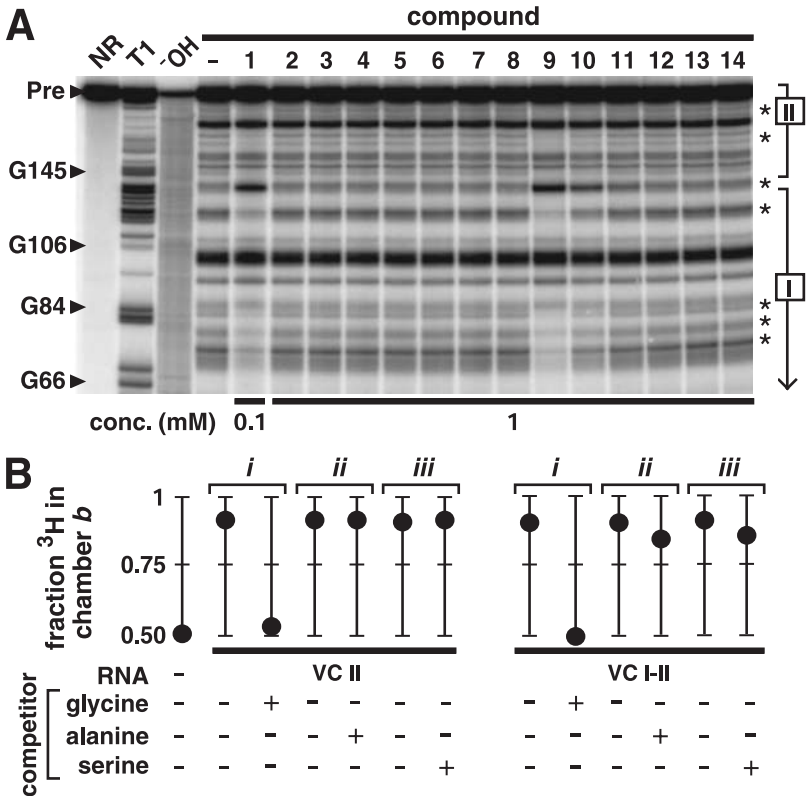

Fig. 2. Ligand specificity of VC II and VC I-II RNAs. (**A**) Inline probing of VC I-II in the absence (–) or presence of glycine (compound 1) or the analogs L-alanine (2), D-alanine (3), L-serine (4), L-threonine (5), sarcosine (6), mercaptoacetic acid (7), β-alanine (8), glycine methyl ester (9), glycine tert-butyl ester (10), glycine hydroxamate (11), glycinamide (12), aminomethane sulfonic acid (13), and glycyl-glycine (14). Other notations are as described in the legend to Fig. 1C. (**B**) Equilibrium dialysis data for VC II and VC I-II (100 μM) in the absence (–) or presence (+) of excess (1 mM) unlabeled glycine, alanine, or serine as indicated. Fraction of ^{3}H-glycine in chamber b reflects the amount of glycine bound by RNA plus half the total amount of free glycine in chambers a and b versus the total amount of ^{3}H-glycine. *i* to *iii*, separate experiments where RNA and ^{3}H are equilibrated (left) and competitor is subsequently added.

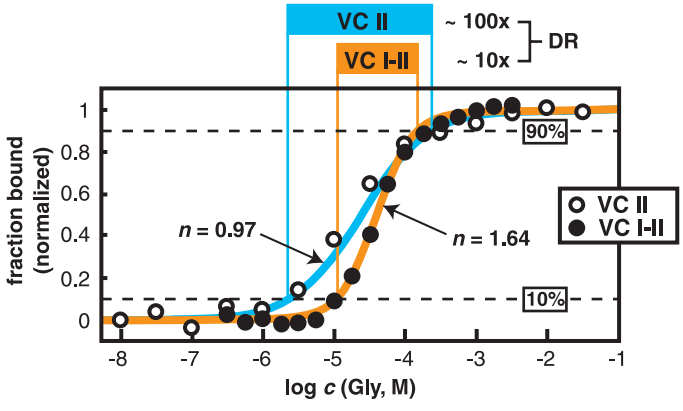

Fig. 3. Cooperative binding of two glycine molecules by the VC I-II RNA. Plot depicts the fraction of VC II (open) and VC I-II (solid) bound to ligand versus the concentration of glycine. The constant, *n*, is the Hill coefficient for the lines as indicated that best fit the aggregate data from four different regions (fig. S3). Shaded boxes demark the dynamic range (DR) of glycine concentrations needed by the RNAs to progress from 10%- to 90%-bound states.

The molecular recognition specificity of VC I-II was examined by using inline probing with a variety of glycine analogs. The RNA exhibited measurable structural modulation with the methyl ester and tertiary butyl ester analogs of glycine but rejected all other analogs when tested at 1 mM (Fig. 2A). The concentrations of ligand needed to cause half-maximal structure modulation of VC II are about 10 μM for glycine, 100 μM for glycine methyl ester, 1 mM for glycine tertiary butyl ester, and 1 mM for glycine hydroxamate (*19*). Specificity for glycine also was observed by using equilibrium dialysis. For example, when an equilibrium dialysis system is preequilibrated with either VC II or VC I-II RNAs, excess glycine restored an equal distribution of ^{3}H-glycine upon subsequent incubation (Fig. 2B). However, the addition of either L-alanine or L-serine failed to restore equal distribution, confirming that the RNAs serve as precise sensors for glycine.

We explored the stoichiometry of glycine binding to these RNAs by using equilibrium dialysis with high glycine concentrations. When three equivalents of the amino acid were present versus one equivalent of VC II RNA (100 μM), we observed a shift in glycine distribution (*19*) that indicates ~0.8 equivalents (1 expected) of glycine were bound by RNA. In contrast, when one equivalent of the VC I-II RNA was present (two aptamer equivalents), there is a ~1.6-fold increase (2 expected) in the amount of glycine that was bound by RNA. These data provide preliminary evidence for a stoichiometry of 1:1 between glycine and each individual aptamer.

Our laboratory created an engineered allosteric RNA construct with a tandem aptamer configuration that demonstrated cooperative binding of multiple ligands (*20*), thus providing a precedent for this more sophisticated form of RNA switch. If the two aptamers of VC I-II function cooperatively, then structural changes in the RNA should be atypically responsive to increasing glycine concentrations compared with those of a single glycine aptamer. The ligand-dependent modulation of VC II structure by glycine (Fig. 3) was typical of that observed for single aptamer domains of known riboswitches (*4*, *6*–*9*, *21*–*24*). The

change from ~10% to ~90% ligand-bound VC I RNA occurred over a ~100-fold increase in glycine concentration, which corresponds with the response predicted for a receptor that binds a single ligand (fig. S3).

In contrast, VC I-II underwent the same change in ligand occupancy over only a ~10-fold increase in glycine concentration (Fig. 3). This reduction in the dynamic range for the glycine-mediated response is consistent with the hypothesis that glycine binding at one site substantially improves the affinity for glycine binding to the other site. The Hill coefficient (*25*, *26*) calculated for VC I-II is 1.64, whereas the maximum value for two binding sites is 2. In comparison, the Hill coefficient for the oxygen-carrying protein hemoglobin is 2.8 (*27*), whereas the maximum value for four binding sites is 4. Thus, the degree of cooperativity per binding site with the two VC I-II aptamers is equal to or greater than that derived for each of the four sites in hemoglobin.

A cooperative mechanism for ligand binding is further supported by the observation that single-point mutations made to either of the conserved cores of VC I-II cause substantial loss of glycine-binding affinity to the mutated aptamer and also cause a dramatic loss of affinity to the unaltered aptamer (fig. S4). Thus, the binding of glycine at one site induces the adjacent site to exhibit an improvement in ligand binding affinity by ~100- to ~1000-fold.

Tandem aptamer architecture (Fig. 4A) and selective glycine recognition (*19*) are also observed with RNA corresponding to the putative 5′-UTR of the *gcvT* operon from *B. subtilis*. This provided us with a construct that is more amenable to experiments that assess whether the *gcvT* RNA is important for genetic control. We used single-round transcription assays (*17*) to determine whether a DNA construct corresponding to the intergenic region (IGR) upstream of the *B. subtilis gcvT* operon yields transcripts whose termination sites are influenced by glycine. In the absence of glycine, only ~30% of the RNA products generated by in vitro transcription were full-length (Fig. 4B). The remaining ~70% were premature termination products that correspond in length to that expected if RNA polymerase stalls at a putative intrinsic terminator (*28*, *29*) that partially overlaps the second glycine aptamer (also fig. S5).

The addition of glycine caused a substantial increase in the amount of full-length RNA transcript relative to the amount of truncated RNA (Fig. 4B). This improvement is induced only by glycine or by other analogs that cause RNA structure modulation. Compounds such as serine, alanine, and other analogs that do not induce modulation also failed to trigger an increase in the production of full-length transcripts (fig. S5) (*19*).

Furthermore, the glycine-dependent increase in the yield of full-length transcripts corresponded with that expected for a cooperative RNA switch requiring two ligand binding events. Fitting the transcription data yields a curve that corresponded to cooperative ligand binding, with a Hill coefficient of 1.4 (Fig. 4B). Therefore, transcription control by

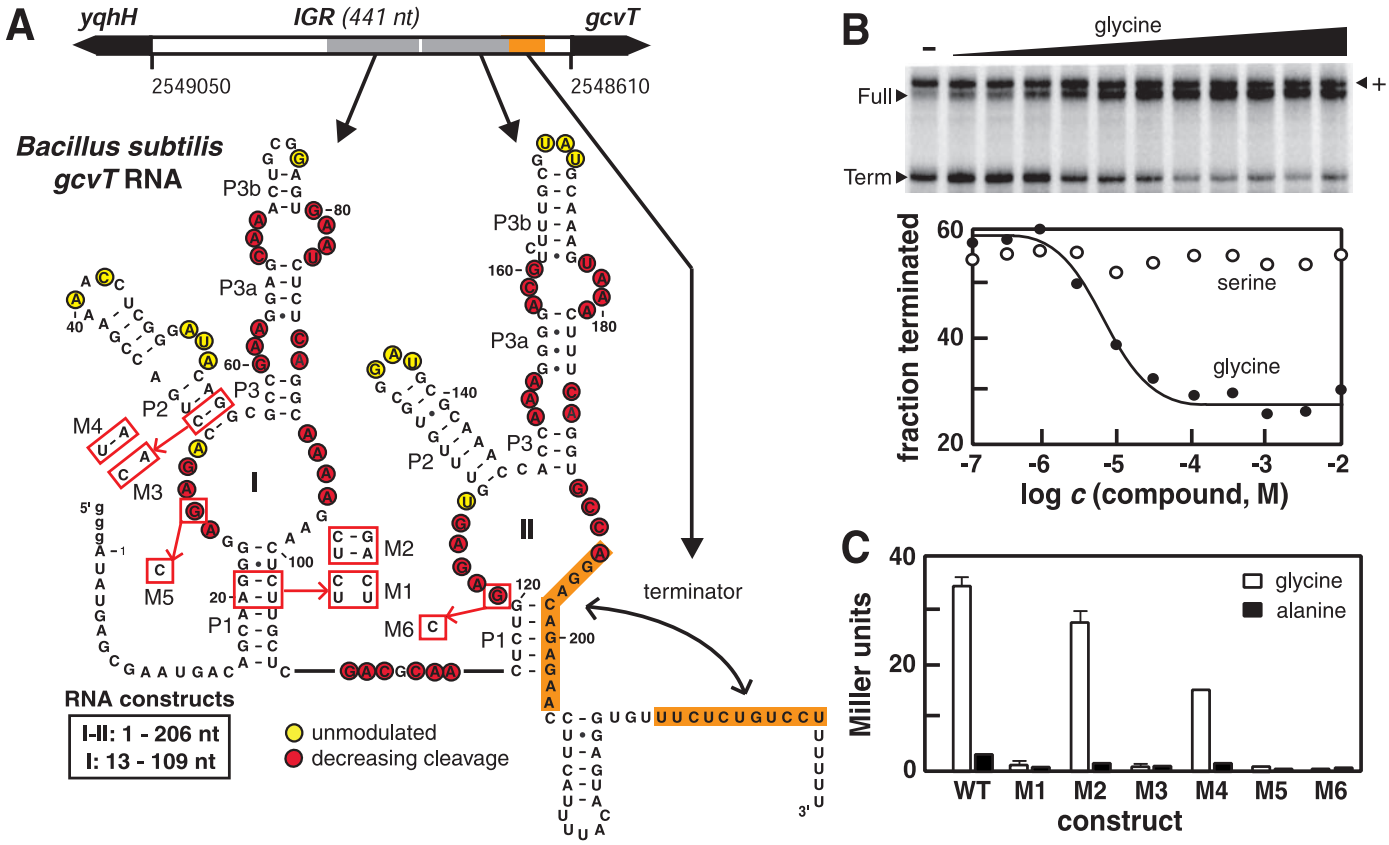

Fig. 4. Control of *B. subtilis gcvT* RNA expression in vitro and in vivo. (**A**) The IGR between the *yqhH* and *gcvT* genes of *B. subtilis* encompassing both aptamers I and II was used for in vitro transcription and in vivo expression assays. Inline probing results were mapped, and mutations used to assess riboswitch function are indicated with red boxes. Orange shading identifies the putative intrinsic terminator stem, which is expected to exhibit mutually exclusive formation of aptamer II when bound to glycine. nt, nucleotide. (**B**) Single-round in vitro transcription assays demonstrating that full-length (Full) transcripts are favored when >10 μM glycine is added to the transcription mixture, whereas serine and most glycine analogs (fig. S5) are rejected by the riboswitch. The line reflects a best-fit curve to an equation reflecting cooperative binding with a Hill coefficient of 1.4 (*19*). An additional transcription product, termed "+," appears to be due to spurious transcription initiation (*17*). (**C**) Plot of the expression of a β-galactosidase reporter gene fused to wild-type (WT) *gcvT* IGR or to a series of mutant IGRs (M1–M6). Data reflect the averages of three assays with two replicates each. Error bars indicate ± two standard deviations.

the *gcvT* 5′-UTR of *B. subtilis* responds to glycine with characteristics that parallel those observed when conducting inline probing of the cooperative VC I-II RNA.

To assess whether glycine binding and in vitro transcription control correspond to genetic control events in vivo, we generated reporter constructs by fusing the IGR upstream of the *gcvT* operon from *B. subtilis* to a β-galactosidase reporter gene and integrated them into the bacterial genome (*17*). The reporter fusion construct carrying the wild-type IGR expresses a high amount of β-galactosidase when glycine is present in the growth medium, whereas a low amount of gene expression results when alanine is present (Fig. 4C). These results indicate that the *gcvT* motif is part of a glycine-responsive riboswitch with a default state that is off. Glycine binding is required to activate gene expression, as was also observed with the in vitro transcription assays (Fig. 4B).

The importance of several conserved features of the motif were examined by mutating the P1 and P2 stems of the first aptamer domain to disrupt (variants M1 and M3, respectively) and restore (M2 and M4, respectively) base pairing (Fig. 4A). Resulting gene expression levels from constructs carrying the mutant IGRs are consistent with base-paired elements predicted from phylogenetic analyses (*14*) (fig. S1). Furthermore, the introduction of mutations into the conserved cores of either aptamer I or aptamer II (variants M5 and M6, respectively) caused a complete loss of reporter gene activation. This latter result suggests that glycine binding to both aptamers is necessary to trigger gene activation, which is consistent with a model wherein cooperative glycine binding is important for riboswitch function.

The glycine-dependent riboswitch is a remarkable genetic control element for several reasons. First, glycine riboswitches form selective binding pockets for a ligand composed of only 10 atoms and thus bind the smallest organic compound among known natural and engineered RNA aptamers. This observation is consistent with the hypothesis that RNA has sufficient structural potential to selectively bind a wide range of biomolecules.

Second, the 5′-UTR of the *B. subtilis gcvT* operon is a genetic on switch, and thus joins the adenine riboswitch (*23*) as a rare type of RNA that has been proven to harness ligand binding and activate gene expression. In most instances, riboswitches cause repression of their associated genes, which is to be expected because many of these genes are involved in biosynthesis or import of the target metabolites. However, the glycine riboswitch from *B. subtilis* controls the expression of three genes required for glycine degradation. A ligand-activated riboswitch would be required to determine whether sufficient amino acid substrate is present to warrant production of the glycine cleavage system, thereby providing a rationale for why this rare on switch is used.

Third, this is the only known metabolite-binding riboswitch class that regularly makes use of a tandem aptamer configuration. In both *V. cholerae* and *B. subtilis*, the juxtaposition of aptamers enables the cooperative binding of two glycine molecules. For the *B. subtilis* riboswitch, this characteristic is expected to result in unusually rapid activation and repression of genes encoding the glycine cleavage system in response to rising and falling concentrations of glycine, respectively. Given the prevalence of the tandem architecture of glycine riboswitches, this more "digital" switch likely gives the bacterium an important selective advantage by controlling gene expression in response to small changes in glycine.

References and Notes

1. W. C. Winkler, R. R. Breaker, *ChemBioChem* **4**, 1024 (2003).
2. A. G. Vitreschak, D. A. Rodionov, A. A. Mironov, M. S. Gelfand, *Trends Genet.* **20**, 44 (2004).
3. E. Nudler, A. S. Mironov, *Trends Biochem. Sci.* **29**, 11 (2004).
4. M. Mandal, B. Boese, J. E. Barrick, W. C. Winkler, R. R. Breaker, *Cell* **113**, 577 (2003).
5. A. S. Mironov *et al.*, *Cell* **111**, 747 (2002).
6. W. C. Winkler, S. Cohen-Chalamish, R. R. Breaker, *Proc. Natl. Acad. Sci. U.S.A.* **99**, 15908 (2002).
7. A. Nahvi *et al.*, *Chem. Biol.* **9**, 1043 (2002).
8. W. Winkler, A. Nahvi, R. R. Breaker, *Nature* **419**, 952 (2002).
9. N. Sudarsan, J. E. Barrick, R. R. Breaker, *RNA* **9**, 644 (2003).
10. W. C. Winkler, A. Nahvi, A. Roth, J. A. Collins, R. R. Breaker, *Nature* **428**, 281 (2004).
11. M. Ptashne, A. Gann, *Genes & Signals* (Cold Spring Harbor Press, Cold Spring Harbor, NY, 2002).
12. B. I. Kurganov, *Allosteric Enzymes* (Wiley, New York, 1978).
13. A. A. Antson *et al.*, *Nature* **374**, 693 (1995).
14. J. F. Barrick *et al.*, *Proc. Natl. Acad. Sci. U.S.A.* **101**, 6421 (2004).
15. G. Kikuchi, *Mol. Cell. Biochem.* **1**, 169 (1973).
16. R. Duce, J. Bourguignon, M. Neuburger, F. Rébeillé, *Trends Plant Sci.* **6**, 167 (2001).
17. Materials and methods are available on *Science* Online.
18. G. A. Soukup, R. R. Breaker, *RNA* **5**, 1308 (1999).
19. M. Mandal *et al.*, unpublished data.
20. A. M. Jose, G. A. Soukup, R. R. Breaker, *Nucleic Acids Res.* **29**, 1631 (2001).
21. W. C. Winkler, A. Nahvi, N. Sudarsan, J. E. Barrick, R. R. Breaker, *Nature Struct. Biol.* **10**, 701 (2003).
22. N. Sudarsan, J. K. Wickiser, S. Nakamura, M. S. Ebert, R. R. Breaker, *Genes Dev.* **17**, 2688 (2003).
23. M. Mandal, R. R. Breaker, *Nature Struct. Mol. Biol.* **11**, 29 (2004).
24. A. Nahvi, J. E. Barrick, R. R. Breaker, *Nucleic Acids Res.* **32**, 143 (2004).
25. A. V. Hill, *J. Physiol.* **40**, iv (1910).
26. M. Weissbluth, in *Molecular Biology Biochemistry and Biophysics*, A. Kleinzeller, Ed. (Springer-Verlag, New York, 1974), vol. 15, pp. 27–41.
27. S. J. Edelstein, *Annu. Rev. Biochem.* **44**, 209 (1975).
28. I. Gusarov, E. Nudler, *Mol. Cell* **3**, 495 (1999).
29. W. S. Yarnell, J. W. Roberts, *Science* **284**, 611 (1999).

30. We thank members of the Breaker laboratory for helpful discussions and G. Reguera and B. Bassler for providing genomic DNA for *V. cholerae*. This work was supported by grants from the NIH and the NSF. R.R.B. is also grateful for support from the Yale Liver Center and the David and Lucile Packard Foundation.

Supporting Online Material

www.sciencemag.org/cgi/content/full/306/5694/275/DC1
Materials and Methods
Figs. S1 to S5

27 May 2004; accepted 24 August 2004

Human PAD4 Regulates Histone Arginine Methylation Levels via Demethylimination

Yanming Wang,[1,2] Joanna Wysocka,[1,2] Joyce Sayegh,[3] Young-Ho Lee,[4] Julie R. Perlin,[1] Lauriebeth Leonelli,[1] Lakshmi S. Sonbuchner,[1] Charles H. McDonald,[5] Richard G. Cook,[5] Yali Dou,[6] Robert G. Roeder,[6] Steven Clarke,[3] Michael R. Stallcup,[4] C. David Allis,[2]* Scott A. Coonrod[1]*

Methylation of arginine (Arg) and lysine residues in histones has been correlated with epigenetic forms of gene regulation. Although histone methyltransferases are known, enzymes that demethylate histones have not been identified. Here, we demonstrate that human peptidylarginine deiminase 4 (PAD4) regulates histone Arg methylation by converting methyl-Arg to citrulline and releasing methylamine. PAD4 targets multiple sites in histones H3 and H4, including those sites methylated by coactivators CARM1 (H3 Arg^{17}) and PRMT1 (H4 Arg^{3}). A decrease of histone Arg methylation, with a concomitant increase of citrullination, requires PAD4 activity in human HL-60 granulocytes. Moreover, PAD4 activity is linked with the transcriptional regulation of estrogen-responsive genes in MCF-7 cells. These data suggest that PAD4 mediates gene expression by regulating Arg methylation and citrullination in histones.

Posttranslational histone modifications, such as phosphorylation, acetylation, and methylation, regulate a broad range of DNA and chromatin-templated nuclear events, including transcription (*1–3*). Pairs of opposing enzymes, such as acetyltransferases-deacetylases

and kinases-phosphatases, regulate the steady-state balance of histone acetylation and phosphorylation, respectively. In contrast, although Arg- and Lys-specific methyltransferases have been identified (*3–5*), enzymes that remove methyl groups from histones or any other cellular proteins remain unknown (*6*).

Arg methylation has been identified on many nuclear and cytosolic proteins involved in various cellular processes, including transcription and cell signaling (*7–10*). The methylation of histones by PRMT1 and CARM1 facilitates transcription in association with nuclear hormone coactivators and p53 (*11–15*). Here, we demonstrate that peptidylarginine deiminase 4 (PAD4), an enzyme previously known to convert Arg to citrulline (Cit) in histones (*16–19*), can also demethyliminate histones in vitro and in vivo, thus regulating both histone Arg methylation and gene activity.

Multiple Arg residues in H3 and H4 can be methylated by CARM1 and PRMT1, respectively (fig. S1A). Free methyl-Arg amino acids (monomethyl-Arg and asymmetric dimethyl-Arg) can be converted to Cit by dimethylarginine dimethylaminohydrolyase (DDAH) (*20–21*). To identify enzymes that might catalyze a similar reaction on protein methyl-Arg substrates as that catalyzed by DDAH, we searched the Homologous Structure Alignment database for proteins homologous to DDAH and identified PAD4 (*22*) (fig. S1). Peptidylarginine deiminases are a family of enzymes known to convert protein Arg to Cit in a calcium- and dithiothreitol (DTT)-dependent reaction [reviewed in (*16*)]. These findings prompted us to test the hypothesis that PAD4 can convert histone methyl-Arg to Cit.

Previous studies have correlated PAD4 expression with histone citrullination (*17–18*). We purified a glutathione *S*-transferase (GST)–PAD4 (human) full-length fusion protein from *Escherichia coli* and tested it on reversed-phase high performance liquid chromatography (RP-HPLC)–purified cellular H3 and H4 as substrates. In the presence of calcium and DTT, GST-PAD4 generated Cit in H3 and H4 as detected by an antibody against a chemically modified form of Cit (Fig. 1, A and B). Cellular H3 and H4 either treated or untreated was probed with site-specific antibodies against methyl-H3 Arg^{17} and -H4 Arg^{3} residues (for antibody specificity, see fig. S2). A dramatic diminishment of H3 Arg^{17} and H4 Arg^{3} methylation was detected after PAD4 treatment (Fig. 1, A and B), suggesting that PAD4 targets select methyl-Arg sites in H3 and H4. Protein microsequencing showed that the N-terminal tail of PAD4-treated H3 and H4 was not being randomly degraded (table S1). To identify potential PAD4 target site(s) in the N-terminal tail of H3, we quantified the amount of Cit detected at cycles of microsequencing. As shown in table S1, PAD4 deiminated multiple Arg residues in H3 (e.g., ~93.6% of H3 Cit^{2} compared to ~98.9% of H3 Cit^{8}) in vitro. Cellular H4 is N-terminally acetylated, thus preventing direct microsequencing analyses. Therefore, we analyzed recombinant H4 after PAD4 treatment and found that its N terminus also remained intact and that ~99.6% of H4 Arg^{3} was citrullinated (table S1).

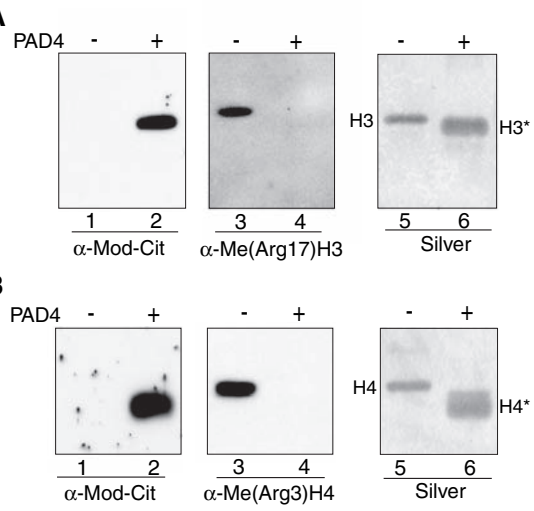

Fig. 1. PAD4 reduces Arg methylation levels and generates citrulline (Cit) in H3 (**A**) and H4 (**B**). (Left) Cit was detected in H3 or H4 when treated with PAD4. (Middle) After PAD4 treatment, the signal of H3 Arg^{17} or H4 Arg^{3} methylation was dramatically diminished (see fig. S2 for antibody specificity). (Right) Silver staining shows H3 and H4, as well as citrullinated H3 and H4 (H3* and H4*) in SDS-PAGE gels. Note the increased mobility of H3* and H4*.

Thus, PAD4 potently converts multiple Arg sites of H3 and H4 to Cit with low site preference in vitro. Neutralization of the positive charge of multiple Lys residues by acetylation alters the electrophoretic behavior of histones in SDS–polyacrylamide gel electrophoresis (SDS-PAGE) gels (*23*). Because the positive charge of Arg is neutralized by citrullination, we postulate that the mass shift of histones observed on SDS-PAGE gels after PAD4 treatment is caused by deiminating multiple Arg residues in H3 and H4 and that the varying degrees of citrullination at different Arg residues caused the expansion of the band width of H3 and H4 (Fig. 1).

Two possible pathways can lead to the loss of methyl-Arg epitope (Fig. 2A). Either PAD4 removes the methylimine group from methyl-Arg, thus producing Cit and releasing methylamine (pathway 1), or the imine group is removed by PAD4 thereby producing methyl-Cit and releasing ammonium (pathway 2). To distinguish between these two pathways, we radioactively labeled recombinant H3 and H4 with CARM1 and PRMT1, respectively, and with [^{3}H]-S-adenosylmethionine as a methyl donor. The amount of [^{3}H]-methyl in H3 and H4 was then detected by fluorography. We found that the amounts of [^{3}H]-methyl in histones were dramatically decreased by PAD4 treatment (Fig. 2B). These results suggest that the methyl-group produced on H3 and H4 by CARM1 and PRMT1, respectively, is directly removed by PAD4.

We sought to analyze the biochemical nature of the released product. If PAD4 acts via pathway 1 (Fig. 2A), methylamine would be generated. To detect methylamine, we first took advantage of the solubility difference of methylamine in H_2O at different pH values (methylamine pK_a = 10.4) (*24*, *25*). After PAD4 treatment of recombinant H4 radioactively labeled by PRMT1, released volatile [^{3}H]-methyl radioactivity was detected from samples adjusted to a high pH (pH = 12, at which methylamine becomes volatile) but not from various control samples (Fig. 2C). The identity of methylamine as a methyl product was further confirmed by chromatography using an amino acid cation-exchange column (*26*). Radioactivity released from PAD4-treated [^{3}H]-methyl-H4 co-migrated with both an unlabeled monomethylamine standard (absorbance, 570 nm) and a [^{14}C]-dimethylamine standard, indicating that the volatile [^{3}H]-methylamine could be released in a monomethyl or dimethyl form (Fig. 2D) (*27*). In contrast, [^{3}H]-methylamine was not detected in the untreated [^{3}H]-methyl-H4 samples (Fig. 2E). These results support the hypothesis that PAD4 can convert methyl-Arg in histones to Cit and methylamine. Hereafter, we will

[1]Department of Genetic Medicine, Weill Medical College of Cornell University, 1300 York Avenue, New York, NY 10021, USA. [2]Laboratory of Chromatin Biology, Rockefeller University, Box 78, 1230 York Avenue, New York, NY 10021, USA. [3]Department of Chemistry and Biochemistry and Molecular Biology Institute, University of California at Los Angeles, Los Angeles, CA 90095–1569, USA. [4]Department of Pathology, University of Southern California, Los Angeles, CA 90089–9092, USA. [5]Department of Microbiology and Immunology, Baylor College of Medicine, Houston, TX 77030, USA. [6]Laboratory of Biochemistry and Molecular Biology, Rockefeller University, New York, NY 10021, USA.

*To whom correspondence should be addressed. E-mail: alliscd@rockefeller.edu (C.D.A.); scc2003@med.cornell.edu (S.A.C.)

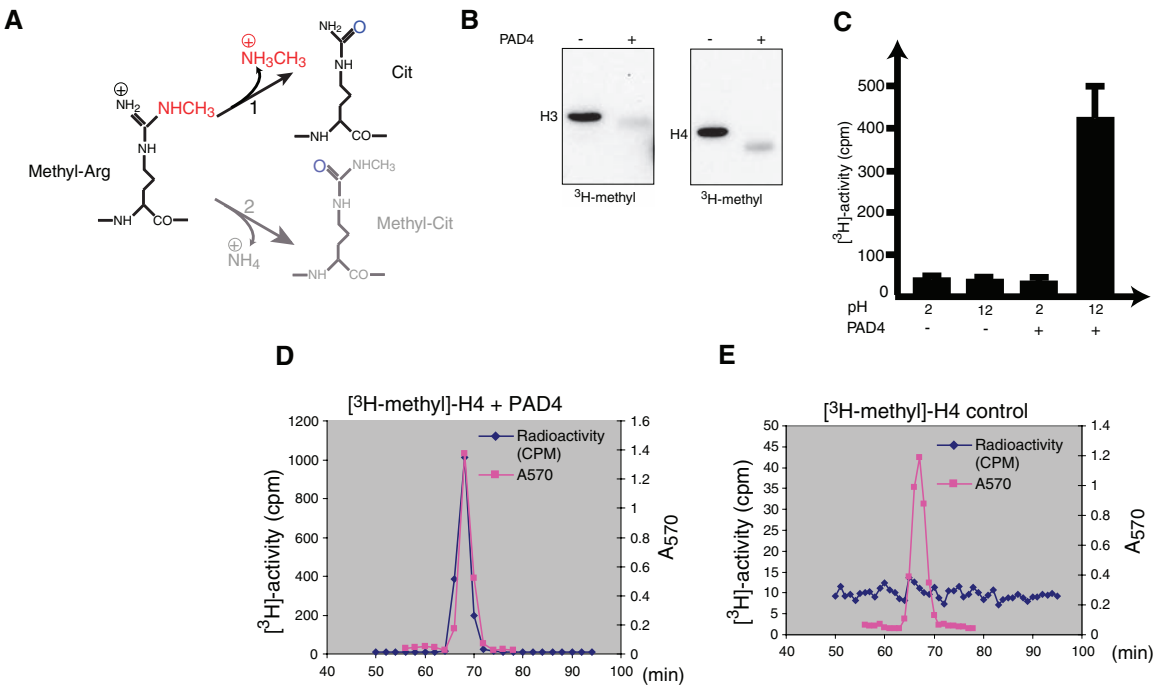

Fig. 2. PAD4 demethyliminates H3 and H4 and produces methylamine and Cit as reaction products. (**A**) Two possible mechanisms of PAD4 reaction on methyl-Arg in a protein substrate. (**B**) Recombinant H3 or H4 was first radioactively labeled by CARM1 or PRMT1, respectively. After PAD4 treatment, the [^{3}H]-methyl radioactivity in H3 and H4 dramatically decreased. (**C**) A volatility assay (*25*) to detect [^{3}H]-methylamine released from radioactively labeled H4 after PAD4 treatment. [^{3}H]-activity was found only from samples at a high pH (12) after-PAD4 treatment. Error bars indicate the means ± SD of three individual experiments. (**D**) A nonradioactive methylamine standard [10 μmol, detected by absorbance (*A*) at 570 nm] was co-eluted with the released radioactive products generated by PAD4 from radioactively labeled recombinant H4, suggesting that [^{3}H]-methylamine was produced. (**E**) [^{3}H]-methylamine was not detected in radioactively labeled recombinant H4 samples that were not treated with PAD4.

refer to this reaction as demethylimination to reflect these findings.

We next examined whether PAD4 modulates histone Arg methylation and citrullination in vivo. We chose to test this in HL-60 granulocytes where PAD4 expression can be induced by dimethyl sulfoxide (DMSO) and PAD4 can be activated by calcium ionophore (*17*, *18*) (Fig. 3A). When total histones were probed with site-specific antibodies against H3 methyl-Arg^{17} or H4 methyl-Arg^3, the signals were dramatically reduced after PAD4 activation (Fig. 3B). In addition, calcium ionophore treatment did not either increase histone citrullination (Fig. 3A) or decrease histone Arg methylation in undifferentiated HL-60 cells (*28*). These results correlate the activation of PAD4 with a loss of histone Arg methylation in a cellular context.

To further analyze the change of Arg methylation in individual cells, we carried out immunofluorescence analyses of HL-60 granulocytes. Before treatment, amounts of H3 Arg^{17} methylation in each cell were roughly comparable (Fig. 3C, top). In contrast, after 15 min of calcium ionophore treatment, H3 Arg^{17} methylation dramatically decreased in most of the cells (~57.3%, $n = 200$) (Fig. 3C, bottom). In contrast, amounts of H3 Lys^4 methylation were unchanged in calcium ionophore-treated cells (fig. S4), suggesting that the N terminus of H3 is intact and that PAD4 does not affect Lys methylation.

To directly demonstrate the conversion of particular H3 Arg residues to Cit in vivo, we

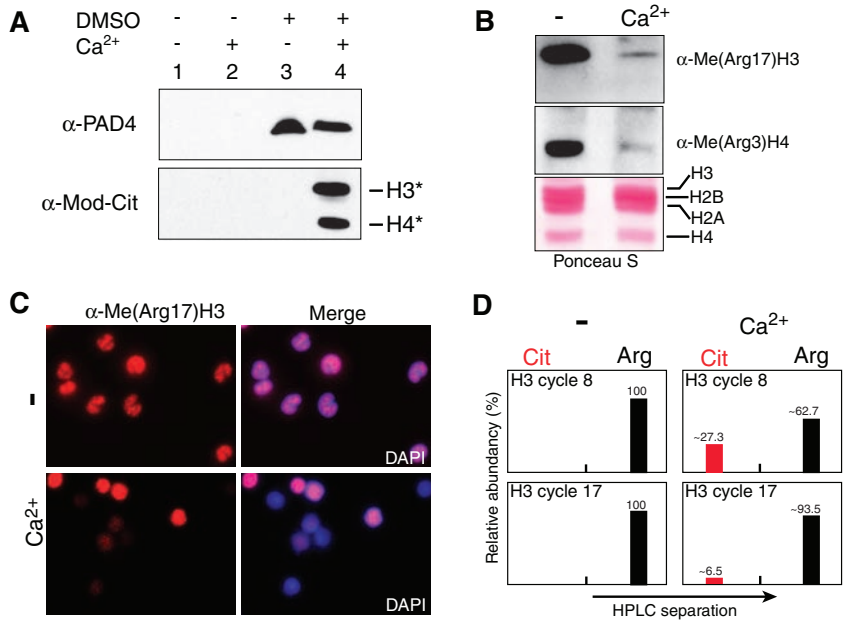

Fig. 3. Linking PAD4 activity with the regulation of H3 Arg^{17} methylation. (**A**) PAD4 protein was expressed in HL-60 granulocytes upon DMSO treatment (lanes 3 and 4). Citrullinated H3 and H4 (denoted by asterisks) were detected in histones purified from cells treated with both DMSO and calcium ionophore (lane 4). (**B**) Amounts H3 Arg^{17} methylation and H4 Arg^3 methylation decreased in HL-60 granulocytes after calcium ionophore treatment. (**C**) Before calcium ionophore treatment, H3 Arg^{17} methylation signals (red) are present at comparable levels in each HL-60 granulocyte. After 15 min of calcium ionophore treatment, methylation of H3 Arg^{17} strongly decreased in the majority of cells. (**D**) Protein microsequencing of H3 and citrullinated H3. Cit was not detected before calcium ionophore treatment. After PAD4 activation, ~27.3% of H3 Arg^8 is citrullinated (2.52 pmol of Cit versus 6.72 pmol of Arg), and ~6.5% of H3 Arg^{17} is citrullinated (0.21 pmol of Cit versus 3.02 pmol of Arg).

performed microsequencing with H3 isolated from HL-60 granulocytes. We found that H3 was only citrullinated after treatment with calcium ionophore and identified major PAD4 target sites at Arg[8] (~27.3% Cit) and Arg[17] (~6.5% Cit) (Fig. 3D). Although the H3 Arg[2] site was deiminated by PAD4 in vitro, its deimination was not detectable in HL-60 granulocytes. In addition, although only ~6.5% of H3 Cit[17] was detected, the majority of methyl-Arg[17] signal was lost (Fig. 3B), suggesting that methyl-Arg[17] was selectively targeted by PAD4. Furthermore, the high percentage of histone Cit[8] detected after calcium activation demonstrates that PAD4 can deiminate Arg in vivo.

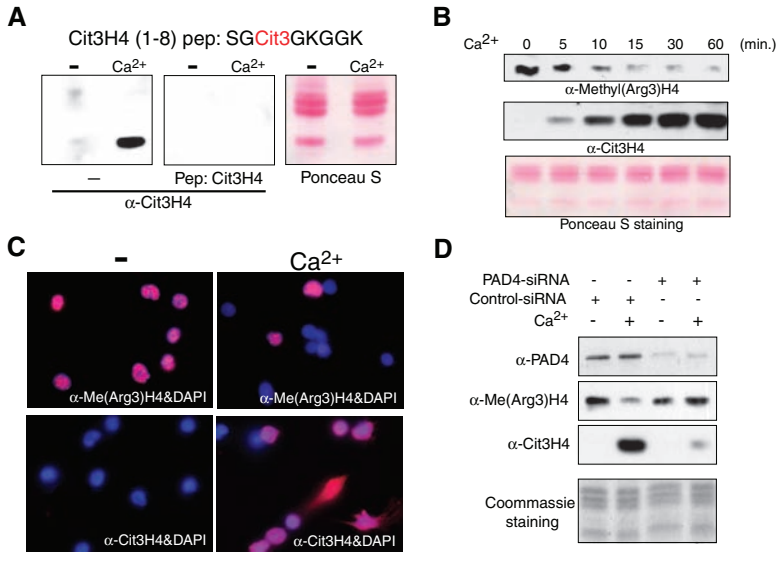

Fig. 4. PAD4 regulates H4 Arg[3] methylation and citrullination levels in HL-60 cells. (**A**) An antibody generated against an H4 Cit[3] peptide (amino acids 1 to 8 of H4) detects H4 after calcium ionophore treatment (left). This signal is specifically competed by the H4 Cit[3] peptide (middle). Equal loading of samples is shown by Ponceau S staining. (**B**) A dynamic decrease of H4 Arg[3] methylation mirrored by a concomitant increase in H4 Arg[3] citrullination after calcium ionophore treatment. (**C**). After calcium ionophore treatment, H4 Arg[3] methylation staining in the majority of cells was dramatically reduced (top). In contrast, a vast majority of cells became positively stained with the Cit3H4 antibody after calcium ionophore treatment (bottom). (**D**). PAD4 siRNA experiments in HL-60 cells. PAD4 protein amounts were dramatically reduced with PAD4 siRNA treatment (top). Cells treated with PAD4 siRNA had no obvious decrease in H4 Arg[3] methylation and little production of H4 Cit[3] after calcium ionophore treatment (middle). Equal protein loading was confirmed by Coomassie Blue staining (bottom).

To investigate whether PAD4 can citrullinate H4 at Arg[3], we developed a specific antibody against H4 Cit[3] (α-Cit3H4). Western blot analyses showed that the Cit3H4 antibody strongly recognized H4 after treatment of HL-60 granulocytes with calcium ionophore (Fig. 4A). This reactivity was specifically decreased by the Cit3H4(1-8) peptide (Fig. 4A). These data suggest that PAD4 can target H4 Arg[3] site for citrullination.

To analyze the temporal changes in H4 Arg[3] methylation and citrullination, we performed Western blot experiments at different time points after calcium ionophore treatment. A gradual loss of H4 Arg[3] methylation was observed (Fig. 4B), which is directly correlated with a concomitant increase of H4 Cit[3] (Fig. 4B). The dynamic and complementary change of H4 Arg[3] methylation and citrullination in HL-60 granulocytes suggests that PAD4 either preferentially targets methyl-Arg[3] in vivo or reacts with both H4 methyl-Arg[3] and Arg[3] equally well.

As is the case of H3 Arg[17] methylation (Fig. 3), H4 methyl-Arg[3] antibody staining was greatly reduced in the majority of cells (~55.2%, n = 200) after 15 min of calcium ionophore treatment (Fig. 4C). By using an H2A/H4 phospho-Ser1 antibody (*29*), we found that this phosphorylation mark was not decreased after calcium ionophore treatment (fig. S4), suggesting that the extreme N terminus of H4 is unaltered. In contrast, although HL-60 granulocytes were not stained with the Cit3H4 antibody before calcium ionophore treatment (merged images in Fig. 4C), the majority of cells (~63.8%, n = 1178) were positively stained with the Cit3H4 antibody after 15 min of calcium ionophore treatment (Fig. 4C).

To address whether the observed decrease of H4 Arg[3] methylation and increase of H4 Cit[3] was dependent on PAD4 activity, we carried out PAD4 RNA interference experiments in HL-60 cells. As shown in Fig. 4D, the amount of PAD4 protein dramatically decreased after PAD4 small interfering RNA (siRNA) treatment but was not affected by a control siRNA (Fig. 4D). As expected, the ability of HL-60 granulocytes to decrease H4 Arg[3] methylation and to increase H4 Cit[3] was lost when PAD4 expression was inhibited (Fig. 4D). These data illustrate that PAD4 is the major, if not the only, enzyme that directly mediates the dy-

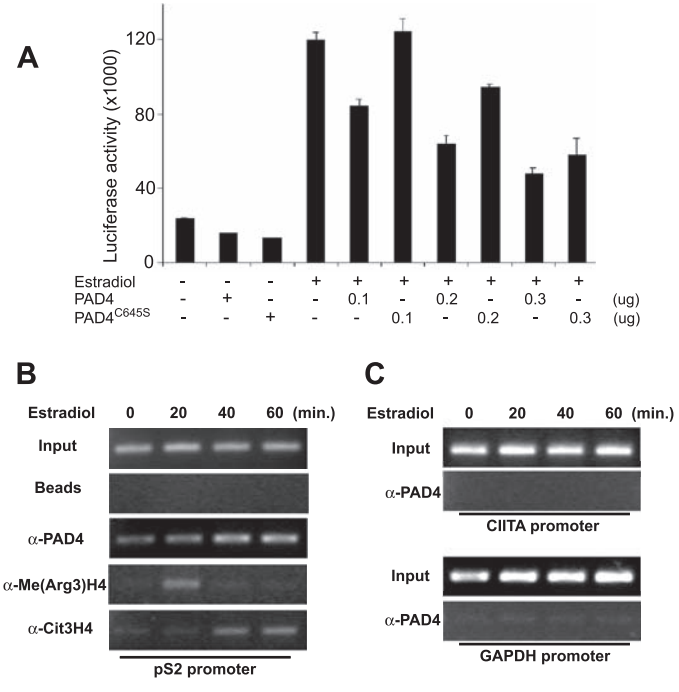

Fig. 5. PAD4 and the regulation of estrogen-responsive genes (**A**) Luciferase activity of an EREII-LUC reporter gene transfected into MCF-7 cells was dramatically increased in response to estradiol stimulation. Various amounts of plasmids (0.1 to 0.3 μg) expressing wild-type PAD4 efficiently inhibited the reporter gene activity in a dose-dependent manner. In contrast, a catalytic inactive form of PAD4 (C645S) displayed significantly reduced inhibitory effect. Error bars indicate the means ± SD of three individual experiments. (**B**) Association of PAD4 and the dynamic change of methylation and citrullination of H4 Arg[3] on the pS2 gene promoter in MCF-7 cells. (**C**) As controls, PAD4 was not associated with the promoter of CIITA gene (specific to immune cells). On the ubiquitously expressed GAPDH promoter, background levels of polymerase chain reaction signals were detected from PAD4 ChIP.

namic change of histone H4 Arg^3 methylation and citrullination in HL-60 granulocytes.

Histone Arg methylation at H3 Arg^{17} and H4 Arg^3 is known to regulate estrogen-responsive genes, such as the pS2 gene in MCF-7 cells (*11*, *30*). The observed demethylimination activity of PAD4 suggests it might regulate histone Arg methylation on specific promoters, leading to a change of gene expression. To test this idea, we first analyzed the effect of PAD4 and an enzymatically inactive form of PAD4 ($PAD4^{C645S}$) (fig. S3) on the activity of an EREII-luciferase reporter gene, which can be strongly induced by β-estradiol in MCF-7 cells (Fig. 5A). We found that the wild-type PAD4 effectively repressed the activity of the luciferase reporter in a dose-dependent manner (Fig. 5A), whereas the $PAD4^{C645S}$ mutant displayed weaker inhibitory effects. Intriguingly, the $PAD4^{C645S}$ mutant displays partial repressive activity when present at higher doses. Whether the mutant retains partial enzymatic activity, recruits additional cofactors, or heterodimerizes with endogenous PAD4 in MCF7 cells [as does wild-type PAD4 (*19*)] remains unclear.

The repressive activity of PAD4 on the EREII-luciferase reporter gene prompted us to test whether PAD4 plays a role in regulating the endogenous pS2 gene in MCF-7 cells after estradiol stimulation. We found both PAD4 expression and low amounts of H4 Cit^3 in MCF-7 cells (*28*). With chromatin immunoprecipitation (ChIP) analyses, we showed that PAD4 is associated with the pS2 gene promoter before the addition of estradiol and that PAD4 amounts increased ~twofold at 40 and 60 min after estradiol induction (Fig. 5B). We observed a strong increase of H4 Arg^3 methylation at 20 min and a decrease at subsequent time points, whereas H4 Cit^3 increased at 40 and 60 min. Therefore, the decrease of H4 Arg^3 methylation correlates with the increase of PAD4 protein and H4 Cit^3 levels on the pS2 gene promoter. In addition, PAD4 was not associated with the control CIITA gene and glyceraldehyde-3-phosphate dehydrogenase (GAPDH) gene promoters before or after estradiol treatment (Fig. 5C). These data suggest that PAD4 acts specifically at the pS2 promoter and that its recruitment does not simply result from increased PAD4 expression upon hormone induction. Thus, our data support the conclusion that the demethylimination activity of PAD4 is likely involved in the subtle balance of the estrogen-inducible pS2 gene expression in MCF-7 cells.

Our finding that PAD4 can both deiminate and demethyliminate histones suggests that PAD4 may affect chromatin structure and function via two related but different mechanisms (fig. S5). Regarding demethylimination, histone Arg methylation mediated by secondary co-activators, such as CARM1 and PRMT1, has been correlated with gene activity (*11*–*15*) (fig. S5). Given the paradigm already established by reversible acetylation (*31*–*33*), it seems reasonable that Arg-directed methylation events, particularly those that lead to gene activation, would be reversible. In the case of estrogen-induced genes in MCF-7 cells, we favor the view that PAD4 also functions to remove histone Arg methylation marks, thereby reversing the transcriptional activation brought about by nuclear hormone receptor coactivators and histone arginine methyltransferases, likely in concert with other chromatin modifying activities (e.g., histone deacetylases) (fig. S5). It remains a formal possibility, however, that the repressive effect of PAD4 may be due to its deimination activity, which, in turn, prevents histone methylation by CARM1 and PRMT1. Because of the dual enzymatic activities of PAD4, deimination versus demethylimination, separating any observed transcriptional or other biological effects brought about by PAD4 at target Arg residues will represent a challenge for future studies.

References and Notes

1. T. Jenuwein, C. D. Allis, *Science* **293**, 1074 (2001).
2. B. D. Strahl, C. D. Allis, *Nature* **403**, 41 (2000).
3. Y. Zhang, D. Reinberg, *Genes Dev.* **15**, 2343 (2001).
4. T. Kouzarides, *Curr. Opin. Genet. Dev.* **12**, 198 (2002).
5. M. Lachner, R. J. O'Sullivan, T. Jenuwein, *J. Cell Sci.* **116**, 2117 (2003).
6. A. J. Bannister, R. Schneider, T. Kouzarides, *Cell* **109**, 801 (2002).
7. F. M. Boisvert, J. Cote, M. C. Boulanger, S. Richard, *Mol. Cell. Proteomics* **2**, 1319 (2003).
8. J. D. Gary, S. Clarke, *Prog. Nucleic Acid Res. Mol. Biol.* **61**, 65 (1998).
9. K. A. Mowen *et al.*, *Cell* **104**, 731 (2001).
10. W. Xu *et al.*, *Science* **294**, 2507 (2001); published online 8 November 2001 (10.1126/science.1065961).
11. U. M. Bauer, S. Daujat, S. J. Nielsen, K. Nightingale, T. Kouzarides, *EMBO Rep.* **3**, 39 (2002).
12. D. Chen *et al.*, *Science* **284**, 2174 (1999).
13. B. D. Strahl *et al.*, *Curr. Biol.* **11**, 996 (2001).
14. H. Wang *et al.*, *Science* **293**, 853 (2001); published online 31 May 2001 (10.1126/science.1060781).
15. W. An, J. Kim, R. Roeder, *Cell* **117**, 735 (2004).
16. E. R. Vossenaar, A. J. Zendman, W. J. van Venrooij, G. J. Pruijn, *Bioessays* **25**, 1106 (2003).
17. K. Nakashima, T. Hagiwara, M. Yamada, *J. Biol. Chem.* **277**, 49562 (2002).
18. T. Hagiwara, K. Nakashima, H. Hirano, T. Senshu, M. Yamada, *Biochem. Biophys. Res. Commun.* **290**, 979 (2002).
19. K. Arita *et al.*, *Nat. Struct. Biol.* **11**, 777 (2004).
20. T. Ogawa, M. Kimoto, K. Sasaoka, *J. Biol. Chem.* **264**, 10205 (1989).
21. J. Murray-Rust *et al.*, *Nat. Struct. Biol.* **8**, 679 (2001).
22. See more information on the Fugue program at www-cryst.bioc.cam.ac.uk/fugue/.
23. E. I. Georgieva, R. Sendra, *Anal. Biochem.* **269**, 399 (1999).
24. H. Xie *et al.*, *Methods* **1**, 276 (1990).
25. Materials and methods are available on *Science* Online.
26. T. L. Branscombe *et al.*, *J. Biol. Chem.* **276**, 32971 (2001).
27. J. Sayegh, S. Clarke, unpublished data.
28. Y. Wang, S. Coonrod, unpublished observations.
29. C. Barber *et al.*, *Chromosoma* **112**, 360 (2004).
30. R. Metivier *et al.*, *Cell* **115**, 751 (2003).
31. S. Y. Roth, J. M. Denu, C. D. Allis, *Annu. Rev. Biochem.* **70**, 81 (2001).
32. C. Tse, T. Sera, A. P. Wolffe, J. C. Hansen, *Mol. Cell. Biol.* **18**, 4629 (1998).
33. M. Grunstein, *Nature* **389**, 349 (1997).

34. We are grateful to members of the Allis and Coonrod laboratories, X. Zhang and X. Cheng (Emory University) for insightful discussions and comments, E. Smith for critical reading of the paper, M. Myers (Cold Spring Harbor Laboratory) for help on mass spectrometry analysis and discussions, T. Senshu and M. Yamada for PAD4 reagents, and F. Campagne for bioinformatics expertise. Upstate Biotech, Incorporated participated in Cit3H4 antibody development. This work was supported by NIH grants GM R01 26020 (S.C.), DK55274 (M.R.S.), GM R01 50659 (C.D.A.), and HD R01 38353 (S.A.C.). J.W. is a fellow of the Damon Runyon Cancer Research Fund.

Supporting Online Material

www.sciencemag.org/cgi/content/full/1101400/DC1
Materials and Methods
Figs. S1 to S5
Table S1
References

14 June 2004; accepted 25 August 2004
Published online 2 September 2004;
10.1126/science.1101400
Include this information when citing this paper.

Carbonyl Sulfide–Mediated Prebiotic Formation of Peptides

Luke Leman,[1] Leslie Orgel,[2] M. Reza Ghadiri[1]*

Almost all discussions of prebiotic chemistry assume that amino acids, nucleotides, and possibly other monomers were first formed on the Earth or brought to it in comets and meteorites, and then condensed nonenzymatically to form oligomeric products. However, attempts to demonstrate plausibly prebiotic polymerization reactions have met with limited success. We show that carbonyl sulfide (COS), a simple volcanic gas, brings about the formation of peptides from amino acids under mild conditions in aqueous solution. Depending on the reaction conditions and additives used, exposure of α-amino acids to COS generates peptides in yields of up to 80% in minutes to hours at room temperature.

The first suggestion that COS might be a prebiotic condensing agent appears in a footnote of a paper by Hirschmann and co-workers on peptide synthesis from 2,5-thiazolidinediones (*1*). The authors reported that traces of dipeptide are formed from phenylalanine

thiocarbamate in aqueous solution, but gave no experimental details. More recently, COS has been proposed as a possible intermediate in the hydrothermal formation of dipeptides from amino acids, but was found to be effective only in the presence of nickel and iron sulfides (*2*, *3*). We speculated that COS might have played a more general role as a condensing agent in prebiotic chemistry.

We initially investigated the utility of COS in promoting condensation of L-phenylalanine (*4*). An approximately eightfold excess of COS gas (20 ml, 400 mM) was admitted into an air-free solution of phenylalanine (50 mM) in borate buffer (500 mM, pH 9.6) (*5*). Analysis of the reaction mixture that had stood for 2 days under argon at 25°C, by liquid chromatography–mass spectrometry (LC-MS) and ^{1}H–nuclear magnetic resonance (NMR) spectroscopy using authentic samples as comparators, revealed production of dipeptide in ~7% yield, along with trace amounts of urea derivative **5** (Table 1, entry 1). Analogous reactions in *N*-cyclohexylethane sulfonic acid [CHES (300 mM, pH 9.1)] or trimethylamine [Me_3N (300 mM, pH 9.4)] gave similar product yields, suggesting that buffer catalysis is not important in the rate-determining step of the condensation process.

[1]Department of Chemistry and The Skaggs Institute for Chemical Biology, The Scripps Research Institute, 10550 North Torrey Pines Road, La Jolla, CA 92037, USA. [2]The Salk Institute for Biological Studies, Post Office Box 85800, San Diego, CA 92186, USA.

*To whom correspondence should be addressed. E-mail: ghadiri@scripps.edu

Encouraged by these initial results, we set out to explore the COS-mediated condensation reaction in greater detail.

From a consideration of the reactivity of amine nucleophiles toward COS (*6*), we hypothesized the reaction sequence illustrated in Scheme 1 (*1*). Amino acid **1** first reacts with COS to give the corresponding α-amino acid thiocarbamate **2**. Intramolecular cyclization of **2** yields the α-amino acid *N*-carboxyanhydride (NCA) **4**, also known as a Leuchs anhydride. Thereafter, the well-known and efficient condensation of NCAs with amino acids would proceed through intermediates **6**, to furnish the dipeptide **7** (*7*). The proposed reaction mechanism is supported by the following series of experiments.

To investigate the production and reactivity of the putative intermediate **2**, we probed by ^{1}H-NMR the reaction of L-phenylalanine (25 mM) in D_2O (500 mM borate, pD 8.9) with COS (bubbled slowly

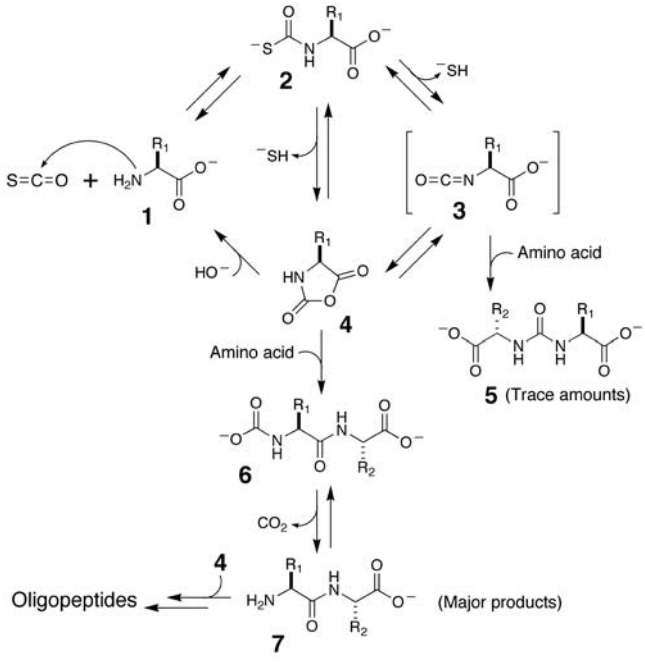

Scheme 1.

Table 1. The yields of major products observed in the COS-mediated condensation of L-phenylalanine under various conditions. All reactions were performed in a 25-ml Schlenk tube with a 2-ml total reaction volume. Reaction yields were determined by reversed-phase HPLC analysis against added acetamidobenzoic acid (ABA) as the internal standard.

Entry	L-Phe (mM)	L-Phe thiocarbamate (mM)	COS (mM)	Additive* (mM)	Final pH†	Time (hours)	Dipeptide (% yield)	Tripeptide (% yield)
1	50	–	400‡	–	8.7§	56	6.8	–
2	–	50	–	–	9.2	65	7.2	–
3	25	25	–	–	9.4†¶	60	5.6	–
4	25	25	–	5 (EDTA)	9.4‖	41	7.2	–
5	50	–	400#	50 ($PbCl_2$)	9.1	11	48.1	1.6
6	50	–	400‡	50 ($PbCl_2$)	8.2	3.5	34.2	1.2
7	25	–	400#	25 ($PbCl_2$)**	8.4	3	20.3	1.6
8	50	–	400‡	50 ($CdCl_2$)	8.4	16	40.0	0.6
9	50	–	400‡	100 [$K_3Fe(CN)_6$]	8.8	20 min	36.3	Nd††
10	25	25	–	50 [$K_3Fe(CN)_6$]	9.2	1.5	55.2	4.4
11	–	70	–	100 [$K_3Fe(CN)_6$]	8.9§	5 min	63.1	12.8‡‡
12	25	25	–	25 ($PbCl_2$)	9.5	27	21.6	0.8
13	25	25	–	25 ($CdCl_2$)	9.2	16	48.0	4.0
14	25	25	–	25 ($FeCl_2$)	9.2	64	23.2	0.8
15	25	25	–	25 ($FeCl_3$)	8.8‖	53	13.6	Nd††
16	25	25	–	25 ($ZnCl_2$)	8.8	17	4.0	–
17	25	25	–	25 (bromoacetate)	9.0‖	31	33.6	0.8
18	–	25	–	25 (bromoacetate)	9.1‖	31	23.2	2.8
19	25	25	–	50 (benzylbromide)§§	9.8‖	32	32.8	–
20	–	50	–	50 (benzylbromide)§§	9.8‖	32	27.3	–

*Metal sulfide precipitates were formed in the reaction mixtures containing divalent metal ions. †Reactions were performed in 300 mM sodium CHES buffer unless otherwise noted. ‡Approximate amounts of COS gas bubbled into the reaction mixture. §500 mM sodium borate, pH 9.6. ¶300 mM Me_3N, pH 9.4. ‖400 mM sodium CHES buffer. #Approximate amounts of COS gas admitted into the Ar-purged reaction vessel. **Reaction was performed in a water sample obtained from the Pacific Ocean, La Jolla, CA. ††Undetermined yield. Product(s) observed by LC-MS. ‡‡Additional products include 2.8% tetrapeptide and traces of penta- and hexapeptide. §§Inhomogeneous reaction mixture due to low aqueous solubility of benzylbromide.

into the NMR tube over 10 min). Surprisingly, the reaction was complete, affording a quantitative yield of phenylalanine thiocarbamate **2** (fig. S1) that was reasonably stable toward hydrolysis under the reaction conditions studied (*8*). To establish that thiocarbamate **2** is a competent reaction intermediate in COS-mediated peptide bond formation, we prepared an authentic sample of analytically pure phenylalanine thiocarbamate **2** (*1*). Anaerobic solutions of L-phenylalanine (25 mM) and phenylalanine thiocarbamate **2** (25 mM) (Table 1, entries 3 and 4) or phenylalanine thiocarbamate **2** (50 mM) alone (Table 1, entry 2), upon standing for 40 to 60 hours, gave dipeptide in 6 to 7% yield. Presumably the free phenylalanine required for dipeptide formation in the latter reaction is produced in situ from the decomposition of phenylalanine thiocarbamate **2** during the course of the reaction. As expected, the yield of peptide from phenylalanine thiocarbamate **2** is pH dependent in the range studied (pH 7.6 to 10.4), with maximum amounts of peptide formed around pH 9.0 (fig. S2). In the lower pH range, an increased rate of thiocarbamate decomposition to the free amino acid and amine protonation can decrease the flux through the productive reaction pathway. At higher than optimal pH values, yields can be reduced by hydrolysis of the thiocarbamate **2** and the NCA intermediate **4**.

Because the thiolate anion is a relatively poor leaving group, the anaerobic intramolecular cyclization of thiocarbamate **2** to give NCA **4** is likely to be the rate-limiting step in the overall condensation process (*9*). To uncover more efficient and thermodynamically more favorable pathways for the conversion of **2** to **4**, we tested a number of additives that could potentially enhance the leaving-group ability of the thiolate anion and provide additional thermodynamic driving force for the reaction (Scheme 2). Dramatic rate accelerations and enhanced product yields were obtained in the presence of metal ions, oxidizing agents, or alkylating agents (Table 1, entries 5 to 20).

The COS-mediated condensation of phenylalanine or the conversion of phenylalanine thiocarbamate **2** to peptide products is substantially enhanced in the presence of stoichiometric amounts of Pb^{2+}, Fe^{2+}, or Cd^{2+} ions (Table 1, entries 5 to 8, 12 to 16; fig. S3) (*10*). Analogous experiments performed with Pb^{2+} or Cd^{2+} under anaerobic conditions gave similar results (Fig. 1A). A reaction was performed in filtered Pacific Ocean water with added Pb^{2+} buffered to pH 9.0 to determine the effect of high salt concentrations and trace inorganic and organic impurities (Table 1, entry 7). Good yields of di- and tripeptide produced after 3.5 hours confirmed the robustness of the reaction. In a similar vein, S-alkylation of the thiocarbamate **2** should enhance the leaving-group ability of the thiol and accelerate its cyclization to the NCA **4** (Scheme 2). The presence of either bromoacetate or benzyl bromide increased the yield of dipeptide formed by a factor of ~4 relative to the basal reaction (Table 1, entries 17 to 20).

Recent reports of oxidative acylation of amines by thioacids (*11*) suggested that oxidative reaction conditions might also accelerate conversion of **2** to **4** via the *bis*-aminoacyl thiocarbamate disulfide **9** (Scheme 2). We confirm that oxygen introduced into the reaction did indeed improve dipeptide yields (fig. S4). However, it is now generally believed that the Earth's primitive atmosphere was free of oxygen (*12*). Alternative plausible prebiotic oxidizing agents are nitrate, nitrite, and ferricyanide ions (*13*). Solutions containing stoichiometric amounts of phenylalanine thiocarbamate **2**, phenylalanine, and potassium ferricyanide afforded greater than 50% yields of dipeptide along with appreciable quantities

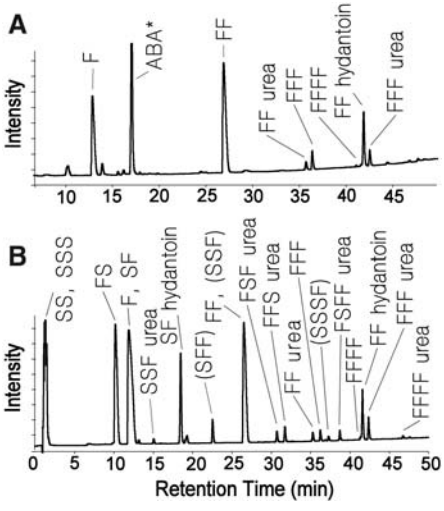

Fig. 1. HPLC-MS chromatograms of COS-mediated condensation of (**A**) L-Phe (Table 1, entry 6) and (**B**) a mixture of L-Phe and L-Ser (Table 2, entry 4) in the presence of $PbCl_2$ analyzed at reactions times of 3.5 hours (wavelength λ = 250 nm) and 3 hours (λ = 220 nm), respectively. Peptides for which product masses were observed but primary amino acid sequences were not determined are indicated in parentheses. ABA was added to the reaction mixture before HPLC analysis as the internal concentration standard. See supporting material for urea and hydantoin chemical structures (fig. S5A). Abbreviations for the amino acid residues: F, Phe; S, Ser.

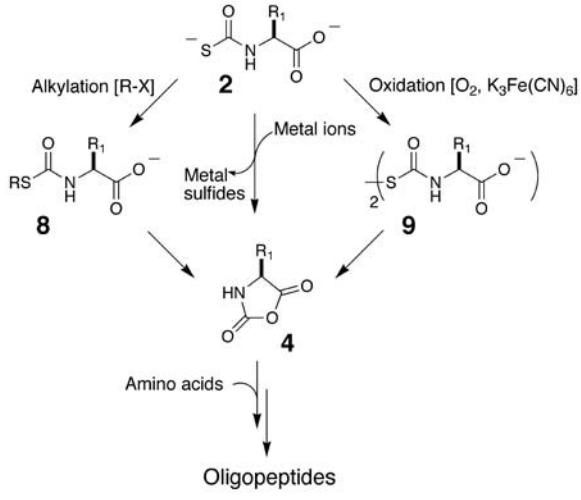

Scheme 2.

Table 2. COS-mediated formation of mixed peptides. Abbreviations for the amino acid residues: A, Ala; F, Phe; L, Leu; S, Ser; Y, Tyr.

Entry*	L-Phe (mM)	Reactant 2 (mM)	$PbCl_2$ (mM)	Final pH	Time (hours)	Observed dipeptides†	Observed tripeptides†
1	10	L-Tyrosine (10)	20	7.2	3	FF, YY, (YF), (FY)	YYY, (YYF), (YFF), FFF
2	25	L-Leucine (25)	50	7.1	3	FF, LL, (FL)	(LLF), (LFF), FFF
3	25	L-Alanine (25)	50	5.9	3	FF, (AF)	(AAF), (AFF), FFF
4	25	L-Serine (25)	50	6.3	3	SS, FF, SF, FS	SSS, (SFF), FFF

*Each experiment was initiated by admitting ~20 ml of COS gas to an argon-purged reaction vessel containing 2 ml of the reaction mixture indicated dissolved in 500 mM Me_3N buffer, at an initial pH of 9.1. Peptide products were identified by LCMS after quenching the reaction at 3 hours. †Peptides for which product masses were observed but primary amino acid sequences which were not determined are indicated in parentheses.

of tri- and tetrapeptides (Table 1, entry 10). When an excess of the oxidizing agent was used with phenylalanine thiocarbamate **2**, LC-MS established that a 63% yield of dipeptide was obtained in just 5 min, along with 13% tripeptide, 3% tetrapeptide, and traces of penta- and hexapeptide (Table 1, entry 11).

In experiments in which a mixture of L-serine (Ser, 50 mM) and the phenylalanine thiocarbamate **2** (25 mM) in CHES (400 mM, pH 9.0) were allowed to react, either in the presence of $CdCl_2$ (25 mM) or $K_3Fe(CN)_6$ (25 mM), a mixture of peptides was produced corresponding to Phe-Ser, Phe-Phe, Phe-Phe-Ser, and Phe-Phe-Phe. No homopolymers of serine were observed. In another experiment, a mixture of L-serine and L-phenylalanine was exposed to COS (Table 2, entry 4). In contrast to the previous reaction, Ser-Ser and Ser-Ser-Ser were produced, along with polymers of phenylalanine and mixed peptides (Fig. 1B). These observations strongly suggest that the activated α-aminoacyl compound derives from the thiocarbamate structure and that, once activation has occurred, peptide formation proceeds via nucleophilic attack by a second α-amino acid molecule on the in situ–formed NCA. The generality of the COS-mediated α-amino acid condensation reactions in the presence of Pb^{2+} was established with reaction mixtures containing equimolar mixtures of L-phenylalanine and either L-tyrosine, L-leucine, L-alanine, or L-serine (Table 2, fig. S5). In all reactions, efficient production of mixed dipeptides and tripeptides was observed.

Present-day levels of COS in volcanic gases have been reported up to 0.09 mol % (*14*). Because the gas hydrolyzes rapidly on a geological time scale, it is unlikely to have accumulated to a high concentration in the atmosphere. Thus, if COS was important in prebiotic chemistry, it is likely to have functioned in localized regions close to its volcanic sources. Although it may be unlikely that a substantial proportion of any amino acids present would have been converted to thiocarbamates, this would have been no obstacle to a "polymerization on the rocks" scenario (*15*, *16*) in which peptides long enough to be irreversibly adsorbed near the source of the COS were subject to slow chain elongation. The direct elongation of peptide chains using COS as a condensing agent and the condensations catalyzed by Fe^{2+} or Pb^{2+} ions seem plausible as prebiotic reactions (*17*). The very efficient polymerizations brought about by oxidizing agents are more problematic as prebiotic reactions, but $[Fe(CN)_6]^{3+}$ has been discussed as a potential prebiotic oxidizing agent (*13*).

It remains to be determined whether COS could have participated in prebiotic chemistry in other ways—for example, as an intermediate in the reduction of CO_2 (*18*, *19*) and as a condensing agent in phosphate chemistry (*20*, *21*).

References and Notes

1. R. S. Dewey *et al.*, *J. Org. Chem.* **36**, 49 (1971).
2. C. Huber, G. Wachtershauser, *Science* **281**, 670 (1998).
3. C. Huber, W. Eisenreich, S. Hecht, G. Wachtershauser, *Science* **301**, 938 (2003).
4. Materials and methods are available as supporting material on *Science* Online.
5. COS is reported to dissolve in water at room temperature to give up to 20 to 30 mM solutions (*6*, *22*).
6. R. J. Ferm, *Chem. Rev.* **57**, 621 (1957).
7. During the course of the reaction substantial quantities of H_2S are generated, for example, through the hydrolysis of COS. Attack of HS^- on the NCA would generate α-amino thioacids that can participate in the formation of peptides and side products (*23*).
8. The observed half-life of phenylalanine thiocarbamate **2** (25 mM in D_2O, pD 8.6) formed in situ from the amino acid and COS was 10 hours. In a separate NMR study using an authentic sample of **2** (50 mM in D_2O, pD 9.0), a hydrolysis half-life of ~20 hours was observed.
9. Condensations of NCAs with free amino acids (100 mM each in borate buffer pH ≈ 10) at 4°C are typically complete in less than 2 min (*1*, *24*).
10. Metal ions that might be present as impurities in the sample are not required for condensation, as demonstrated by formation of product in the presence of the metal chelator EDTA (Table 1, entry 4).
11. R. Liu, L. E. Orgel, *Nature* **389**, 52 (1997).
12. J. F. Kasting, L. L. Brown, in *The Molecular Origins of Life*, A. Brack, Ed. (Cambridge Univ. Press, New York, 1998), pp. 35–56.
13. A. D. Keefe, S. L. Miller, *Origins Life Evol. Biosphere* **2**, 111 (1996).
14. R. B. Symonds, W. I. Rose, G. J. S. Bluth, T. M. Gerlach, *Rev. Mineral.* **30**, 1 (1994).
15. L. E. Orgel, *Origins Life Evol. Biosphere* **28**, 227 (1998).
16. A. R. Hill Jr., C. Bohler, L. E. Orgel, *Origins Life Evol. Biosphere* **28**, 235 (1998).
17. Alternative potentially prebiotic condensing agents with relatively high efficiency are inorganic polyphosphates (*25*, *26*).
18. W. Heinen, A. M. Lauwers, *Origins Life Evol. Biosphere* **2**, 131 (1996).
19. D. R. Herrington, P. L. Kuch, U.S. Patent 4,618,723 (1986).
20. W. C. Buningh, U.S. Patent 3,507,613 (1970).
21. J.-P. Biron, R. Pascal, *J. Am. Chem. Soc.* **126**, 9189 (2004).
22. U.S. Environmental Protection Agency, *Chemical Summary for Carbonyl Sulfide* (Publication 749-F-94-009a, Environmental Protection Agency, Washington, DC, 1994; www.epa.gov/chemfact/s_carbns.txt).
23. T. Wieland, K. E. Euler, *Chem. Ber.* **91**, 2305 (1958).
24. R. Hirschmann *et al.*, *J. Org. Chem.* **32**, 3415 (1967).
25. Y. Yamagata, H. Watanabe, M. Saitoh, T. Namba, *Nature* **352**, 516 (1991).
26. J. Rabinowitz, J. Flores, R. Kresbach, G. Rogers, *Nature* **224**, 795 (1969).

27. We thank NASA Astrobiology Institute and NASA Exobiology (NAG5-12160) for financial support. L.L. is the recipient of an NSF Predoctoral Fellowship.

Supporting Online Material

www.sciencemag.org/cgi/content/full/306/5694/283/DC1
Materials and Methods
Figs. S1 to S5
Reference

13 July 2004; accepted 25 August 2004

Genome Sequence of a Polydnavirus: Insights into Symbiotic Virus Evolution

Eric Espagne,[1]*† Catherine Dupuy,[1]†‡ Elisabeth Huguet,[1] Laurence Cattolico,[2] Bertille Provost,[1] Nathalie Martins,[2] Marylène Poirié,[1] Georges Periquet,[1] Jean Michel Drezen[1]

Little is known of the fate of viruses involved in long-term obligatory associations with eukaryotes. For example, many species of parasitoid wasps have symbiotic viruses to manipulate host defenses and to allow development of parasitoid larvae. The complete nucleotide sequence of the DNA enclosed in the virus particles injected by a parasitoid wasp revealed a complex organization, resembling a eukaryote genomic region more than a viral genome. Although endocellular symbiont genomes have undergone a dramatic loss of genes, the evolution of symbiotic viruses appears to be characterized by extensive duplication of virulence genes coding for truncated versions of cellular proteins.

Once regarded as a rare biological event, symbiosis is now known to be central to the origin of eukaryotic cellular organelles. The genomes of mitochondria and plastids are known to be dramatically reduced compared with those of their ancestors—free-living bacteria (*1*). There are also examples of viral symbionts, but almost nothing is known about the genome rearrangements these have undergone during their evolution.

Polydnaviruses (PDVs) are used by parasitoid wasps to facilitate development of their progeny within the body of immunocompetent insect hosts, which are typically lepidopteran larvae (*2*). Viral particles are produced in the

[1]Institut de Recherche sur la Biologie de l'Insecte, CNRS UMR 6035, UFR Sciences et Techniques, Parc de Grandmont, 37200 Tours, France. [2]Genoscope, Centre National de Séquençage, 2 rue Gaston Crémieux, CP 5706, 91057 Evry, France.

*Present address: Institut de Génétique et Microbiologie, Université Paris Sud, Bat. 400, 91405 Orsay cedex, France.

†These authors contributed equally to this work.

‡To whom correspondence should be addressed. E-mail: catherine.dupuy@univ-tours.fr

wasp ovaries and are injected via the wasp ovipositor into the insect host along with the parasitoid eggs (*2*). Viral gene products act by manipulating host immune defenses and development, thereby ensuring the emergence of adult parasitoid wasps (*3*). Unlike most viruses, polydnaviruses are not transmitted by infection, because no virus replication occurs in parasitized host tissues. They are exclusively inherited as an endogenous "provirus" integrated in the wasp genome (*4*–*6*).

The Polydnaviridae are a unique insect virus family on the basis of the molecular features of their genome and of their obligate association with endoparasitoid wasps (*7*, *8*). They are composed of two genera, bracoviruses and ichnoviruses, associated with braconid and ichneumonid wasps, respectively, with distinct evolutionary origins (*2*). Bracovirus-bearing species have a common ancestor (*9*). The classical hypothesis is that bracoviruses originate from an "ancestor virus" initially integrated into the genome of the ancestor wasp species that lived 73.7 ± 10 million years ago (*10*).

Several PDV genes expressed in parasitized host tissues have been isolated from various wasp species but the organization and content of PDV genomes are largely unknown (*11*). Here, we present the complete nucleotide sequence of the bracovirus (CcBV) injected by the wasp *Cotesia congregata* into its lepidopteran host *Manduca sexta*.

With a full length of 567,670 base pairs (bp), the CcBV genome (Table 1) is one of the largest viral genomes sequenced so far (*11*). The segmented genome is composed of 30 DNA circles ranging from 5 to 40 kb and contains 156 coding DNA sequences (CDSs) (Fig. 1). The overall sequence displays a strong bias toward A-T content (66%), and more than 70% of the sequence corresponds to noncoding DNA. The circles encode at least one gene (with the exception of a single noncoding circle), and the percentage of potential coding sequences varies from 7.4 to 53.9% depending on the circle, a gene density that is markedly different from the highly compact structure of a "classical" virus genome. Unlike most viral genes, many CcBV genes contain introns (69%), and 42.3% of putative CDSs have no similarity to previously described genes (Fig. 2). Another unique feature of the CcBV genome, compared with classical viruses, is the abundance of gene families: 66 genes (42.5%) are organized in nine families (Table 2). It is noteworthy that the proteins encoded by four of these gene families contain highly conserved domains previously described in virulence factors used by bacterial pathogens or parasitic nematodes.

Table 1. Genomic features of CcBV (*Cotesia congregata* bracovirus).

Genomic features	Complete genome
Length (bp)	567670
A+T ratio (%)	66.05
Percent coding sequence	26.9
tRNA coding genes	7
Predicted genes encoding proteins	156
Genes with functional assignments	42
LTR and transposons	10

The largest CcBV gene family comprises 27 genes encoding protein tyrosine phosphatases (CcBV PTP). PTPs are known to play a key role in the control of signal transduction pathways by dephosphorylating tyrosine residues on regulatory proteins (*12*). We recently identified PTPs in bracoviruses of two distantly related braconid subfamilies (*13*) (Table 2), which suggests that they constitute a common component of bracovirus genomes. Bracovirus PTPs share significant similarity with cellular PTPs, but they are not homologous to baculovirus or poxviruses PTPs, which counters the hypothesis that bracoviruses originated from baculoviruses as initially suspected (*14*). Note hat some bacterial pathogens, such as *Yersinia pestis*, inhibit host macrophage phagocytosis by injecting PTPs that interfere with the signal transduction pathways controlling actin cytoskeleton dynamics (*15*). In response to the injection of a foreign body, insect hosts enclose it in a cellular sheath of hemocytes in an encapsulation process that requires adherence, spreading, and attachment of immune cells. Like pathogenic bacteria, parasitoid wasps may inhibit the cytoskeleton dynamics of immune cells using viral PTPs and thus may prevent encapsulation of parasitoid eggs.

The second largest CcBV gene family (CcBV *ank*) comprises six genes encoding proteins with ankyrin repeat motifs. These proteins belong to the IκB family (*16*), whose members are inhibitors of nuclear factor κB (NF-κB)/Rel transcriptional factors, implicated in vertebrate and *Drosophila* immune responses (*17*). As reported recently for other PDVs, CcBV Ank proteins lack the regulatory elements associated with the basal degradation of IκB proteins. Normally, proteolysis of the inhibitor of nuclear factor κB (IκB) releases NF-κB/Rel, sequestered in the cytoplasm by IκB, to translocate to the nucleus and to initiate transcription of immune response genes (*17*). A similarly truncated IκB-like protein is used by a poxvirus (the African swine fever virus) to inhibit the vertebrate immune response (*18*). The truncated forms of the six CcBV Ank proteins may play the same role in lepidopteran hosts.

The third gene family encodes for four predicted cysteine-rich proteins (CcBV *crp*) containing a particular cysteine knot motif (*19*). A similar protein—teratocyte secreted protein 14 (TSP 14)—is encoded by a cellular gene of a braconid wasp species (*20*). The TSP14 protein is secreted by teratocytes (i.e., wasp cells circulating within the host's hemolymph) and, notably, inhibits storage protein synthesis. CcBV Crp proteins may also inhibit translation of storage proteins, such as arylphorin, the level of

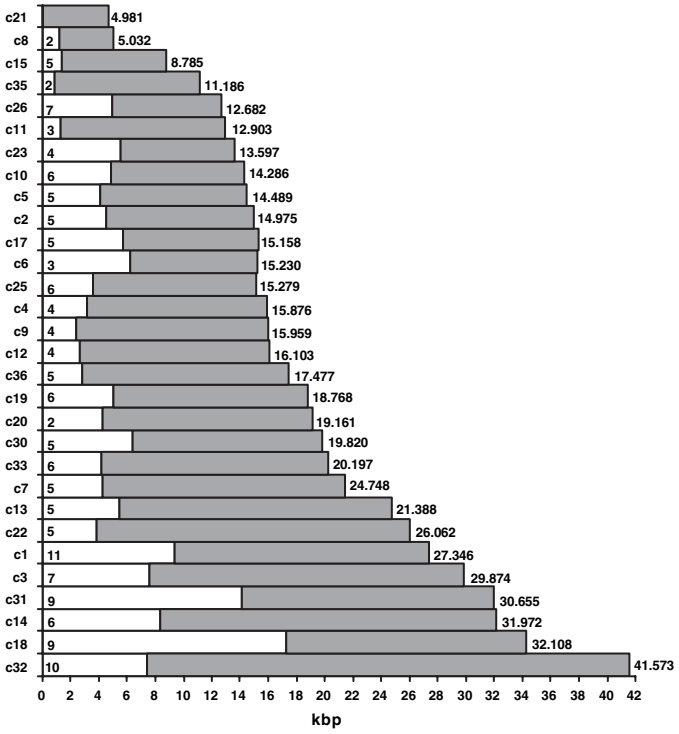

Fig. 1. Graphical representation of the gene distribution for each CcBV circle. Each circle is represented by a bar. Areas in white represent the length of the coding sequence, with the number of coding sequences indicated in black. Areas in gray represent noncoding sequences. The total length of each circle (bp) is indicated in black.

which is dramatically decreased in the hemolymph of parasitized *Manduca sexta* (*21*). Selective disruption of host protein translation is thought to redirect host metabolism to support endoparasite growth and development.

The fourth gene family encodes three cysteine protease inhibitors (CcBV *cyst*) of the cystatin superfamily. Cystatins have been described in a variety of organisms (*22*) but have apparently not previously been found in viruses (*23*). Interestingly, cystatins are also secreted by parasitic filarial nematodes and account for a major part of their immunosuppressive activity (*24*).

The products of the five other gene families do not contain any conserved domains that would allow prediction of their function (Fig. 2). Two genes are only known from *Cotesia congregata* bracovirus (CcBV *hypothetical1* and CcBV *hypothetical2* families), and the other three families contain genes described in viruses associated with other *Cotesia* species (*25*) (CcBV *EP1-like*, CcBV *family1*, CcBV *family2*). Most of these genes are expressed in the host tissues—the EP1 protein, for example, can account for 10% of the hemolymph protein content in parasitized hosts (*26*)—and presumably are required for successful parasitism.

The complex genome of CcBV devotes at least 26% of its CDS to potential virulence factors. Several genes probably originate from duplication events, resulting in multiple multigenic families consisting of up to 27 genes and constituting almost half the CDS. Such gene diversification may have facilitated the radiation of the bracovirus-bearing wasp complex, which now consists of 17,500 species (*9*). Strikingly, CcBV *ank* and CcBV *PTP* resemble truncated versions of cellular genes. Cysteine-knot motif genes have not only been described in PDV genomes, but also in the genome of a braconid wasp (*Microplitis croceipes*) (*20*). Finally, some of the CcBV genes, such as cystatin and histone H4 genes, have apparently not yet been described previously in viral genomes, which suggests that some of the PDV genes have been acquired from the cellular genome. Gene transfer may have occurred into the chromosomally integrated form of the virus, after recombination or transposition events.

Apart from the abundance of virulence factors, the CcBV genome lacks CDS with significant similarity to other virus genes. There are remnants of genes from retrovirus-like elements, but only three genes share significant similarities with sequences from free replicating viruses. Two putative proteins have a significant similarity with a baculovirus protein (48% similarity with *Autographa californica* M nuclear polyhedrosis virus gp94) nonessential for infectivity (*27*). A third protein shows significant similarity (39.9%) to a hypothetical protein from *Spodoptera frugiperda* ascovirus 1 (SfAV1), a member of a family of lepidopteran-infecting viruses (*28*).

Unexpectedly, the bracovirus genome does not contain any set of genes that offers a hallmark for a known virus family. The paucity of "virus-like" genes may be partly explained by the selection pressures acting on PDVs. The genes involved in the production of virus particles do not have to be present on the DNA injected into insect hosts, because virus particles' replication is restricted to wasp ovaries. The demonstration that the p44 gene encoding a structural protein of the *Campoletis sonorensis* ichnovirus is amplified in female wasps undergoing virus

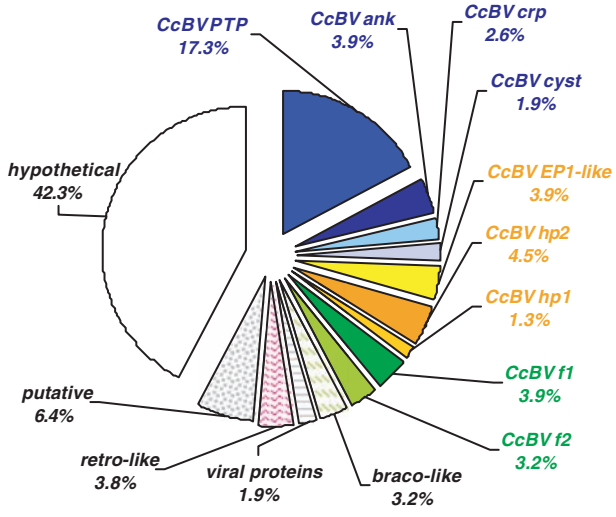

Fig. 2. Classification of the 156 genes identified in the CcBV genome: 42.3% of the genes encode proteins showing no similarity to proteins in databanks (in white); 42.5% of the genes are organized in nine multigenic families (indicated with different colors). In blue are shown genes encoding proteins with well-known conserved domains (PTPs, protein tyrosine phosphatases; ank, ankyrin; crp, cysteine-rich proteins; cyst, cystatins). In orange are shown gene families specific of CcBV (hp1 and hp2: hypothetical 1 and 2). In green are shown gene families common to other species of the *Cotesia* genus. Of the genes, 3.2% are single genes encoding proteins that are homologous to "bracovirus proteins" (hatched green); 1.9% (hatched gray) correspond to the three genes encoding proteins with viral structural domains and 3.8% to the genes that resemble retrovirus-like elements (hatched pink). In dotted-line gray are shown 6.4% of the genes encoding proteins that have similarity with proteins in hypothetical databanks.

Table 2. Features of the CcBV gene families. The features of each gene family are detailed with the circle (C) localization of each gene and the number of related genes on each circle. The average % of similarity of the related proteins are indicated for each gene family. Other PDVs containing such families are indicated. GiBV, *Glyptapanteles indiensis* bracovirus; CsIV, *Campoletis sonorensis* ichnovirus; MdBV, *Microplitis demolitor* bracovirus; HfIV, *Hyposoter fugitidus* ichnovirus; TnBV, *Toxoneuron nigriceps* bracovirus; CkBV, *Cotesia kariyai* bracovirus; CgBV, *Cotesia glomerata* bracovirus.

Parameter	CcBV families								
	PTP	ank	crp	cyst	EP1-like	hp1	hp2	f1	f2
Number of related genes	27	6	4	3	6	2	7	6	5
Circle no.: no. of related genes	C1:8	C11:1	C18:2	C19:3	C1:3	C30:1	C3:1	C9:2	C19:3
	C4:2	C14:2	C32:1		C5:1	C18:1	C6:1	C23:1	C25:1
	C7:1	C15:1	C35:1		C7:1		C9:1	C25:1	C30:1
	C10:5	C26:2			C8:1		C20:1	C33:2	
	C14:3						C23:1		
	C17:5						C25:1		
	C26:3						C33:1		
Percent similarity	<5	19.49	13.79	75	16.34	63.28	33	41.48	75.14
PDVs in which similar gene families are found	GiBV	CsIV	CsIV	None	CkBV	None	None	CkBV	CkBV
	TnBV	HfIV	CgBV					GiBV	
		TnBV	MdBV						
		MdBV							

replication, but is not encapsidated, lends support to this hypothesis (*29*).

The idea that all the genes involved in viral DNA replication and virion production have been transferred to the wasp genome is nevertheless difficult to sustain. A more parsimonious hypothesis would be that bracoviruses do not originate from any of the large genome viruses characterized to date (*30*). They may have been built up from a simple system producing circular DNA intermediates, such as mobile elements, within the wasp genome. The acquisition of a capsid protein, possibly of viral origin, around the circular DNA intermediates would have allowed infection of lepidopteran cells. Finally, virulence genes could have been acquired from the wasp genome at different times during evolution of bracovirus-bearing wasp lineages, thus explaining why CcBV genes encoding proteins with a predicted function resemble cellular genes.

From their genome content, bracoviruses can be discerned as biological weapons directed by the wasps against their hosts. The wasp strategy for delivery of bracovirus genes could inspire medical applications for gene therapy, whereas PDV virulence factors are of interest in agriculture. Currently, a parasitoid gene is already in use in pest-control studies: TSP 14–producing transgenic plants significantly reduce *Manduca sexta* larvae growth and development (*31*). Cystatins also have pesticide activity, because when expressed in transgenic plants, they can reduce the growth of nematodes (*32*). Other potential virulence factors encoded by PDV genomes may also serve as a source of natural molecules with insecticide activity of high specificity (*33*).

References and Notes

1. S. D. Dyall, M. T. Brown, P. T. Johnson, *Science* **304**, 253 (2004).
2. M. Turnbull, B. A. Webb, *Adv. Virus Res.* **58**, 203 (2002).
3. N. E. Beckage, *Parasitology* **116** (Suppl.), S57 (1998).
4. D. B. Stoltz, *J. Gen. Virol.* **71**, 1051 (1990).
5. E. Belle *et al.*, *J. Virol.* **76**, 5793 (2002).
6. J.-M. Drezen *et al.*, *J. Insect Physiol.* **49**, 407 (2003).
7. D. B. Stoltz, P. Krell, M. D. Summers, S. B. Vinson, *Intervirology* **21**, 1 (1984).
8. B. A. Webb *et al.*, in *Virus Taxonomy*, M. H. V. Van Regenmortel *et al.*, Eds. (Academic Press, San Diego, 2002), pp. 253–260.
9. J. B. Whitfield, *Naturwissenschaften* **84**, 502 (1997).
10. J. B. Whitfield, *Proc. Natl. Acad. Sci. U.S.A.* **99**, 7508 (2002).
11. J. A. Kroemer, B. A. Webb, *Annu. Rev. Entomol.* **49**, 431 (2004).
12. J. N. Andersen *et al.*, *Mol. Cell. Biol.* **21**, 7117 (2001).
13. B. Provost *et al.*, *J. Virol.*, in press.
14. J. B. Whitfield, *Parasitol. Today* **6**, 381 (1990).
15. F. Deleuil, L. Mogemark, M. S. Francis, H. Wolf-Watz, M. Fallman, *Cell. Microbiol.* **5**, 53 (2003).
16. S. Ghosh, M. J. May, E. B. Kopp, *Annu. Rev. Immunol.* **16**, 225 (1998).
17. M. S. Dushay, B. Asling, D. Hultmark, *Proc. Natl. Acad. Sci. U.S.A.* **93**, 10343 (1996).
18. Y. Revilla *et al.*, *J. Biol. Chem.* **273**, 5405 (1998).
19. J. Einerwold, M. Jaseja, K. Hapner, B. A. Webb, V. Copie, *Biochemistry* **40**, 14404 (2001).
20. D. L. Dahlman *et al.*, *Insect Mol. Biol.* **12**, 527 (2003).
21. N. E. Beckage, M. R. Kanost, *Insect Biochem. Mol. Biol.* **23**, 643 (1993).
22. M. Abrahamson, M. Alvarez-Fernandez, C. M. Nathanson, *Biochem. Soc. Symp.* **70**, 179 (2003).
23. E. Espagne *et al.*, in preparation.
24. P. Schierack, R. Lucius, B. Sonnenburg, K. Schilling, S. Hartmann, *Infect. Immun.* **71**, 2422 (2003).
25. T. Teramato, T. Tanake, *J. Insect Physiol.* **49**, 463 (2003).
26. S. H. Harwood, A. J. Grosovsky, E. A. Cowles, J. W. Davis, N. E. Beckage, *Virology* **205**, 381 (1994).
27. R. J. Clem, M. Robson, L. K. Miller, *J. Virol.* **68**, 6759 (1994).
28. K. Staziak, M. V. Demattei, B. A. Federici, Y. Bigot, *J. Gen. Virol.* **81**, 3059 (2000).
29. L. Deng, D. B. Stoltz, B. A. Webb, *Virology* **269**, 440 (2000).
30. L. M. Iyer, L. Aravind, E. V. Koonin, *J. Virol.* **75**, 11720 (2001).
31. I. B. Maiti *et al.*, *Plant Biotechnol. J.* **1**, 209 (2003).
32. P. E. Urwin, M. J. McPherson, H. J. Atkinson, *Planta* **204**, 472 (1998).
33. N. E. Beckage, D. B. Gelman, *Annu. Rev. Entomol.* **49**, 299 (2004).

34. This work was supported by the European Community program "Bioinsecticides from Insect Parasitoids" (QLK3-CT-2001-01586). The authors thank A. Bézier and F. Hericourt for useful suggestions; C. Ménoret and J. Dérisson for insect rearing; and N. Beckage for early contribution to the project. Genome circle sequences have been deposited in the EMBL Nucleotide Sequence Database under accession numbers (to circle 1 to 36 respectively): AJ632304; AJ632305; AJ632306; AJ632307; AJ632308; AJ632309; AJ632310; AJ632311; AJ632312; AJ632313; AJ632314; AJ632315; AJ632316; AJ632317; AJ632318; AJ632319; AJ632320; AJ632321; AJ632322; AJ632323; AJ632324; AJ632325; AJ632326; AJ632327; AJ632328; AJ632329; AJ632330; AJ632331; AJ632332; AJ632333.

Supporting Online Material

www.sciencemag.org/cgi/content/full/306/5694/286/DC1
Materials and Methods
References and Notes

21 July 2004; accepted 26 August 2004

New Products

Upstate
For more information
410-218-9121
www.upstate.com
www.scienceproductlink.org

Western Blot Detection Kit

The Visualizer Western Blot Detection Kit provides fast and sensitive detection of antigens, a long-lasting signal, and low background compared with other chemiluminescent detection kits. The combination of high sensitivity and low background is important for working with hard-to-detect proteins. Visualizer is designed to make protein detection easier by using a superior version of the chemiluminescent horseradish peroxidase substrate luminol.

Wolfram Research
For more information
217-398-0700
www.wolfram.com
www.scienceproductlink.org

Graphical User Interface for Math Software

Mathematica users and application developers now have access to a tool that makes it easy to create graphical user interfaces (GUIs) for a wide range of custom implementations. GUIKit is a new development tool built on Java that can be downloaded for free from the Wolfram Research website. GUIKit provides a high-level Mathematica expression syntax for defining graphical user interfaces. Users can quickly build innovative applications that capitalize on Mathematica's trusted computational, graphical, and language capabilities. These applications then enable end-users to perform sophisticated computations with just a few mouse clicks, with no knowledge of Mathematica required. GUIKit can be used to build interfaces to databases or to generate interactive graphics, presentations, and simulations.

BD Biosciences
For more information
800-343-2035
www.bdbiosciences.com
www.scienceproductlink.org

Pin Tool

The BD Pin Tool provides the reusable dispensing performance of a pin tool with the programming convenience of standard pipet tips. The BD Pin Tool fastens to any 96- or 384-well fluid handler just like a standard set of pipet tips. Users can rapidly and reliably transfer both microliter and nanoliter quantities without an intermediate dilution step.

R&D Systems
For more information
800-343-7475
www.RnDSystems.com
www.scienceproductlink.org

Stem Cell Starter Panel

A Human Embryonic Stem Cell Starter Panel is designed for the in vitro expansion of human embryonic stem (ES) cells. It contains recombinant human FGF basic (a growth factor used in human ES cell culture) and a group of antibodies: anti-Oct-3/4, anti-SSEA-4, and anti-alkaline phosphatase for monitoring the differentiation status of human ES cells.

The Baker Co.
For more information
800-992-2537
www.bakerco.com
www.scienceproductlink.org

Class III Glovebox

The IsoGARD series class III glovebox is designed for research when a high level of containment is required. The cabinets are well-suited for aerosolization studies, vaccine research, infectious disease diagnostics and research, handling of sterile potent pharmaceutical compounds, and inspection of suspected chemical and biological terrorism samples. It is built to the highest leak-tightness specifications to ensure the safety of laboratory workers. "Plug-and-seal" canister-style high-efficiency particulate air (HEPA) exhaust filters provide environmental protection and allow for safe and convenient changing of loaded filters. It comes in three standard models, which offer two-, three-, and four-glove primary working chambers. It includes an integral, full-size, HEPA-filtered pass-through chamber with a unique front-opening glass panel door that allows users to introduce samples into the main working chamber with ease.

Upchurch Scientific
For more information
800-426-0191
www.upchurch.com
www.scienceproductlink.org

Nano-Fluidic Module

The Confluent NFM (nano-fluidic module) delivers isocratic solvents at flow rates from near zero nL/min to 4.5 μL/min. The unit includes three major components: a single sapphire piston displacement pump, a noninvasive flow sensor, and a four-position selection valve. The Confluent NFM facilitates ultralow flow fluid handling applications such as nanospray mass spectrometry, trap column regeneration, lab-on-chip infusion, mass spectrometric mass calibration, and nano-liquid chromatography.

Matrix Technologies
For more information
800-345-0206
www.matrixtechcorp.com
www.scienceproductlink.org

Ceramic Pins for Microarraying

A new ceramic microarraying pin dramatically improves spot uniformity and efficiency of sample utilization, shortens printing run times, and eliminates pre-blotting with most print buffers. Matrix NanoPins offer printing performance equal to non-contact technologies at prices below traditional contact printing pins. The uniformity of spot size and morphology achievable with NanoPins exceeds that of comparable metal pins. The capillary design reduces sample loss due to evaporation and the chemically inert ceramic material has a significantly longer lifetime than metal quill pins. In addition, NanoPins are produced to extremely tight dimensional tolerances, which eliminates the tedious testing required to produce matched pin sets.

Bender MedSystems
For more information
+43 1 796 40 40-0
www.bendermedsystems.com
www.scienceproductlink.org

Multiple Cytokine Detection

The new mouse FlowCytomix Kits allow simultaneous quantification of multiple cytokines (GM-CSF, IFN-γ, IL-1α, IL-2, IL-4, IL-5, IL-6, IL-10, IL-17, TNF-α). The kits are suitable for use on all commonly used flow cytometers and offer flexibility: combinations of any of the nine cytokines are possible. The 96-well filter plate format provides easy handling.

Newly offered instrumentation, apparatus, and laboratory materials of interest to researchers in all disciplines in academic, industrial, and government organizations are featured in this space. Emphasis is given to purpose, chief characteristics, and availability of products and materials. Endorsement by *Science* or AAAS of any products or materials mentioned is not implied. Additional information may be obtained from the manufacturer or supplier by visiting www.scienceproductlink.org on the Web, where you can request that the information be sent to you by e-mail, fax, mail, or telephone.